FLUORESCENT MICROSCOPY IN THE NUCLEUS: INVESTIGATING PROTEIN
DIFFUSION AND BINDING IN LIVE CELLS

Matthew Kyle Daddysman

A dissertation submitted to the faculty of the University of North Carolina at Chapel Hill
in partial fulfillment of the requirements for the degree of Doctor of Philosophy in the
Department of Chemistry

Chapel Hill
2013

Approved by:

Christopher Fecko

John Papanikolas

Dorothy Erie

Andrew Moran

Linda Spremulli

ABSTRACT

Matthew Kyle Daddysman: Fluorescent Microscopy in the Nucleus: Investigating Protein Diffusion and Binding in Live Cells
(Under the direction of Christopher J. Fecko)

One of the open questions in biophysics is the process by which DNA-binding proteins, transcription and repair proteins, find very specific binding sites that are minuscule in comparison to the size of the genome. *In vitro* results have provided some insight into the search mechanism; however, these studies simulate neither the complicated DNA topography nor the crowded macromolecular environment present inside live cells. The focus of this dissertation is the development of microscope technology and experiments that build toward the ultimate goal of probing DNA-binding protein transport and binding in live cells.

Fluorescence recovery after photobleaching (FRAP) is used to study anomalous diffusion of unconjugated green fluorescence protein (GFP) in the polytene cells of *Drosophila* larval salivary glands. Polytene nuclei contain optically resolvable chromosomes, permitting FRAP experiments that focus separately on chromosomal or interchromosomal regions. GFP exhibits anomalous diffusion in the chromosomal regions, but diffuses normally in regions devoid of chromatin. This observation indicates that obstructed transport through chromatin is the source of anomalous diffusion in polytene nuclei and likely other cells. *In vitro* studies of GFP diffusion in artificial crowding environments confirm normal diffusive behavior in crowded

environments similar to the interchromatin space. The diffusion dynamics of two RNA Polymerase II subunits in the interchromatin space exhibit anomalous diffusion in direct contrast to the normal diffusion of unconjugated GFP. This *apparent* anomalous diffusion in both unengaged subunits is a result of the subunits' incorporation into a broad distribution of complexes, with sizes ranging from free proteins to fully assembled gene transcription units. The broad distribution of macromolecular species allows for mechanistic flexibility in the recruitment of RNA Polymerase II.

Perturbations of the DNA environment with an optical microscope, such as generating well-defined regions of ultraviolet (UV)-like photolesions, assist investigations into the spatiotemporal dynamics of a class of DNA-binding proteins, DNA repair proteins. The production of thymine cyclopyrimidine dimers, the primary UV DNA photoproduct, is demonstrated using multiphoton excitation of DNA in live cells with visible light pulses. The spatiotemporal recruitment of GFP-tagged topoisomerase I to sites of localized DNA damage is investigated through this method.

To my grandmother, Mallador Mathew, who always asked about my red-eyed fruit flies

ACKNOWLEDGEMENTS

"You teach me, I forget. You show me, I remember. You involve me, I understand."

– E.O. Wilson

As I begin to write this section I realize that it is not humanly possible to thank all of my friends, family, and teachers that have inspired me and assisted in my journey to this point. If your name is not mentioned below, please recognize yourself in this general statement of my gratitude.

First and foremost, I want to thank my graduate advisor, Chris Fecko. I am lucky to have studied under such a caring mentor and capable scientist. I am glad that our research interests aligned, allowing me to continue dabbling in biology while becoming a physical chemist. I hope that I have picked up your skills of skeptical and thorough inquiry. It may be cliché, but if I become half the scientist that you are, I will consider myself well accomplished.

I could not have asked for a better group of lab mates for my graduate studies, Ian McNeil, Michael Tycon, and Catherine Dial. Ian, I thank you for your assistance in "learning the ropes" of microscopy and always being willing to assist in re-aligning the laser in the early years after I had messed everything up. Your willingness to discuss topics both inside and out of science helped me greatly. Catherine, I thank you for patience, hard work, and humor for the time while you worked under my guidance. Michael, thank you for your scientific guidance and continuing to create

weight lifting programs for me, even though I never followed them to completion. I appreciate your willingness to discuss life both inside and outside of work, and your advice, though always taken with a grain of salt, is worthwhile all the same.

I was lucky to have excellent science educators as early as middle school. Karen Hyde and the late Glenn Righman, I thank you for sparking my interest in science from an early age. From high school, I want to thank Joseph Boutwell, who taught me science was investigation and not a collection of facts; David Everson, who first interested me in the Biological sciences; and Pat Maruca, who taught me (almost) everything I know from Algebra to Calculus and everything in between.

All of my professors at Alderson-Broaddus College deserve mention; however, I will selectively highlight these four. First, Charlie Chen, who gave me my first laboratory research experience. Thank you for your faith in me and your continued friendship. I am grateful for the knowledge that you gave to me, some of which I was able to carry over into my graduate research. David Aylmer, who taught me most everything I know about chemistry. I thank you for your patience and that your office door was always open for my questions. John Enz, who convinced me to attend Alderson-Broaddus and pursue a double chemistry and biology major (despite his best efforts to kill my desire with his Botany class). And finally David Unger, whose focus on "thinking outside the box" when it came to viewing world issues in light of scientific fact greatly influenced me. You handed me the shovel for the groundbreaking of my scientific worldview.

My life would not have as high as quality without the influences of the arts. I would be remiss if I did not thank Victor Iapalucci for his development of my passion for consuming and making music. I am thankful for the opportunity of stepping back from

my scientific world -- even as I sit here now in late July 2013 at band camp composing part of this dissertation -- to offer my skills in the production of the field show for "The Pride of Barbour County." I look forward to seeing you and the entire band camp team each year.

My family has been a constant source of support over the years. To my sister Jennifer, your gift with English to take my rambling, awkward writing and edit it into fine, flowing prose has been extremely beneficial. Furthermore, your friendship, advice, and willingness to listen have been indescribably helpful. I cannot thank you enough. To my parents, Jim and Jean Daddysman, I want to thank you for all the support you have given me the past twenty-six years. I can never repay my debt, and I hope that I have successfully followed Dad's advice when I was young: "Be like a sponge and soak up everything you can learn."

TABLE OF CONTENTS

LIST OF TABLES

LIST OF FIGURES

LIST OF ABBREVIATIONS AND SYMBOLS

$<\Delta r^2>$	Mean squared displacement
BBO	β-barium borate
BIC	Bayesian information criterion
BSA	Bovine serum albumin
c	Concentration of bright state flurphore (Chapter 1); Concentration of the crowder (Chapter 3); Weighting coefficient in the distribution model (Chapter 4)
CPD	Cyclopyrimidine dimers (thymine-thymine CPD unless otherwise stated)
CW	Continuous wave
D	Diffusion coefficient
d	Dimensionality of the system
D_{eff}	Effective diffusion coefficient
DIMED	Damaged induced by multiphoton excitation of DNA
DNA	Deoxyribonucleic acid
$F(t)$	FRAP signal
F_0	Pre-bleach intensity in a FRAP experiment
$\mathcal{F}(t)$	Distribution model FRAP signal
FCS	Fluorescent correlation spectroscopy
Fl	Emitting (bright-state) fluorophores
FRAP	Fluorescence recovery after photobleaching
FWHM	Full width half max
GaAs	Gallium Arsenide

GaAsP	Gallium Arsenide Phosphide
GFP	Enhanced green fluorescence protein
H2B	Histone 2B
I^2	Excitation intensity profile of the two-photon microscope
i	BIC model index (Chapter 2); Summation index (Chapter 4)
IB	Irreversibly bleached (permanent dark-state) fluorophores
IR	Infrared
j	Summation index
K	Number of parameters in a model for the BIC test
ln	Natural logarithm
M	Molar mass
mRFP	Monomeric red fluorescent protein
n	Number of points fit (eq. 2.1); Summation index (Chapter 1; eq. 2.4 & 2.6)
n_D	refractive index (specifically measured at 589 nm and $20^{\circ}C$)
NA	Numerical aperture
PBS	Phosphate buffered saline
PBT	PBS with 0.1% Triton-X-100
PMT	Photomultiplier tube
ptFRAP	Point FRAP
Q_{FI}	Constant related to the efficiency of imaging
RB	Reversibly bleached (dark-state) fluorophores
RNA	Ribonucleic acid
RNAPII	RNA Polymerase II

Rpb3	RNA Polymerase II subunit 3
Rpb9	RNA Polymerase II subunit 9
t	Time
t_{laser}	Time of laser observation in a FRAP experiment
TopI	Topoisomerase I
UV	Ultraviolet
UVC	Ultraviolet subtype C (100 – 280 nm)
w	Akaike weight of a model in the BIC test
α	Anomalous parameter
β	Factor related to the bleach depth
Γ	Transport coefficient
Δ	Difference between each model and the best model in BIC test
δ	Magnitude of the photophysics decay
η	Viscosity
τ_D	Residence time of area of radius ω
τ_{PP}	Photophysics decay constant
ω_r	Beam radius ($1/e^2$) in the xy plane
ω_z	Beam radius ($1/e^2$) in the z plane

CHAPTER 1: INTRODUCTION

"Somewhere, something incredible is waiting to be known." – Carl Sagan

1.1. Motivation for Research

1.1.1. Motivation for Studying Diffusive Transport in Cellular Systems

One of the open questions in biophysics is how DNA-binding proteins (e.g. RNA transcription factors and DNA repair proteins) navigate both the crowded nucleoplasm environment and the complicated topology of DNA *in vivo* to 1) locate specific binding sites that are only a few base pairs long, miniscule in comparison to the genome which consists of more than 10^9 base pairs and 2) conduct this search on a timescale fast enough to sustain metabolic processes necessary for life to exist. The transport of proteins through the nucleoplasm is not unique to DNA binding proteins as many biological processes rely on the transport of macromolecules through the cellular milieu. However, this crowded environment of macromolecules, membranes, and cellular skeletal structures, each tailored to a specific purpose inside the cell, could present obstacles to transport. This hindrance is exhibited as deviations of a particle's mean squared displacement from linearity as predicted by the diffusion equation. Although the observation of sublinear deviations of the mean squared displacement, termed anomalous subdiffusion, is ubiquitously observed in cells,[1-6] the observation of anomalous subdiffusion does not indicate the source.[7] Therefore, careful understanding of the nature of the transport physics must precede any investigations

concerning DNA-protein binding interactions. Otherwise, hindered diffusion may be mistaken for binding interactions.

1.1.2. Finding DNA binding sites

The spatiotemporal dynamics of the protein-DNA interaction is of particular interest to biophysical chemists because *in vitro* data indicate that the interaction occurs on timescales that are much faster than those predicted by simple diffusion models. In 1970, Riggs and coworkers found that the association rate of the *Escherichia coli* Lac repressor and a single operator site on a large DNA molecule is ~10^{10} M^{-1} s^{-1},[8] which is at least two-orders of magnitude faster than predicted by the Debye-Smoluchowski one-step diffusion limited model. To account for this discrepancy, a two step model was proposed where nonspecific DNA-protein binding is followed by subsequent "facilitated diffusion" to a binding site.[9] These models predict an ideal sliding length of ~100 bp and then dissociation to 3D diffusion[9-15] (Figure 1.1). However, direct experimental confirmation of the hypothesis of a facilitated diffusion model is limited to *in vitro* single molecule studies,[16-19] with only limited results from work *in vivo*.[20]

1.2. Background

1.2.1. Nature of Transport in Cells

In a neat, homogenous solution, a particle will diffuse according to Brownian dynamics in which the mean squared displacement will grow linearly in time (t):

$$\langle \Delta r^2 \rangle = 2dDt \qquad (1.1)$$

where $\langle \Delta r^2 \rangle$ is the mean squared displacement, d is the dimensionality of the system, and D is the diffusion coefficient. However, highly heterogeneous environments, such as cells, complicate the transport picture which results in deviations from linearity in the
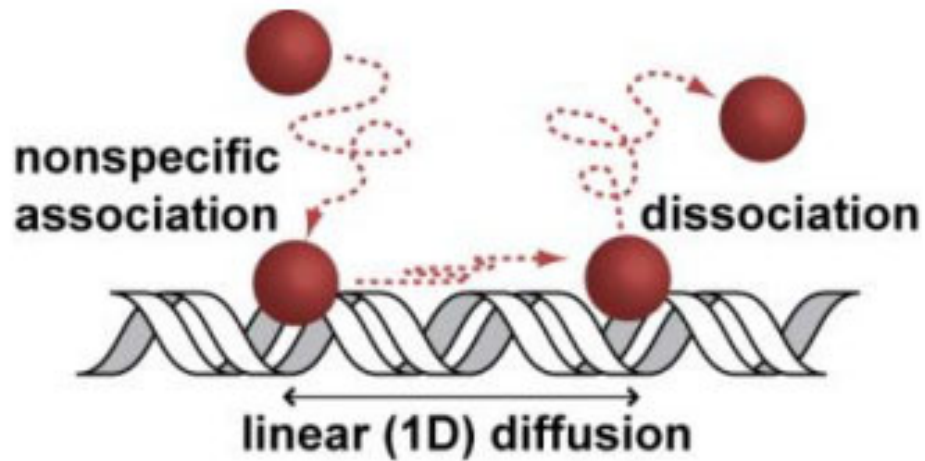
Figure 1.1: A schematic of a DNA-binding protein search for a binding site. This proposed scheme is hypothesized to account for the faster then 3-D diffusion limit search observed by the Lac repressor.[8] The DNA-binding protein has nonspecific affinity for DNA; therefore, the protein will transiently bind to the DNA nonspecifically to conduct a 1-D search along DNA. This model has support from single molecule studies *in vitro*.[17-19]

mean squared displacement.   Termed anomalous diffusion, the mean squared displacement is now modeled by a non-linear power-law in time[21,22] which modifies Eq. 1.1 as follows:

$$\langle \Delta r^2 \rangle = 2d\frac{\Gamma}{\alpha}t^\alpha \qquad (1.2)$$

where Γ is the transport coefficient and α is the anomalous parameter. The anomalous parameter indicates the deviation from normal Brownian behavior. If $\alpha > 1$ the process is considered superdiffusive.   Active cellular transport of proteins is indicated by superdiffusive behavior.   If $\alpha < 1$ the process is considered subdiffusive and the transport is hindered inside the cell. Subdiffusion is the primary consideration of this dissertation and has been shown to be fairly universal in the cellular environment.[1-6] Theoretical studies have shown that subdiffusive behavior may increase the efficiency of enzymatic action.[23,24]

Several underlying physical mechanisms have been proposed for subdiffusive behavior including interaction with a distribution of energetic traps, obstructed diffusion in the presence of immobile obstacles, and correlated motion that arises an interacting system.[7,25]   Each of these sources has a unique underlying physical model that gives rise to the anomalous behavior. However, in order to observe these signatures single molecule experiments are required to distinguish between slight variations in the mean squared displacement. For example, the continuous time random walk model proposed to model energy traps would exhibit weak ergodicity breaking; whereas, all the other models are ergodic.[7]   These variations are averaged out in ensemble measurements and, therefore, only discernible with single molecule imaging. As I discuss in **Chapter 2** control of the experimental parameters can eliminate potential sources of anomalous

diffusion allowing ensemble measurements, such as fluorescence recovery after photobleaching (FRAP), to reveal the underlying source of anomalous diffusion in some cases. For example, by probing a biologically inactive molecule, such as unconjugated green fluorescent protein (GFP), energy traps can be eliminated as a potential source of anomalous diffusion since unconjugated GFP should not have specific binding sites inside the cell. Another method, described in **Chapter 3**, is creating artificial cellular environments crowded by high concentrations of macromolecular crowders. Such an environment allows the contribution of macromolecular crowding, if any, to anomalous diffusion to be quantified.

1.2.2. Assembly of macromolecular complexes

Most processes in the nucleus occur through the coordinated effort of several proteins working in concert to perform a specific task.[26-28] However, these proteins are produced and exist as discrete entities inside the cell. The processes by which these proteins assemble to form a functional macromolecular complex is blended into the term "protein recruitment," a black box of sorts which is often passed over in pursuit of the understanding of the function of the complex. The two common models for the assemble of the multi-protein complexes are a "top-down" and "bottom-up" approach.[29] In a "top-down" approach, the proteins are assembled into a large macromolecular complex prior to association with a binding site, forming a long lived molecular factory.[30,31] This is in contrast to a "bottom-up" approach, in which the complex is assembled piece by piece at the promoter site. The distinct dynamics of individual proteins involved in a complex is cited in support the latter model;[32-34] however, this result is debatable.[35-37]

The process of RNA transcription, accomplished by RNA Polymerase II (RNAP II) along with a large complex of transcription factors and stabilizing factors, provides a system by which the two models of macromolecular complex formation can be tested. In previous studies of RNAP II, the diffusion of the protein has been measured near the promoter site[32,34,38] which cofounds the ability to probe the nature of the assembly of the complex. Details about the association between the proteins in a complex can be ascertained by measuring the dynamics of RNAP II away from DNA promoter sites. The proteins that assemble to form a complex may continue to have some intrinsic affinity even away from the promoter site, and therefore complexes may still form away from the DNA binding site. A possible exception is if binding with DNA changes a protein conformation to stabilize an interaction with another protein. However, it is quite possible that even in these circumstances the proteins still retain weak affinity. In **Chapter 4**, I present a model that is used to analyze FRAP data collected by Michael Tycon on the RNAP II system in the interchromatin space of the *Drosophila melanogaster* polytenes. This model is used to observe distribution in sizes of diffusing complexes of proteins.

1.2.3. Finding specific binding sites on DNA

Binding sites (energy traps) are one of the possible contributions to anomalous diffusion in live cells.[7] However, applying a FRAP reaction-diffusion model (which has been derived)[39] requires that the contribution of the other potential sources of anomalous diffusion described above are quantified so that the binding is not misinterpreted as another form of anomalous diffusion. There are several strategies creating a binding site that is observed using live cell microscopy, such as introducing

an exogenous binding site,[20] probing an endogenous site that is activated by an outside perturbation such as heat shock,[40] or by introducing DNA damage that is then repaired by DNA repair enzymes.[41-45] The last option is ideal for my research as the same tools that are used for imaging are only slightly modified to produce damage. In **Chapter 6**, I develop a method for creating "UV-like" photolesons using direct multiphoton excitation of DNA. The spatiotemporal recruitment of topoisomerase I (TopI) is measured to the damaged regions of DNA. TopI relaxes supercoiled DNA by creating a transient single strand break in one strand of the DNA backbone through which the other strand can pass. TopI activity is implicated in DNA transcription, replication, and repair,[46] and, therefore, is an essential gene in the *Drosophila* model.[47] TopI is an ideal system for this study as it is a monomeric system so protein complexes do not need to be considered.

1.3. Methods

1.3.1. Two-photon microscopy

All of the investigations undertaken in this dissertation use a laser scanning two-photon microscope. In nonresonant two-photon absorption, a molecule exposed to a high photon flux can simultaneously (within attoseconds) interact with two photons, producing an excited state equivalent in energy to the summation of the energy of the interacting photons.[48] The probability of a two-photon absorption event depends quadratically on the intensity of the applied light. For light focused at an objective lens, the intensity drops quickly outside of the focal point, resulting in a steep drop in the probability of two-photon excitation. This steeply decreasing probability of excitation outside of the focal point of the objective is leveraged to obtain depth discrimination in

two-photon microscopy (Figure 1.2).[49,50] The advantage of two-photon microscopy over confocal microscopy is that the depth discrimination is obtained in the excitation rather than the imaging pathway. Since only imaged fluorophores are excited, out of plane photobleaching is eliminated. Likewise, localized photochemical reactions can be inducted by two-photon excitation. An application of two-photon photochemistry to induce DNA "UV-like" photolesions is discussed in **Chapter 6**.

The microscope setup uses a tunable (680 – 1080 nm) Ti:sapphire laser in a laser scanning configuration (Figure 1.3).[51] The output beam from the laser is attenuated by a Pockels cell and half wave plate, allowing microsecond control of the beam intensity. The beam is introduced into the sample through an Olympus IX81 inverted microscope. A 60x, 1.20 NA objective focuses the beam into the sample and collects the fluorescence from the sample. The fluorescence is separated from the excitation light via a dichroic mirror. The fluorescence is detected by non-descanned GaAsP PMTs. Separation into red and green channels is accomplished using another dichroic mirror and band pass filters for two-color imaging. The setup also serves a dual purpose of creating spatially confined DNA photolesions. As described in **Chapter 6**, a separate beam pathway incorporating a nonlinear β-barium borate crystal is used to frequency double the output of the Ti:sapphire laser to produce the photolesions using a photochemical reaction.

1.3.2. *Drosophila melanogaster* **Polytenes**

The model organism used for most of the live cell microscopy in this dissertation is the *Drosophila melanogaster*. The salivary glands of *Drosophila* larva contain polytene chromosomes. The polytene chromosome contains approximately a thousand
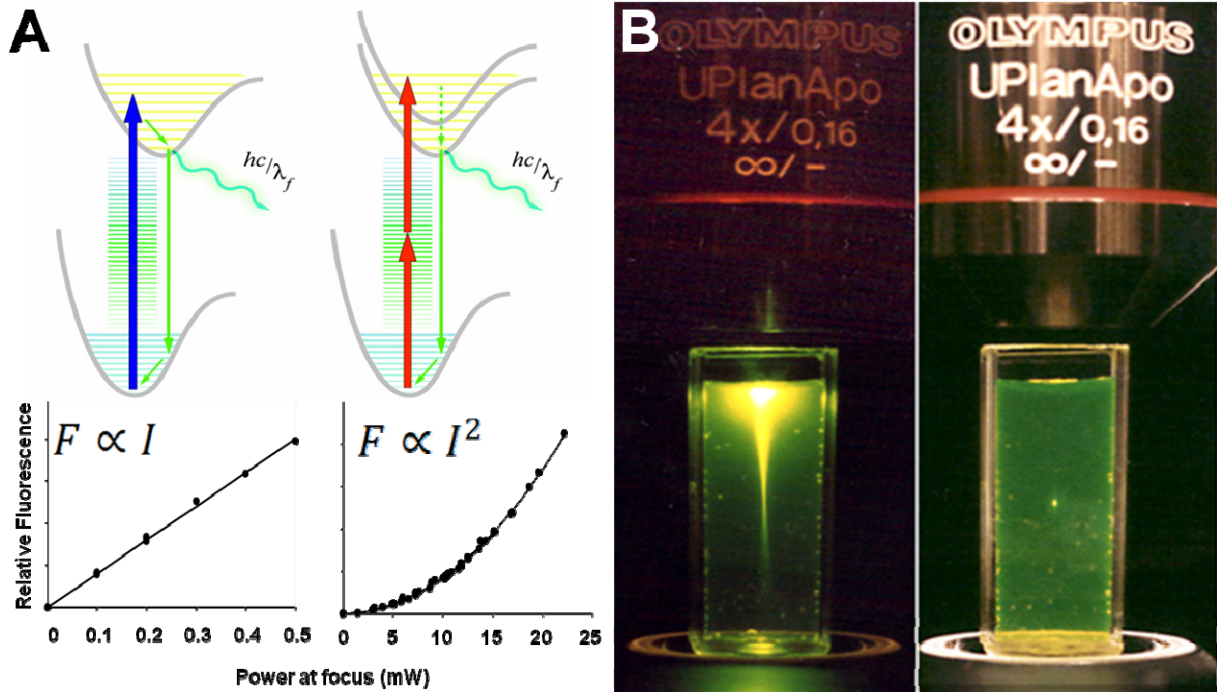
Figure 1.2: Two-photon excitation is used for depth discrimination in two-photon microscopy. (A) In conventional linear excitation, a single photon with sufficient energy excites an electron from the ground state to the excited state of a fluorophore. After excited-state vibrational relaxation, the remaining energy is released as a photon of light as the electron returns to the ground electronic state. The number of excitation events (and, therefore, the number of fluorescent photons produced) is directly proportional to the intensity of the excitation light. In two-photon excitation, two non-resonate photons with approximately half the energy of the electronic energy gap are absorbed simultaneously. Since two photons are necessary the number of excitations events is quadratically proportional to the intensity of the excitation light. (B) The axial confinement of two-photon excitation is demonstrated using a cuvette of fluorescein. On the left, a 488 nm laser is focused into sample exciting fluorophores throughout the focusing cone of the object. In contrast on the right, a 900 nm pulsed laser is focused into the sample. Sufficient photon flux to excite the fluorescein only occurs it the focal point of the objective, where a small dot of fluorescence occurs.
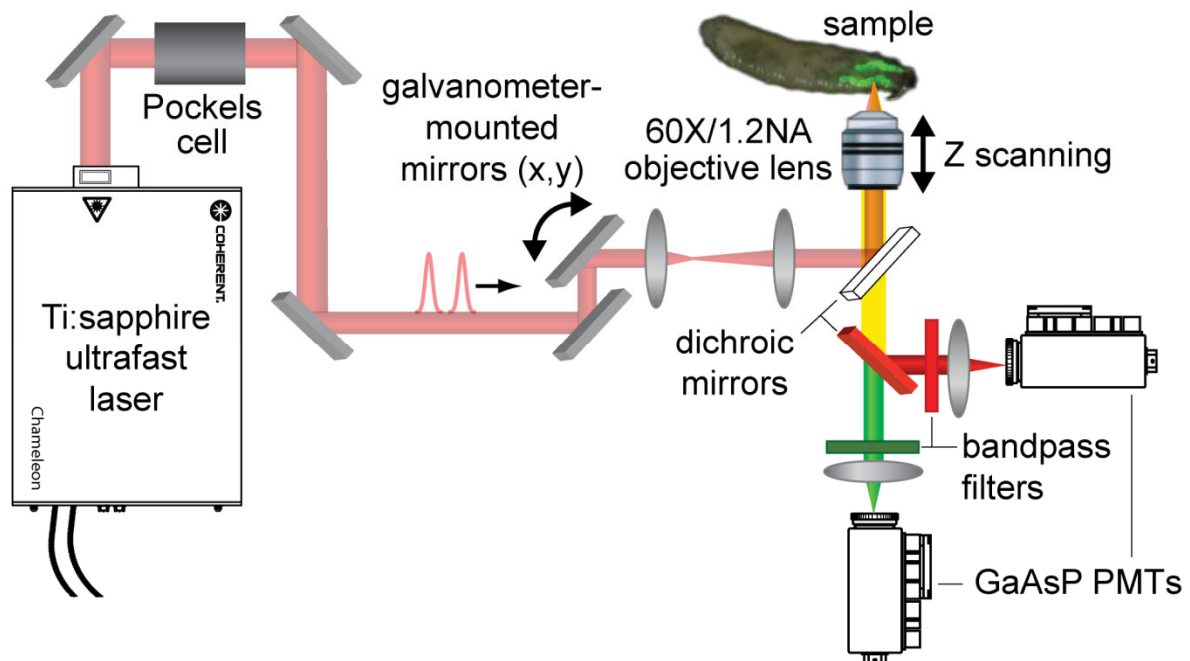
Figure 1.3: Schematic of the laser scanning two-photon microscope used for experiments in this dissertation. Details of the setup are given in section 3.1.

copies of the genome in contrast to the one or two copies carried by normal cells, depending on the stage of the cell cycle. The chromosomes remain structurally organized, allowing chromosomes to be distinguished from nuceloplasm without DNA, and is referred to as the interchromatin space. In contrast, the diffuse chromatin of typical cells contains DNA and nucleoplasm in an indistinguishable mixture. Several *Drosophila* lines stabling expressing fluorescent protein fusions are used in this dissertation. The line containing TopI fused to GFP was tagged at its endogenous locus using a "trap strategy" as described by Morin *et al.*[52] The remaining *Drosophila* lines express transgenes using a *Gal4* upstream activation sequence. The *Gal4* driver line (Bloomington Fly Stock #6979) used in this dissertation activates the transgene during the larval stage of the *Drosophila* in the salivary glands only. The unconjugated GFP line was purchased from the Bloomington Stock center (line #5430). The histone 2B conjugated to red fluorescence protein, and the RNA Polymerase units, Rpb3 and Rpb9, conjugated to GFP constructs are described in Zobeck *et al.*[53] and are a gift from John Lis's lab at Cornell University.

1.3.3. Fluorescence Recovery after Photobleaching

FRAP is the microscopy technique used extensively in this dissertation. The principle of FRAP is simple. A region of fluorescent protein is permanently photobleached by short exposure of high intensity laser light. This region is then monitored for a recovery in fluorescence intensity as unbleached fluorophores diffuse into the region. The boundary conditions of the bleach region can be used to solve the diffusion equation to back out the diffusion coefficient and other information about the system such as binding constants based on the speed of recovery of the fluorescence.
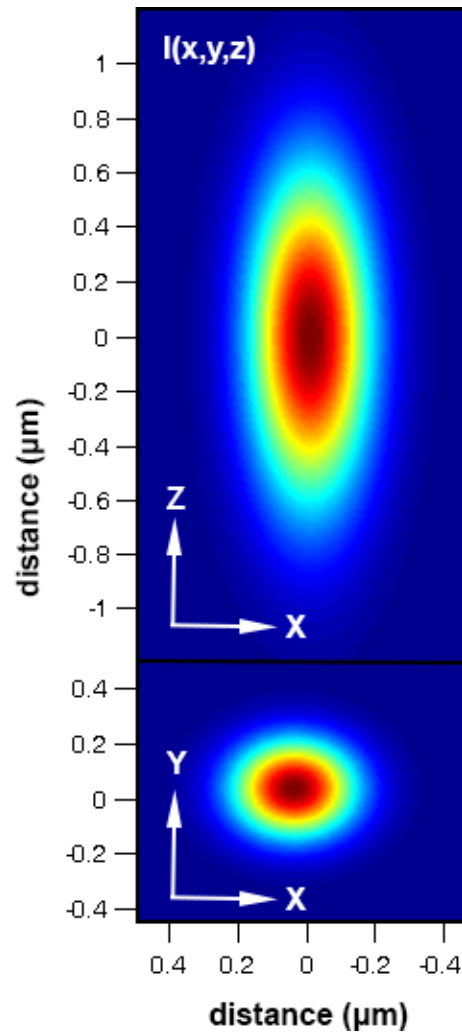
Figure 1.4: Point spread function of the two-photon microscope used as the bleach and observation regions of interest in a FRAP experiment. (A) Heat map of the point spread function as a slice through the X, Z plane. The $1/e^2$ radius used was 350 nm in X and Y and 1200 nm in Z. (B) Same point spread function presented in panel A except showing a slice in the X, Y plane.

In this dissertation, I use a flavor of FRAP, referred to as point FRAP, where the region of interest is the point spread function of a two-photon microscope. The point spread function can be accurately approximated by a three-dimensional Gaussian[54] (Figure 1.4):

$$\langle I(x,y,z)\rangle^2 = \langle I(0,0,0)\rangle^2 \exp\left[-\frac{4(x^2+y^2)}{\omega_{xy}{}^2} - \frac{4z^2}{\omega_z{}^2}\right] \tag{1.3}$$

where $\langle I(0,0,0)\rangle^2$ is the peak intensity at the center (origin) of the focused beam and ω_{xy} and ω_z are the $1/e^2$ radius of the beam in the x,y and z planes respectively. Note that the intensity is squared since all excitation occurs due to a two-photon process. The peak intensity term is time averaged since the dector averages over many pulse cycles. The FRAP equation for two-photon point FRAP has been solved previouly.[54] In short, the model in **Chapter 2**, Eq. 2.4 is derived as follows. The change in concentration of bright fluorophore, c, due to bleaching is given by:

$$\frac{dc(x,y,z,t)}{dt} = -\beta'\langle I(x,y,z)\rangle^2 c(x,y,z,t) \tag{1.4}$$

where β' is a factor related to the bleach depth that depends on the quantum efficiency of photobleaching, the two-photon cross-section of the fluorophore, and the bleach pulse duration. During a short bleach time, Δt, during which diffusion can be neglected, Eq. 1.4 can be solved trivially:

$$c(x,y,z,t) = c_0 \exp\left(-\beta'\langle I(x,y,z)\rangle^2 \Delta t\right) \tag{1.5}$$

where c_0 is the prebleach concentration of fluorophore. The intial condition after photobleach is expressed by combining Eq. 1.3 and 1.5 as follows and simplified using a Taylor expansion (β is the new bleach factor including the constants of β', $\langle I(0,0,0)\rangle^2$, and Δt).

$$c(x, y, z, t = 0) = c_0 \exp\left(-\beta \exp\left[-\frac{4(x^2 + y^2)}{\omega_{xy}^2} - \frac{4z^2}{\omega_z^2}\right]\right) \tag{1.6a}$$

$$c(x, y, z, t = 0) = c_0 \sum_{n=0}^{\infty} \frac{(-\beta)^n}{n!} \exp\left[-\frac{4n(x^2 + y^2)}{\omega_{xy}^2} - \frac{4nz^2}{\omega_z^2}\right] \tag{1.6b}$$

After bleaching, the change in concentration is given by Fick's second law:

$$\frac{\partial c(x, y, z, t)}{\partial t} = D\nabla^2 c(\text{x}, \text{y}, \text{z}, \text{t}) \tag{1.7}$$

where ∇^2 is the Laplace operator. The fluorescence signal at any point in time after bleach, $F(t)$, is given by the convolution:

$$F(t) = Q_{Fl} \iiint \langle I(x, y, z)\rangle^2 c(x, y, z, t) dx dy dz \tag{1.8}$$

where Q_{Fl} is a constant accounting for several imaging constants such as quantum yield, efficiency of the collection system, etc. Combining Eq. 1.6b, 1.7 and 1.8 and solving is best done in the Fourier domain. The Fourier transform of generic function, f, is given by:

$$f(q_x, q_y, q_z, t) = (2\pi)^{-\frac{3}{2}} \iiint f(x, y, z, t) e^{-iq_x x - iq_y y - iq_z z} dx dy dz \tag{1.9}$$

Applying Eq. 1.9 to Eq. 1.6b and 1.7 yields the following Fouier domain Eq. 1.10 and 1.11 respectively:

$$c(q_x, q_y, q_z, t = 0) = c_0 \sum_{n=0}^{\infty} \frac{(-\beta)^n}{n!} \left[\frac{\omega_{xy}^2 \omega_z}{8(2n)^{3/2}}\right] \exp\left[-\frac{\omega_{xy}^2(q_x^2 + q_y^2)}{16n} - \frac{\omega_z^2 q_z^2}{16n}\right] \tag{1.10}$$

$$\frac{\partial c(q_x, q_y, q_z, t)}{\partial t} = -(q_x^2 + q_y^2 + q_z^2) D c(q_x, q_y, q_z, t) \tag{1.11a}$$

$$c(q_x, q_y, q_z, t) = c(q_x, q_y, q_z, t = 0) \times exp\left[-(q_x^2 + q_y^2 + q_z^2) Dt\right] \tag{1.11b}$$

Eq. 1.10, the initial condition after photobleaching, is propagated in time according to Eq. 1.11b yielding Eq. 1.12.

14

$$c(q_x, q_y, q_z, t) = c_0 exp\left[-\left(q_x{}^2 + q_y{}^2 + q_z{}^2\right)Dt\right]$$

$$\times \sum_{n=0}^{\infty} \frac{(-\beta)^n}{n!}\left[\frac{\omega_{xy}{}^2\omega_z}{8(2\text{n})^{3/2}}\right]\exp\left[-\frac{\omega_{xy}{}^2(q_x{}^2 + q_y{}^2)}{16n} - \frac{\omega_z{}^2q_z{}^2}{16n}\right] \tag{1.12}$$

To obtain the final expression for the point FRAP signal, *F(t)*, Eq. 12 is convolved with the point spread function of the detection beam according to Eq. 1.8 (in the Fourier domain) and intergrated over all Fourier space, yielding the end result:

$$F(t) = F_0 \sum_{n=0}^{\infty} \frac{(-\beta)^n}{n!}\left[1 + n\left(1 + \frac{16Dt}{\omega_{xy}{}^2}\right)\right]^{-1}\left[1 + n\left(1 + \frac{16Dt}{\omega_z{}^2}\right)\right]^{-1/2} \tag{1.13}$$

which is Eq. 2.4 in **Chapter 2** without modification for anomalous diffusion and with ω_{xy}

= ω_r.

1.4. Outline of Dissertation

The dissertation is divided into two parts. In the first part (consisting of **Chapters 2-4**), I present my work on developing FRAP methods and models for quantifying diffusion in live cells. **Chapter 2** presents my work perfecting the point FRAP method quantifying protein diffusion in live cells. This work improves on previous FRAP modeling work by presenting a method for accounting for the photophysics of fluorophores. The key result of this work was that obstructed transport through chromatin, and not macromolecular crowding, is the primary source of anomalous diffusion in cell nuclei. This result is further explored in **Chapter 3** in which I measure the diffusion of GFP *in vitro* in highly crowded solutions of dextran and bovine serum albumin. I found that anomalous diffusion is not observed under these conditions on the timescale of a FRAP experiment, a result that is also predicted by theoretical

calculations of crowded polymer solutions. In **Chapter 4**, I model FRAP data of RNA Polymerase II collected by Michael Tycon. The FRAP data of RNA Polymerase II shows anomalous diffusive behavior in nuclei away from DNA in contrast with data presented in **Chapter 2**. The FRAP model derived in **Chapter 2** is modified to account for a distribution of normally diffusing species which gives rise to a FRAP signature of anomalous diffusion.

The second part (**Chapters 5 & 6**) concerns cellular damage, both intentional and unintentional, that can occur due to fluorescence imaging of live cells. **Chapter 5** reviews potential damage mechanisms that one should be aware of when conducting live cell fluorescent microscopy. **Chapter 6** details a method I developed to create spatially localized regions of "UV-like" DNA damage with optical microscopy. This method is then used to measure the recruitment of topoisomerase I to the site of DNA damage.

REFERENCES

1. Banks, D. S.; Fradin, C. Anomalous diffusion of proteins due to molecular crowding. *Biophys. J.* **2005**, *89*, 2960-2971.

2. Masuda, A.; Ushida, K.; Okamoto, T. New Fluorescence Correlation Spectroscopy Enabling Direct Observation of Spatiotemporal Dependence of Diffusion Constants as an Evidence of Anomalous Transport in Extracellular Matrices. *Biophys. J.* **2005**, *88*, 3584-3591.

3. Bancaud, A.; Huet, S.; Daigle, N.; Mozziconacci, J.; Beaudouin, J.; Ellenberg, J. Molecular crowding affects diffusion and binding of nuclear proteins in heterochromatin and reveals the fractal organization of chromatin. *EMBO J.* **2009**, *28*, 3785-3798.

4. Guigas, G.; Kalla, C.; Weiss, M. The degree of macromolecular crowding in the cytoplasm and nucleoplasm of mammalian cells is conserved. *FEBS Lett.* **2007**, *581*, 5094-5098.

5. Weiss, M.; Elsner, M.; Kartberg, F.; Nilsson, T. Anomalous Subdiffusion Is a Measure for Cytoplasmic Crowding in Living Cells. *Biophys. J.* **2004**, *87*, 3518-3524.

6. Daddysman, M. K.; Fecko, C. J. Revisiting Point FRAP to Quantitatively Characterize Anomalous Diffusion in Live Cells. *J. Phys. Chem. B* **2013**, *117*, 1241-1251.

7. Sokolov, I. M. Models of anomalous diffusion in crowded environments. *Soft Matter* **2012**, *8*, 9043-9052.

8. Riggs, A. D.; Bourgeois, S.; Cohn, M. The *Lac* repressor-operator interaction. III. Kinetic studies. *J. of Mol. Biol.* **1970**, *53*, 401-417.

9. Berg, O. G.; Winter, R. B.; Hippel, P. H. v. Diffusion-driven mechanisms of protein translocation on nucleic acids. 1. Models and theory. *Biochemistry-US* **1981**, *20*, 6929-6948.

10. Berg, O. G.; Blomberg, C. Association kinetics with coupled diffusional flows. Special application to the*lac*repressor-operator system. *Biophys. Chem.* **1976**, *4*, 367-381.

11. Berg, O. G.; Bloomberg, C. Association kinetics with coupled diffusion. An extension to coiled-chain macromolecules applied to the*lac*repressor-operator system. *Biophys. Chem.* **1977**, *7*, 33-39.

12. Winter, R. B.; Berg, O. G.; Hippel, P. H. v. Diffusion-driven mechanisms of protein translocation on nucleic acids. 3. The *Escherichia coli lac* repressor-operator interaction: Kinetic measurements and conclusions. *Biochemistry-US* **1981**, *20*, 6961-6977.

13. Berg, O. G.; Hippel, P. H. v. Diffusion-controlled macromolecular interactions. *Annual Review of Biophysics and Biophys. Chem.* **1985**, *14*, 131-160.

14. Shimamoto, N. One-dimensional diffusion of proteins along DNA. *Journal of Biol. Chem.* **1999**, *274*, 15293-15296.

15. Halford, S. E.; Marko, J. F. How do site-specific DNA-binding proteins find their targets? *Nucleic Acids Res.* **2004**, *32*, 3040-3052.

16. Tafvizi, A.; Huang, F.; Leith, J. S.; Fersht, A. R.; Mirny, L. A.; Oijen, A. M. v. Tumor suppressor p53 slides on DNA with low friction and high stability. *Biophys. J.* **2008**, *95*, L01-L03.

17. Kad, N.M., Wang, H., Kennedy, G.G., Warshaw, D.M., Van Houten,B. Collaborative Dynamic DNA Scanning by Nucleotide Excision Repair Proteins Investigated by Single-Molecule Imaging of Quantum-Dot-Labeled Proteins. *Mol. Cell* **2010**, *37*, 702-713.

18. Graneli, A.; Yeykal, C. C.; Robertson, R. B.; Greene, E. C. Long-distance lateral diffusion of human Rad51 on double-stranded DNA. *P. Natl. Acad. Sci. USA* **2006**, *103*, 1221-1226.

19. Gorman, J.; Wang, F.; Redding, S.; Plys, A. J.; Fazio, T.; Wind, S.; Alani, E. E.; Greene, E. C. Single-molecule imaging reveals target-search mechanisms during DNA mismatch repair. *P. Natl. Acad. Sci. USA* **2012**, *109*, E3074-E3083.

20. Elf, J.; Li, G.; Xie, X. S. Probing transcription factor dynamics at the single-molecule level in a living cell. *Science* **2007**, *316*, 1191-1194.

21. Feder, T. J.; Burst-Mascher, I.; Slattery, J. P.; Baird, B.; Webb, W. W. Constrained diffusion or immobile fraction on cell surfaces: A new interpretation. *Biophys. J.* **1996**, *70*, 2767-2773.

22. Kang, M.; DiBenedetto, E.; Kenworthy, A. Proposed Correction to Feder's Anomalous Diffusion FRAP Equations. *Biophys. J.* **2011**, *100*, 791-792.

23. Guigas, G.; Weiss, M. Sampling the Cell with Anomalous Diffusion—The Discovery of Slowness. *Biophys. J.* **2008**, *94*, 90-94.

24. Sereshki, L. E.; Lomholt, M. A.; Metzler, R. A solution to the subdiffusion-efficiency paradox: Inactive states enhance reaction efficiency at subdiffusion conditions in living cells. *Europhys. Lett.* **2012**, *97*, 20008.

25. Saxton, M. J. Anomalous Subdiffusion in Fluorescence Photobleaching Recovery: A Monte Carlo Study. *Biophys. J.* **2001**, *81*, 2226-2240.

26. Kruhlak, M. J.; Lever, M. A.; Fischle, W.; Verdin, E.; Bazett-Jones, D. P.; Hendzel, M. J. Reduced Mobility of the Alternate Splicing Factor (Asf) through the

Nucleoplasm and Steady State Speckle Compartments. *J. Cell Biol.* **2000**, *150*, 41-52.

27. Meister, P.; Poldevin, M.; Francesconi, S.; Tratner,Isabelle, Zarzov, Patrick; Baldacci, G. Nuclear factories for signally and repairing DNA double strand breaks in living fission yeast. *Nucleic Acids Res.* **2003**, *31*, 5064.

28. Melnik, S.; Deng, B.; Papantonis, A.; Baboo, S.; Carr, I. M.; Cook, P. The proteomes of transcription factories containing RNA polymerases I,II, or III. *Nat. Methods* **2012**, *8*, 963.

29. Houtsmuller, A. B.; Vermeulen, W. Macromolecular dyanmics in living cell nuclei reveals by fluorescence redistribution after photobleaching. *Histochem. Cell Biol.* **2001**, *115*, 13.

30. Cook, P. R. A Model for all Genomes: The Role of Transcription Factories. *J. Mol. Biol.* **2010**, *395*, 1-10.

31. Misteli, T. Protein dynamics: Implications for nuclear architecture and gene expression. *Science* **2001**, *291*, 843-847.

32. Gorski, S. A.; Snyder, S. K.; John, S.; Grummt, I.; Misteli, T. Modulation of RNA Polymerase Assembly Dynamics in Transcriptional Regulation. *Mol. Cell* **2008**, *30*, 486-497.

33. Chen, D.; Dundr, M.; Wang, C.; Leung, A.; Lamond, A.; Misteli, T.; Huang, S. Condensed mitotic chromatin is accessible to transcription factors and chromatin structural proteins. *J. Cell Biol.* **2005**, *168*, 41-54.

34. Dundr, M.; Hoffmann-Rohrer, U.; Hu, Q.; Grummt, I.; Rothblum, L. I.; Phair, R. D.; Misteli, T. A Kinetic Framework for a Mammalian RNA Polymerase in Vivo. *Science* **2002**, *298*, 1623-1626.

35. Hannan, R.D., Cavanaugh, A.,Hempel, W.M., Moss, T., Rothblum, L. Identification of a mammalian RNA Polymerase I holenezyme containing components of the DNA repair/replication system. *Nucleic Acids Res.* **1999**, *27*, 3720.

36. Grummt, I. Life on a planet of its own: regulation of RNA Polymerase I transcription in the nucleolus. *Genes Dev.* **2003**, *17*, 1691.

37. Schneider, D. A.; Nomura, M. RNA polymerase I remains intact without subunit exchange through multiple rounds of transcription in Saccharomyces cerevisiae. *P. Natl. Acad. Sci. USA* **2004**, *101*, 15112-15117.

38. Kimura, H.; Sugaya, K.; Cook, P. R. The transcription cycle of RNA polymerase II in living cells. *J. Cell Biol.* **2002**, *159*, 777-782.

39. Mueller, F.; Karpova, T.; Mazza, D.; McNally, J. In *Monitoring Dynamic Binding of Chromatin Proteins In Vivo by Fluorescence Recovery After Photobleaching;* Morse, R. H., Ed.; Humana Press: 2012; Vol. 833, pp 153-176.

40. Yao, J.; Munson, K. M.; Webb, W. W.; Lis, J. T. Dynamics of heat shock factor association with native gene loci in living cells. *Nature* **2006**, *442*, 1050-1053.

41. Houtsmuller, A. B.; Rademakers, S.; Nigg, A. L.; Hoogstraten, D.; Hoeijmakers, J. H. J.; Vermeulen, W. Action of DNA repair endonuclease ERCC1/ XPF in living cells. *Science* **1999**, *284*, 958-961.

42. Dinant, C.; Jager, M. d.; Essers, J.; Cappellen, W. A. v.; Kanaar, R.; Houtsmuller, A. B.; Vermeulen, W. Activation of multiple DNA repair pathways by sub-nuclear damage induction methods. *J. Cell Sci.* **2007**, *120*, 2731-2740.

43. Kong, X.; Mohanty, S. K.; Stephens, J.; Heale, J. T.; Gomez-Godinez, V.; Shi, L. Z.; Kim, J.; Yokomori, K.; Berns, M. W. Comparative analysis of different laser systems to study cellular responses to DNA damage in mammalian cells. *Nucleic Acids Res.* **2009**, *37*, e68-e68.

44. Essers, J.; Houtsmuller, A. B.; Veelen, L. v.; Paulusma, C.; Nigg, A. L.; Pastink, A.; Vermeulen, W.; Hoeijmakers, J. H. J.; Kanaar, R. Nuclear dynamics of RAD52 group homologous recombination proteins in response to DNA damage. *EMBO J.* **2002**, *21*, 2030-2037.

45. Daddysman, M.; Fecko, C. DNA Multiphoton Absorption Generates Localized Damage for Studying Repair Dynamics in Live Cells. *Biophys. J.* **2011**, *101*, 2294-2303.

46. Leppard, J. B.; Champoux, J. J. Human DNA topoisomerase I: relaxation, roles, and damage control. *Chromosoma* **2005**, *114*, 75-85.

47. Lee, M. P.; Brown, S. D.; Chen, A.; Hsieh, T. S. DNA topoisomerase I is essential in *Drosophila melanogaster*. *P. Natl. Acad. Sci. USA.* **1993**, *90*, 6656-6660.

48. Lakowicz, J. R., Ed.; In *Nonlinear and two-photon-induced fluorescence;* Topics in Fluorescence Spectroscopy; Kluwer Academic Publishers: New York, 1997; Vol. 5.

49. Denk, W.; Strickler, J. H.; Webb, W. W. Two-photon laser scanning fluorescence microscopy. *Science* **1990**, *248*, 73-76.

50. Zipfel, W. R.; Williams, R. M.; Webb, W. W. Nonlinear magic: Multiphoton microscopy in the biosciences. *Nat. Biotechnol.* **2003**, *21*, 1369-1377.

51. Davidovits, P.; Egger, M. D. Scanning Laser Microscope. *Nature* **1969**, *223*, 831-831.

52. Morin, X.; Daneman, R.; Zavortink, M.; Chia, W. A protein trap strategy to detect GFP-tagged proteins expressed from their endogenous loci in Drosophila. *P. Natl. Acad. Sci. USA* **2001***, 98*, 15050-15055.

53. Zobeck, K. L.; Buckley, M. S.; Zipfel, W. R.; Lis, J. T. Recruitment Timing and Dynamics of Transcription Factors at the Hsp70 Loci in Living Cells. *Mol. Cell* **2010***, 40*, 965-975.

54. Brown, E. B.; Wu, E. S.; Zipfel, W. R.; Webb, W. W. Measurement of Molecular Diffusion in Solution by Multiphoton Fluorescence Photobleaching Recovery. *Biophys. J.* **1999***, 77*, 2837-2849.

CHAPTER 2: REVISITING POINT FRAP TO QUANTITATIVELY CHARACTERIZE ANOMALOUS DIFFUSION IN LIVE CELLS[*]

"The best way to have a good idea is to have a lot of ideas." – Linus Pauling

2.1. Introduction

Many biological processes rely on the diffusive transport of proteins in cellular environments that are crowded by a high concentration of macromolecules. Previous studies have established that proteins typically exhibit anomalous subdiffusion under these conditions.[1-8] As opposed to normal Brownian diffusion in which mean squared displacement grows linearly in time, anomalous diffusion is characterized by a mean squared displacement that follows a sub-linear power law in time, $\langle \Delta r^2 \rangle \propto t^\alpha$. Theoretical studies have indicated that anomalous diffusion may increase the efficiency with which proteins bind to target sites,[9,10] but the physical origin of this behavior is not entirely clear.

Non-Brownian diffusion is predicted by several theoretical models, including mass transport in the presence of a broad distribution of energetic traps (specific and/or nonspecific binding partners), obstructed diffusion in the presence of immobile fractal obstacles, or correlated motion that arises in an interacting system such as a polymer network.[11,12] Anomalous protein diffusion in cells is likely due to a combination of these origins, but it would be useful to devise experiments that probe individual contributions.

Previous studies that use non-interacting tracer molecules to eliminate the possibility of binding interactions have observed anomalous diffusion in cells.[5-8] However, it is more difficult to separate the impact of immobile obstacles from the impact of correlations due to macromolecules in a biologically relevant environment. The main purpose of the present study is to isolate contributions from these two physical origins in cell nuclei by separately probing diffusion in regions that contain chromosomes and regions that are devoid of chromatin. Both regions are crowded by a high concentration of mobile macromolecules, but the chromosomal regions additionally contain relatively immobile obstacles (chromatin) that have been suggested to exhibit fractal behavior.[5] We investigate these regions separately by applying fluorescence recovery after photobleaching (FRAP) to diffraction-limited regions of polytene cell nuclei. Polytene nuclei contain giant, optically-resolvable chromosomes in interphase, in contrast to more typical cell types in which chromatin is too diffuse to be resolved with conventional optics.

FRAP is used widely in live cell microscopy for assessing the movement and binding of fluorescent molecules. Experiments are typically performed by photobleaching a spatially limited region within a fluorescent sample, and then observing the subsequent evolution of fluorescence from that same region. The time-dependent signal recovery can be related to molecular process such as diffusion, directed transport, binding interactions and chemical reactions.[13,14] Early implementations of FRAP used a stationary focused laser beam to quantitatively measure diffusion coefficients of fluorescent species (hereafter referred to as point FRAP), mostly for membrane samples in which diffusion is constrained to two-

dimensions.[15] The development of commercial confocal microscopes led to the widespread application of FRAP methods that bleach spatial regions much larger than the diffraction limit by scanning the focused laser spot within the sample (hereafter referred to as area FRAP).[16-19] Although this latter method is straightforward to implement, the use of arbitrarily-shaped bleach regions, three-dimensional diffusion and sample heterogeneities makes it technically challenging to extract meaningful quantitative information from the experimental data. As a result, many FRAP studies in recent literature are inherently qualitative in nature. Such qualitative measurements are acceptable for some applications, but it is important to recognize their limitations and to adopt a more rigorous approach when necessary. This issue is often not sufficiently considered in studies that attempt to extract microscopic information by fitting area FRAP data according to a kinetic model derived using various simplifying assumptions, some of which may not be appropriate for the experimental conditions,[20] resulting in poor agreement of corresponding parameters reported by various studies. For example, the residence time for one transcription factor reported by two studies differed by about four orders of magnitude.[21]

The original implementation of quantitative FRAP was intended to measure the mobility of fluorescence particles in a membrane,[15] so the bleach region of interest is the microscope point spread function projected onto a two-dimensional surface. To apply an analogous point FRAP technique to three-dimensional samples, it is advantageous to restrict the bleach volume in the axial dimension by using two-photon excitation. Nonresonant two-photon absorption is the process by which a molecule exposed to a high photon flux interacts with two photons simultaneously, producing an

excited state equivalent in energy to the summation of the energy of the interacting photons.[22] Two-photon microscopy takes advantage of this phenomenon by combining the nonlinear intensity dependence with a steeply decreasing intensity profile outside of the focal point of the objective lens to enhance imaging depth discrimination.[23,24] The diffusion equations have been solved for multiphoton FRAP bleach and observation profiles previously.[25-27] Although point FRAP is not commonly used currently compared to other FRAP methods, we see several advantages for perfecting this method, especially the use of a well defined bleaching-observation region and sufficiently high time resolution to capture all relevant dynamic processes. The main disadvantage is a decreased signal to noise ratio, requiring the collection of numerous data sets to achieve acceptable results. In some cases point FRAP measurements could be used to complement area FRAP methods and fluorescent correlation spectroscopy (FCS) in order to fully characterize diffusion and binding over a wide range of time scales inside living cells.

This chapter investigates the use of two-photon excitation point FRAP to quantitatively assess diffusion of unconjugated enhanced green fluorescent protein (GFP) *in vitro*, in HeLa cells and in polytene cells of *Drosophila* salivary glands. By using the polytene cells and point FRAP, we are able to separately probe GFP diffusion in the presence (chromatin) and absence (interchromatin space) of relatively immobile DNA obstacles in the nucleus. In addition to extracting diffusion coefficients, we have examined whether a model that includes anomalous diffusion[28,29] is required to fit the FRAP results. The observation and degree of anomalous subdiffusion could provide information about the nature of molecular obstructions or transient interactions, but

previous studies have arrived at varying conclusions about the nature of free protein diffusion in cells.[1-8] We find that, in addition to transport physics (diffusion), it is critical to carefully consider the impact of reversible fluorophore bleaching photophysics to accurately interpret time-dependent FRAP recoveries.[30-32] If not taken into account, signal contributions from photophysics can cause normally diffusing fluorophores to appear to exhibit anomalous diffusion. When these photophysics are properly modeled, GFP diffusion in the solution samples is normal but most of the cellular regions exhibit some degree of anomalous diffusion. One notable exception to this trend is the interchromatin space of polytene nuclei, in which GFP exhibits normal diffusion.

2.2. Materials and Methods

2.2.1. Sample preparation

Purified enhanced green fluorescent protein was a generous gift from Dr. Gary Pielak. The GFP was diluted to a concentration of 10 μM in phosphate buffered saline (PBS) for the aqueous solution measurements. For samples in glycerol, GFP was diluted in a solution of 62% (w/w) glycerol (n_D = 1.4151 at 20°C)[33] to a final concentration of 10 μM GFP and 60% glycerol. Alexa Fluor 488 (Invitrogen, Carlsbad, CA) was diluted to a final concentration of 10 μM in PBS. Polyacrylamide GFP gels were made by diluting the GFP stock to a concentration of 10 μM in a 1:1 mixture of 40% acrylamide (Fisher Scientific, Fair Lawn, NJ) and 2% bisacrylamide (Fisher Scientific). To form the gel, 1 μL of tetramethylethylenediamine (Fisher Scientific) and 1 μL of ammonium persulfate (Fisher Scientific) were added to 200 μL of the acrylamide GFP mixture. The mixture was then quickly transferred to glass bottom culture dish

(MatTek Corporation, Ashland, MA) and sealed with another coverslip. The gel was allowed to polymerize for 1 h before the experiment.

HeLa cells stably expressing GFP (Cell Biolabs, Inc., San Diego, CA) were cultured in phenol-red free Dulbecco's modified Eagle's medium (Gibco, Billings, MT) supplemented with antibiotics and 10% fetal bovine serum (Gibco) at 37°C and 5% CO_2. For FRAP experiments, cells were seeded on MatTek glass bottom culture dishes at a density of 2.5 x 10^5 cells per dish ~18 h before the experiment.

Polytene cells were imaged in intact salivary glands extracted from transgenic Drosophila melanogaster larvae. The larvae were produced by crossing a transgenic fly line that expresses free GFP with another transgenic line that expresses a histone 2B (H2B)-mRFP fusion protein.   The fluorescent histones were used to permit the differentiation of chromosomal and nucleoplasmic regions using two color imaging. The transgenic line that expresses the H2B-mRFP fusion protein under the control of a Gal4 upstream activation sequence was described in Zobeck *et al.*;[34] the protein was expressed in salivary gland cells by generating a homozygous cross with the c147 *Gal4* driver line (Bloomington Stock Center line #6979). This homozygous cross was mated with the line containing a GFP transgene (Bloomington Stock Center line #5430), which was also under the control of a *Gal4* upstream activating sequence. Larva were raised at room temperature in standard cornmeal yeast medium, collected at the third-instar stage 8-9 days after eggs were laid, and dissected in Grace's Insect Medium (Gibco). For FRAP experiments, salivary glands were transferred to MatTek glass-bottomed culture dish in Grace's medium and gently sealed under another glass coverslip to

minimize sample movement. All experiments were completed within 1 h after salivary gland extraction.

2.2.2. Two-photon microscope setup

FRAP experiments were performed with a home-built laser-scanning two-photon microscope.[35] A near-infrared Coherent Chameleon Ultra II Ti:sapphire oscillator produced femtosecond pulses at a wavelength maximum of 950 nm and a repetition rate of 80 MHz. An electro-optic modulator with a 1 μs response time (Conoptics 350-80LA/BK) and polarizer placed directly after the laser controlled the intensity used for imaging and FRAP. Note that any mention of the laser power in the procedures actually refers to the power transmitted by the electro-optic modulator and measured at the objective (e.g. turning the laser off means that the power transmitted by the modulator was extinguished). Galvanometer-mounted mirrors and relay lenses in the beam path determined the angle with which the laser beam enters a 60X, 1.2 NA water-immersion objective lens mounted on an Olympus IX81 inverted microscope. Computer control of this incident angle is used to raster scan images of the sample or point the beam for point FRAP experiments. The back aperture of the lens was slightly overfilled to maintain a tight focus; the point spread function was determined by imaging 100 nm diameter immobilized fluorescent microspheres (ω_r = 293 nm and ω_z = 951 nm). The imaging and FRAP bleach and observation powers were measured after the objective using a calibrated power meter. Epifluorescence was detected by a Hamamatsu H7422P-40MOD non-descanned GaAsP photomultiplier tube (PMT) module. To detect GFP fluorescence, a 510/70 bandpass filer was placed in front of the PMT. For multicolor experiments, the epifluorescence beam was split using a 570 dichroic mirror

to an GaAs PMT (Hamamatsu H7422P-50MOD) with a 630/100 bandpass filter for detecting mRFP fluorescence. Signals from the PMTs were processed and enhanced by high gain preamplifiers. The output from the preamplifiers was read into an A/D card (National Instruments) with a sampling time of 100 ns; ten samples were averaged to produce 1 μs time points during data collection. We note that the high gain preamplifers we typically use for imaging dim samples could not recover quickly enough from the voltage saturation that occurred during the bleach pulse. The reduced gain, a result of saturation, recovered on the timescale of several milliseconds, obscuring the bleach recovery. This "detector blinding" effect and the methods used to characterize it have been reported previously.[21] One possible method of correcting for the detector blinding effect was to reduce the gain on the PMT during the bleach pulse, but the gain control on the PMT electronics was too slow. Therefore, we used a modified current preamplifier (sensitivity of 20 μA/V), which was designed to minimize the impact of signal saturation during bleaching.

2.2.3. FRAP procedure

To identify regions of interests an image was acquired using Labview-based software developed in-house and then one or more points were selected for bleaching. In cellular samples, care was taken to ensure selected points were sufficiently far from membranes. FRAP data were collected at each point using an intermittent data collection scheme designed to reduce observational photobleaching by only illuminating the sample for a small fraction of the time it takes the fluorescence to fully recover from a 20 μs bleach. Details of this scheme are provided in Figure 2.1 and in Appendix A. Control data sets were taken with the same timing sequence at the observation power
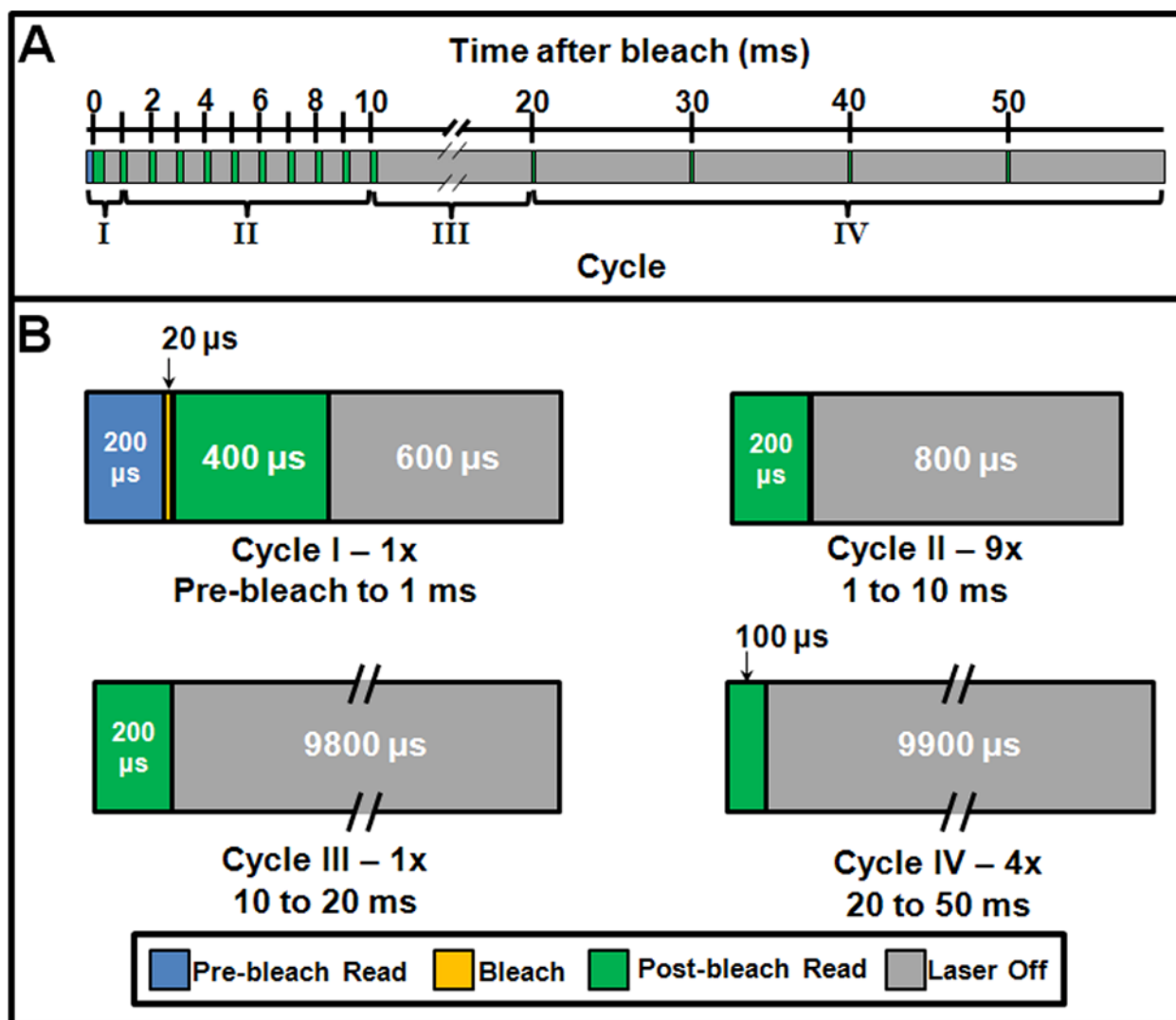
Figure 2.1: Timing diagram of the point FRAP method. (A) One FRAP measurement covered 50 milliseconds, which was broken up into four different cycles as described in panel B. (B) Timing within each cycle is shown in detail. The number of times that each cycle was repeated is indicated by the number of repeats followed by an x, e.g. Cycle II was repeated 9 times indicated by 9x. Pre-bleach and post-bleach reads indicate that the observation laser power was applied and data collected, bleach indicates that the bleaching laser power was applied, and laser off indicates that the laser power was extinguished during that period.

except with a 20 μs mock bleach (i.e. the observation power is used in place of the bleach power). Five hundred replicates were taken for both the bleach and control curves to improve the signal to noise ratio, which obeyed Poisson statistics (Figure A.1 in the Appendix). Each replicate was normalized to the average of the pre-bleach values before averaging replicates. In all figures except Figure 2.3, FRAP data are obtained by dividing the bleach data set by the control data set. All measurements were made at room temperature (22 ^{o}C).

2.2.4. Fitting and statistical model

FRAP data was fit to the curve in equation 2.4 or 2.6 using the *lsqnonlin* routine in MATLAB (The MathWorks, Natick, MA). Data collected during the first 50-70 μs following the bleach were excluded from the fits to eliminate the influence of detector/preamplifier saturation (Figure A.2 in the Appendix). The fitting equations included a floated parameter to measure an immobile fraction; however, we found that the value was always within the noise of the measurement indicating no immobile fraction. The residuals were weighted to emphasize early time points in the FRAP recovery and to account for the gaps in data collection. To account for a broad range of recovery timescales, FCS data is binned logarithmically in time. In analogy, we weighted residuals of data points spaced equally in time by the inverse of the time after bleaching, which is mathematically equivalent to spacing the points logarithmically. Details on fitting are provided in Appendix A.

When fitting for anomalous diffusion, an additional parameter (an anomalous exponent) was introduced into the model; as a result, fits using the anomalous diffusion model usually had lower residuals than normal diffusion. However, this lower residual

31

does not necessarily justify the additional degree of freedom introduced into the fitting model. To statically distinguish the better of the two candidate models, we applied the Bayesian information criterion (BIC).[36-38] The advantage of this test over other similar statistical tests was that for large sample sizes (n ≈ 2700) the BIC still penalizes for extra parameters. The BIC value for each model, i, was calculated by

$$BIC_i = n * \ln(\frac{res_i}{n}) + K_i * \ln(n) \tag{2.1}$$

where n was the number of data points fit, res_i was the square root of the sum of the squares of the residuals of the fit for each model i, and K_i was the number of parameters for each model (K = 4 for normal diffusion and K = 5 for anomalous diffusion). The candidate with the lowest BIC score was considered to be the better model. To quantify the likelihood that each candidate represents the true model, we used:

$$\Delta_i = BIC_i - \min BIC \tag{2.2}$$

to calculate the Akaike weight, w_i, of each model according to:

$$w_i = \frac{\exp(-0.5\Delta_i)}{\sum_{j=1}^{J} \exp(-0.5\Delta_j)} \tag{2.3}$$

where J is the total number of candidate models (J = 2). These Akaike weights are the probability that each candidate is the true model.

2.3. Results

2.3.1. GFP appears to exhibit anomalous subdiffusion in solution

Particles that diffuse freely in simple systems typically exhibit normal Brownian diffusion, which is characterized by a mean square displacement that grows linearly with

time $\langle \Delta r^2 \rangle = 2dDt$, where d is the dimensionality of the system and D is the diffusion coefficient. In more complex systems, particles may exhibit anomalous diffusion in which the mean squared displacement follows a nonlinear power law in time $\langle \Delta r^2 \rangle = 2d\frac{\Gamma}{\alpha}t^\alpha$, where Γ is the transport coefficient and α is the anomalous exponent. (We note that previous literature contains several different definitions for the transport coefficient and that we have adopted the approach proposed by Kang *et al.*[39].) The signal measured in a two-photon excited point FRAP experiment derived by Brown *et. al.*[25] and modified to include anomalous diffusion is:

$$F(t) = F_0 \sum_{n=0}^{\infty} \frac{(-\beta)^n}{n!} \left[1 + n\left(1 + \frac{16\Gamma t^\alpha}{\alpha \omega_r^2}\right) \right]^{-1} \left[1 + n\left(1 + \frac{16\Gamma t^\alpha}{\alpha \omega_z^2}\right) \right]^{-1/2} \qquad (2.4)$$

where F_0 is the pre-bleach fluorescence intensity, β is a factor related to the bleach depth, and ω_r and ω_z are size of the focused Gaussian beam in the radial and axial dimensions respectively.

We initially used this Eq. 2.4 to estimate the time range necessary to experimentally characterize diffusion *in vitro* and in cells. Assuming normal diffusion with a diffusion coefficient typical for unconjugated GFP in solution (80 $\mu m^2 s^{-1}$),[31] a moderate bleach depth and the size of our focused laser, the fluorescence signal recovers halfway from its bleached value in about 140 μs and 90% from its bleached value in about 1 ms. Using subdiffusive values in the range that has been reported for GFP in cells ($\alpha \sim 0.8$, $\Gamma \sim 20$ $\mu m^2 s^{-1}$), the half and 90% recovery values are about 2 ms and 25 ms, respectively. We cover this range of experimental time scales using a detection system with microsecond observation time bins collected over a period of 50 ms after the initial bleach. To avoid excessive photobleaching (and photophysical

processes discussed below), we adopt an intermittent data collection strategy that involves toggling the observation laser power on-and-off during the 50 ms period (Figure 2.1). In analogy with fluorescence correlation spectroscopy (FCS), the broad time range over which the FRAP signal recovers lends itself to data binned logarithmically in time. Rather than directly collecting data spaced in this way, we fit data collected according to the aforementioned sequence using a weighting algorithm equivalent to logarithmically binning data points (see Appendix A). The analogy with FCS also prompted us to plot data using logarithmic time axes, which is beneficial for visualizing signals that vary over a large range of time.

To verify that our data collection and analysis method correctly determines diffusion coefficients, we measured the diffusion coefficient of GFP in PBS (Figure 2.2A). We fit point bleach curves to Eq. 2.4 using either a value of α that was fixed to 1.0 (normal diffusion) or floated in the fit (anomalous diffusion). We were surprised to find that the FRAP curves were best fit by the anomalous diffusion model with exponents (α) as low as 0.8. (According to a BIC statistical analysis, the anomalous diffusion model was nearly always more likely than normal diffusion, sometimes with 100% likelihood.) This result is clearly not consistent with simple Brownian diffusion. In contrast, FRAP curves of GFP in 60% glycerol consistently exhibited recoveries that were nearly Brownian.

While the observation of anomalous diffusion in dilute solution could have been attributed to various experimental inaccuracies, one set of additional experiments revealed that the model used to fit the data was the source of the problem. To obtain the GFP FRAP data, we had corrected for observational photobleaching using a

34
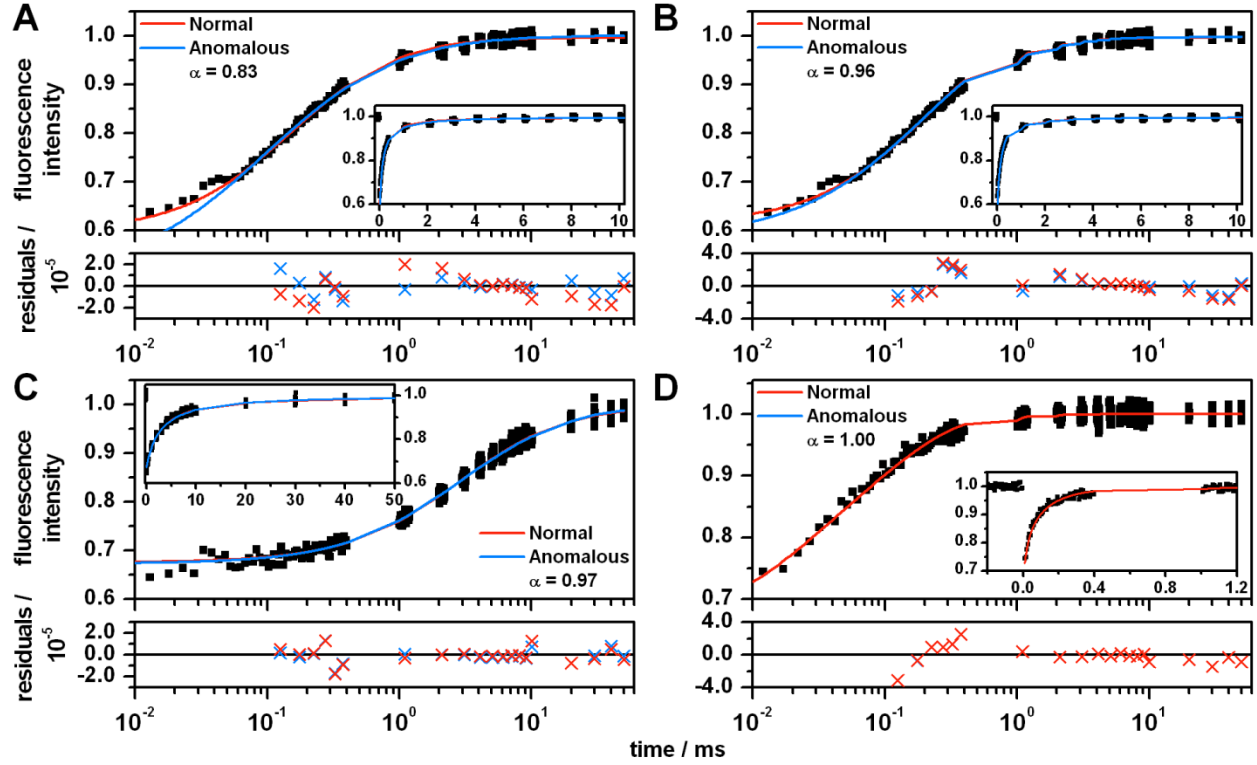
Figure 2.2: *In vitro* point FRAP data (points) and fits (lines) plotted using logarithmic time axes and linear time axes (insert). For clarity, the fit residuals (lower plot in each panel) were averaged over 50 μs intervals from 100 to 400 μs (cycle I) and for each read time period of either 100 or 200 μs (cycles II-IV). (A) GFP in a PBS solution fit by a FRAP model that does not account for reversible bleaching. The data were fit to Eq. 2.4 using a value of α that was either fixed to 1.0 (normal diffusion) or floated in the fit (anomalous diffusion). For the normal diffusion fit, D is equal to 76 ± 2 $\mu m^2 s^{-1}$, and for the anomalous diffusion fit D_{eff} is equal to 100 ± 17 $\mu m^2 s^{-1}$. (B-D) FRAP data fit by a model that accounts for reversible bleaching (Eq. 2.6). Again, the value of α was either fixed to 1.0 (normal diffusion) or floated in the fit (anomalous diffusion). The samples are GFP in PBS (B), GFP in 60% glycerol (C), and Alexa Flour 488 in PBS (D).

standard method, by dividing the fluorescence signal from a sample that had been intentionally bleached by the signal from a control sample that had not been intentionally bleached (Figure 2.3A-C). However, this correction may not fully account for the photophysics observed in the data. Mueller *et al.*[20] reported an unexpected signal contribution in some FRAP experiments that arises from reversible photobleaching. To determine the influence of these photophysics on our data, we fixed GFP in a polyacrylamide gel and conducted FRAP experiments (Figure 2.3D-F). By fixing the sample and thus eliminating the transport physics from consideration, signal contributions from reversible fluorophore photophyiscs are exposed. Even though the raw bleach curve (Figure 2.3D) does not exhibit a recovery and in fact shows slow photobleaching, the corrected curve (Figure 2.3F) clearly exhibits a recovery. This apparent recovery arises from a decay of the control curve (Figure 2.3E) at early times that is absent from the bleach curve. This observation led us to question the validity of correcting for observational photobleaching by dividing the bleach curve by a control curve, a practice common to nearly all FRAP methods. The fundamental assumption behind this procedure is that the photobleaching kinetics at a particular observation power are independent of initial conditions. Although true for a first-order process, this condition is not satisfied in the case of highly non-exponential bleaching kinetics. Thus, a model that accounts for more realistic bleaching photophysics is required.

2.3.2. FRAP model that accounts for reversible photobleaching

Single-molecule spectroscopy has established that one primary source of non-exponential photobleaching kinetics is the intermittency (i.e. "blinking") exhibited by nearly all fluorophores.[40] This universal behavior can be incorporated by considering a
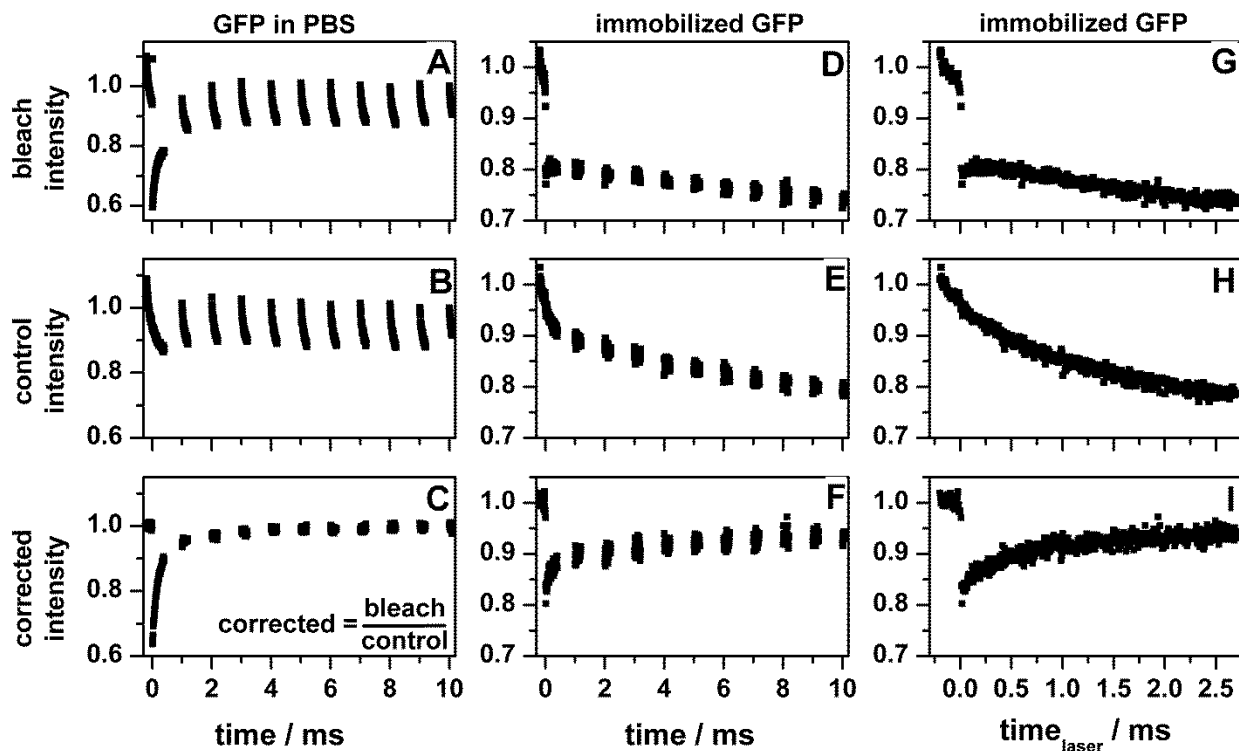
Figure 2.3: Demonstration of the importance of accounting for reversible fluorophore bleaching. (A-C) Raw FRAP signals of GFP in PBS, including the bleach (A) and control (B) data before division. Note that all other figures plot only the corrected (bleach divided by control) FRAP data (C). The necessity of this division is demonstrated by the rapid photobleaching of new fluorophores that have diffused into the observation volume during the laser off times; the division removes this rapid photobleaching, as demonstrated by the long time points. (D-F) Raw FRAP signals of GFP immobilized in a polyacrylamide gel. The corrected (F) curve showed a recovery even though diffusion was not present. The source of this apparent recovery was that the slope of the control curve (E) was steeper than the bleach curve (D) due to the non-exponential nature of the bleaching photophysics. (G-I) The same data from D-F was plotted on a laser time axis showing only the laser on time and removing the laser off time gaps. Note that the data are continuous demonstrating that the time-dependent signals are light driven and that the recovery is not due to incomplete immobilization. Also, the fluorescence recovery during the laser off time is negligible. Therefore, the reversible photobleaching correction depends only on the laser illumination time, t_{laser}, rather than the actual time after photobleaching.

photophysical model in which fluorophores (*Fl*) can be converted to either a reversibly bleached (*RB*) or an irreversibly bleached (*IB*) state:[41]

$$RB \underset{k_{-1}}{\overset{k_1}{\rightleftharpoons}} Fl \overset{k_2}{\rightarrow} IB \tag{2.5}$$

The conceptual and mathematical impact of this photophysical process on a FRAP measurement is provided in Appendix A. In brief, irradiation of a sample disturbs the pre-existing equilibrium of *Fl* and *RB* states, leading to a relaxation process that approaches a new equilibrium value with a rate constant given by the sum of the forward and reverse reactions. Because these photochemical transformations depend on the intensity of light, the bleached sample approaches the new equilibrium much more rapidly (likely during the bleach pulse) than the control sample. Thus, the control curve contains a decay at short times whose amplitude is absent (or greatly reduced) in the bleach curve. Both curves decay similarly at longer times due to irreversible fluorophore bleaching. Therefore, dividing the bleach curve by the control curve correctly accounts for irreversible bleaching but also introduces a signal contribution due to reversible bleaching. The contribution of these processes to a FRAP signal are complicated by diffusion, but our reaction-diffusion model includes coupled equations that account for both transport physics and photophysics.

In the presence of reversible photobleaching, the FRAP signal (derived in Appendix A) is:

$$F(t) = F_0[1 + \delta \exp(\frac{-t_{laser}}{\tau_{PP}})] \sum_{n=0}^{\infty} \frac{(-\beta)^n}{n!} \left[1 + n\left(1 + \frac{16\Gamma t^\alpha}{\alpha \omega_r^2}\right) \right]^{-1} \left[1 + n\left(1 + \frac{16\Gamma t^\alpha}{\alpha \omega_z^2}\right) \right]^{-1/2} \tag{2.6}$$

In comparison to Eq. 2.4, reversible bleaching introduces an additional factor that depends on the photophysics decay time constant, τ_{PP}, and magnitude, δ. This factor

depends on t_{laser}, which is the time that the laser has irradiated the sample; it differs from the time dependence of the diffusion factors because we applied an intermittent data collection scheme. The dependence on t_{laser} is motivated by the observation that the photophysical signal varies only when the laser is on, as demonstrated by the lack of signal change during laser off times in immobilized samples (Figure 2.3G-I). This observation is consistent with transformations driven by photon absorption.

To examine the influence of the photophysical correction on the FRAP signal, normal (Brownian) diffusion curves with a diffusion coefficient of 82 $\mu m^2 s^{-1}$ or 25 $\mu m^2 s^{-1}$ were simulated using different values of τ_{PP} and δ. The curves were then fit to an anomalous model without a photophysics correction (Eq. 2.4). Depending on the exact values of the photoswitching parameters the diffusion could appear to be normal, subdiffusive, or superdiffusive (Figure 2.4).

The most straightforward way to fit experimental data according to Eq. 2.6 would be to simply float the additional parameters introduced in the photophysical model, τ_{PP} and δ. However, this approach introduces too many degrees of freedom into the model, making it challenging to separate photophysical contributions from anomalous diffusion. One way to isolate the photophysical parameters is to immobilize the GFP and then fit the resulting FRAP curve to the model with a vanishingly small diffusion coefficient. However, we found that δ is very dependent on the bleach depth and small variations in experimental conditions lead to difficulties matching the bleach depth of mobile and immobile samples. After exploring these options, we found that the most reliable procedure to determine the value of δ is to fit the early part of the control curve (for 600 μs) with an exponential to account for reversible bleaching equilibration. This fit gave a
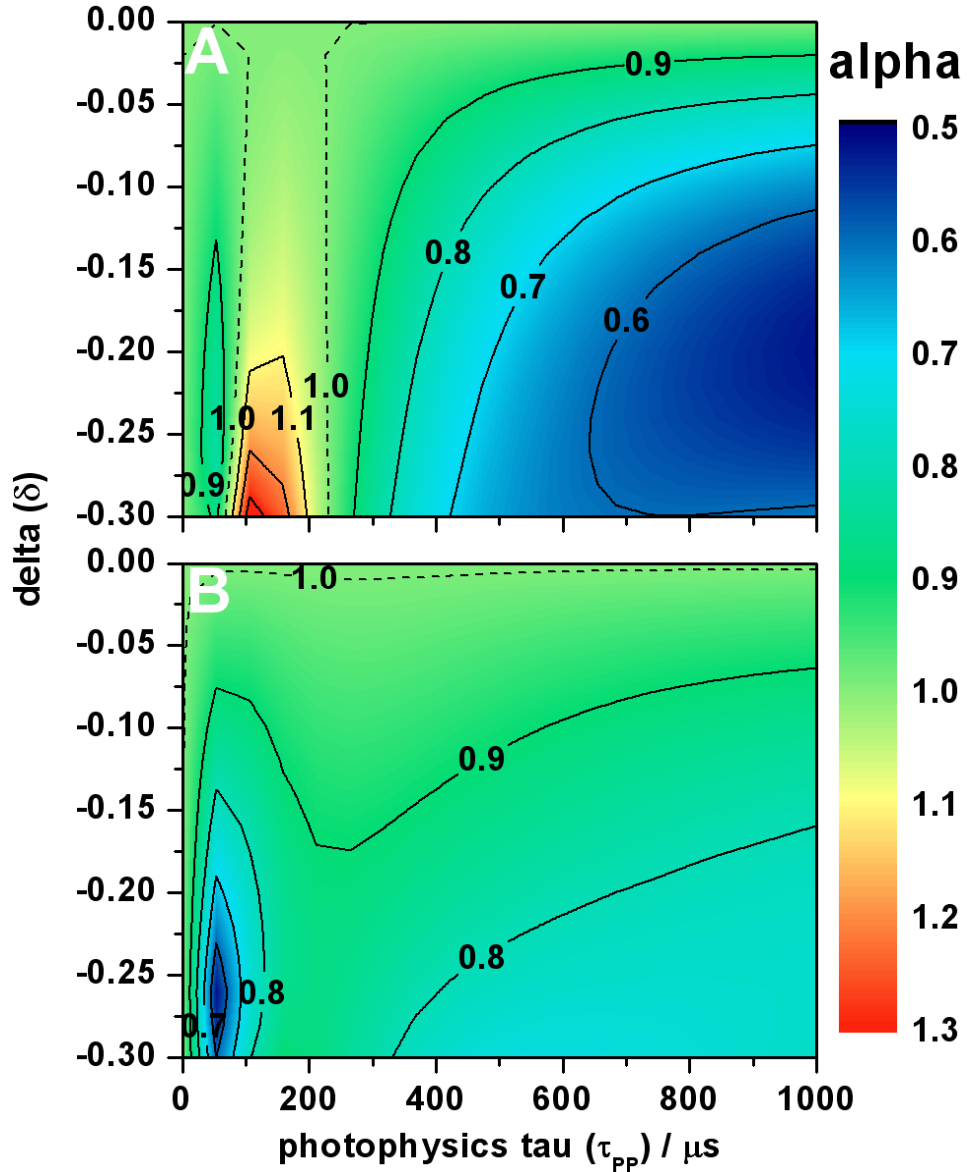
Figure 2.4: When not taken into account, reversible photobleaching can cause fluorophores that diffuse normally appear to exhibit anomalous diffusion. Shown are contour plots of the anomalous factor obtained when data simulated by a Brownian diffusion ($\alpha=1$) FRAP model that includes reversible photobleaching (Eq. 2.6) were fit using the FRAP model that did not account for these photophysics (Eq. 2.4). Delta and photophysics tau refer to the parameters δ and τ_{pp} in Eq. 2.6. The data were simulated using diffusion coefficients of D = 82 $\mu m^2 s^{-1}$ (A) or D = 25 $\mu m^2 s^{-1}$ (B), the approximate diffusion coefficients of GFP in solution and cellular samples respectively.

similar value of τ_{PP} as the fixed sample and yielded a more accurate δ value for each sample. Therefore, this procedure was used to obtain the values of τ_{PP} and δ, which were then fixed when fitting the corrected FRAP curve according to Eq. 2.6.

2.3.3. Reversible photobleaching FRAP model indicates GFP in solution diffuses normally

After applying the above correction, the anomalous diffusion factor of GFP in PBS changes from 0.83 to 0.96 which is in the same range as the glycerol fits (Figure 2.2B). More importantly, the BIC value indicated that the normal diffusion model became the more likely of the two after the photophysics correction (Table 2.1). The diffusion coefficient of GFP was found to be $84 \pm 6 \ \mu m^2 s^{-1}$ in excellent agreement with other sources.[31,42] The glycerol fits (Figure 2.2C) did not change with the photophysics correction. There are two possible explanations. One is that polyethylene glycol has been shown to have photoprotectant properties[43] and it is possible that glycerol as the monomer would reduce the impact of photophysics as well. We did observe that our fits to the control curve in the glycerol samples had much larger τ_{PP} than the other samples because the control curve was nearly flat over the timescale of our experiment, indicating that the photophysics correction may not be necessary. The other possible explanation is that the diffusion coefficients measured in glycerol are much slower than any of the other diffusion coefficients measured in this study, perhaps minimizing the impact of rapid photophysics. The 60% glycerol solution shows a 20-fold reduction in the diffusion coefficient which is larger than expected from the 10-fold increase in viscosity over aqueous solution.[44] One possible explanation for this discrepancy is the distortion of the point spread function by glycerol.[45] We were also able to measure the

Table 2.1: Summary of model fits for GFP in solution

Sample	Photophysics Correction	Type of Diffusion	Anomalous Factor	BIC w_i
GFP in PBS	No	Normal	1.00	0.0000
		Anomalous	0.82	1.0000
	Yes	Normal	1.00	0.8806
		Anomalous	0.99	0.1194
GFP in 60% Glycerol	N/A*	Normal	1.00	0.1191
		Anomalous	0.96	0.8809

(*) Applying the photophysics correction did not change the fits for the glycerol sample.

Table 2.2: Summary of best fit models for GFP and Alexa Fluor 488

Sample	BIC Indicated Best Model	Range of BIC w_i for Best Model	D ($\mu m^2 s^{-1}$) or Γ ($\mu m^2 s^{-\alpha}$)	α
GFP in PBS	Normal	0.8806* – 0.9797	84 ± 6	-
GFP in 60% Glycerol	Anomalous	0.8809 – 0.9973	6.2 ± 0.9	0.95 ± 0.01
Alexa Fluor 488 in PBS	Normal	0.9637* – 0.9811	438 ± 12	-
GFP in HeLa – Nucleus	Anomalous	1.0000 – 1.0000	70 ± 27	0.84 ± 0.05
GFP in HeLa – Cytoplasm	Anomalous	1.0000 – 1.0000	130 ± 60	0.76 ± 0.07
GFP in Polytene – Chromosome	Anomalous	1.0000 – 1.0000	66 ± 1	0.79 ± 0.01
GFP in Polytene – Interchromatin space	Normal	0.9808 – 0.9809	32 ± 6	-
GFP in Polytene – Cytoplasm	Anomalous	1.0000 – 1.0000	335 ± 236	0.56 ± 0.11

The errors reported are the standard deviation between fits to three independent experiments.
(*) One replicate for both PBS and Alexa Fluor 488 had a score of 0.0000 for the normal diffusion model. These models are excluded from the weighting range but are included in the average. The alpha values for both of these models were greater than 0.9.

diffusion coefficient of Alexa Fluor 488 in solution (Figure 2.2D). We found a diffusion coefficient of $438 \pm 12 \, \mu m^2 s^{-1}$ in excellent agreement with literature values.[42]

2.3.4. GFP exhibits anomalous diffusion in most cellular environments

For all of the unconjugated GFP in cell samples, the FRAP curves were fit with both the normal and anomalous model with the photophysics correction in Eq. 2.6. First, HeLa cells expressing unconjugated GFP were imaged (Figure 2.5A), and FRAP was performed on points in the nucleus and cytoplasm. Diffusion of GFP in both the nucleus (Figure 2.5B) and cytoplasm (Figure 2.5C) of HeLa cells were found to be best fit by the anomalous model as indicated by the BIC test, even after accounting for reversible bleaching photophysics (Table 2.2). The cytoplasm had a smaller anomalous exponent ($\alpha = 0.76$) than the nucleus ($\alpha = 0.84$).

Drosophila polytene cells were used because the large cell nuclei contained optically resolvable chromosomes in interphase, in contrast with HeLa cells. Therefore, we could probe the difference between GFP diffusion in nuclear areas that contained chromosomes and in the interchromatin space. To experimentally distinguish between the chromosomal and interchromatin space, the flies coexpressed a histone 2B-mRFP construct that marked chromosomal regions (Figure 2.6A-C). The GFP was partially excluded from the chromosomes which further helped discriminate between the two regions. GFP diffusion in the chromosome region in the polytene nuclei (Figure 2.6D) behaved similarly to the HeLa nucleus with an average anomalous factor of 0.79 (Table 2.2) comparable to the 0.84 value in the HeLa nucleus. In contrast, GFP in the interchromatin space of the polytene nuclei diffuses normally (Figure 2.7C), though its effective viscosity is 2.6 times that of water (comparable to a 30-40% glycerol solution)
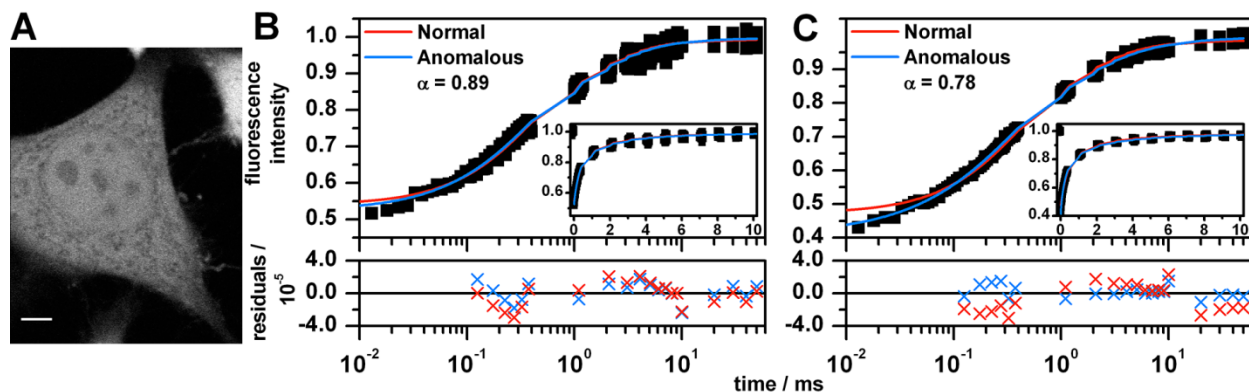
Figure 2.5: Summary of unconjugated GFP FRAP data in HeLa cells. (A) Two-photon microscopy image of a HeLa cell expressing unconjugated GFP. Scale bar, 5 μm. (B-C) FRAP data (points) and fits (lines) of GFP in HeLa cells plotted on logarithmic time axes and linear time axes (insert). The residuals were averaged as in Figure 2.2. The data were fit to Eq. 2.6 using a value of α that was either fixed to 1.0 (normal diffusion) or floated in the fit (anomalous diffusion). The data were recorded by focusing on points in the nucleus (B) and in the cytoplasm (C).
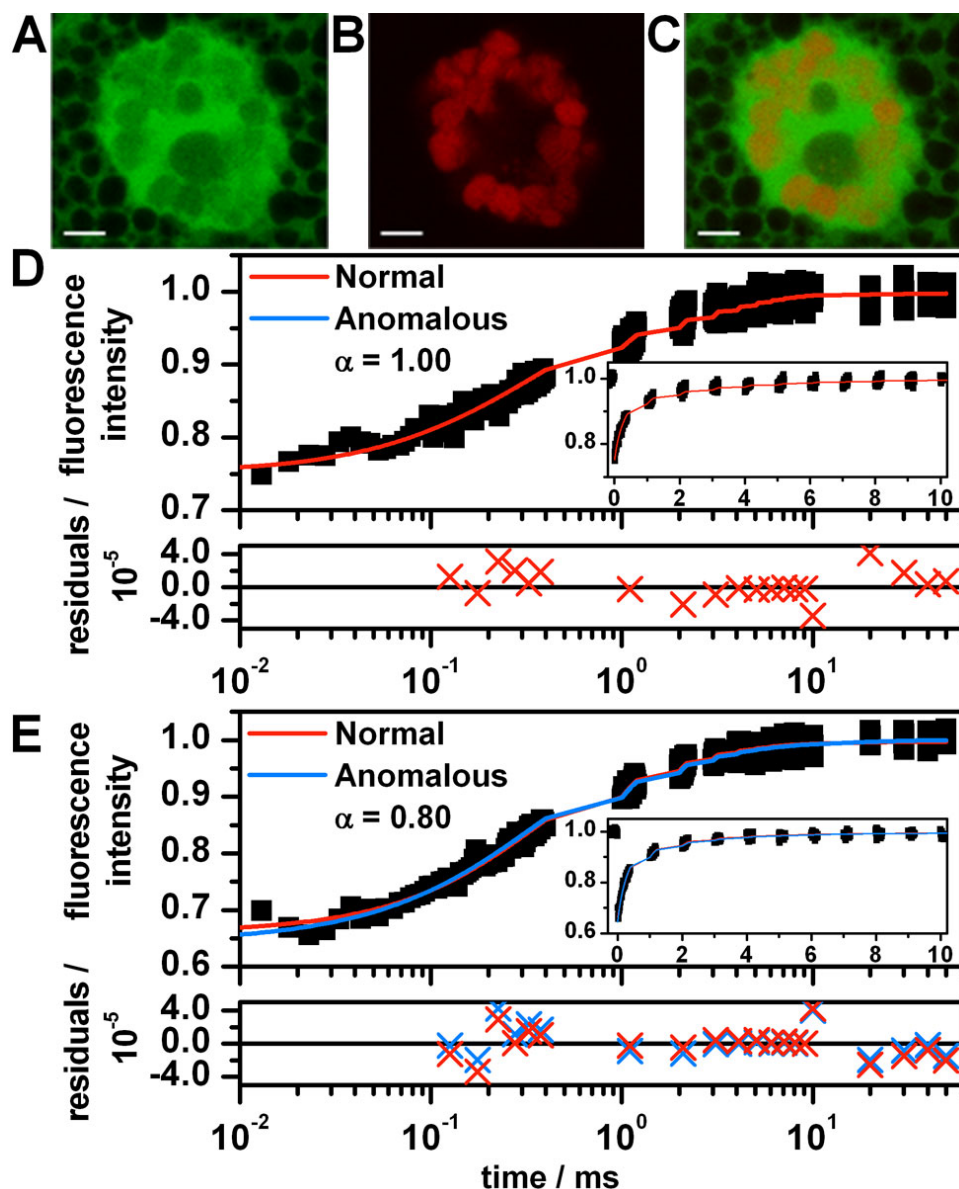
Figure 2.6: (A-C) Two-photon microscopy images of a polytene cell expressing both unconjugated GFP (A) and H2B-mRFP (B) to mark the chromosomes. Panel C is the merge of panels A & B. Scale bar, 5 μm. (D-E) FRAP data (points) and fits (lines) of GFP in polytene cells plotted on logarithmic time axes and linear time axes (insert). The residuals were averaged as in Figure 2.2. The data were fit to Eq. 2.6 using a value of α that was either fixed to 1.0 (normal diffusion) or floated in the fit (anomalous diffusion). The data were recorded by focusing on points in the interchromatin space (D) and on the chromosomes (E).

45

which clearly indicates that crowding is occurring (since the base solvent of the cell is also water); however, the crowding does not cause anomalous diffusion. The observation that GFP diffuses normally in the interchromatin space but anomalously within the polytene chromosomes is notable, since neighboring biological regions unseparated by a membrane typically do not exhibit different types (anomalous vs. normal) of diffusion. Unconjugated GFP should not interact specifically with DNA or other elements of chromatin, so it is likely that the anomalous diffusion in the chromosomal regions is due to the presence of obstructions. This issue is considered further in the Discussion section. We also investigated GFP diffusion in the cytoplasm of polytene cells (Figure A.5 in the Appendix); it exhibited diffusion that was more anomalous than the nucleus, in agreement with the HeLa result.

In order to compare diffusion across samples with different anomalous factors we calculated an effective diffusion coefficient defined as D_{eff}:

$$D_{eff} \equiv \frac{\omega^2}{6\tau_D} = \frac{\omega^2}{6}\left[\frac{\alpha\omega^2}{6\Gamma}\right]^{-\frac{1}{\alpha}} \tag{2.7}$$

where τ_D is the residence time (as defined by Kang *et al.*[39]) for a region of interest of radius ω. The effective diffusion coefficient reflects the diffusion coefficient that would have been measured in the experiment if diffusion were Brownian; its value is specific to the size of the observation region. The transport coefficients and anomalous factors listed in Table 2.2 (along with the focused spot size) were used to calculate a D_{eff}. These values are plotted along with normal diffusion coefficients of samples that exhibited Brownian diffusion in Figure 2.7. The effective diffusion coefficients of all of
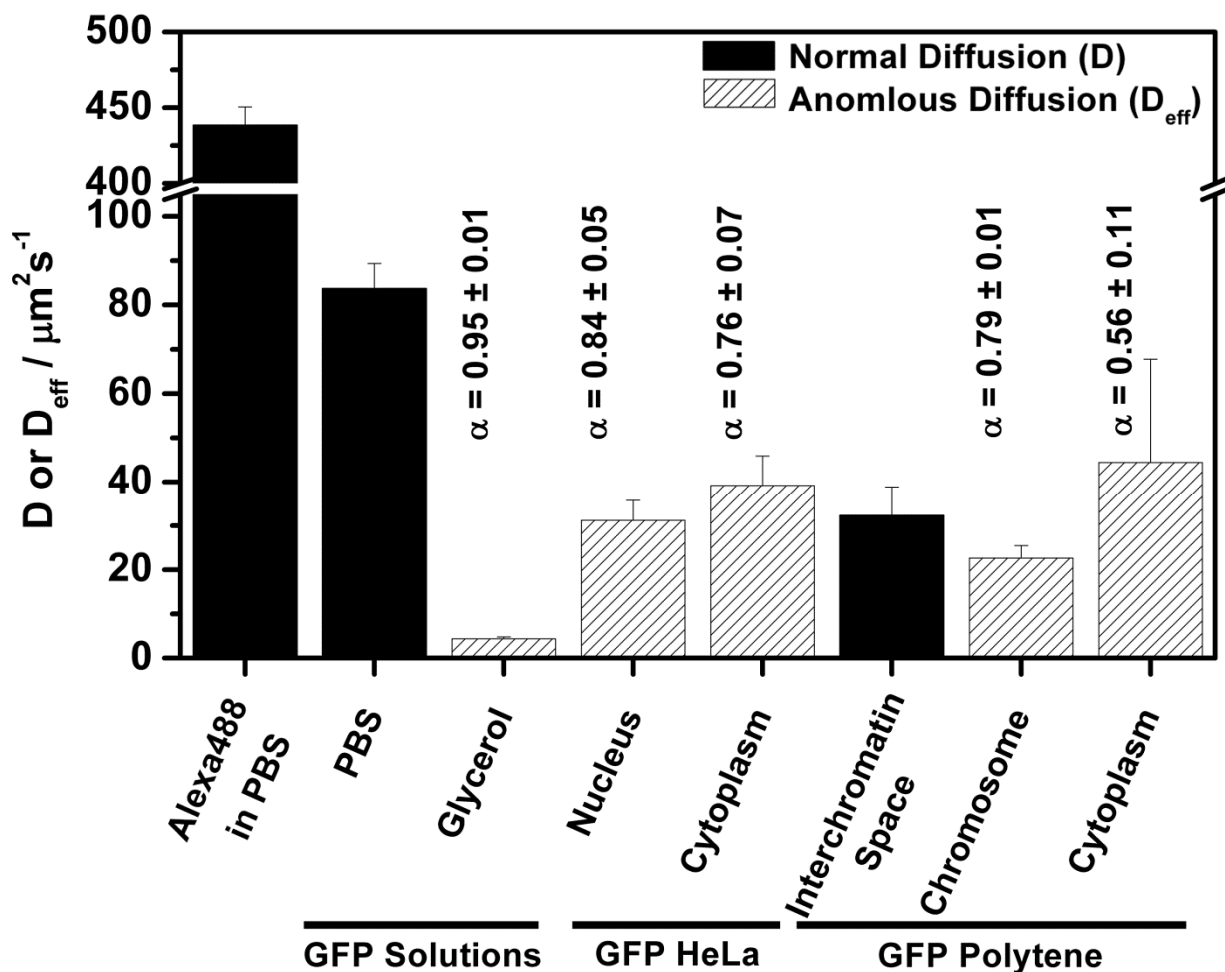
Figure 2.7: Summary of diffusion (or effective diffusion) coefficients for each sample. Brownian (or normal) diffusion is indicated by the solid bars and anomalous diffusion is indicated by the striped bars. For anomalous diffusion samples, the effective diffusion coefficients were calculated using dimensions of the focused point spread function, and the average anomalous parameter is listed above the bar. All values are the average of three independent fits of data sets consisting of an average of 500 samples each. The errors are the standard deviation of the fit results.

the cellular samples were similar regardless of the environment, even though they differed in the magnitude of the anomalous factor.

2.4. Discussion

2.4.1. Revisiting point FRAP

We have investigated the use of point FRAP with a diffraction-limited bleach and observation volume to quantitatively characterize fluorophore diffusion. In addition to providing a well-defined region of interest, point FRAP allows for highly specific regions of a cell to be selected, which reduces possible sample heterogeneities within the region of interest. Area FRAP methods with larger observation regions average out these variations. Point FRAP can determine diffusion coefficients over a wide range of time scales due to its superior time resolution over other FRAP methods. When using other FRAP regions of interest, it is necessary to scan over the region of interest which can take tens to hundreds of milliseconds. With point FRAP we are able to measure diffusion coefficients ranging from 438 μm^{2}s^{-1} (Alexa Flour 488) to 4 μm^{2}s^{-1} (GFP in glycerol), a range that covers over two orders of magnitude. It is quite possible to measure diffusion coefficients that are slower than the one measured for glycerol, as it is straightforward to increase the amount of time that data is collected. Additionally, point FRAP could be used to measure binding on longer time scales. Since binding dynamics can occur over a broad range of timescales, it may be helpful to augment point FRAP measurements with quantitative area FRAP, since this latter method is able to achieve long observation times with less averaging.

FCS can also be used to measure protein dynamics in a diffraction limited spot, but we believe point FRAP offers two advantages over FCS. First, FCS requires a very

low concentration (nanomolar) of fluorescent species, which is not always achievable in cellular samples. Point FRAP can be used at a wider range of concentrations and is ideal for samples in which the fluorescent species is highly expressed. Second, in order to measure dynamics FCS requires constant illumination for seconds or longer, resulting in photobleaching and photodamage artifacts for samples in which there is slow diffusion or an immobile fraction. In point FRAP, the laser may be turned off for periods of time to reduce photobleaching while the dynamics can still be measured.

2.4.2. Application of the photophysics correction to general FRAP procedures

We have demonstrated that it is critical to account for reversible fluorophore photobleaching to extract quantitative information from point FRAP measurements. By separately considering the raw bleach recovery data and control data of an immobilized fluorophore sample, we determined that reversible bleaching primarily affected the control data. This is not a general result; reversible bleaching may affect the raw bleach recovery in other FRAP implementations (including area FRAP, as discussed below). Therefore, we recommend that all FRAP investigations should test for the importance of reversible bleaching by performing control experiments similar to those in the present study. First, an experiment should be preformed where diffusion is eliminated (e.g. by fixation) to isolate the influence of photophysics. If the sample shows recovery, then reversible photobleaching needs to be taken into account, and the raw bleach and control curves of these samples should be carefully investigated separately to determine from what behavior photophysics anomaly is arising. Another test is to measure the recovery in solution to ensure that the sample recovers according to

49

Brownian diffusion, though of course this test only applies to FRAP implements with sufficient time resolution to observe diffusion.

The FRAP model we have derived (Eq. 2.6) can generally account for the influence of reversible bleaching in the raw bleach curve and/or in the control curve. However, because only the control curve was affected by reversible bleaching in our experiments, we chose to implement the model in a way that specifically accounts for this case. Determining the reversible bleach parameters by fitting the initial decay of the control curve would not yield accurate results if the raw bleach curve were also influenced by reversible bleaching.

We also note that the importance of accounting for reversible photobleaching is not specific to point FRAP experiments. This assertion is substantiated by a recent study in which McNally and coworkers[32] demonstrated the detrimental impact of reversible photoswitching on area FRAP experiments of nuclear proteins. Given the ~600 µs photophysics timescale measured in the present study, it may sound surprising that area FRAP measurements on much longer timescales (time resolution of milliseconds to seconds) would be affected by reversible bleaching. However, the time scale for photobleaching reversion is affected by illumination intensity[41]; reversion takes much longer at lower light intensities and can even proceed in the absence of illumination with time constants of a few seconds. Thus, FRAP experiments on much longer time scales can be affected by reversion. Additionally, area FRAP experiments that employ high intensity focused illumination can be affected by reversion on long time scales because each pixel is typically only illuminated for a few microseconds per frame. Raster scanning the focused laser effectively introduces an intermittent

illumination, similar to the intermittent scheme employed in the present point FRAP experiments; the cumulative experimental time after photobleaching does not accurately reflect the time that each pixel has actually been irradiated. In conclusion, it is difficult to generally assess the importance of reversible photobleaching on various FRAP procedures, so it is important to test for the importance of reversible bleaching as discussed above.

2.4.3. Observation of both normal and anomalous diffusion in live cells

The detection of anomalous diffusion in most of the cellular samples is consistent with several previous findings.[5-8] However, the observation of Brownian diffusion in the interchromatin space of polytene nuclei is unique. Unlike normal diploid cells where the chromatin is diffuse and occupies the entire nucleus, polytene cells contain large chromosomes between which are regions of nucleoplasm that is free of DNA. Our point FRAP measurements indicate that unconjugated GFP diffuses normally in these interchromatin spaces, while it exhibits anomalous diffusion in the chromosomal regions of the same cell. This result is notable for several reasons. First, since anomalous diffusion is observed only in chromosomal regions of the polytene cells, it is likely that the primary crowding agent responsible for anomalous diffusion in the nucleus of other cell types is chromatin. Although this result is not entirely surprising, it has been suggested that the high degree of macromolecular crowding in cells could generally cause anomalous diffusion. The interchromatin space exhibits a viscosity about 2.6 times that of water and it undoubtedly contains high concentrations of macromolecules other than DNA, yet GFP diffuses freely. We therefore conclude that transport through

51

chromatin, and not crowding by other macromolecules, causes unconjugated GFP to exhibit subdiffusion in cell nuclei.

A second and closely related point has to do with the molecular origin of anomalous diffusion within regions that contain chromatin. Subdiffusion can result from various types of obstructions or binding interactions. Since unconjugated GFP is not expected to have binding activity, the anomalous behavior observed in chromosomal regions must be due to obstructed diffusion through DNA and other elements of chromatin. The anomalous exponent observed in polytene nuclei (α = 0.79) is less than in HeLa nuclei (α = 0.84), which is consistent with a higher obstacle concentration as might be expected for a relatively dense bundle of chromatin in which the polymers are either stationary or moving on a much slower timescale than the GFP diffusion resulting in transient pockets of GFP. However, both values are well above the asymptotic percolation cluster limit, which is α ~ 0.53 in three-dimensions.[8, 29]

Finally, the observation that GFP diffuses normally in the interchromatin space and measurement of its anomalous exponent in chromatin will serve as a useful basis for future investigations of proteins that may exhibit binding and other biological activity. For example, if future measurements determine that other proteins diffuse anomalously in the interchromatin space of polytene nuclei, it can be reasonably concluded that this result is due to binding heterogeneity and not crowding. Furthermore, the analysis of FRAP experiments intended to probe the DNA-binding properties of other proteins will require a model that accounts for anomalous diffusion in chromosomal regions, in addition to binding.

2.5. Conclusion

We introduce a new model to interpret quantitative measurements from point FRAP in cellular samples over a wide range of diffusion coefficients. This model takes into account reversible photobleaching to distinguish between fluorophore photophysics and anomalous diffusion. Reversible photobleaching plays a key role in many FRAP experiments, and should therefore be accounted for if accurate quantitative information is to be obtained. We found that anomalous diffusion occurs in most cellular samples expressing unconjugated GFP, with the notable exception of the interchromatin space in polytene samples. The Brownian diffusion observed in these samples were a key result that can be used to interpret future experiments that study binding interactions of biologically active proteins.

REFERENCES

1. Periasamy, N.; Verkman, A. S. Analysis of Fluorophore Diffusion by Continuous Distributions of Diffusion Coefficients: Application to Photobleaching Measurements of Multicomponent and Anomalous Diffusion. *Biophys. J.* **1998***, 75*, 557-567

2. Banks, D. S.; Fradin, C. Anomalous Diffusion of Proteins Due to Molecular Crowding. *Biophys. J.* **2005***, 89*, 2960-2971

3. Masuda, A.; Ushida, K.; Okamoto, T. New Fluorescence Correlation Spectroscopy Enabling Direct Observation of Spatiotemporal Dependence of Diffusion Constants as an Evidence of Anomalous Transport in Extracellular Matrices. *Biophys. J.* **2005***, 88*, 3584-3591

4. Haugh, J. M. Analysis of Reaction-Diffusion Systems with Anomalous Subdiffusion. *Biophys. J.* **2009***, 97*, 435-442

5. Bancaud, A.; Huet, S.; Daigle, N.; Mozziconacci, J.; Beaudouin, J.; Ellenberg, J. Molecular Crowding Affects Diffusion and Binding of Nuclear Proteins in Heterochromatin and Reveals the Fractal Organization of Chromatin. *EMBO J.* **2009***, 28*, 3785-3798

6. Wu, J.; Corbett, A. H.; Berland, K. M. The Intracellular Mobility of Nuclear Import Receptors and NLS Cargoes. *Biophys. J.* **2009***, 96*, 3840-3849

7. Guigas, G.; Kalla, C.; Weiss, M. The Degree of Macromolecular Crowding in the Cytoplasm and Nucleoplasm of Mammalian Cells is Conserved. *FEBS Lett.* **2007***, 581*, 5094-5098

8. Weiss, M.; Elsner, M.; Kartberg, F.; Nilsson, T. Anomalous Subdiffusion Is a Measure for Cytoplasmic Crowding in Living Cells. *Biophys. J.* **2004***, 87*, 3518-3524

9. Guigas, G.; Weiss, M. Sampling the Cell with Anomalous Diffusion—The Discovery of Slowness. *Biophys. J.* **2008***, 94*, 90-94

10. Sereshki, L. E.; Lomholt, M. A.; Metzler, R. A Solution to the Subdiffusion-efficiency Paradox: Inactive States Enhance Reaction Efficiency at Subdiffusion Conditions in Living Cells. *Europhys. Lett.* **2012***, 97*, 20008

11. Saxton, M. J. Anomalous Subdiffusion in Fluorescence Photobleaching Recovery: A Monte Carlo Study. *Biophys. J.* **2001***, 81*, 2226-2240

12. Sokolov, I. M. Models of Anomalous Diffusion in Crowded Environments. *Soft Matter* **2012***, 8*, 9043-9052

13. Sprague, B. L.; Pego, R. L.; Stavreva, D. A.; McNally, J. G. Analysis of Binding Reactions by Fluorescence Recovery after Photobleaching. *Biophys. J.* **2004**, *86*, 3473-3495

14. Kang, M.; Day, C. A.; DiBenedetto, E.; Kenworthy, A. K. A Quantitative Approach to Analyze Binding Diffusion Kinetics by Confocal FRAP. *Biophys. J.* **2010**, *99*, 2737-2747

15. Axelrod, D.; Koppel, D. E.; Schlessinger, J.; Elson, E.; Webb, W. W. Mobility Measurement by Analysis of Fluorescence Photobleaching Recovery Kinetics. *Biophys. J.* **1976**, *16*, 1055-1069

16. Braga, J.; Desterro, J. M. P.; Carmo-Fonseca, M. Intracellular Macromolecular Mobility Measured by Fluorescence Recovery after Photobleaching with Confocal Laser Scanning Microscopes. *Mol. Biol. Cell* **2004**, *15*, 4749-4760

17. Braeckmans, K.; Remaut, K.; Vandenbroucke, R. E.; Lucas, B.; De Smedt, S. C.; Demeester, J. Line FRAP with the Confocal Laser Scanning Microscope for Diffusion Measurements in Small Regions of 3-D Samples. *Biophys. J.* **2007**, *92*, 2172-2183

18. Kang, M.; Day, C. A.; Drake, K.; Kenworthy, A. K.; DiBenedetto, E. A Generalization of Theory for Two-Dimensional Fluorescence Recovery after Photobleaching Applicable to Confocal Laser Scanning Microscopes. *Biophys. J.* **2009**, *97*, 1501-1511

19. Smisdom, N.; Braeckmans, K.; Deschout, H.; vandeVen, M.; Rigo, J.; De Smedt, S. C.; Ameloot, M. Fluorescence Recovery after Photobleaching on the Confocal Laser-scanning Microscope: Generalized Model without Restriction on the Size of the Photobleached Disk. *J. Biomed. Opt.* **2011**, *16*, 046021-046021

20. Mueller, F.; Mazza, D.; Stasevich, T. J.; McNally, J. G. FRAP and Kinetic Modeling in the Analysis of Nuclear Protein Dynamics: What do We Really Know? *Curr. Opin. Cell Biol.* **2010**, *22*, 403-411

21. Mueller, F.; Wach, P.; McNally, J. G. Evidence for a Common Mode of Transcription Factor Interaction with Chromatin as Revealed by Improved Quantitative Fluorescence Recovery after Photobleaching. *Biophys. J.* **2008**, *94*, 3323-3339

22. Lakowicz, J. R., Ed.; In *Nonlinear and Two-photon-induced Fluorescence;* Topics in Fluorescence Spectroscopy; Kluwer Academic Publishers: New York, 1997; Vol. 5.

23. Denk, W.; Strickler, J. H.; Webb, W. W. Two-photon Laser Scanning Fluorescence Microscopy. *Science* **1990**, *248*, 73-76

24. Zipfel, W. R.; Williams, R. M.; Webb, W. W. Nonlinear Magic: Multiphoton Microscopy in the Biosciences. *Nat. Biotechnol.* **2003**, *21*, 1369-1377

25. Brown, E. B.; Wu, E. S.; Zipfel, W. R.; Webb, W. W. Measurement of Molecular Diffusion in Solution by Multiphoton Fluorescence Photobleaching Recovery. *Biophys. J.* **1999**, *77*, 2837-2849

26. Calvert, P. D.; Peet, J. A.; Bragin, A.; Schiesser, W. E.; Pugh, E. N. Fluorescence Relaxation in 3D from Diffraction-limited Sources of PAGFP or Sinks of EGFP Created by Multiphoton Photoconversion. *J. Microsc.* **2007**, *225*, 49-71

27. Schnell, E. A.; Eikenes, L.; Tufto, I.; Erikson, A.; Juthajan, A.; Lindgren, M.; de, L. D. Diffusion Measured by Fluorescence Recovery after Photobleaching based on Multiphoton Excitation Laser Scanning Microscopy. *J. Biomed. Opt.* **2008**, *13*, 064037-064037

28. Feder, T. J.; Burst-Mascher, I.; Slattery, J. P.; Baird, B.; Webb, W. W. Constrained Diffusion or Immobile Fraction on Cell Surfaces: A New Interpretation. *Biophys. J.* **1996**, *70*, 2767-2773

29. Bouchaud, J.; Georges, A. Anomalous Diffusion in Disordered Media: Statistical Mechanisms, Models and Physical Applications. *Phys. Rep.* **1990**, *195*, 127-293

30. Braeckmans, K.; Stubbe, B. G.; Remaut, K.; Demeester, J.; De Smedt, S. C. Anomalous Photobleaching in Fluorescence Recovery after Photobleaching Measurements due to Excitation Saturation a Case Study for Fluorescein. *J. Biomed. Opt.* **2006**, *11*, 044013-044013

31. Stasevich, T. J.; Mueller, F.; Michelman-Ribeiro, A.; Rosales, T.; Knutson, J. R.; McNally, J. G. Cross-Validating FRAP and FCS to Quantify the Impact of Photobleaching on In Vivo Binding Estimates. *Biophys. J.* **2010**, *99*, 3093-3101

32. Mueller, F.; Morisaki, T.; Mazza, D.; McNally, J. Minimizing the Impact of Photoswitching of Fluorescent Proteins on FRAP Analysis. *Biophys. J.* **2012**, *102*, 1656-1665

33. Hoyt, L. F. New Table of the Refractive Index of Pure Glycerol at 20°C. *Ind. Eng. Chem.* **1934**, *26*, 329-332

34. Zobeck, K. L.; Buckley, M. S.; Zipfel, W. R.; Lis, J. T. Recruitment Timing and Dynamics of Transcription Factors at the Hsp70 Loci in Living Cells. *Mol. Cell* **2010**, *40*, 965-975

35. Daddysman, M.; Fecko, C. DNA Multiphoton Absorption Generates Localized Damage for Studying Repair Dynamics in Live Cells. *Biophys. J.* **2011**, *101*, 2294-2303.

36. Schwarz, G. Estimating The Dimension of a Model. *Ann. Stat.* **1978**, *6*, 461-464.

37. Akaike, H. A New Look at the Bayes Procedure. *Biometrika* **1978**, *65*, 53-59

38. Claeskens, G.; Hjort, N. L. *Model Selection and Model Averaging;* Cambridge University Press: Cambridge, UK, 2008

39. Kang, M.; DiBenedetto, E.; Kenworthy, A. Proposed Correction to Feder's Anomalous Diffusion FRAP Equations. *Biophys. J.* **2011***, 100*, 791-792

40. Dickson, R. M.; Cubitt, A. B.; Tsien, R. Y.; Moerner, W. E. On/off Blinking and Switching Behaviour of Single Molecules of Green Fluorescent Protein. *Nature* **1997***, 388*, 355-358

41. Sinnecker, D.; Voigt, P.; Hellwig, N.; Schaefer, M. Reversible Photobleaching of Enhanced Green Fluorescent Proteins. *Biochemistry-USA* **2005***, 44*, 7085-7094

42. Petrášek, Z.; Schwille, P. Precise Measurement of Diffusion Coefficients using Scanning Fluorescence Correlation Spectroscopy. *Biophys. J.* **2008***, 94*, 1437-1448

43. Miller, G. G.; Raleigh, J. A. Action of some Hydroxyl Radical Scavengers on Radiation-induced Haemolysis. *Int. J. Radiat. Biol.* **1983***, 43*, 411-419

44. Segur, J. B.; Oberstar, H. E. Viscosity of Glycerol and Its Aqueous Solutions. *Ind. Eng. Chem.* **1951***, 43*, 2117-2120

45. Chattopadhyay, K.; Saffarian, S.; Elson, E. L.; Frieden, C. Measuring Unfolding of Proteins in the Presence of Denaturant Using Fluorescence Correlation Spectroscopy. *Biophys. J.* **2005***, 88*, 1413-1422

CHAPTER 3: FLUORESCENCE RECOVERY AFTER PHOTOBLEACHING STUDY OF GFP DIFFUSION IN CROWDED MACROMOLECULAR SOLUTIONS

"Research is what I'm doing when I don't know what I'm doing." – Wernher von Braun

3.1. Introduction

The interior of a cell is characterized by a high concentration of macromolecules. Previous studies have shown that proteins exhibit anomalous diffusion under these conditions which is often attributed to and used as a method of quantifying macromolecular crowding inside of cells.[1-4]   Normal Brownian diffusion, which occurs in homogenous samples, is described by a mean squared displacement which grows linearly in time. In contrast, anomalous diffusion is characterized by a mean squared displacement which follows a sublinear power law in time, $\langle r^2 \rangle \propto t^\alpha$, as a result of the heterogeneity in the diffusive environment.   Several potential sources of anomalous diffusion, characterized by α in the mean squared displacement equation above, have been predicted by theoretical models, including mass transport in the presence of a broad distribution of energetic traps (protein binding partners), obstructed diffusion in the presence of immobile fractal obstacles, or correlated motion that arises in an interacting system such as a polymer network.[5,6] Ensemble microscopy techniques such as fluorescence recovery after photobleaching (FRAP) and fluorescence correlation spectroscopy (FCS) mask the underlying mechanism of the anomalous diffusion.[7] A recent study in our group using FRAP that eliminated the above potential sources of anomalous diffusion showed normal diffusion of a small protein tracer.[8]

However, it would be useful to simulate the crowded macromolecular environment *in vitro* to measure the contribution of anomalous diffusion, if any, to transport of small proteins.

Previous studies on model systems of macromolecular crowding have produced conflicting results between the observation of anomalous diffusion[9] or Brownian diffusion.[10-15] The theoretical community has been split if diffusion in crowded solutions should be normal[16,17] or anomalous[18,19] on the time scale of optical microscopy experiments (10's of µs to 10's of ms or longer). However, all of the experimental studies used FCS as the optical microscopy technique of choice. Therefore, studies on artificially crowded systems using FRAP would help settle the debate between the two camps. FRAP is a widely used microscopy technique for interrogating the diffusion and binding of fluorescent molecules. A FRAP experiment is typically performed by photobleaching a small region with a brief exposure to intense laser light, and then observing the time-dependant evolution of florescence signal as unbleached fluorophore migrate into the region. The resulting FRAP signal can be related to molecular processes such as diffusion, binding interactions, active transport, and chemical reactions through the application of an appropriate model.[20,21] Our lab has recently demonstrated a quantitative FRAP model that can be used to accurately identify anomalous diffusions both in solutions and in live cells.[8] Herein, we describe the application of our FRAP method and model to the question of the presence of anomalous diffusion due to macromolecular crowding. Our model systems consist of dextran and bovine serum albumin (BSA) as crowders representing an entangled and globular system respectively. As a tracer we measure the diffusion of dilute

unconjugated green fluorescence protein (GFP) as a model for a small globular protein in the cellular environment. We find that an anomalous model is *not* necessary to describe GFP diffusion in our model systems except possibly at high concentrations that are unrealistic for the cellular environment. Furthermore, we compare our results to the recently developed theory of spherical tracers in dextran solutions by Cai *et al.*[17] and find that our experimental results agree well with the theoretical predictions of the model.

3.2. Materials and Methods

To create the crowded stock solutions, three different molecular weights of dextran (Sigma), and samples of dextrose (Fisher) and BSA (Fisher) were dissolved in PBS to a concentration of ~400 mg/mL (dextran and dextrose) and ~300 mg/mL (BSA). Five (BSA) or ten (dextran and dextrose) samples were produced by serial dilution of the stock solution. GFP was added after the dilution to give each sample a constant concentration of 10 μM. A 50 μL drop of each sample was placed on a coverslip, imaged, and FRAP experiments were performed as described previously (Chapter 2).[8] Each FRAP data set consisted of 500-600 bleach and control points. Each sample had a FRAP data set taken in three different locations in the solution. Each of these locations were individually fit using the FRAP model previously described[8] to obtain diffusion coefficients, transport coefficients, and anomalous parameters.

The above dilutions were completed in duplicate; therefore, a total of 6 individual data sets comprise each measurement. The presented diffusion coefficients, transport coefficients, and anomalous parameters are the average of the fitting results of these 6 data sets. The error bars on the diffusion coefficients, transport coefficients, and

anomalous parameters were calculated from the propagated error of the 95% confidence interval on each fit. In the vast majority of cases, the 95% confidence interval was larger than the standard deviation between the fitting results of the 6 data sets; therefore, the 95% confidence interval gives a fairer presentation of the error present on each measurement.

3.3. Results

3.3.1. Diffusion coefficient of GFP decreases with increasing crowder concentration

Crowed solutions were produced by dissolving three different molecular weights of dextran (average molecular weight of 38, 115, and 566 kDa) and dextrose in phosphate buffered saline (PBS) to create concentrated stock solutions of 400 mg/mL. BSA was dissolved in PBS to create a concentrated stock solution of 300 mg/mL (higher concentrations congealed). The high concentration stock solution was serially diluted to produce ten samples for dextran and dextrose and five samples for BSA. GFP was added to each sample at the same concentration of 10 µM, as the fluorescent tracer. FRAP experiments were then conducted and fit as previously described[8] with modifications detailed in Appendix B. The first model used to fit the FRAP data assumed normal Brownian diffusion of the tracer molecule to acquire a diffusion coefficient (example curve and fit given in Figure B.1 in the Appendix). These diffusion coefficients are plotted in Figure 3.1. The lines of best fit were to a phenomenological stretched exponential[10] given by:

$$D = \exp\left(-kc^n\right) \tag{3.1}$$
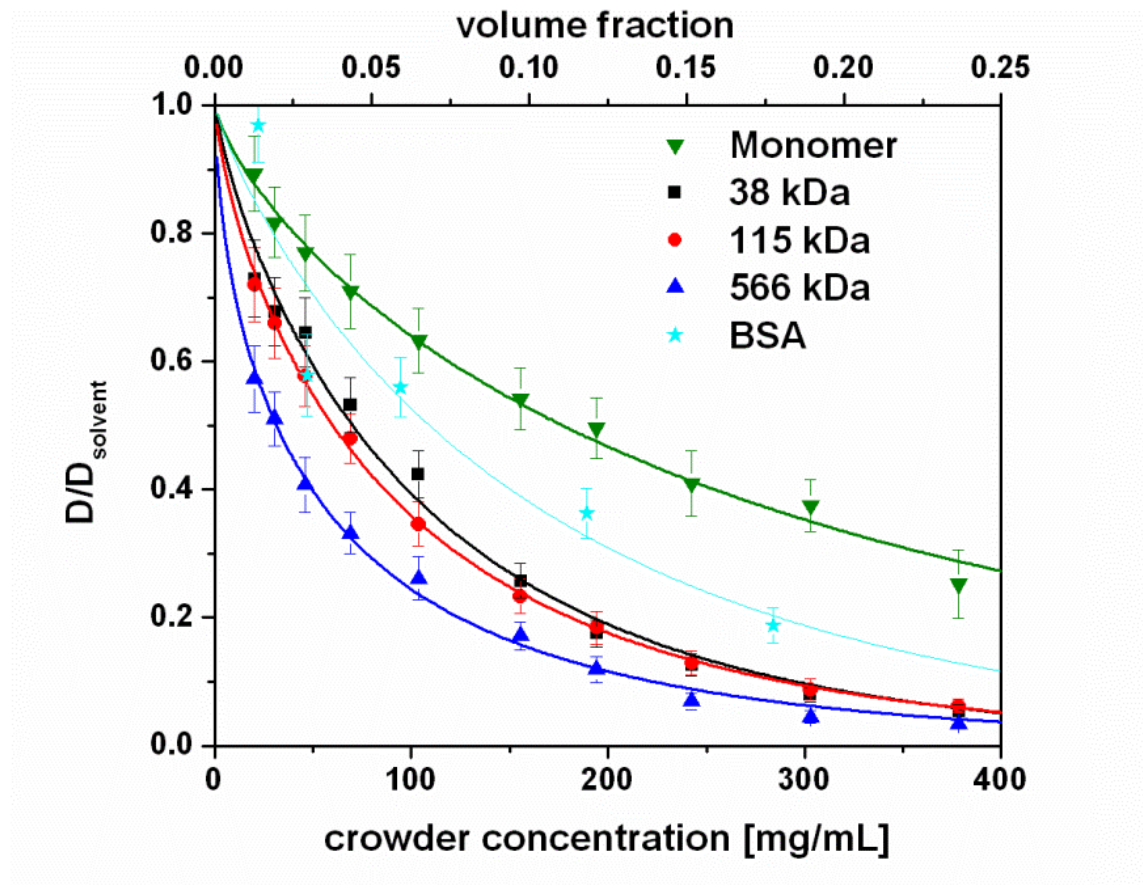
Figure 3.1: Plot of the diffusion coefficient of GFP (normalized to diffusion in buffer) in solutions crowded with different sizes of dextran, dextrose, or BSA. The diffusion coefficient is measured using FRAP and modeled by assuming Brownian diffusion. The crowder concentration for all crowders is listed on the bottom x-axis with the volume fraction for the dextran solutions only listed on the top x-axis. The volume fraction was calculated by multiplying the dextran crowder concentration by 0.625 mL/g, the specific volume of dextran. The concentration of GFP is kept constant in all solutions at 10 μM.

Table 3.1: Parameters used for the stretched exponential fit used in Figures 3.1 & 3.2

	Figure 3.1 (Eq. 3.1)		Figure 3.2 (Eq. 3.2)	
Crowder	k	n	k	n
Dextrose (Monomer)	0.01274	0.7719	0.02424	0.6696
38 kDa Dextran	0.01976	0.8365	0.02422	0.7788
115 kDa Dextran	0.03025	0.7642	0.05704	0.6317
566 kDa Dextran	0.08355	0.6132	0.1549	0.4797
BSA	0.01150	0.8731	0.02545	0.6957

The best fit lines shown in Figure 3.1 and 3.2 are from a phenomenological stretched exponential equation from Eq 3.1 and 3.2 respectively.

where D is the diffusion coefficient and c is the concentration of the crowder and k and n are fitting parameters describing the decay of the diffusion coefficient with increasing crowder concentration and the same of the exponential respectively. The results of the fit to Eq. 3.1 are given in Table 3.1. The curves followed the expected trend where the heaviest dextran retards the diffusion of GFP more abruptly with increasing concentration and the monomer of dextran, dextrose, the least. BSA slowed the diffusion of GFP at an intermediated rate between the dextrans and the dextrose. This was an expected result since the dextran polymers can entangle creating a mesh network through which the GFP must diffuse; whereas, the BSA acts more like "ball-pit" of hard sphere obstacles.

3.3.2. Anomalous diffusion is not required to fit the FRAP data of GFP in crowded solutions

The same FRAP data used to produce Figure 3.1 were refit with a model that allowed for anomalous diffusion (example curve and fit given in Figure B.2 in the Appendix). The resulting transport coefficients and anomalous parameters are given in Figure 3.2. The transport coefficients were fit with a stretched exponential just as the diffusion coefficients were in Figure 3.1. The fitting function is given by

$$\Gamma = \exp\left(-kc^n\right) \tag{3.2}$$

where Γ is the transport coefficient. The results of the fit to Eq. 3.2 are also given in Table 3.1. The transport coefficient follows the same trend as the diffusion coefficient (Figure 3.2A). The key result was that the anomalous parameter was within error of 1, indicating normal diffusion for most samples (Figure 3.2B). For the few samples which were outside of the range of error of 1, none had an anomalous parameter smaller than
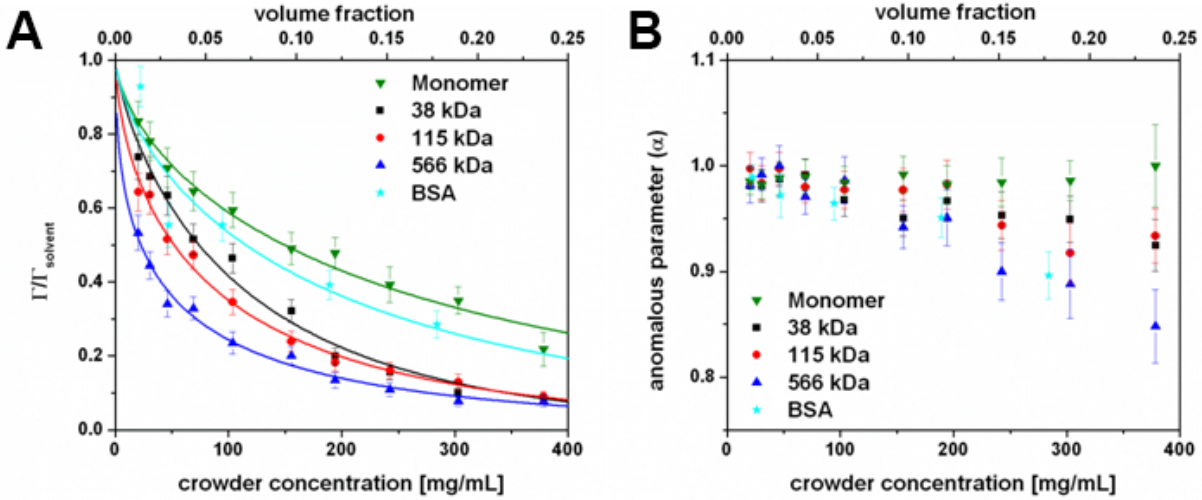
Figure 3.2: The same data presented in Figure 3.1 is refit with a model that includes the potential for anomalous diffusion. The crowder concentration is varied; the concentration of GFP is kept constant in all solutions at 10 µM. (A) The transport coefficient of GFP (normalized to transport coefficient in buffer) in solutions crowded with different sizes of dextran, dextrose, or BSA. The crowder concentration for all crowders is listed on the bottom x-axis with the volume fraction for the dextran solutions only listed on the top x-axis. (B) The anomalous parameter in solutions crowded with different sizes of dextran, dextrose, or BSA.

0.85. Values of the anomalous parameter in cellular samples in the cytoplasm and nucleoplasm are often smaller than 0.8.[8] Furthermore, the samples that potentially exhibited anomalous diffusion had scaled diffusion coefficients of <0.1 (<8 μm^2/s) which is much slower than the scaled diffusion coefficient of GFP observed in cellular samples of 0.3 (25 μm^2/s).[8] Therefore, although the potential exists for macromolecular crowding to exhibit slight levels of anomalous diffusion of a small tracer, it is not relevant at cellular crowding concentrations. Additionally, the observed anomalous diffusion may have been due to a secondary effect of the crowded solution such as an increased likelihood of GFP aggregates.

3.3.3. Dextrose exhibits Stokes-Einstein behavior while the polymer solutions deviate from Stokes-Einstein.

The bulk viscosity, also referenced as the macroviscosity, was measured on the dextran and dextrose polymer solutions using a rheometer. The macroviscosity data are shown in Figure B.3 in the Appendix. The viscosity data was used to calculate the overlap concentration, c*, and for plotting the FRAP data, which probes the microviscosity, against the macroviscosity.   The overlap concentration is the concentration at which the power-law behaviors of viscosities of the system are expected to change due to entanglement of the dextran polymers. In Figure 3.3A, the diffusion coefficients from Figure 3.1 are divided by the expected diffusion coefficient according to the Stokes-Einstein (SE) equation for the measured viscosity. The SE equation is normalized to the viscosity in the bulk solvent in all cases so the equation is reduced to the following proportion:

$$\frac{D_1}{D_2} = \frac{\eta_2}{\eta_1}$$

(3.3)
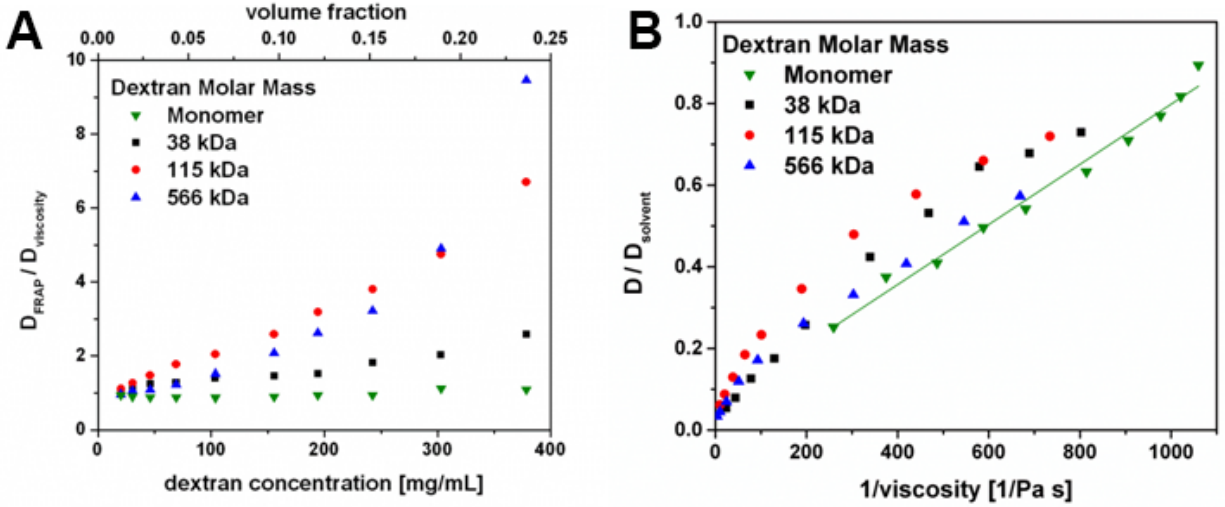
Figure 3.3: The measured diffusion coefficient of GFP using FRAP compared to the bulk macroviscosity of dextran and dextrose solutions. (A) The microviscosity of the crowded GFP solutions is divided by the bulk macroviscosity as measured using a rheometer and plotted on the vertical axis. A value of 1 indicates that the micro and macro viscosities are the same (as in the case of the monomer, dextrose). Values > 1 indicate that the microviscosity is less than the macroviscosity indicating that the diffusion of the particle is less hindered on the microscopic level. (B) Plot of inverse viscosity verses normalized diffusion coefficient. This plot compares the microviscosity to the macroviscosity regardless of the molar mass of the dextran. Additionally, the monomer follows SE behavior according to the following best fit equation: $D/D_0 = 0.000736 \pm 0.000032 \, (1/\eta) + 0.062 \pm 0.025$ with a coefficient of determination of 0.983.

where η is the macroviscosity. The dextrose solutions exhibit behavior that is consistent with SE predictions (the microviscosity is the same as the macroviscosity hence all the data are 1). However, the dextran solutions show increasing deviation from the SE equation with increasing crowder concentration. This result agrees with the predictions of a theoretical model of the microviscosity of GFP as it is expected to increase with a power law of 1.5 after the overlap concentration;[17] whereas, the dextran macroviscosity has been shown to increase with a power law of 4 after the overlap concentration.[22] Therefore, the difference between the micro and macro viscosity should diverge faster with increasing crowder concentration. Figure 3.3B is a direct comparison of the macroviscosity (horizontal axis) and microviscosity (vertical axis). In this presentation, the dextrose is confirmed to correspond to the SE equation by the fit to a linear regression. The dextran samples diverge from linearity after approximately the first five data points. The overlap concentration occurs between 130-150 mg/mL which is where the transition from a linear to non-linear curve is observed.

3.3.4. Quantitative comparison of microviscosity results to polymer theory

The theory presented in Cai *et al.*[17] predicts a power law of 1.5 for the microviscosity above the overlap concentration and 0 below the overlap concentration. The same data presented in Figure 3.1 are plotted on a log-log scale in Figure 3.4A. The points after the overlap concentration are fit with a linear regression to measure the power-law behavior in this region. The results of the fit are shown in Table 3.2. The post-overlap concentration points show good agreement with the theoretical predictions. However, there is a slight increase in the microviscosity observed before the overlap concentration which is not predicted by the theoretical calculations. Additionally, the
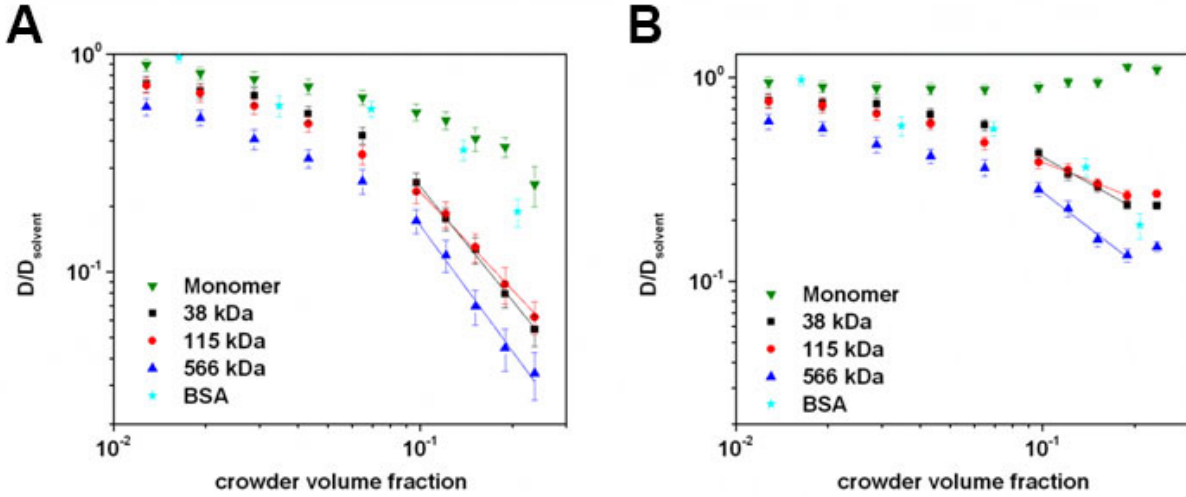
Figure 3.4: Comparison of our FRAP viscosity results to a theoretical model. (A) The model presented in Cai et al.[17] predicts a power law behavior of the microviscosity with a power of 1.5 after the overlap concentration. Data are plotted against the volume fraction and the last five points of the dextran samples (corresponding to the points after the overlap concentration, c*) are fit to a linear regression on a log-log plot. The results of the fit are shown in Table 3.2. (B) Same data as in panel A except that the dextran microviscosity is divided by the microviscosity experienced in the monomer solution to isolate the effects of polymer entanglement only and remove any contributions due to changed composition of the solvent (i.e. an increase in hydrogen bonding). Results of the fits are shown in Table 3.2.

Table 3.2: Linear regression results from the log-log plots in Figure 3.4. The linear regression is taken from the last five points of the data showing the power law behavior after the overlap concentration c*. The slope indicates the power of the power law.

Average Dextran Molar Mass	Overlap concentration (mg/mL)	Slope in Panel A	Slope in Panel B
38 kDa	139	-1.7467 ± 0.0487	-0.8453 ± 0.0520
115 kDa	133	-1.4963 ± 0.0787	-0.5899 ± 0.0427
566 kDa	150	-1.9226 ± 0.0991	-1.1578 ± 0.0939

monomer solutions also show an increase in microviscosity with increasing concentration indicating that there are additional contributions to the microviscosity other than the polymer entanglement. To remove these contributions, the measured diffusion coefficient is divided by the expected diffusion coefficient from the bulk viscosity measurements of the monomer dextrose solution[23] (Figure 3.4B). This "normalizes out" the additional contributions to the microviscosity other than the polymer entanglement. As a result, the monomer solution shows no change in microviscosity while the power-law behavior is reduced in the dextran solutions after the entanglement concentration.

3.4. Discussion

3.4.1. Brownian diffusion describes the diffusion of GFP in crowded solutions

Attributing anomalous diffusion of tracer molecules to macromolecular crowding in crowded solutions is a controversial topic with theory[16-19] and experiment[9-15] supporting both sides. However, the experimental evidence consists mostly of FCS studies prompting the need for another technique to corroborate results. Our lab has perfected a FRAP method and model ideally suited to answering this question. We modeled our study after the main paper supporting anomalous diffusion in solutions crowded with dextran.[9] NMR studies on a similar system have already shown conflicting results[15] to the prior study, and our results agree with the NMR data showing that anomalous diffusion is not necessary to explain interpret diffusion in crowded solutions of dextran. It is not clear why the Banks and Fradin study does not agree with our results and others; however, it has been shown that improperly calibrated FCS focal volumes can give rise to anomalous results.[16] Finally, a few of our high concentration of

crowder experiments do show anomalous diffusion; however, it is not clear that this result is due to a direct crowding effect. At such high concentrations interactions between GFP molecules become more likely (due to reduced solvent concentration) possibly resulting in aggregation.

3.4.2. FRAP data confirms theoretical studies on the diffusion of spherical tracer particles in dextran solutions

Our results agree qualitatively, if not quantitatively, with the theory presented in Cai *et al.*[17] Firstly, the theory predicts that anomalous diffusion should only be observed after the overlap concentration in a brief transition region between two normal diffusion regions of the particle at different diffusion coefficients. This transition region can only be detected with methods that are sensitive for < 10 µs for particles the size of GFP. Therefore, our FRAP experiments should not detect anomalous diffusion which is what our results show. Our microviscosity diffusion coefficients show the two regimes of power-law behavior (with the transition at the overlap concentration) predicted for the tracer particle in a dextran solution. However, when correcting for the non-polymer contributions to the viscosity, the power-law observed in our experiments does not agree with the result predicted by the theory.

3.5. Conclusion

We found that macromolecular crowding of dextrans and BSA does not contribute to the anomalous diffusion of GFP as measured using FRAP. This result agrees with our previous work measuring the diffusion of GFP in live cell nuclei away from immobile obstacles such as membranes and chromatin. Our control experiments measuring diffusion in dextrose solutions follow normal diffusion and Stokes-Einstein behavior. Furthermore, our experimental results match a previously derived theoretical

model for small spherical tracers in dextran solution in both its predictions of Brownian diffusion on the time scale of our experiment and the observed microviscosity power-law transition that occurs at the overlap concentration of the dextran crowder.

Acknowledgement

REFERENCES

1. Bancaud, A.; Huet, S.; Daigle, N.; Mozziconacci, J.; Beaudouin, J.; Ellenberg, J. Molecular crowding affects diffusion and binding of nuclear proteins in heterochromatin and reveals the fractal organization of chromatin. *EMBO J.* **2009**, *28*, 3785-3798.

2. Guigas, G.; Kalla, C.; Weiss, M. The degree of macromolecular crowding in the cytoplasm and nucleoplasm of mammalian cells is conserved. *FEBS Lett.* **2007**, *581*, 5094-5098.

3. Weiss, M.; Elsner, M.; Kartberg, F.; Nilsson, T. Anomalous Subdiffusion Is a Measure for Cytoplasmic Crowding in Living Cells. *Biophys. J.* **2004**, *87*, 3518-3524.

4. Wu, J.; Corbett, A. H.; Berland, K. M. The Intracellular Mobility of Nuclear Import Receptors and NLS Cargoes. *Biophys. J.* **2009**, *96*, 3840-3849.

5. Sokolov, I. M. Models of anomalous diffusion in crowded environments. *Soft Matter* **2012**, *8*, 9043-9052.

6. Saxton, M. J. Anomalous Subdiffusion in Fluorescence Photobleaching Recovery: A Monte Carlo Study. *Biophys. J.* **2001**, *81*, 2226-2240.

7. Saxton, M. Wanted: A Positive Control for Anomalous Subdiffusion. *Biophys. J.* **2012**, *103*, 2411-2422.

8. Daddysman, M. K.; Fecko, C. J. Revisiting Point FRAP to Quantitatively Characterize Anomalous Diffusion in Live Cells. *J. Phys. Chem. B* **2013**, *117*, 1241-1251.

9. Banks, D. S.; Fradin, C. Anomalous diffusion of proteins due to molecular crowding. *Biophys. J.* **2005**, *89*, 2960-2971.

10. Goins, A. B.; Sanabria, H.; Waxham, M. N. Macromolecular Crowding and Size Effects on Probe Microviscosity. *Biophys. J.* **2008**, *95*, 5362-5373.

11. Balbo, J.; Mereghetti, P.; Herten, D.; Wade, R. The Shape of Protein Crowders is a Major Determinant of Protein Diffusion. *Biophys. J.* **2013**, *104*, 1576-1584.

12. Dauty, E.; Verkman, A. S. Molecular crowding reduces to a similar extent the diffusion of small solutes and macromolecules: measurement by fluorescence correlation spectroscopy. *J. of Mol. Recognit.* **2004**, *17*, 441-447.

13. Engelke, H.; Dorn, I.; Radler, J. O. Diffusion and molecular binding in crowded vesicle solutions measured by fluorescence correlation spectroscopy. *Soft Matter* **2009**, *5*, 4283-4289.

14. Muller, C. B.; Eckert, T.; Loman, A.; Enderlein, J.; Richtering, W. Dual-focus fluorescence correlation spectroscopy: a robust tool for studying molecular crowding. *Soft Matter* **2009**, *5*, 1358-1366.

15. Shakhov, A.; Valiullin, R.; Karger, J. Tracing Molecular Propagation in Dextran Solutions by Pulsed Field Gradient NMR. *J. Phys. Chem. Lett.* **2012**, *3*, 1854-1857.

16. Dix, J. A.; Verkman, A. S. Crowding Effects on Diffusion in Solutions and Cells. *Ann. Rev. Biophys. Biomol. Struct.* **2008**, *37*, 247.

17. Cai, L.; Panyukov, S.; Rubinstein, M. Mobility of Nonsticky Nanoparticles in Polymer Liquids. *Macromolecules* **2011**, *44*, 7853-7863.

18. Hafling, F.; Franosch, T. Crossover in the Slow Decay of Dynamic Correlations in the Lorentz Model. *Phys. Rev. Lett.* **2007**, *98*, 140601.

19. Horton, M. R.; Hofling, F.; Radler, J. O.; Franosch, T. Development of anomalous diffusion among crowding proteins. *Soft Matter* **2010**, *6*, 2648-2656.

20. Sprague, B. L.; Pego, R. L.; Stavreva, D. A.; McNally, J. G. Analysis of Binding Reactions by Fluorescence Recovery after Photobleaching. *Biophys. J.* **2004**, *86*, 3473-3495.

21. Kang, M.; Day, C. A.; DiBenedetto, E.; Kenworthy, A. K. A Quantitative Approach to Analyze Binding Diffusion Kinetics by Confocal FRAP. *Biophys. J.* **2010**, *99*, 2737-2747.

22. Tirtaatmadja, V.; Dunstan, D. E.; Boger, D. V. Rheology of dextran solutions. *J. Non Newtonian Fluid Mech.* **2001**, *97*, 295-301.

23. Powell, C. W. R. I.-The viscosity of sugar solutions. *J. Chem. Soc. , Trans.* **1914**, *105*, 1-23.

CHAPTER 4: RNA POLYMERASE II SUBUNITS EXHIBIT A BROAD DISTRIBUTION OF MACROMOLECULAR ASSEMBLY STATES IN THE INTERCHROMATIN SPACE OF CELL NUCLEI[*]

"Science is a way of thinking much more than it is a body of knowledge." – Carl Sagan

4.1. Introduction

A central question in modern molecular biology is the mechanism by which large, multi-subunit protein complexes assemble inside a cell. Essential cellular processes such as transcription,[1] splicing,[1,2] and genome repair[3] are undertaken by massive assemblies involving many distinct molecular modules that efficiently carry out specific tasks. While "protein recruitment" is cavalierly viewed as the initial step in assembly, molecular-level details about how this process is initiated and through what intermediates such complexes form remain ambiguous.[4] Two primary models have emerged to explain how cellular machinery assembles to handle the dynamic demands they must meet.[5] One proposal is a top-down approach, in which the components of a macromolecular assembly bind one another prior to receiving an activation signal, forming a stable supra-assembly that is often called a molecular factory. Such a factory would be poised for efficient handling of cellular tasks but would be slow to traverse the cellular interior and poorly suited to respond to changing external stimuli. On the other extreme is a bottom-up approach, in which each component of the final molecular

assembly diffuses through the cellular interior individually and stochastically encounters binding partners at the metabolic site (such as a transcription factor) until the entire complex is amassed. This stochastic model would enable rapid movement of the smaller molecular modules within the cell, but the binding steps to form a full complex from individual components may limit the overall activation rate. Interestingly, proponents of both models invoke the crowded nuclear milieu as corroborating evidence, either in support of factory domains or restrictive nuclear architecture.[6,7] In an effort to distinguish between these paradigms, we decided to investigate the incorporation of individual components of the RNA Polymerase II (RNAPII) transcription complex in regions of live cell nuclei devoid of chromatin binding sites.

The present study specifically investigates RNAPII since it is responsible for mRNA production and occupies a critical position in the central dogma. While extensive *in vitro* molecular biology research has elucidated the mechanical intricacies of how the RNAPII complex transcribes template DNA, the advent of *in vivo* fluorescent labeling and the widespread use of fluorescent microscopy have enabled detailed observations of RNAPII complex interactions with chromatin in the native cellular environment.[8-11] Much work has been conducted to characterize RNAPII behavior in bacterial, insect, and mammalian systems; however, the majority focus specifically on subunit assembly and interactions on chromatin, typically in the vicinity of DNA binding sequences. In studies using both RNAPI and RNAPII, polymerase subunits and transcription factors have been found to have distinct dynamics, arguing against preassembled complexes,[8,9,12] though these results contradict some earlier work.[13-15] Thus, it remains

unresolved whether the assembly is stochastic[9] or stepwise,[8,16] with implications for a generalized framework of multi-component protein assemblies.[17]

No previous investigations have characterized RNAPII component diffusion dynamics preceding chromatin interactions in cells and most studies have completely neglected the importance of diffusion. We postulated that measuring the diffusion dynamics of RNAPII components prior to chromatin binding could yield insights into the mode of assembly. We sought to better understand the process of RNAPII complex assembly and nuclear mobility by investigating the dynamics of the Rpb3 and Rpb9 subunits in the interchromatin space (nucleoplasm devoid of chromatin) of cell nuclei using fluorescence recovery after photobleaching (FRAP).

We express fusions of Rpb3 and Rpb9, two subunits exclusive to RNAPII , with enhanced green fluorescent protein (GFP) in the polytene cells of *Drosophila melanogaster* larvae.[18] These polytene cells contain many copies of the genomic DNA that form large chromosomal bundles during interphase (Figure 4.1a,b). By expressing RNAPII subunit-GFP fusions and H2B-mRFP tagged histones in polytene cells, we are able to optically resolve nuclear regions containing chromatin and restrict our analysis exclusively to the interchromatin space (Figure 4.1). This region is devoid of chromatin and therefore lacks DNA binding sites. We find the diffusion of both RNAPII subunits was non-Brownian and the recovery dynamics of the two subunits are different.

While non-Brownian diffusive behavior is often termed anomalous and attributed to molecular crowding,[19] we propose a fundamentally different interpretation. Through a comparison to the mobility of unconjugated GFP (lacking a localization sequence),[20] which does exhibit Brownian diffusion, we determine that molecular crowding is not

responsible for the observed diffusive behavior. Rather, both RNAPII subunits must participate in heterogeneous distributions of complexes with a broad range of sizes, from isolated subunits to fully assembled transcription complexes. We term this type of diffusive behavior *apparent anomalous diffusion,* in which non-Brownian behavior is observed by simultaneously probing many states of pre-formed complexes with different diffusion coefficients.

4.2. Results

4.2.1. Automated "shotgun ptFRAP" data collection

We chose to study the transport properties of the RNAPII subunits Rpb3 and Rpb9 in the absence of chromatin binding sites or membrane perturbations by restricting the region of FRAP investigation to the interchromatin space of cell nuclei. We used a point-FRAP (ptFRAP) method to probe diffusion, which is an implementation where optical diffraction-limited spots are photobleached and the fluorescent recovery tracked in time with sub-millisecond resolution.[20] In contrast to the more common area-FRAP in which micron-sized features are photobleached,[21] ptFRAP probes smaller sample regions and enables several orders of magnitude higher time resolution. To restrict the analysis of photobleaching recovery to the interchromatin space of polytene nuclei (avoiding both cellular membranes and chromatin regions) and prevent datapoints from overlapping in space during collection, we implemented an automated datapoint collection method termed "shotgun ptFRAP" (Figure 4.1).

The method consists of a data collection program in which evenly spaced datapoints are collected across the entire cell nuclei (i.e. the entire cell is "hit" Figure 4.1b), followed by a post-experiment screening step that retains only datapoints in

GFP-fusion

H2B-RFP line

a.

g.

Coarse Threshold
& Bleach Grid

b.

Median
Filter

Median

c.

h.

Binary

Binary

d.

i.

Select
Largest Object

Dilation

e.

j.

Erosion

Overlay

f.

k.

l.

m.
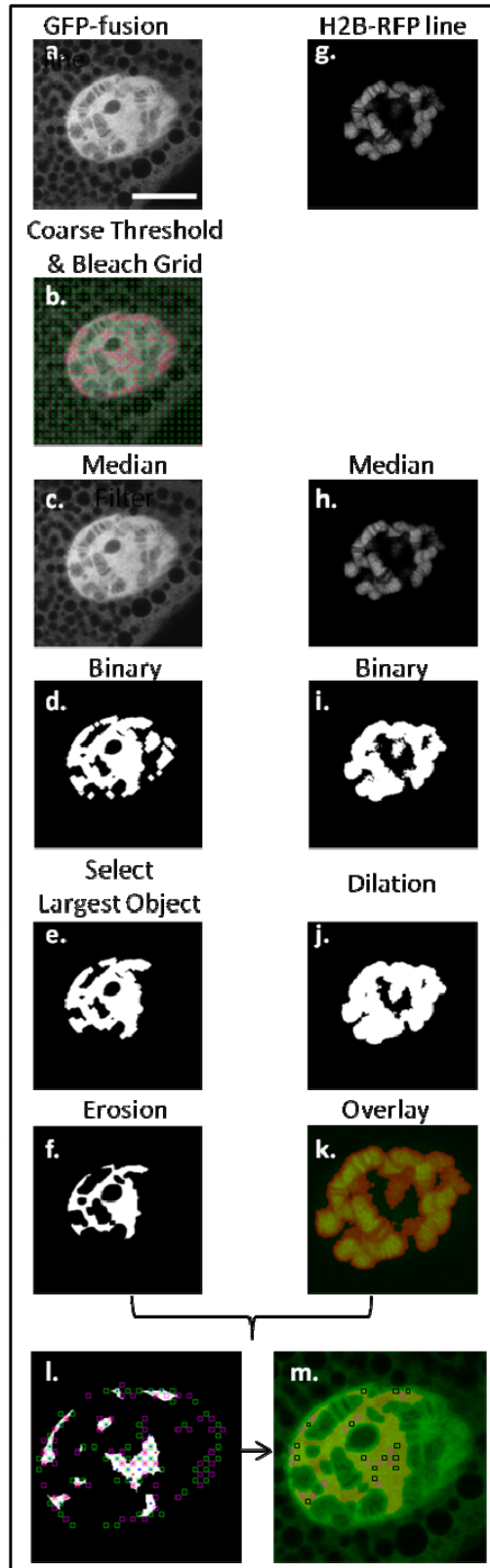
Figure 4.1: Image Collection and Automated Processing Methodology "Shotgun ptFRAP". The primary limitation of the ptFRAP method is the low SNR, requiring averaging over hundreds of individual bleach and control points. Collecting sufficient data necessitated an automated collection method in which an image of the sample is collected followed by the collection of ptFRAP curves at evenly spaced grid points in the sample. Only the subset of ptFRAP curves collected at grid points that meet the image selection criteria are used for subsequent analysis. (a,g) An initial image of both color channels is captured and used in subsequent thresholding operations. The GFP channel corresponds to the protein of interest, the RFP channel to the labeled polytene chromosomes. (b) A grid with 20 μm spacing is applied to the entire field of view. These grid points define the positions where FRAP data is collected. This is several times larger than the 300 nm PSF of the laser beam. A coarse threshold is applied to the GFP channel; only grid points contained within the thresholded region are collected (magenta boxes). Alternating points of the grid correspond to bleach and control datapoints. Post-processing steps are performed using MATLAB scripts developed in-house. (c,h) After data collection, a median filter is applied to both images to remove noise. (d,i) Threshold values are carefully selected for each image to capture the contours of the nuclear features. (e,f) In the GFP channel, the largest object in the field of view, corresponding to the nucleus, is retained. This eliminates any contributions from cytoplasmic signal. The binary mask is processed to remove sharp edge features then eroded 500 nm from every periphery to eliminate grid points in the vicinity of cellular membranes. (j) The polytene binary mask is dilated 300 nm to remove any grid points nearby the chromatin. (k) The mask (red can be seen overlaid with the image) confirms the entire region containing the polytenes will be excluded from analysis. (l,m) The RFP channel mask is subtracted from the GFP channel mask; the resulting region corresponds to the interchromatin space. The open squares (green=control power, magenta=bleach power) indicate all grid points at which FRAP data is collected during the experiment, while squares enclosing dots indicate the grid points retained for analysis. The distribution of the retained grid points are inspected visually to verify the selection criteria have been met.

regions of interest that match our selection criteria (Figure 4.1l-m). Thus all regions of the nuclei are probed over the course of the experiment and individual regions can be analyzed afterwards. This procedure enables over a thousand datapoints to be collected, without user bias, and are averaged into a single FRAP dataset.

4.2.2. RNAPII subunits exhibit apparent anomalous diffusion in cells

Rpb3 is the third largest RNAPII subunit, having a native mass of 35 kDa; the GFP- fusion construct has a mass of 62 kDa. Native Rpb9 is less massive at 14 kDa; the fusion construct has a mass of 41 kDa. Both tagged subunits are incorporated into active transcription complexes[22] and the subunits have high binding affinities for most of the ten remaining RNAPII subunits.[23] Additionally, RNAPII has strong affinities for transcription factors and promoter proteins, giving rise to a large distribution of complexes in which Rpb3 and Rpb9 may participate. Using the ptFRAP method, we compared the recovery dynamics of both subunits in the interchromatin space of polytene nuclei, which were then compared to the recovery of unconjugated GFP under the same conditions. The GFP acts as an inert protein with no binding partners in the nucleus and is only subject to molecular crowding (Figure 4.2).

We have previously shown that unconjugated GFP obeys Brownian diffusion in the interchromatin space[20] exhibiting a reduced diffusion coefficient due to nuclear viscosity. For this study, GFP serves as an approximate molecular mass standard to account for the effects of nuclear crowding as a reduction in the translational diffusion coefficient.[24] However, it is apparent that differences in the FRAP curves between the RNAPII subunits and GFP (Figure 4.2c) indicate that the transport of these former species is not well described by Brownian diffusion. This result is striking given the
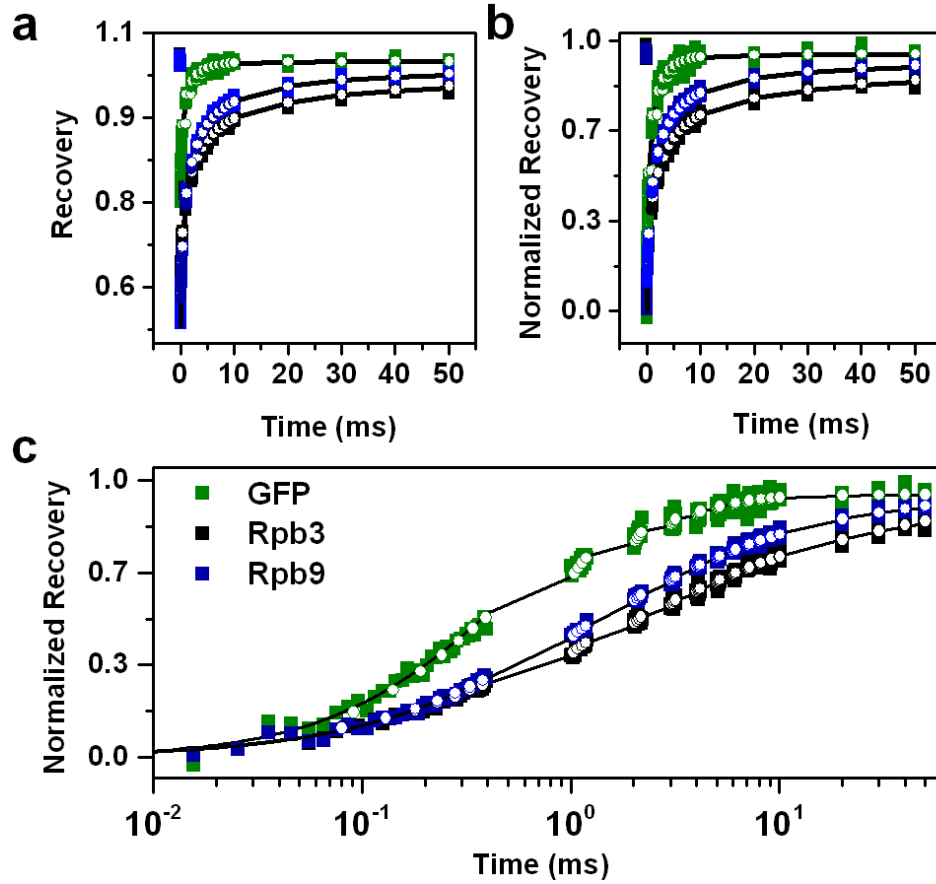
Figure 4.2: Comparison of *in vivo* subunit recovery dynamics. (a) The FRAP curves for the unconjugated GFP (green), the Rpb3-GFP (black), and Rpb9-GFP (blue) are shown. Data are plotted as closed squares, the best-fits to an anomalous diffusion model are shown as black lines, best-fits to the distribution model are shown are white circles. The data was collected with an intermittent collection technique that minimizes photobleaching while enabling long-duration interrogation. Numerous FRAP curves were averaged for each sample (GFP-1505 pts, Rpb3-1694 pts, Rpb9-833 pts) to achieve a high SNR. All displayed data has been treated to a 10-point rolling average smooth to aid clarity but all fitting was performed on the un-treated datasets starting at the 80 μs time-point. (b) Evident from the immediate post-bleach datapoint, each protein exhibits a different bleach depth. This reflects a sample-specific protein expression level effect that significantly influences the bleach depth. To enable qualitative comparison of the FRAP recovery curves, we normalized the FRAP bleach depth for each sample to zero. The rescaled FRAP curves clearly indicate differences between the recovery profiles of GFP, Rpb3, and Rpb9. The recovery differences are striking given the similar molecular masses and identical nuclear environment. (c) For better comparison of short-time data, the rescaled recovery curves are displayed on a logarithmic time axis. Here, the differences in the slopes of recovery curves can be visualized: the flatter the slope, the greater the apparent anomlity factor.

similar masses of the three proteins and the weak dependence of diffusional mobility with molecular mass predicted by the Stokes-Einstein Equation.

Given the large differences between the recovery of GFP and the RNAPII subunits, we chose to initially fit the Rpb3 and Rpb9 FRAP curves with a model that allows for anomalous subdiffusion. Anomalous subdiffusion equations are often invoked to describe mass transport in which the mean squared displacement of each particle is sublinear with time, which can result from heterogeneity in the molecular environment:

$$\langle \Delta r^2 \rangle = 6\frac{\Gamma}{\alpha}t^{\alpha} \tag{4.1}$$

The particle displacement is Δr, Γ is the transport coefficient, t is the time interval, and α is the anomlity value. The principle parameter describing anomalous diffusion is the anomlity value, bound between zero and unity, which indicates the magnitude of the deviation from Brownian behavior. An anomlity factor of unity corresponds to Brownian behavior (for which the transport coefficient is the diffusion coefficient); smaller values indicate progressively larger deviations. Such hindered molecular motion is often attributed to intracellular factors that retard the motion of a particle, such as binding to immobile traps, participation in viscoelastic complexes, and physical obstruction through labyrinthine corralling.[25]

The ptFRAP model was previously developed by our group[20] accounts for both anomalous diffusion[26] and a reversible photobleaching correction due to dark-state transitions of GFP during data collection. The FRAP signal is:

$$F(t) = F_0 [1 + \delta \exp(\frac{-t_{laser}}{\tau_{PP}})] \sum_{n=0}^{\infty} \frac{(-\beta)^n}{n!} \left[1 + n\left(1 + \frac{16\Gamma t^\alpha}{\alpha\omega_r^2}\right) \right]^{-1} \left[1 + n\left(1 + \frac{16\Gamma t^\alpha}{\alpha\omega_z^2}\right) \right]^{-1/2} \quad (4.2)$$

Here, F_0 is the pre-bleach fluorescence intensity, β is a factor related to the bleach depth, δ and t_{laser} are the reversible bleaching magnitude and timescale, and ω_r and ω_z are the size of the focused Gaussian beam in the radial and axial dimensions respectively. All of our data exhibited a near complete recovery on the 50 ms timescale indicating no immobile fractions. We fit the averaged FRAP curves according to Eq. 4.2 (Figure 4.2, black lines, see Table C.1 in the appendix for fit parameters from individual datasets); the best fit parameters are compared (Figure 4.3). We found that both RNAPII subunit recoveries were well fit by the anomalous subdiffusion model. This is in contrast to the GFP recovery dynamics which were well fit by Brownian diffusion.[20] Since our GFP experiments have revealed that molecular crowding is not a source of anomalous diffusion and these experiments restricted the analysis to an identical nuclear environment devoid of RNAPII binding sites or membrane induced labyrinthine regions, we can infer that the observed subunit recovery is not true anomalous diffusion.

As another possible source of observed anomalous behavior, we considered the possibility that the simultaneous measurement of multiple diffusing species (a distribution) undergoing Brownian motion can produce an identical FRAP recovery profile to a single species undergoing anomalous diffusion.[27] We term this phenomenon *apparent anomalous diffusion*. Thus, we strongly believe that the subunits must be in a heterogeneous distribution of complexes resulting in the observation of apparent anomalous diffusion, as described in **section 4.2.4**.
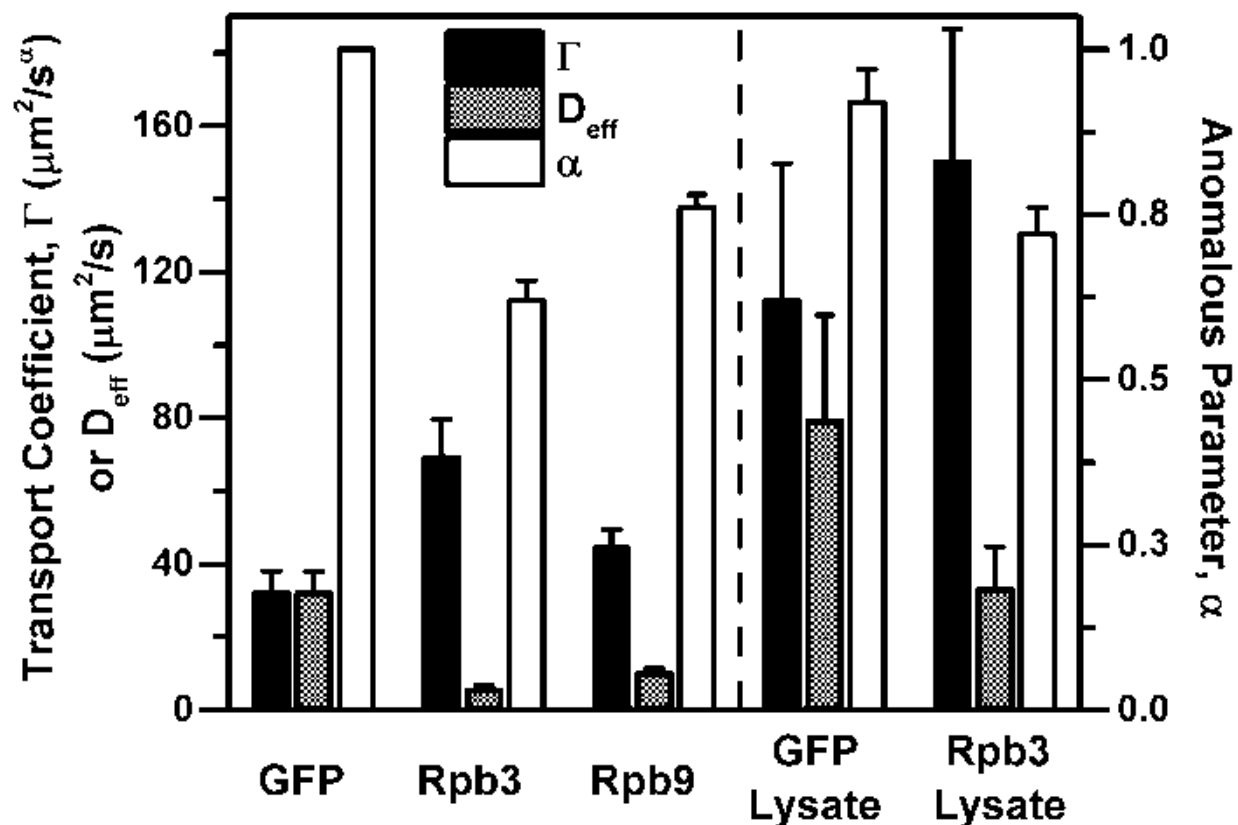
Figure 4.3: Summary of the best-fit apparent anomalous modeling parameters. The alpha value varies between zero and unity and is a measure of deviation from Brownian diffusion. The transport coefficient is measure of translational diffusion speed, the effective diffusion coefficient (D_{eff}) represents the diffusion coefficient if the particle obeyed Brownian diffusion. Error bars are shown at the 95% confidence interval. The GFP expressing line was found to diffuse normally with a diffusion coefficient of 32±6 μm^2/s. The RNAPII subunits showed apparent anomalous diffusion, with each exhibiting different diffusive kinetics. Rpb3 exhibited an apparent anomlity value of 0.62±0.03 while Rpb9 exhibited an anomlity value of 0.76±0.02. This reveals that the subunits are not bound in identical complexes. To the right of the dotted line are the parameters for the *in vitro* lysate experiments. Within experimental error, the diffusion of GFP is found to be Brownian and of the same magnitude as GFP in dilute buffer. The Rpb3 lysate continues to indicate apparent anomalous diffusion.

4.2.3. Rpb3 exhibits apparent anomalous diffusion in cell lysate

We reasoned if the apparent non-Brownian transport persisted in dilute solution then the deviations from Brownian diffusion must be attributed to a distribution of complexes. To completely eliminate macromolecular crowding as a possible source of anomalous diffusion, we performed FRAP experiments on cellular lysates of the salivary gland polytene cells expressing either GFP or Rpb3 (Figure 4.4).

The cell lysates are whole cell preparations made by sonicating the salivary glands in a lysis buffer and extracting the soluble proteins. The cell contents were centrifuged and the supernatant used for FRAP experiments. A comparison of the fluorescence intensity between the lysates and the intact polytene cells revealed up to a 30-fold decrease in signal. We were unable to collect data on lysates made from Rpb9 due to extremely low sample signal.

The GFP lysate FRAP recovery indicated a normally diffusing species (Figure 4.4). Further, the diffusion coefficient determined by the FRAP model described in Eq. 4.2 of 79.1 ± 30.0 $\mu m^2/s$, is in excellent agreement with the diffusion of free GFP (purified from bacteria) in solution, measured on our set-up as 84 ± 6 $\mu m^2/s$.[20] Thus our lysate preparation recapitulated a dilute solute environment by eliminating macromolecular crowding. We note that the GFP lysate yielded a slightly non-Brownian anomlity parameter (Figure 4.3), which is the result of the very rapid recovery of the species coupled with low signal strength. Both of these factors reduce the accuracy and precision of the fitting algorithm.

Despite the highly dilute solvent environment, the Rpb3 lysate FRAP recovery reveals very different behavior (Figure 4.4), displaying apparent anomalous diffusion

(Figure 4.3). Due to the lower viscosity of the lysate solvent, both the transport and effective diffusion coefficients, determined by Eq. 4.1, are increased compared to Rpb3 diffusion *in vivo*. Further, the lysate recovery indicated a reduction in the measured anomlity value (Figure 4.3). This reduction could stem from very large complexes no longer experiencing crowding effects[24] and reveals the degree of apparent anomlity resulting solely from the distribution of species in the absence of crowding effects. Alternatively, this could indicate the disintegration of complexes that coalesce *in vivo* but destabilize in the absence of molecular crowding.

4.2.4. Distribution modeling: decomposing apparently anomalous recovery curves into components exhibiting Brownian diffusion

In any FRAP measurement the observed signal is the sum of the signals from each species present in the sample. In a many component system, if the species have diffusion coefficients that are sufficiently different, it may be possible to distinguish distinct timescales in the recovery. More often, the observed signal takes a form that can appear as anomalous diffusion.[28, 29] In our experimental systems, we observed that GFP exhibits Brownian diffusion in the interchromatin space, but Rpb3 and Rpb9 do not. There is little reason to suggest that individual proteins similar in size to GFP would exhibit true anomalous diffusion. Therefore, we investigated the possibility that each protein species is incorporated into a heterogeneous size-distribution of macromolecular complexes by applying a multi-component fit to the FRAP recovery that we term the *distribution model*. The distribution model was implemented as:[28]
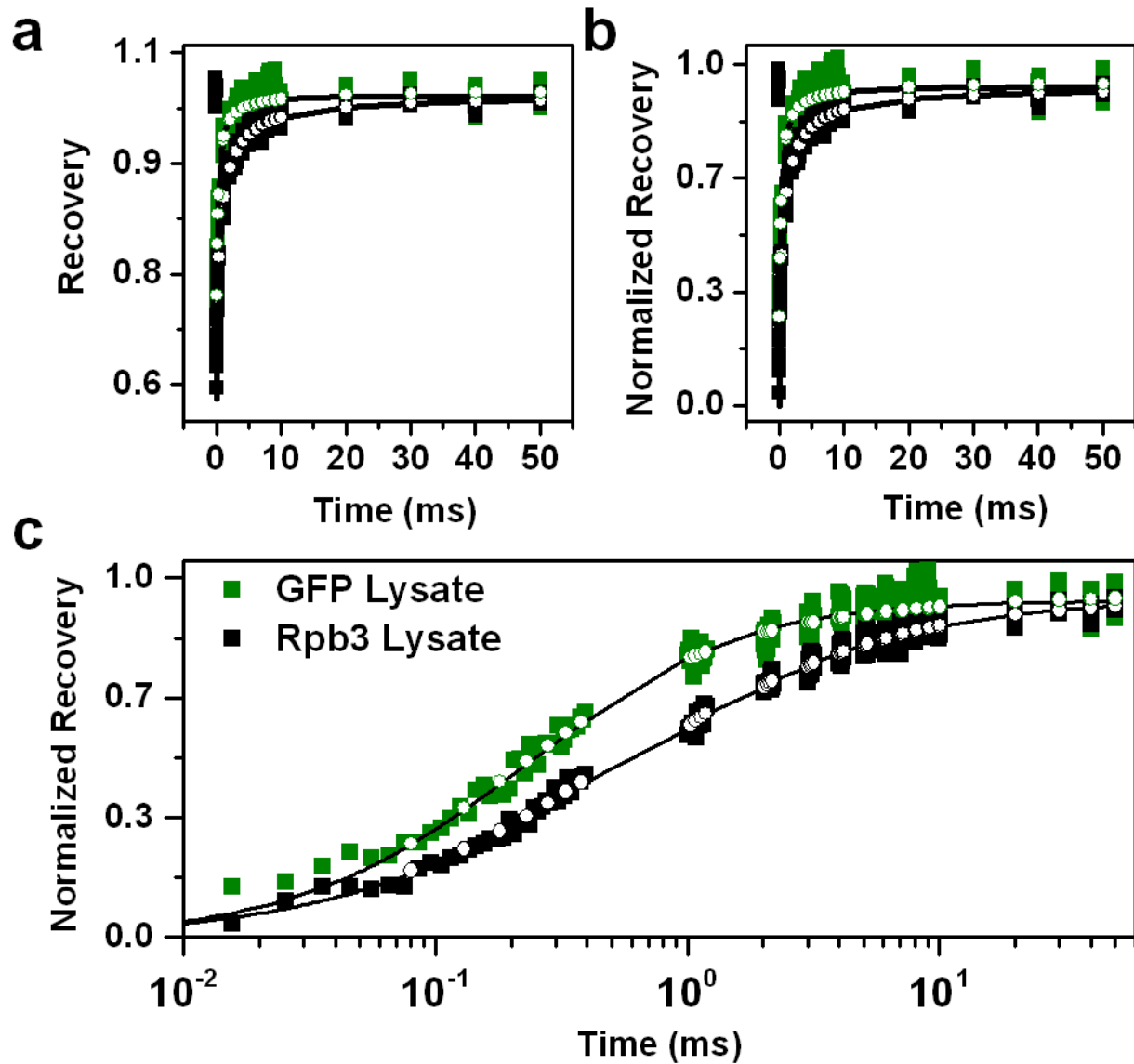
Figure 4.4: Comparison of *in vitro* subunit recovery dynamics. The FRAP curves for the GFP expressing control line and the Rpb3 subunit lysate experiments are shown. Numerous FRAP curves were averaged for each sample due to low signal intensity of the lysates (GFP- 6090 pts, Rpb3- 17420 pts) (a,b,c) Data are plotted as closed squares, the best-fits to an anomalous diffusion model are shown as black lines; best-fits to the Distribution Model are shown are white circles. (c) The flattened slope and slower recovery of the Rpb3 lysate is a clear indication that the sample is not undergoing Brownian diffusion.

$$\mathcal{F}(t) = \sum_{i=1}^{m} c_i F(D_i, t, \alpha = 1) \qquad (4.3)$$

The recorded FRAP recovery, $\mathcal{F}(t)$ is a linear combination of Brownian diffusion basis functions, $F(D,t,\alpha=1)$ that are given by Eq. 4.2 with α=1 and a range of individual diffusion coefficients. The coefficient c of each species is allowed to float and the resulting output defines a distribution of species with various diffusion coefficients (the robustness of the distribution model is detailed in Figure C.3 in the appendix).

The distribution model was first tested by fitting the *in vivo* FRAP recovery of unconjugated GFP for an underlying distribution (Figure 4.5a, green). In agreement with the aforementioned fits to the anomalous diffusion model that indicated a single Brownian diffusing component, fits to the distribution model output collapsed to a Delta function, yielding a single diffusion coefficient of 27 μm^2/s (peak 1). This is within 15% of our previously determined *in vivo* GFP diffusion coefficient.[20] Having validated the distribution model (Figure C.4 in the appendix), we applied it to the cellular FRAP recoveries of Rpb3 and Rpb9, along with the GFP and Rpb3 lysate data. In general, the breadth of the distribution for each sample qualitatively agrees with its degree of apparent anomalous diffusion. For example, the protein exhibiting less apparent anomlity, Rpb9, exhibits a distribution of species that have Brownian diffusion coefficients in a peak from about 10 through 30 μm^2/s (Figure 4.5a, red), while the Rpb3 exhibits a distribution that is even broader and more structured. However, much more information is contained in the shape of the distributions than is available from the anomlity parameter, as discussed below. Another notable observation about the distributions is that none contains diffusion components faster than unconjugated GFP.
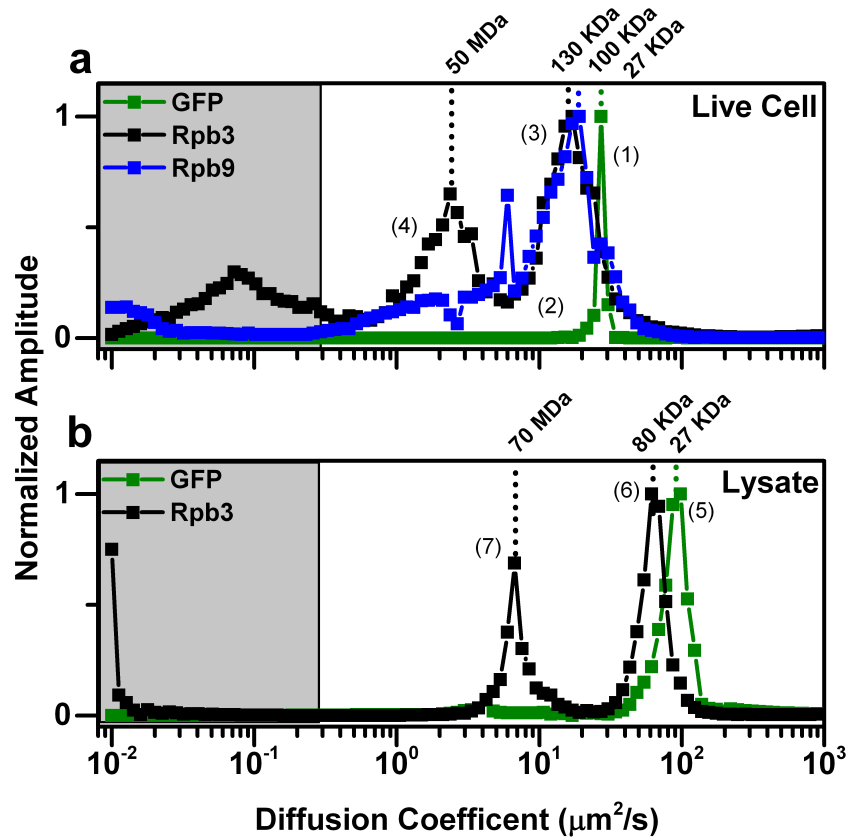
Figure 4.5: Brownian diffusion coefficient distributions. The distribution model (Eq. 4.4) was applied to *in vivo* (a) and (b) *in vitro* FRAP recovery curves. To implement the model, we defined 100 species with logarithmically spaced diffusion coefficients ranging from 0.20 to 1000 µm²/s. This range of diffusion coefficients corresponds to a massive size range of species. Components with diffusion coefficients slower than 0.29 µm²/ are below the limit of the recovery threshold of our FRAP method. (a) The distribution of unconjugated GFP (green) collapses to a delta function with a diffusion coefficient of 27 µm²/s. The observation of a single diffusing species demonstrates good agreement with the apparent anomalous diffusion model. The distributions for Rpb3 (black) and Rpb9 (blue) exhibit major peaks at 17 and 18 µm²/s respectively, corresponding at Stokes-Einstein predicted masses of 130±50 and 100±40 kDa respectively. These values are in good agreement with the predicted GFP-fusion construct masses. The Rpb3 distribution is bimodal, with the slower peak indicating a diffusion coefficient of 2 µm²/s, mapping to a mass of 50±20 MDa. This peak indicates the presence of fully formed transcription factories. (b) The *in vitro* distribution for unconjugated GFP is narrow and indicates a diffusion coefficient of 92 µm²/s, in good agreement with measurements of GFP in dilute buffer. The Rpb3 lysate distribution again reveals two well resolved peaks, corresponding to masses of 74±20 MDa and 82±24 kDa, similar to the peaks in the *in vivo* measurements.

The Stokes-Einstein Equation, which predicts the diffusion coefficient of a particle undergoing Brownian diffusion, can be re-arranged to estimate the relative diffusion coefficients of the proteins (assuming globular structures and the same viscosity) based on their molecular masses:

$$\frac{D_1}{D_2} = \left(\frac{M_2}{M_1}\right)^{1/3} \qquad (4.4)$$

Here, D is the protein diffusion coefficient and M is the protein molecular mass. Using the molar mass of GFP and measured diffusion coefficient as a standard, the approximate mass corresponding to each diffusion component in the subunit distributions can be estimated using Eq. 4.4. The peak of the Rpb9 distribution (Figure 4.5a, peak 2) corresponds to a mass of 100±40 kDa, reasonable given the 41 kDa mass of the fusion construct (we confirmed that this is independent of protein expression level, Figure C.1 in the appendix). The width of the distribution maps to species ranging in molecular mass from 27 kDa through 10^8 kDa. While the enormous upper limit on molecular mass should be viewed with incredulity, these results indicate that species are present ranging from unconjugated GFP through aggregates of multiprotein complexes. The upper mass limit defined by the distribution is unrealistically large and likely reflects components sufficiently large to be influenced by molecular crowding that undergo true anomalous diffusion.

In contrast to Rpb9, the Rpb3 subunit exhibited a wider and more structured distribution (Figure 4.5a, black). Interestingly, the distribution is bimodal, with two well-resolved peaks bridged by components of lower amplitude. As expected, the fastest components are bound by an upper limit of diffusion coefficients similar to unconjugated GFP. Assuming Stokes-Einstein, the "faster" peak (Figure 4.5a, peak 3) corresponds to

a molecular mass of 130±50kDa, in good agreement with mass of the Rpb3-GFP fusion construct. The second, "slower" peak (Figure 4.5a, peak 4) corresponds to a mass of 50±20 MDa. The mass of a complete transcription complex[30] consisting of RNAPII and associated transcription factors has been estimated to be ~3 MDa; the mass of full transcription factories (aggregates of full transcription complexes and associated promoters) has been estimated up to ~38 MDa.[1, 31] Thus, the second major peak in the Rpb3 distribution is very close to the size of fully assembled gene transcription units.[1, 30, 31] Its presence indicates that these transcription units are present in the interchromatin space, in the absence of chromatin. We also note that the Rpb9 distribution exhibits a pronounced shoulder in the same range as the 50 MDa peak in the Rpb3 distribution.

The Rpb3 distribution also contains lower frequency components. Our FRAP method is insensitive to species slower than 0.29 μm^2/s (explained in Figure C.2 in the appendix). These species are likely contributions to the distribution but the true amplitudes are uncertain.   Importantly, the fit residuals are better than those produced by the anomalous diffusion model. The quality of the fits can be compared in Figure 4.2 and Figure 4.4, where the white circles indicate the distribution model fits, in comparison to the anomalous diffusion model fits in black.

As a comparison to the *in vivo* distributions obtained for GFP and Rpb3, we applied the Distribution model to the results of the lysate FRAP experiments, keeping the same number of components and the same bounds on diffusion coefficients (Figure 4.5b). By eliminating the stabilizing effects of macromolecular crowding, this analysis examines how the distribution of complexes is altered by a dilute solvent.   The distribution for the GFP lysate (Figure 4.5b, green) indicates a narrow range of diffusion

93

coefficients, with the major peak indicating a diffusion coefficient of 92 μm^2/s. This is within a 10% error of the previously determined diffusion coefficient of GFP in buffer solution (84±6 um^2/s),[20] confirming that the lysate provides a dilute environment that eliminates macromolecular crowding.

The results for the Rpb3 lysate (Figure 4.5b, black) are very similar to the distribution found *in vivo*, except shifted towards faster components due to the reduced solution viscosity. The lysate distribution indicates two major peaks, the "faster" peak at 65 μm^2/s and the "slower" peak at 6.7 μm^2/s. These correspond to masses of 82±24 kDa and 74±20 MDa. Notably, the major peaks detected map to the same molecular masses as the *in vivo* fitting results, providing independent confirmation of the bimodal distribution. However, the lysate distribution differs from the *in vivo* distribution in two important locations. First, the middle range of diffusing components (inter-modal), between the two peaks is absent in the lysate distribution. This indicates that the protein complexes present in the crowded nuclear environment are destabilized in dilute solvent. These species, intermediate between complete and incomplete transcription factories have implications for the pre-assembly of transcription complexes. Their presence suggests that the formation of large protein assemblies proceeds through partially-assembled intermediates whose formation is favored in the crowded nuclear environment. Second, the very slow components that are technically below our FRAP resolution limit are largely absent in the lysate distribution. This supports the suspicion that those components *in vivo* represent complexes sufficiently large to experience macromolecular crowding and truly exhibit anomalous diffusion.

4.3. Discussion

4.3.1. A new perspective on *in vivo* diffusion of macromolecular components: apparent anomalous diffusion

Our experiments with RNAPII subunits sought to directly probe the nucleoplasm, devoid of chromatin, for evidence of the holoenzyme or larger transcription complexes. We determined that RNAPII subunits exhibit complex transport dynamics even in the absence of chromatin, that can be attributed to a staggeringly large distribution of assembly states, ranging from fully assembled transcription factories to unengaged subunits. The existence of such nuclear assemblies concerns one of the current fundamental dilemmas in modern biology- determining how large DNA-binding protein complexes assemble and subsequently find their binding sites. Recent studies have supported the theory that many DNA binding complexes encounter and bind to chromatin through a stochastic diffusion-mediated process, but little evidence exists to explain what governs the assembly of these multi-component complexes away from binding sites. Given the centrality of RNAP to transcription and possible mechanistic universality with regards to other large nuclear-localized complexes,[32] this multi-subunit complex has been the subject of great scrutiny over the past decade.

Information about the assembly and interactions of large protein complexes can be obtained by investigating transport properties of individual components, since protein mobility not in accordance with Brownian diffusion can indicate the presence of binding interactions or molecular hindrance.[21, 33, 34] Two types of passive transport are typically identified *in vivo*- Brownian motion and anomalous subdiffusion.[27, 35, 36] Given the widespread implementation of FRAP and FCS, it is interesting to note that with very few exceptions,[27] the preponderance of eukaryotic proteins studied *in vivo* have been found

to exhibit anomalous subdiffusion, while similar sized molecules studied in aqueous or viscous solvents typically have been found to obey Brownian motion.[24, 27, 37, 38]

We compared the transport dynamics of the RNAPII subunits Rpb3 and Rpb9 to unconjugated GFP. Suspecting that the chromatin organization of typical eukaryotic cells could pose a potential interference to diffusion mobility, we avoided confounding structures present in the nuclear environment by choosing the polytene salivary glands of *Drosophila melanogaster* larvae as our model system. Our FRAP experiments performed with unconjugated GFP revealed that this inert protein is subject to Brownian diffusion. Nuclear molecular crowding was experienced as a change in viscosity resulting in a reduction of the diffusion coefficient of GFP from 84 ± 6 μm^2/s in dilute solvent to 32 ± 6 μm^2/s in *Drosophila* cells. In contrast to GFP, we observed apparent anomalous diffusion for both RNAPII subunits. This is very surprising as the approximately two-fold increase in molecular mass of the fusion proteins relative to GFP would be expected to yield a very minor 1.2-fold change in diffusion coefficient based on Stokes-Einstein estimations (Eq. 4.4). This is hardly a large enough increase in size to make either subunit susceptible to extreme molecular crowding. Having eliminated all other contributions to anomalous diffusion, we have shown that molecular crowding is not a cause of anomalous diffusion for proteins in this size range. Therefore we reason that the subunits are actually engaged in distributions of complexes displaying an extremely large range of diffusion coefficients and therefore molecular sizes. We term this phenomenon *apparent anomalous diffusion*.

Apparent anomalous diffusion was suggested in the 1990s and experimentally confirmed to affect FRAP curves by using simple two component systems with inert

solutes.[28, 29, 39]   These previous groups demonstrated that multicomponent FRAP recovery curves of Brownian diffusing species can be represented by an anomalous fit, but this was not confirmed in a living system until now. Our experiments simultaneously probe the diffusion of assemblies with vastly different mobilities, from isolated subunits to possible aggregates of fully formed transcription units. Observed differences in the recovery dynamics of the two subunits (Figure 4.2) indicates that they participate in different distributions of complexes (Figure 4.5). This reflects differential affinities for the other RNAPII subunits and associated transcription factors, as well as suggesting that distribution width and subunit incorporation sequence are entwined.

We further explored the cellular transport behavior by performing FRAP experiments on *in vitro* lysates prepared from the GFP and Rpb3 polytene samples (Figure 4.4). The diluted solvent abolished macromolecular crowding and ensured that the proteins did not experience crowding effects or find binding partners. This left only a distribution of diffusing species as the remaining source of perceived anomalous diffusion.[36]   The results indicate that many of the Rpb3 complexes remained intact during the lysate preparation, since it still exhibited apparent anomalous diffusion (Figure 4.3).

It has been reported previously that the extent of anomalous diffusion can be used as a measure for environmental heterogeneity.[19] We argue that having shown that interchromatin space represents a homogenous diffusive environment, the degree of anomlity can instead be a proxy for the width of the distribution in which the tagged protein participates. This makes intuitive sense- if an anomlity factor of unity represents normal diffusion and therefore a single diffusing component, any departure from unity is

describing an increasingly heterogeneous mixture. We found the Rpb3 subunit was associated with the highest degree of apparent anomalous diffusion (Figure 4.3) indicating it participates in the widest size range of complexes (Figure 4.5). The Rpb9 subunit was found to exhibit less apparent anomlity (Figure 4.3), corresponding to a more narrow distribution (Figure 4.5), while GFP, which does not interact with any other species, was found to show normal diffusion.

We applied a multi-component model to extract the underlying distributions of nuclear Rpb3 and Rpb9 to determine their participation in pre-assembled RNAPII complexes. The distribution model is advantageous as no *a priori* assumptions about the underlying distribution are made, thus protein complex sub-populations can be resolved. In reality, this model faces three limitations. The model assumes all component species obey Brownian diffusion- it is unable to resolve simultaneous diffusion of Brownian and anomalous species. Secondly, the application of the model is affected by the quality of the data. As reported by others[28, 29] the SNR of the data impacts the ability of the model to accurately resolve separate species, even in well resolved binary systems. Our implementation is sufficient to reliably predict two components at our experimental SNR, yet the potential complexity of the protein distributions means that discerning fine structure of sub-populations is difficult. Finally, our FRAP implementation poses a resolution limit on how slowly diffusing a species we can accurately measure.

As anticipated, the comparison of the Rpb3 and Rpb9 distributions confirm that the greater the degree of apparent anomalous diffusion (Figure 4.3), the wider the predicted distribution (Figure 4.5a). We can immediately detect that the Rpb3 subunit is

involved in a wider array of complexes than Rpb9, with more of them involving very large molecular weight assemblies. The distribution modeling of the Rpb3 lysate reveals essentially the same structure, though shifted to faster diffusion components due to the reduced solvent viscosity. This provides two different experimental samples that confirm that same finding. Significantly, the more massive population is identical between both samples and corresponds to overlapping molecular mass ranges of 50 ± 20 MDa *in vivo* and 70 ± 20 MDa *in vitro*. Given the several mega-Dalton mass of a complete transcription complex[30] and the much larger mass of transcription factories,[1, 31] this population represents a fully assembled transcription factory. Such complexes likely arise given the affinities between transcription complex subunits and the crowded cellular environment in which they dwell, meshing well with reports that transcription factories remain even in the absence of transcription.[40]

While the envelope shape of Rpb3 associated complexes is preserved in the lysate preparation (Figure 4.5), it is noteworthy that the majority of the *in vivo* distribution components lying between the major peaks are eliminated in the lysate distribution. These represent dynamic complexes that are stabilized in the crowded nuclear environment, where dissociation and re-binding is rapid due to partner proximity. In the dilute lysate solvent, once a complex of low stability dissociates, rebinding is inhibited by the low concentration of binding partner. Further, the width of both peaks is similar to the width of the GFP peak. This indicates the remaining species show less dispersion. Finally, the lysate data does not exhibit the same structures at very slow diffusion coefficients (mapping to greater than a GDa), possibly an indication

that Brownian diffusion was restored for very large complexes affected by macromolecular crowding.

4.3.2. Broad assembly distributions allow flexibility in the mechanism of transcription complex formation

Previous work has established the dynamic turnover of RNAPI and RNAPII associated proteins during transcription. It has been shown that four subunits of RNAPI as well as several preinitiation factors all exhibit unique diffusion properties even in the vicinity of chromatin and do not diffuse as an ensemble. Further, engaged RNAPII has been found to continuously exchange with nucleoplasmic RNAPII in transcriptionally active chromatin regions.[8, 9, 16, 41, 42] These findings have led to the developing consensus that complexes assemble at a promoter site through stochastic interactions. However, the continued evidence for the formation and stability of fully assembled transcription factories even in the absence of transcription throws uncertainty on the spatiotemporal formation of such assemblies.[7, 9, 13, 43, 44] Unfortunately, previous studies could not track the dynamics of the RNAP subunits prior to recruitment or localization.

Using our method which is sensitive to the diffusion, and, therefore, mass of a complex, but not to the activity state, our experiments have probed the dynamics of multiple subunits within the same binding complex, enabling us to observe the degree of pre-assembly. This is significant as our analysis was restricted to the interchromatin space, representing a cellular location that we found to precede incorporation of all subunits into higher order assemblies but that follows subunit mRNA translation. Our work has shown that two subunits of RNAPII, including the central binding subunit Rpb3, exhibit different diffusion dynamics (Figure 4.2). This casts doubt on *complete* pre-assembly of all RNAPII substituents prior to chromatin binding.[6-13] For both

subunits, we detect a subpopulation of molecular complexes approaching a limit of a hundred mega-Daltons (Figure 4.5), which corresponds to aggregates of fully assembled transcription factories. This indicates that transcription complex subunits have high affinities that experience enhanced stability conferred by the crowded cellular environment in which they dwell.

These distributions indicate that the formation of large protein complexes is driven by stabilizing interactions even in the absence of chromatin, yet this subpopulation does not account for all of the RNAPII subunits present within the interchromatin space. This has implications for large multi-complex assembly pathways, as stochastic protein-chromatin interactions can be reframed in terms of sampling interactions between complexes in various states of completeness. Such a model is at odds with the more static, top-down view of factory formation. While our results clearly indicate that large macromolecular complexes, such as transcription factories, are stable *in vivo*, the unanswered question is how long they remain assembled. Most studies documenting transcription factories have relied on the appearance of punctuate structures observed in fixed cells or on the purification of stable transcription complexes *in vitro*[4, 14] Additionally, electron microscopy measurements that document the size of these complexes place an upper limit of <200 nm in diameter, still too small to be accurately resolved with optical microscopy on living cells.[31] These complicating factors, combined with our findings of the stability of large protein complexes *in vitro*, make it difficult to determine the longevity of these species.

As investigations into the dynamics of polymerase components and associated transcription factors reveal a conserved intrinsic turnover and universally accepted

inefficiency of transcription initiation, the previously posited model of stochastic gene expression has gained traction.[7, 43] Mounting evidence indicates that RNAPII is not always recruited as a holoenzyme, though our findings clearly indicate that full transcription factories do form prior to RNAPII recruitment.[43] RNAPII is currently seen as assembling at a promoter through a multi-step process marked by efficient chromatin capture rates of up to 50%[9] but highly inefficient transcription initiation (<1%),[10] leading to an overall transient promoter interaction prior to elongation (which is unlikely if full transcription factories migrated throughout the nucleus).

We believe our findings of RNAPII subunits existing in complex distributions lend validity to both models. Our essential finding is that transcription subunits form large, stable, and mobile complexes, indicating the true assembly behavior lies mid-way on a spectrum of pre-assembly. We measured diffusion coefficients for transcription factories in line with those determined for other proteins involved in nuclear macromolecular assemblies.[41] This suggests that large complexes are mobile (but slow) and can diffuse to binding sites, in contrast to static factory models in which chromatin must migrate to stationary factories. This proposal integrates well with current observations, but helps to redefine the nature of assembly. Our results provide experimental evidence to considerations proffered by Phair and Misteli that protein complexes can form stochastically, distal to their site of action, enabling rapid recruitment and dynamic responses to changes in binding partner availability.[7, 41-43] However, the large population of individual subunits and partially-formed complexes also allows *de novo* assembly at gene loci.

As opposed to a hit-and-run model of polymerase factors encountering a chromatin binding site, our findings show that transcription complexes assemble to varying levels of completion in the interchromatin space removed from and prior to encountering chromatin. These partially formed assemblies, through diffusion, experience stochastic encounters with potential binding sites; the duration of the encounter depending on the completeness of the polymerase assembly. More complete RNAPII complexes, having a greater compliment of binding partners, form more stable chromatin interactions than less well developed sub-assemblies. As our distribution modeling shows, the majority of the subunits exist as incomplete assemblies, therefore the majority of chromatin interactions are likely aborted, leading to the inefficiency of transcription initiation. Our observation of a bias towards larger complexes exhibited by the more massive RNAPII Rpb3 (Figure 4.5) subunit may reveal a measure of stepwise assembly. In this scenario, the larger subunits complex first, leading to stable chromatin-binding assemblies, forming nucleation sites for smaller subunit assemblies. Such a model ensures maximum flexibility in gene expression for different chromatin regions. The two assembly regimes we observe mean that fully formed transcription complexes, in the presence of open chromatin regions are likely to remain stably assembled and engage in high throughput transcription. These large structures experience slow diffusion and would remain relatively stationary, in alignment with transcription factory theory. Conversely, the smaller sub-assembled modules, which account for a large fraction of the assembly states, are capable of rapid diffusion and permit protein recruitment to congested chromatin regions that experience lower basal transcription levels. The partial pre-assembly of the transcription complex

enhances the efficiency of full complex assembly and is complimented by greater nuclear mobility than near-immobile transcription factories. Thus through a partially modular assembly mechanism the cell is endowed with a flexible response to changing transcription demands.

Additionally, while not the focus of this work, we have previously observed true anomalous diffusion due to confinement in the vicinity of the chromatin lattice even for small proteins.[20] Coupled with the findings of other researchers concerning the role of molecular crowding in gene expression,[45,46,47] it stands to reason that large, partially assembled complexes, once in the vicinity of a promoter, sample increasingly frequent binding events due to molecular confinement and reduced mobility.

4.4. Conclusion

By applying FRAP in the polytene salivary glands of *D. melanogaster* as a model system, we show for the first time that RNAPII exists in a large distribution of partially assembled complexes in the interchromatin space, including fully assembled transcription factories. Having determined that the Rpb3 and Rpb9 subunits exhibit different diffusion properties, we confirm that RNAPII is a dynamic complex, though we detect a population of complete pre-assembled transcription factories prior to chromatin binding. Using GFP as an inert internal control protein, we have shown *in vivo* that the diffusion of the subunit distributions display apparent anomalous diffusion. This arises from the simultaneous interrogation of multiple diffusing species using an ensemble measurement method. When considered individually, these complexes move primarily by Brownian diffusion throughout the crowded interchromatin space, experiencing a reduction in mobility due to the high viscosity but not experiencing molecular

confinement. We confirmed the existence of these subunit assembly distributions through the use of cell lysates, in which apparent anomalous diffusion persisted in the absence of macromolecular crowding. The discovery of these partially assembled RNAPII complexes helps integrate current contradictory observations regarding the mode of transcription complex assembly. Our findings are consistent with the simultaneous action of a top-down and bottom-up assembly. While the exact nature of the species that initiate transcription cannot yet be determined, for the first time our data shows evidence for a distribution of pre-assembled complexes. Finally, the distribution of assembly states suggests that a partially modular mechanism of macromolecular assembly enables a flexible response to gene transcription.

4.5. Materials and Methods

All chemicals are Fisher brand unless noted.

4.5.1. Fly Strains

Drosophila lines that express Rpb3-GFP, Rpb9-GFP or H2B-mRFP using the GAL4/UAS system have been described previously.[22,44] Fly lines containing transgenes for unconjugated GFP and Gal4-C147 were obtained from the Bloomington Drosophila Stock Center (lines #5430 and #6979 respectively). All GFP samples are enhanced green fluorescent protein. To simultaneously express H2B-mRFP with GFP or GFP fusions for dual color imaging, the homozygous line Gal4-C140; H2B-mRFP was first generated and then crossed to the appropriate GFP fusion transgenic line. Flies were raised using a standard cornmeal medium at room temperature; larvae were collected after 8-9 days. To prepare samples for imaging, wandering third-instar larvae were dissected in Grace's Insect Medium and intact salivary glands were used for imaging

polytene cells. All imaging experiments were completed within one hour of dissection to maintain cell viability.

4.5.2. Salivary Gland Extract Preparation

To prepare polytene cellular extract samples of GFP and EGFP-Rpb3, 80 larvae were dissected and the glands placed on ice cold Tris-HCl buffer (50 mM, pH 7.4). The glands were mini-centrifuged for 60 s, the supernatant removed, and the glands re-suspended in ice cold lysis buffer (50 µL), followed by vortexing for 45 s and sonication for 30 min to rupture the glands. The lysis buffer consisted of Tris-HCl (50 mM, pH 7.4), NaCl (150 mM), NP-40 detergent (0.5% w/v), Pefabloc SC (1 mM in Tris-HCl buffer), leupeptin (2 µg/mL, in methanol), and pepstatin (2µg/mL, in methanol). After sonication in ice cold lysis buffer, the sample was mini-centrifuged for 4 min. The supernatant was used immediately for FRAP experiments.

4.5.3. Two-photon microscopy configuration and FRAP procedures

Imaging and FRAP were done as described in our previous paper.[20] In brief, polytene cells were imaged with a 1.2NA/60x Olympus objective using a home-built laser scanning two-photon microscope. GFP and mRFP were excited at 950 nm by a Chameleon Ultra II Ti:sapphire pulsed laser with a 140 fs pulse duration; the fluorophore emissions separated with a 570 short pass dichroic mirror. The GFP emission was collected with a 510/30 bandpass filter while RFP emission was collected with a 630/100 dichroic mirror. Quantitative bleaching studies were performed with a point-bleaching method (ptFRAP) developed previously in our laboratory, featuring an online image thresholding and data acquisition procedure followed by offline image analysis and data modeling. For all conditions studied, between 20-40 cells were analyzed; the

number of datapoints collected and averaged are indicated in Figures 4.2 and 4.4. Data collection consists of two phases- recording bleach and control datapoints. Bleach points are established by photobleaching a diffraction limited volume (spot size of 300 nm diameter and 1 μm axial length) at a high laser power (bleach power) followed by recording the intensity of the spot during the diffusive recovery at a lower laser power (read power). Control points are established in the same manner but with the read power used in place of the bleaching power. A bleach depth of between 40-60% of the initial fluorescent intensity was achieved using a bleach power of 71.5 mW, while control measurements were taken at a read power of 11.5 mW (both values measured at the microscope objective using a calibrated power meter). For all proteins studied, FRAP recovery data was collected for 50 ms and data fitting was applied to datapoints collected starting at 80 μs post-bleach. The data was fit with a model for anomalous subdiffusion,[20] which indicates the degree of anomlity and the diffusion coefficient (for normally diffusing species) or the transport coefficient of the diffusing species. The anomlity factor ranges between 1 and 0, with unity indicating Brownian diffusion. Detailed information on the microscope configuration, FRAP timing sequence, and fitting recovery data to an anomalous subdiffusion model with a photophysics correction for observational photobleaching is described in **Chapter 2**.

REFERENCES

1. Melnik, S.; Deng, B.; Papantonis, A.; Baboo, S.; Carr, I. M.; Cook, P. The proteomes of transcription factories containing RNA polymerases I,II, or III. *Nat. Methods* **2012***, 8*, 963.

2. Kruhlak, M. J.; Lever, M. A.; Fischle, W.; Verdin, E.; Bazett-Jones, D. P.; Hendzel, M. J. Reduced Mobility of the Alternate Splicing Factor (Asf) through the Nucleoplasm and Steady State Speckle Compartments. *J. Cell Biol.* **2000***, 150*, 41-52.

3. Meister, P.; Poldevin, M.; Francesconi, S.; Tratner,Isabelle, Zarzov, Patrick; Baldacci, G. Nuclear factories for signally and repairing DNA double strand breaks in living fission yeast. *Nucleic Acids Res.* **2003***, 31*, 5064.

4. Hemmerich, P. Assessing protein dynamics in the cell nucleus. *Zellbiologie* **2005***, 31*, 18.

5. Houtsmuller, A. B.; Vermeulen, W. Macromolecular dyanmics in living cell nuclei reveals by fluorescence redistribution after photobleaching. *Histochem. Cell Biol.* **2001***, 115*, 13.

6. Cook, P. R. A Model for all Genomes: The Role of Transcription Factories. *J. Mol. Biol.* **2010***, 395*, 1-10.

7. Misteli, T. Protein dynamics: Implications for nuclear architecture and gene expression. *Science* **2001***, 291*, 843-847.

8. Gorski, S. A.; Snyder, S. K.; John, S.; Grummt, I.; Misteli, T. Modulation of RNA Polymerase Assembly Dynamics in Transcriptional Regulation. *Mol. Cell* **2008***, 30*, 486-497.

9. Dundr, M.; Hoffmann-Rohrer, U.; Hu, Q.; Grummt, I.; Rothblum, L. I.; Phair, R. D.; Misteli, T. A Kinetic Framework for a Mammalian RNA Polymerase in Vivo. *Science* **2002***, 298*, 1623-1626.

10. Darzacq, X.; Shav-Tal, Y.; de Turris, V.; Brody, Y.; Shenoy, S. M.; Phair, R. D.; Singer, R. H. In vivo dynamics of RNA polymerase II transcription. *Nat. Struct. Mol. Biol.* **2007***, 14*, 796-806.

11. Yao, J.; Ardehali, M. B.; Fecko, C. J.; Webb, W. W.; Lis, J. T. Intranuclear distribution and local dynamics of RNA polymerase II during transcription activation. *Mol. Cell* **2007***, 28*, 978-990.

12. Chen, D.; Dundr, M.; Wang, C.; Leung, A.; Lamond, A.; Misteli, T.; Huang, S. Condensed mitotic chromatin is accessible to transcription factors and chromatin structural proteins. *J. Cell Biol.* **2005***, 168*, 41-54.

13. Schneider, D. A.; Nomura, M. RNA polymerase I remains intact without subunit exchange through multiple rounds of transcription in Saccharomyces cerevisiae. *P. Natl. Acad. Sci. USA* **2004**, *101*, 15112-15117.

14. Hannan, R.D., Cavanaugh, A.,Hempel, W.M., Moss, T., Rothblum, L. Identification of a mammalian RNA Polymerase I holenezyme containing components of the DNA repair/replication system. *Nucleic Acids Res.* **1999**, *27*, 3720.

15. Grummt, I. Life on a planet of its own: regulation of RNA Polymerase I transcription in the nucleolus. *Genes Dev.* **2003**, *17*, 1691.

16. Kimura, H.; Sugaya, K.; Cook, P. R. The transcription cycle of RNA polymerase II in living cells. *J. Cell Biol.* **2002**, *159*, 777-782.

17. Politi, A.; Moné, M. J.; Houtsmuller, A. B.; Hoogstraten, D.; Vermeulen, W.; Heinrich, R.; van Driel, R. Mathematical Modeling of Nucleotide Excision Repair Reveals Efficiency of Sequential Assembly Strategies. *Mol. Cell* **2005**, *19*, 679-690.

18. Yao, J.; Zobeck, K. L.; Lis, J. T.; Webb, W. W. Imaging transcription dynamics at endogenous genes in living Drosophila tissues. *Methods* **2008**, *45*, 233-241.

19. Weiss, M.; Elsner, M.; Kartberg, F.; Nilsson, T. Anomalous Subdiffusion Is a Measure for Cytoplasmic Crowding in Living Cells. *Biophys. J.* **2004**, *87*, 3518-3524.

20. Daddysman, M. K.; Fecko, C. J. Revisiting Point FRAP to Quantitatively Characterize Anomalous Diffusion in Live Cells. *J. Phys. Chem. B* **2013**, *117*, 1241-1251.

21. Sprague, B. L.; McNally, J. G. FRAP analysis of binding: proper and fitting. *Trends in Cell Biol.* **2005**, *15*.

22. Zobeck, K. L.; Buckley, M. S.; Zipfel, W. R.; Lis, J. T. Recruitment Timing and Dynamics of Transcription Factors at the Hsp70 Loci in Living Cells. *Mol. Cell* **2010**, *40*, 965-975.

23. Acker, J.; de Graaff, M.; Cheynel, I.; Khazak, V.; Kedinger, C.; Vigneron, M. Interactions between the Human RNA Polymerase II Subunits. *J. Biol. Chem.* **1997**, *272*, 16815-16821.

24. Seksek, O.; Biwersi, J.; Verkman, A. S. Translational diffusion of macromolecule-sized solutes in cytoplasm and nucleus. *J. Cell Biol.* **1997**, *138*, 131-142.

25. Sokolov, I. M. Models of anomalous diffusion in crowded environments. *Soft Matter* **2012**, *8*, 9043-9052.

26. Brown, E. B.; Wu, E. S.; Zipfel, W. R.; Webb, W. W. Measurement of Molecular Diffusion in Solution by Multiphoton Fluorescence Photobleaching Recovery. *Biophys. J.* **1999**, *77*, 2837-2849.

27. Dix, J. A.; Verkman, A. S. Crowding Effects on Diffusion in Solutions and Cells. *Ann. Rev. Biophys. Biomol. Struct.* **2008**, *37*, 247.

28. Periasamy,N., Verkman, A.S Analysis of Fluorphore Diffusion by Continuous Distributions of Diffusion Coefficients: Application to Photobleaching Measurements of Multicomponent and Anomalous Diffusion. *Biophys. J.* **1998**, *75*, 557.

29. Gordon, G., W.; Chazotte, B.; Wang, X. F.; Herman, B. Analysis of Simulated and Experimental Fluorescence Recovery After Photobleaching. Data for Two Diffusing Components. *Biophys. J.* **1995**, *68*, 766.

30. Wilson, C. J.; Chao, D. M.; Imbalzano, A. N.; Schnitzler, G. R.; Kingston, R. E.; Young, R. A. RNA Polymerase II Holoenzyme Contains SWI/SNF Regulators Involved in Chromatin Remodeling. *Cell* **1996**, *84*, 235-244.

31. Eskiw, C.; Fraser, P. Ultrastructural study of transcription factories in mouse erythroblasts. *J. Cell Sci.* **2011**, *124*, 3676.

32. Hager, G.; Elbi, C.; Becker, M. Protein dynamics in the nuclear compartment. *Genetics and Development* **2002**, *12*, 137.

33. Mueller, F.; Wach, P.; McNally, J. G. Evidence for a Common Mode of Transcription Factor Interaction with Chromatin as Revealed by Improved Quantitative Fluorescence Recovery after Photobleaching. *Biophys. J.* **2008**, *94*, 3323-3339.

34. Feder, T. J.; Burst-Mascher, I.; Slattery, J. P.; Baird, B.; Webb, W. W. Constrained diffusion or immobile fraction on cell surfaces: A new interpretation. *Biophys. J.* **1996**, *70*, 2767-2773.

35. Malchus, N.; Weiss, M. Elucidating Anomalous Protein Diffusion in Living Cells with Fluorescence Correlation Spectroscopy-Fatcs and Pitfalls. *J. Fluoresc.* **2010**, *20*, 19.

36. Stasevich, T. J.; Mueller, F.; Michelman-Ribeiro, A.; Rosales, T.; Knutson, J. R.; McNally, J. G. Cross-Validating FRAP and FCS to Quantify the Impact of Photobleaching on In Vivo Binding Estimates. *Biophys. J.* **2010**, *99*, 3093-3101.

37. Fushimi, K.; Verkman, A. S. Low viscosity in the aqueous domain of cell cytoplasm measured by picosecond polarization microfluorimetry. *J. Cell Biol.* **1991**, *112*, 719-725.

38. Mika, J. T.; Poolman, B. Macromolecule diffusion and confinement in prokaryotic cells. *Curr. Opin. Biotechnol.* **2011**, *22*, 117-126.

39. Hauser, G. I.; Seiffert, S.; Oppermann, W. Systematic evaluation of FRAP experiments performed in a confocal laser scanning microscope ? Part II: Multiple diffusion processes. *J. Microsc.* **2008***, 230*, 353-362.

40. Mitchell, J. A.; Fraser, P. Transcription factories are nuclear subcompartments that remain in the absence of transcription. *Gene. Dev.* **2008***, 22*, 20.

41. Phair, R. D.; Misteli, T. High mobility of proteins in the mammalian cell nucleus. *Nature* **2000***, 404*, 604.

42. Hager, G.; McNally, J. G.; Misteli, T. Transcription Dynamics. *Mol. Cell* **2009***, 35*, 741.

43. Misteli, T. Beyond the Sequence: Cellular Organization of Genome Function. *Cell* **2007***, 128*, 787.

44. Yao, J.; Munson, K. M.; Webb, W. W.; Lis, J. T. Dynamics of heat shock factor association with native gene loci in living cells. *Nature* **2006***, 442*, 1050-1053.

45. Guigas, G.; Weiss, M. Sampling the Cell with Anomalous Diffusion—The Discovery of Slowness. *Biophys. J.* **2008***, 94*, 90-94.

46. Hancock, R. A role for macromolecular crowding effects in the assembly and function of compartments in the nucleus. *J. Struct. Biol.* **2004***, 146*, 281-290.

47. Minton, A. P. Implications of macromolecular crowding for protein assembly. *Curr. Opin. Struc. Biol.* **2000***, 10*, 34-39.

CHAPTER 5: PHOTOINDUCED DAMAGE RESULTING FROM FLUORESCENCE IMAGING OF LIVE CELLS[*]

"Science is a wonderful thing if one does not have to earn one's living at it."

– Albert Einstein

5.1. Introduction

The use of light to interrogate live-cell processes has resulted in great mechanistic and structural insight. Fluorescence microscopy has become one of the most widely used light microscopy techniques due to inherent advantages that include selective labeling and imaging of low concentrations of fluorophore.[1,2] However, the introduction of exogenous fluorophores necessary for fluorescence microscopy inherently modifies the photochemistry of the cell, particularly in the vicinity of the tagged molecule. It is important to be aware of the potential for unnatural cellular damage that can be attributed to these alien molecules, which presents as a confounding variable in live cell microscopy experiments. We note that the presence of the fluorophore may have adverse consequences even in the absence of light (e.g. protein inactivation due to the addition of a GFP tag[3,4]), but this chapter only considers negative photoinduced effects due to imaging the sample.

Damage resulting from fluorescence microscopy can generally be divided into two broad categories, photochemical or photophysical. The likelihood that each type of damage will adversely affect the experiment is determined by the choice of microscopy method and fluorophore. As will be described later, the illumination parameters are critically important in determining the potential photoreactions that occur in a system. Therefore, it is important that these parameters are included in publications. We have noticed that laser powers are sometimes not expressed as useful or reproducible quantities in the literature, e.g. including a percentage of the maximum laser power, a specific setting on the imaging software, or as the level of current used to operate the laser. Such specifications are not useful for most outside researchers. Even researchers that have the same microscope setup can experience differences in beam alignment and laser (or arc lamp) age that will result in different powers at the objective. Therefore, it is imperative that *all* powers should be measured with a power meter at the objective as part of the experiment and reported along with the objective used so that the experiments can be reproduced by others.

5.2. Cellular damage

5.2.1. Mechanisms of damage

Optical imaging of cells or tissue can introduce excess energy that may lead to biological damage of the sample. However, it is important to note that simple exposure to light does not necessarily cause the deposition of optical energy into the sample. For example, transmitted light microscopies are based on phenomena such as scattering and diffraction that typically deposit little or no energy into the sample. On the other hand, fluorescence microscopy and related techniques usually require photon

absorption and are thus much more likely to cause photodamage. We note that our discussion is restricted to biological samples that do not contain endogenous species that strongly absorb visible or near-infrared light, such as melanin or hemoglobin.

There are many mechanisms by which light-matter interactions can damage biomolecules, but most fall into one of two general categories. The first category includes photochemical mechanisms that produce damage via absorption-induced generation of highly reactive chemical species, such as free radicals and reactive oxygen species (ROS). The second category encompasses photophysical mechanisms in which photon absorption modifies the physical properties of the system, such as local heating due to non-radiative relaxation of excited molecules. Damage mechanisms in both categories are important for all forms of fluorescence microscopy techniques, but some imaging methods are more prone to a particular subset, as described below.

In some cases, optical techniques have been developed to intentionally induce specific types of damage in samples. For example, it is sometimes desirable to damage a small portion of genomic DNA, to investigate mechanisms of DNA damage repair.[5] However, it is more often desirable to avoid perturbing samples during optical imaging, so it is important to consider how to avoid introducing unwanted damage and how to determine if photodamage is occurring.

We consider specific photochemical and photophysical mechanisms in more detail below by first introducing several microscopy-based techniques that are specifically intended to generate damage. We then discuss ways to detect and avoid unwanted damage during optical imaging experiments.

5.2.2. Photochemical mediated damage

Paramount among the assumptions made in the use of fluorescent reporter molecules is that they do not perturb the system under observation. Unfortunately, this assumption is not always valid. One common source of photodamage arises from chemical reactions of the fluorophore in its lowest energy electronic excited state, which we refer to as photochemical damage. The usual pathway for energy relaxation from this excited state is photon emission, but there often exist other possible excitation relaxation pathways, such as the chemical reactions discussed below. These reactions can also lead to fluorophore photobleaching, which is a permanent chemical rearrangement of the fluorophore such that fluorescence is no longer the primary relaxation pathway. Most fluorophores undergo $10^5 - 10^6$ excitation cycles before photobleaching. As discussed below, photobleaching may indicate the production of reactive oxygen species;[6,7] however, the production of these damaging species may be cryptically occurring even without a visible loss of fluorescence from the sample. In either case, photochemical damage is typically cumulative as it relies upon the net number of excitation events (i.e. the net amount of energy deposited) only and not the rate at which the excitation events occur (i.e. the power or intensity).

Excited fluorophores can occasionally interact with their solvent environment creating short-lived, damaging radical species capable of destabilizing or destroying other biomolecules. The process begins when molecular fluorophores, excited by an appropriate wavelength of visible light, are promoted to a singlet excited state. One mode for the energetic relaxation of these species is to emit a photon; however, the high cycling rate induced by high light intensities used in confocal or MPM increases the

population of triplet state species (the triplet state quantum yield can be as high as 5% for some molecular fluorophores). Molecular oxygen, which exists in a triplet ground state configuration, can readily interact with this excited state fluorophore. Energy transfer between these species results in the formation of singlet oxygen, while electron transfer results in the formation of super-oxide and a fluorophore radical. All of these species are high reactive and are generated by the favorable downhill energetics of electron transfer to ground state oxygen, coupled with the rapid diffusion of molecular oxygen and therefore frequent interactions.[7] These highly unstable species are rapidly quenched in aqueous environments leading to the formation of hydroxyl radicals. The short-lived hydroxyl radical is the prime damage mediating species, resulting in radical induced damage to proximal biomolecules.[8]

The creation of singlet oxygen and radicals has a proximal effect on surrounding biomolecules. The most intuitive directed use of this phenomenon to directly create damage and inactivate proteins is chromophore-assisted light inactivation (CALI) which directly inactivates proteins through photochemical damage. CALI has found wide spread application in cell biology to selectively inactivate proteins or fragment chromosomes.[9] Original implementations of CALI used organic molecules conjugated to protein specific antibodies. However, these methods are being replaced by the use of encoded protein markers such as GFP. The encoded protein markers have the advantage of being present in the cell without microinjection and are "background free," avoiding potential complications from unbound, excess antibody. However, GFP is not as effective a CALI agent as molecular fluorophores. The GFP chromophore is embedded in a β-barrel structure, isolating the chromophore center from the cellular

milieu[10] and limiting singlet oxygen production which is the primary cytotoxic mechanism generated by fluorescent proteins.[11] To counter this problem a more phototoxic GFP variant, KillerRed, was evolved to increase the phototoxicity of GFP by three orders of magnitude.[12] This protein works as an excellent genetically encoded CALI agent. In general, GFP and the normal variants are excellent fluorophores for imaging while reducing, but not eliminating, the potential for production of ROS that are common with molecular fluorophores.

ROS are also generated when imaging nucleic acids stained with intercalating dyes. This can lead to widespread genomic damage, the effect of which must be carefully considered when using DNA stains.[13] The formation of damaging hydroxyl radicals proximal to the site of fluorophore incorporation results in species that can attack DNA to produce various forms of oxidative radical photodamage,[14] notably single strand breaks.[15,16] Individual damage events typically cleave only one strand of the DNA sugar-phosphate backbone;[17,18] the accumulation of many single-strand breaks leads to double-strand cleavage.[19] Since many proteins involved in DNA replication and repair bind to single strand breaks on DNA,[20-22] the presence of single strand breaks induced by photoexcitation of intercalating dyes could strongly bias protein-DNA interactions. Additionally, wide-spread genomic damage can induce apoptotic pathways resulting in cell death. While favorable in emerging cancer treatments, this is likely to induce artifacts in experiments probing native cellular function.

Although the generation of damage mediating radicals is detrimental for most experiments, it can offer a degree of spatiotemporal user control in instances when initiating cellular damage is desirable.[13,16] The common DNA intercalating dyes used

117

for *in vivo* imaging application, such as Hoechst and DAPI, are all capable of selectively targeting DNA for fragmentation.[23] The incorporation of these intercalating dyes enables DNA fragmentation to be initiated at particular wavelengths and in a dose dependent manner. This is useful for studies of DNA damage and repair mechanisms, where localized photochemical damage can be used to elucidate repair pathways. It has been shown that careful selection of the type of dye and DNA binding mode can be applied to tune the DNA backbone cleavage, biasing damage towards double strand cleavage or single strand breaks.[24] For clinical applications, the generation of singlet oxygen by fluorophore sensitization has been leveraged to treat disease states using photodynamic therapy. Here, high-quantum efficiency fluorophores are engineered to absorb at specific wavelengths and are delivered to biological tissue that is targeted for destruction.[25] Using a myriad of light transducers, such as NIR sources with deep tissue penetration or fiber-optics for the guidance of visible light, high intensity light sources can be brought to bear on a limited tissue region. Through the mechanisms explained, apoptotic pathways are initiated following widespread genome and cell membrane disruption; therefore, the conditions mentioned in the above references should be avoided.

Finally, ROS can be generated from other sources in a sample, such as the cell medium. For example, N-2-hydroxyethylpiperazine-N'-2-ethanesulfonic acid (HEPES), a common buffer in cell culture medium, has the unfortunate side effect of producing hydrogen peroxide when used for fluorescence microscopy.[26] Even ambient light can be enough to induce H_2O_2 production and the onset of cell death due to the oxidative stress of the cell culture medium, which was a confounding source of error in cell culture

experiments until the mechanism was identified (thus always confirm your buffer system is compatible with your imaging conditions).

5.2.3. Photophysical mediated damage

Photophysical damage mechanisms involve excited states that are more energetic than the lowest energy singlet state from which fluorescence typically arises. As examples, this category includes local solvent heating due to the dissipation of excess vibrational energy from the initial (Franck-Condon) fluorophore excited state, and free electrons ejected by the fluorophore or solvent as a result of multiphoton ionization. In contrast with photochemical mediated damage, photophysical damage mechanisms typically depend less on the total energy deposited into a sample and more on the intensity. For example, thermal photophysical effects such as localized heating due to excited state vibrational relaxations in the fluorophore can raise the temperature of solvent molecules in the vicinity of the fluorophore for short periods of time. Thermal energy dissipates from the ~femtoliter excitation volume on a nanosecond time scale. Thus, the use of a pulsed excitation laser that transiently raises the local temperature by a few degrees per pulse does not cause appreciable damage if the repetition rate is low enough to allow for thermal relaxation between pulses. However, higher repetition rates (higher powers) may induce severe thermal damage after an equivalent number of excitation pulses. Such thermal damage is more common in laser scanning experiments that use higher powers, but can also occur in widefield imaging experiments.[27]

Local thermal energy deposition can result in the proximal denaturing of proteins, but in a more extreme case, it can lead the formation of microbubbles. These

microbubbles form from localized solvent expansion creating unstable low pressure zones that rapidly implode, resulting in subsequent cavitation damage.[27] Depending on the laser spot size and pixel-dwell time, cavitation damage may be restricted to nearly the laser spot region resulting in mechanical damage and bond breaking of proximal biomolecules. In the cases of long dwell times and larger spot sizes, the membrane can become permeable or cell ablation can result. In an imaging context, this damage can create significant artifacts, reduce cell viability, and alter cellular behavior.

Another important photophysical damage mechanism is the formation of highly reactive radical species due to multiphoton ionization of the fluorophore or solvent (often referred to as solvated electrons). Due to the involvement of a multiphoton process, this mechanism depends nonlinearly on the excitation intensity and is thus typically a problem only for microscopy techniques that used pulsed lasers. In aqueous solution, solvated electrons attack biomolecules in the opposite manner of radical species, causing reductive as opposed to oxidative damage.[28] These chemical pathways have been shown to be equally, if not more destructive than oxidative damage. Further, the reduced mass of solvated electrons compared to more typical free radical species confers a larger mean free path of diffusion, and therefore larger damage radius. Lipid membranes are especially vulnerable to attack due to the unstable radical fatty acids formed. These residues compromise the cell membrane.[29] If generated inside the cellular confines, nuclear material and mitochondria become vulnerable; damage to either species can initiate cell death.

In some cases, the high peak intensities cause photoionization of the cellular material generating a large population of electrons that exist as plasma. These

electrons are capable of absorbing additional light pulses sustaining the plasma and further propagating its production. In water, intensities generated by femtosecond pulsed lasers greater than 1 TW/cm^2 for ultraviolet-B (280 – 315 nm) light and in the range of 4-10 TW/cm^2 for green light[30] are required to initiate optical breakdown. These high intensities are unlikely to be encountered during most imaging experiments but can be achieved during certain single-molecule techniques (notably optical trapping). However, longer duration laser pulses can reduce this high intensity threshold, as pico- and nano-second green laser systems can lower the threshold intensity to sub-TW/cm^2.[31] Plasma generation has been harnessed for optical tissue micro-dissection such as creating cuts of DNA strands and microtubules inside of live cells.[32-35] The plasma-mediated ablation occurs only at the focal point of the objective due to the high-photon flux required for off resonance ionization.[27,36] In one study, the energy onset of plasma mediation ablation in chromatin and microtubules was systematically confirmed using electron microscopy in addition to the observation of photobleaching with fluorescence microscopy. The onset of ablation occurs at pulse energies of just above 1 nJ at 790 nm and a 1.4 NA objective.[34] The onset of severe photobleaching occurred at pulse energies slightly lower than 1 nJ; therefore, although photobleaching itself is not a definite indicator of ablation it can be used to show the likelihood that photophysical damage is occurring.

Cellular components other than typical fluorophores can also be damaged by directly exciting electronic transitions in the biomolecules themselves. Both proteins and nucleic acids absorb in the ultraviolet-C (100 – 280 nm) region of the spectrum. The DNA base thymine readily undergoes a photochemically induced dimerization

121

reaction when exposed to UV-C light. Although these wavelengths are much shorter than the excitations for fluorophores used in fluorescence microscopy, these transitions can be accessed by a higher order non-linearity when using pulsed lasers in MPM. The nonlinear absorption of biomolecules is dependent on the peak intensity not the net energy, just like nonlinear absorption by fluorophores. The generation of both "UV-like" lesions and single and double strand breaks on DNA has been demonstrated for both visible[37,38] and infrared[39-41] pulsed laser light. In both studies, the required powers to achieve damage were often at least an order of magnitude larger than the powers required for typical MP imaging and therefore are not typically encountered in most MP and confocal microscopy applications. However, the potential for damage in experiments that require brief, intense flashes of light (examples include inducing desired phototransitions in caged proteins, switching of photoactivatable flourophores, or photobleaching in fluorescence recovery after photobleaching (FRAP)) cannot be ruled out.

5.2.4. Checking for cellular damage due to fluorescent microscopy

In this section, we briefly consider several approaches to detect cellular damage in live-cell microscopy. Before doing so, we note that fluorescence-based imaging is likely to cause photodamage in nearly all biological samples, even if the damage is not readily apparent. In many cases, it is possible to detect only relatively large amounts of damage due to a low assay sensitivity or limited dynamic range. Thus, it is important to consider the impact low levels of photodamage could have on experimental results even if undetectable. For example, it is commonplace to locate cell nuclei by imaging samples stained with Hoechst (or similar DNA-associating dyes), but this procedure

undoubtedly causes DNA strand breakage as discussed above. Such damage is inconsequential in some types of experiments, but it may have a large impact on experiments intended to probe dynamics of DNA-associating proteins.

Perhaps the simplest method to detect damage is to observe the morphology of cellular structures in initial and final images within an experimental sequence to determine if ablation or cell death has occurred. For example, the use of high power near infrared pulses intended for three-photon absorption of DNA creates cavitation bubbles in *Drosophila* salivary glands and destroys cultured HeLa cells. However, the lower power visible light used to excite DNA via two-photon absorption does not produce such damage.[38] In many cases, light-induced ablation may be much less apparent or even undetectable after recording a single image, but may become evident after several frames. Thus, it is advisable to perform control experiments in which a slightly higher excitation power is used or additional images of the same sample are collected. If the final image in such control experiment does not contain unexpected morphological changes, it is generally safe to assume the actual experimental conditions are acceptable.

Less severe photodamage can often be detected by observing the subsequent growth and division of cell populations that have been used in microscopy experiments. For example, unchecked cell growth without cell division can occur in Chinese hamster ovary (CHO) cells that were exposed to low intensity near-IR pulsed light resulting in oversized cells days after NIR pulsed light exposure.[42] Other qualitative indicators of damage include long-term (hours to days) measures of cell responses like delayed apoptosis[43] or reduction in cell reproductive viability.[44,45]

123

Although qualitative measures of cell damage are convenient, it is helpful to be aware of cryptic forms of damage that may occur, so various assays have been developed to test for such damage. A large number of cell viability kits are commercially available. One example is the LIVE/DEAD Reduced Biohazard Cell Viability Kit (Molecular Probes) that stains live cells with a green florescent dye while dead or dying cells are stained with a red fluorescent dye. This simple test checks for membrane integrity as a sign of cell viability and can reveal membrane destruction that cannot be resolved using light microscopy. As an example of other damage-specific assays, dyes such as Ni-3,3-diaminobenzidine or Jenchrom px blue (JenLab GmbH) can be used to test for ROS.[46] DNA damage can be assayed using immunohistochemistry with antibodies specific to proteins that are markers for DNA damage, such as γ-H2A.X for single and double strand breaks. Antibodies also exist to assay specific types of UV-induced lesions, such as thymine cyclobutane and 6-4 dimers or oxidative stress lesions such as 8-oxoguanine.[40]

5.2.5. Preventing unwanted damage in fluorescent microscopy

In live cell experiments it is desirable to avoid unintentional photodamage that could potentially bias the results. As stated previously, nearly all fluorescence imaging induces some amount of damage, so it is critical to consider what types and degree of damage are acceptable for a given experiment. It is always prudent to reduce potential damage artifacts by optimizing imaging conditions, as described below, because such changes can also improve the general quality of the results (signal-to-noise, etc.). However, the addition of additives or other potentially perturbative measures should only be considered when photodamage is likely affecting the experimental outcome. In

this case, it is usually beneficial to consider the type of photodamage or mechanism by which it is produced, in order to determine the best approach to reduce its impact.

The best way to prevent unintentional photodamage is to maximize the efficiency of the microscope so that the minimal amount of incident power can be used to image the sample. Rather than resorting to "turning up the power" as a solution for low signal, using a more efficient fluorophore, filters or better detection hardware can improve signal without increasing the risk of unwanted photoeffects. At a minimum, it is important to ensure the optical filters are optimal for the excitation and emission spectra of the fluorophore. Unless it is necessary, UV radiation should be well filtered from arc lamp excitation. In general, the longest practical wavelength excitation band should be used for any fluorophore, since it reduces excess energy delivered to the fluorophore (e.g. due to excitation to higher energy electronic states or highly excited vibrational states) and reduces the potential of exciting endogenous fluorophores. Single-fluorophore experiments should utilize emission filters with a wide bandpass, while multicolor experiments should use the widest bandpass that still prevents crosstalk.

The choice of fluorophore can also be important for preventing photodamage. Some fluorophores have a higher probability than others of producing radicals when excited; this probability can be correlated with the photobleaching rate since the same photochemical mechanisms can cause both damage and bleaching. For example, Alexa 488 is less prone to bleaching and causing photodamage than fluorescein. In addition to photostability, the wavelength range of a fluorophore can affect detection sensitivity and thus photodamage. Photomultiplier tubes used in laser scanning instruments are typically most sensitive in the blue or green spectral regions, while

charge coupled devices used for widefield imaging experiments are often most sensitive in the red and near-IR spectral region. Choosing the most sensitive detectors and fluorophores that are optimal for the detector wavelength sensitivity are good ways to reduce the amount of incident power and often the amount of photodamage.

Chemical methods can also be undertaken to reduce photodamage. Since one of the most common mediators in producing damage is singlet oxygen, reducing the overall oxygen concentration in the sample can reduce the presence of reactive oxygen species in the sample. The simplest method is to use deoxygenated buffers and oxygen impermeable materials, but oxygen depletion agents such as Oxyrase can also accomplish this purpose. Adding antioxidants as radical scavengers are also common in single molecule experiments and can be used for live cell imaging. For example, compounds such as ascorbate and Trolox can decrease oxidative damage in cells. However, it has also been shown that ascorbate can also introduce DNA damage through other means,[24] so it is best to introduce such chemicals only when absolutely necessary.

5.3. Conclusion

Fluorescence microscopy is a useful tool for imaging and manipulating live cells. High resolution methods as well as dynamic perturbation[47] and fluctuation spectroscopy[48] have garnered unprecedented structural and mechanistic details, previously only accessible through electron microscopy or *in vitro* biochemistry. The ability to specifically target cellular substructures for imaging, or genetically encode fluorophore tagged to proteins of interest means that fluorescence microscopy will only continue to grow in applications and utility. Furthermore, the use of fluorescence

microscopy to selectively manipulate live cell metabolism through photoswitching proteins or CALI offers many exciting opportunities for research. However, this growth must be accompanied by a respect for the ways in which the input of optical energy can alter or even destroy a biological system, since deposition of energy into live cells can have unintended consequences for damaging live cell tissue. This damage can cause experimental anomalies that can result in unreliable experimental data or worse, inducing result altering artifacts leading to incorrect conclusions. Therefore, we recommend caution and consistent reporting of experimental conditions when undertaking florescence microscopy experiments. A good understanding of the amount of energy subsumed by the cell is crucial along with an analysis of what the prime absorbers are in a system. This, coupled with limiting the application of ROS generating dye molecules can significantly reduce the potential for tissue damage. However, it cannot be over emphasized that the best method to prevent damage is a well configured and optimized microscopy experiment to limit the required optical power.

REFERENCES

1. Stephens, D. J.; Allan, V. J. Light Microscopy Techniques for Live Cell Imaging. *Science* **2003***, 300*, 82-86.

2. Lichtman, J. W.; Conchello, J. Fluorescence microscopy. *Nat. Methods* **2005***, 2*, 910-919.

3. Giepmans, B. N. G.; Adams, S. R.; Ellisman, M. H.; Tsien, R. Y. The Fluorescent Toolbox for Assessing Protein Location and Function. *Science* **2006***, 312*, 217-224.

4. Wombacher, R.; Cornish, V. W. Chemical tags: Applications in live cell fluorescence imaging. *J. Biophotonics* **2011***, 4*, 391-402.

5. Essers, J.; Vermeulen, W.; Houtsmuller, A. B. DNA damage repair: anytime, anywhere? *Curr. Opin. Cell Biol.* **2006***, 18*, 240-246.

6. Halliwell, B.; Aruoma, O. I. DNA damage by oxygen-derived species Its mechanism and measurement in mammalian systems. *FEBS Lett.* **1991***, 281*, 9-19.

7. Schweitzer, C.; Schmidt, R. Physical Mechanisms of Generation and Deactivation of Singlet Oxygen. *Chem. Rev.* **2003***, 103*, 1685-1757.

8. SIES, H. Strategies of antioxidant defense. *Eur. J. Biochem.* **1993***, 215*, 213-219.

9. Jacobson, K.; Rajfur, Z.; Vitriol, E.; Hahn, K. Chromophore-assisted laser inactivation in cell biology. *Trends Cell Biol.* **2008***, 18*, 443-450.

10. Remington, S. J. Fluorescent proteins: maturation, photochemistry and photophysics. *Curr. Opin. Struct. Biol.* **2006***, 16*, 714-721.

11. Ragàs, X.; Cooper, L. P.; White, J. H.; Nonell, S.; Flors, C. Quantification of Photosensitized Singlet Oxygen Production by a Fluorescent Protein. *ChemPhysChem* **2011***, 12*, 161-165.

12. Bulina, M. E.; Lukyanov, K. A.; Britanova, O. V.; Onichtchouk, D.; Lukyanov, S.; Chudakov, D. M. Chromophore-assisted light inactivation (CALI) using the phototoxic fluorescent protein KillerRed. *Nat. Protocols* **2006***, 1*, 947-953.

13. Limoli, C. L.; Ward, J. F. A new method for introducing double-strand breaks into cellular DNA. *Radiat. Res* **1993***, 134*, 160-169.

14. Saran, M.; Bors, W. Radical reactions in vivo- an overview. *Radiat. Environ. Biophys.* **1990***, 29*, 249-262.

15. Teoule, R. Radiation-induced DNA damage and its repair. *Int. J. Radiat. Biol.* **1987***, 51*, 573-589.

16. Ward, J. F. The yield of DNA double strand breaks produced intracellularly by ionizing radiation: a review. *Int. J. Radiat. Biol.* **1990***, 57*, 1141-1150.

17. Guo, H.; Tullius, T. D. Gapped DNA is anisotropically bent. *P. Natl. Acad. Sci. USA* **2003***, 100*, 3743-3747.

18. Siddiqi, M. A.; Bothe, E. Single- and double-strand break formation in DNA irradiated in aqueous solution: dependence on dose and OH radical scavenger concentration. *Radiat. Res , 112*, 449-463.

19. Patrick, M. H.; Rahn, R. O. *Photochemistry and Photobiology of Nucleic Acids;* Academic Press: New York, 1976; Vol. II, pp 35-96.

20. Houten, B. V.; Croteau, D. L.; Vecchia, M. J. D.; Wang, H.; Kisker, C. 'Close-fitting sleeves': DNA damage recognition by the UvrABC nuclease system. *Mutat. Res.* **2005***, 577*, 92-117.

21. Friedberg, E. C. DNA Damage and Repair. *Nature* **2003***, 421*, 436-440.

22. Caldecott, K. W. Single Strand Break Reapr and Genetic Disease. *Nat. Rev. Genet.* **2008***, 9*, 619-631.

23. Akerman, B., Tuite, E. Single- and double-strand photocleavage of DNA by YO, YOYO, and TOTO. *Nucleic Acids Res.* **1996***, 24*, 1080.

24. Tycon, M. A.; Dial, C. F.; Faison, K.; Melvin, W.; Fecko, C. J. Quantification of dye-mediated photodamage during single-molecule DNA imaging. *Anal. Biochem.* **2012***, 426*, 13-21.

25. Robertson, C. A.; Evans, D. H.; Abrahamse, H. Photodynamic therapy (PDT): A short review on cellular mechanisms and cancer research applications for PDT. *J. Photochem. Photobiol. B, Biol.* **2009***, 96*, 1-8.

26. Zigler, J. S., J.; Lepe-Zuniga, J.; Vistica, B.; Gery, I. Analysis of the cytotoxic effects of light-exposed hepes-containing culture medium. *In Vitro Cell. Dev. B.* **1985***, 21*, 282-287.

27. Vogel, A.; Noack, J.; Hüttman, G.; Paltauf, G. Mechanisms of femtosecond laser nanosurgery of cells and tissues. *Appl. Phys. B* **2005***, 81*, 1015-1047.

28. Nguyen, J.; Ma, Y.; Luo, T.; Bristow, R. G.; Jaffray, D. A.; Lu, Q. Direct observation of ultrafast-electron-transfer reactions unravels high effectiveness of reductive DNA damage. *P. Natl. Acad. Sci. USA* **2011***, 108*, 11778.

29. Pratt, D. A.; Tallman, K. A.; Porter, N. A. Free Radical Oxidation of Polyunsaturated Lipids: New Mechanistic Insights and the Development of Peroxyl Radical Clocks. *Acc. Chem. Res.* **2011**, *44*, 458-467.

30. Fan., C. H., Sun., J., Longtin, J.,P. Breakdown threshold and localized electron density in water induced by ultrashort laser pulses. *J. Appl. Phys.* **2002**, *91*, 2530-2536.

31. Kong, X.; Mohanty, S. K.; Stephens, J.; Heale, J. T.; Gomez-Godinez, V.; Shi, L. Z.; Kim, J.; Yokomori, K.; Berns, M. W. Comparative analysis of different laser systems to study cellular responses to DNA damage in mammalian cells. *Nucleic Acids Res.* **2009**, *37*, e68-e68.

32. Konig, K.; Riemann, I.; Fritzsche, W. Nanodissection of human chromosomes with near-infrared femtosecond laser pulses. *Opt. Lett.* **2001**, *26*, 819-821.

33. Supatto, W.; Debarre, D.; Moulia, B.; Brouzes, E.; Martin, J.; Farge, E.; Beaurepaire, E. *In vivo*modulation of morphogenetic movements in *Drosophila* embryos with femtosecond laser pulses. *P. Natl. Acad. Sci. USA* **2005**, *102*, 1047-1052.

34. Heisterkamp, A.; Maxwell, I. Z.; Mazur, E.; Underwood, J. M.; Nickerson, J. A.; Kumar, S.; Ingber, D. E. Pulse energy dependence of subcellular dissection by femtosecond laser pulses. *Opt. Express* **2005**, *13*, 3690-3696.

35. Kuetemeyer, K.; Rezgui, R.; Lubatschowski, H.; Heisterkamp, A. Influence of laser parameters and staining on femtosecond laser-based intracellular nanosurgery. *Biomed. Opt. Express* **2010**, *1*, 587-597.

36. Vogel, A.; Venugopalan, V. Mechanisms of Pulsed Laser Ablation of Biological Tissues. *Chem. Rev.* **2003**, *103*, 577-644.

37. Tycon, M. A.; Chakraborty, A.; Fecko, C. J. Generation of DNA photolesions by two-photon absorption of a frequency-doubled Ti:sapphire laser. *J. Photochem. Photobiol. B, Biol.* **2011**, *102*, 161-168.

38. Daddysman, M.; Fecko, C. DNA Multiphoton Absorption Generates Localized Damage for Studying Repair Dynamics in Live Cells. *Biophys. J.* **2011**, *101*, 2294-2303.

39. Meldrum, R. A.; Botchway, S. W.; Wharton, C. W.; Hirst, G. J. Nanoscale spatial induction of ultraviolet photoproducts in cellular DNA by three-photon near-infrared absorption. *EMBO Rep.* **2003**, *4*, 1144-1149.

40. Dinant, C.; Jager, M. d.; Essers, J.; Cappellen, W. A. v.; Kanaar, R.; Houtsmuller, A. B.; Vermeulen, W. Activation of multiple DNA repair pathways by sub-nuclear damage induction methods. *J. Cell Sci.* **2007**, *120*, 2731-2740.

41. Trautlein, D.; Deibler, M.; Leitenstorfer, A.; Ferrando-May, E. Specific local induction of DNA strand breaks by infrared multi-photon absorption. *Nucleic Acids Res.* **2010**, *38*, e14.

42. König, K. In *Cellular Response to Laser Radiation in Fluorescence Microscopes;* Periasamy, A., Ed.; Methods in Cellular Imaging; Oxford University Press: Oxford, 2001; pp 236-251.

43. Tirlapur, U. K.; Konig, K.; Peuckert, C.; Krieg, R.; Halbhuber, K. Femtosecond near-infrared laser pulses elicit generation of reactive oxygen species in mammalian cells leading to apoptosis-like death. *Exp. Cell Res.* **2001**, *263*, 88-97.

44. König, K.; So, P. T. C.; Mantulin, W. W.; Gratton, E. Cellular response to near-infrared femtosecond laser pulses in two-photon microscopes. *Opt. Lett.* **1997**, *22*, 135-136.

45. König, K.; Becker, T. W.; Fischer, P.; Riemann, I.; Halbhuber, K. -. Pulse-length dependence of cellular response to intense near-infrared laser pulses in multiphoton microscopes. *Opt. Lett.* **1999**, *24*, 113-115.

46. Tirlapur, U. K.; Konig, K. Femtosecond near-infrared laser pulse induced strand breaks in mammalian cells. *Cell. Mol. Biol.* **2001**, *47*, OL131-OL134.

47. Mueller, F.; Mazza, D.; Stasevich, T. J.; McNally, J. G. FRAP and kinetic modeling in the analysis of nuclear protein dynamics: what do we really know? *Curr. Opin. Cell Biol.* **2010**, *22*, 403-411.

48. Krichevsky, O.; Bonnet, G. Fluorescence correlation spectroscopy: the technique and its applications. *Rep. Prog. Phys.* **2002**, *65*, 251-297.

CHAPTER 6: DNA MULTIPHOTON ABSORPTION GENERATES LOCALIZED DAMAGE FOR STUDYING REPAIR DYNAMICS IN LIVE CELLS[*]

"There is no better high than discovery." – E.O. Wilson

6.1. Introduction

The study of DNA damage repair has long been aided by experiments that examine cellular responses to DNA lesions produced by ultraviolet light. All of the nucleic acids absorb 200-300 nm light efficiently, but the main photoproducts that result from absorption of light in this spectral region are thymine cyclopyrimidine dimers (CPDs).[1,2] It is straightforward to create CPDs by exposing cells to the ~254 light emitted by low pressure mercury vapor lamps, however this method results in a random spatial distribution of lesions. To investigate the spatiotemporal dynamics of proteins involved in the repair of CPDs in live cells with fluorescence-based microscopy, it is more desirable to create photolesions in spatially restricted, user-defined regions of cell nuclei.

Several methods to generate localized DNA damage been investigated previously.[3] Perhaps the most obvious option, irradiation by a focused UV laser,[4] is somewhat limited by the relatively low numerical aperture of objective lenses that transmit UVC (100 – 280 nm) light. Furthermore, chromatic aberrations of these

---

objectives as well as the poor UV transmission of other common optical elements prevent the easy paring of UV sources with a conventional microscopy apparatus. More recently, localized DNA damage has been introduced by passing UVC light through 3-5 μm pores in a polycarbonate filter placed near the sample.[5-8] However, when applied to cultured mammalian cells, the spatial extent of DNA damage is still a considerable fraction of the nucleus. It is also difficult to pre-select the nuclear region to be damaged, which would be advantageous for investigating repair protein recruitment to specific locations. Finally, laser-based irradiation of pre-sensitized cells in the 337-405 nm range efficiently generates damage, but the focus of this method is to form strand breaks preferentially over nitrogen base photoproducts[9-12] which excludes the investigation of processes that repair UV lesions, such as nucleotide excision repair. This method also suffers from the potentially serious drawback that the sensitizing agent could perturb the natural response of the biological system. Ultimately, each of these methods only localizes the extent of DNA damage in two dimensions, but they do not offer confinement in the third (axial) dimension. The lack of axial confinement is acceptable for a thin monolayer of cultured cells; however, in order to selectively damage thick tissues or nuclei a method providing axial confinement is necessary. As an alternative, multiphoton excitation of DNA has the potential to create spatially localized CPDs without the aforementioned limitations.

Nonresonant multiphoton absorption is the process by which a molecule exposed to a high photon flux interacts with two or more photons simultaneously, producing an excited state equivalent in energy to the summation of the energy of the interacting photons.[13] Multiphoton microscopy takes advantage of this phenomenon by combining

the nonlinear intensity dependence with a steeply decreasing intensity profile outside of the focal point of the objective lens to enhance imaging depth discrimination.[14,15] Our group has previously demonstrated that DNA exhibits multiphoton absorption when exposed to visible femtosecond pulses *in vitro*;[16] in contrast to its application for imaging purposes, multiphoton absorption of DNA photochemically produces lesions that are subject to cellular repair mechanisms (Figure 6.1A). Herein, we investigate the use of multiphoton absorption of visible light as a means to produce three-dimensionally localized thymine CPDs in cells, and demonstrate its utility in studying the spatiotemporal recruitment of topoisomerase I (TopI) to sites of DNA damage. We refer to this method as Damage Induced by Multiphoton Excitation of DNA with visible light (DIMED-Vis).

We first establish that multiphoton absorption of visible light produces thymine-thymine CPDs in HeLa cells and in the polytene chromosomes of *Drosophila melanogaster* larval salivary gland cells. Our experiments focus ultrafast 400-525 nm pulses generated by frequency–doubling the output of a Ti:sapphire laser into cellular samples using a home-built multiphoton microscope (Figure 6.1B). The blue-green light is harmless to cells directly, but multiphoton absorption at the objective lens focal point produces the DNA photolesions. We use HeLa cells to characterize the wavelength and power dependence of our *in vivo* procedure and polytene chromosomes to demonstrate the localized nature of the lesions. Previous studies have found that ultrashort near infrared pulses can also generate DNA damage *in vivo*[17,18] via multiphoton absorption; however the irradiation conditions required to generate DNA damage with near IR pulses also introduce other types of cellular damage, including
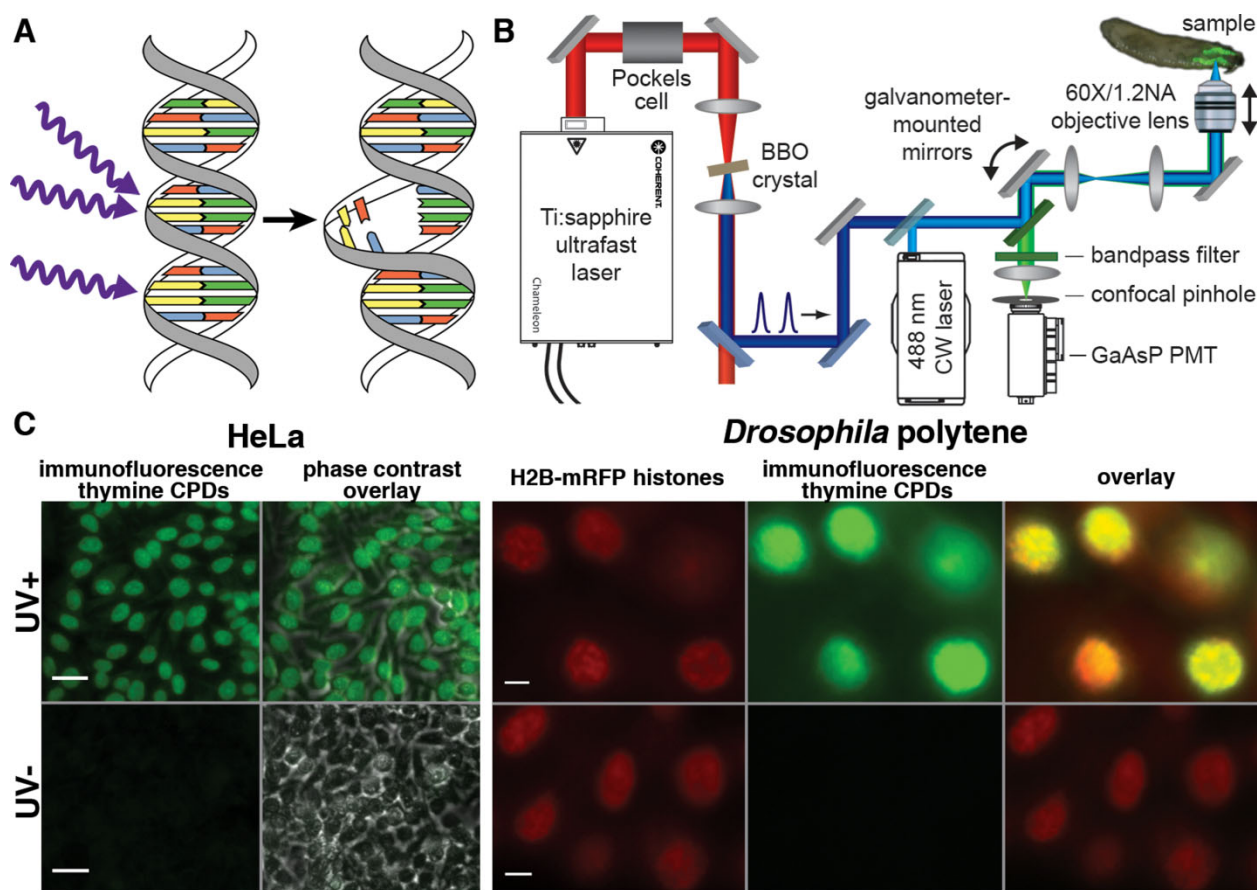
Figure 6.1: Scheme of apparatus to image and perform DIMED on cells with verification of immunochemical CPD assay. (A) Simultaneous absorption of two blue photons by DNA leads to the production of a thymine CPD. Interaction with a single blue photon does not affect the DNA. (B) Schematic of the apparatus used to irradiate and image cells. The near-IR output of a femtosecond Ti:sapphire laser is attenuated by a Pockels cell/polarizer and then frequency doubled by a β-barium borate (BBO) crystal. Dichroic mirrors remove the fundamental before the beam, focused by a 60X 1.2NA water-immersion objective lens, is scanned through the sample. A 488nm CW laser can be introduced into the setup to perform control experiments. (C) Verification of thymine CPD detection using an immunochemical assay. Samples were irradiated with 1.6 kJ/m^2 (UV+, HeLa), 6.6 kJ/m^2 (UV+, Drosophila) or no (UV-) 254 nm UV radiation. After staining for thymine CPDs, the UV+ cells showed immunofluorescence that was at least an order of magnitude brighter than the control group and showed nuclear localization. Additionally, the *Drosophila* fluorescence shows chromosomal localization as indicated in the overlay with the H2B-mRFP image. HeLa scale bar is 40 μm and *Drosophila* scale bar is 20 μm.

apoptosis in some cases[19-22] or require long pixel dwell times which can be difficult to implement on conventional confocal laser scanning microscopes. Therefore, the use of ultrashort <u>visible</u> pulses, which is relatively harmless to cells, provides an alternative method to near IR wavelengths for generating three-dimensionally localized CPDs in cells with microsecond scan times and powers commonly used for multiphoton microscopy.

6.2. Materials and Methods

6.2.1. HeLa cell culture

HeLa cells were cultured in Dulbecco's modified Eagle's medium (Sigma) supplemented with antibiotics and 10% fetal bovine serum (Gibco) at 37 $^{\circ}$C and 5% CO_2. For DNA damage experiments, cells were seeded on glass bottom culture dishes (MatTek Corporation Ashland, MA) at a density of 3 x 10^5 cells per dish approximately 18 hours before the experiment. Immediately before irradiation, the growth medium was removed and cells were washed and immersed in PBS.

6.2.2. Drosophila strains and procedures

Three *Drosophila melanogaster* lines were used. The transgenic line that expresses the histone 2B-mRFP fusion protein under the control of a *Gal4* upstream activation sequence was described in Zobeck *et al.*[23]; the protein was expressed in salivary gland cells by generating a homozygous cross with the c147 *Gal4* driver line. The endogenous eGFP-tagged TopI fusion line was obtained from the FlyTrap stocks (line CC01414).[24] The w[1118] line and the c147 *Gal4* line were obtained from the Bloomington Stock Center. Larva were raised at room temperature, collected at the third-instar stage 8-9 days after eggs were laid, and dissected in Grace's Insect Medium

(Gibco). Salivary glands were transferred to MatTek glass-bottomed culture dish in PBS for irradiation.

6.2.3. UV irradiation setup

UV DNA damage was generated with a Spectroline Crosslinker containing low-pressure mercury vapor lamps (λ_{max} = 254 nm). HeLa cells were irradiated in PBS to receive a dosage of approximately 1.6 kJ/m^2. *Drosophila* salivary glands were iradiated in PBS to receive an approximate dosage of 6.6 kJ/m^2.

6.2.4. Laser apparatus for producing DNA photolesions

In order to investigate multiphoton absorption-induced photolesion formation, HeLa cell monolayers or *Drosophila* salivary glands were irradiated by focused near-IR or visible ultrashort pulses using the apparatus diagrammed in Figure 6.1B. Our setup used tunable near-infrared, femtosecond pulses produced at 80 MHz by a Coherent Chameleon Ultra II Ti:sapphire oscillator. An electro-optic modulator and polarizer placed directly after the laser controlled the intensity used for each experiment. The near-IR pulse duration was 200 fs at 750 nm, as determined by a background-free autocorrelator placed just after the modulator/polarizer. As indicated, most experiments used pulses at the second harmonic of the Ti:sapphire output wavelength, which were generated by focusing the beam into a 2 mm path length β-barium borate crystal cut for type-I phase matching. The residual near-infrared light was rejected with a contrast ratio of at least 100:1 by reflecting the visible beam off of two dichroic mirrors before introducing it into a home-built laser-scanning microscope. The duration of the visible pulses before entering the microscope was 210 fs at 425 nm, which was determined by background-free cross-correlation with the near-IR pulses. The pulses are further

broadened by lenses in the laser-scanner and the objective lens; we did not measure the pulse duration after the objective, but we estimate that the 425 nm pulse duration is approximately 450 fs at the sample (details of this calculation are provided in Appendix D). For experiments that use the near-IR pulses directly, we estimate the 750 nm pulse duration is 275 fs at the sample.

The laser-scanning setup was based on an Olympus IX81 inverted microscope with a dedicated laser port. External galvanometer-mounted mirrors and relay lenses determined the angle with which the laser beam enters a 60X, 1.20 NA water-immersion objective lens. All experiments used a 0.05 µm/µs scan rate and a 0.1 µm pixel size, resulting in a single-pixel dwell time of 2 µs per frame. Most experiments generated damage by scanning a selected region multiple times; for each experiment, we report the total pixel dwell time, which is the product of the number of passes and 2 µs. The back aperture of the lens was slightly overfilled to maintain a tight focus. The irradiation power was measured after the objective using a calibrated power meter. For damaging DNA in salivary gland cells, the mRFP-histones were excited by the same laser at a greatly reduced power (< 1 mW) and the resulting epifluorescence was detected by a GaAsP photomultiplier tube in a confocal setup. Using Labview-based software developed in-house, a region of the chromosome was selected for multiple passes of a higher power laser beam. For HeLa cell monolayers, phase contrast microscopy was used to locate and focus the cells before high power laser irradiation. To perform control experiments that involved continuous-wave irradiation, a Coherent 488 nm Sapphire laser beam was introduced into the same setup by a dichroic mirror, as indicated in Figure 6.1B.

6.2.5. Multiphoton microscopy

Cells were imaged by multiphoton microscopy using the aforementioned laser-scanning microscope, except without frequency-doubling the Ti:sapphire laser output. Epifluorescence was detected by a non-descanned GaAsP photomultiplier tube.

6.2.6. Immunocytochemistry

After irradiation, cells or glands were fixed in methanol for 15 min at -20 ^{o}C, washed thrice with PBT (PBS, 0.1% (v/v) Triton-X-100), and then blocked in PBT with 1% (w/v) BSA for 1 h. Samples were incubated in mouse monoclonal anti-CPD antibody (Kamiya Biomedical, Seattle, WA) solution in PBT, 1% BSA overnight at 4 ^{o}C. After washing, immunofluorescence was accomplished with Alexa Fluor 488 conjugated to goat anti-mouse IgG (Invitrogen) in PBT, 1% BSA for 2 h at room temperature. After washing, glands were imaged in PBT using the two-photon microscopy setup described above. Alexa Fluor 488 fluorescence was excited by two-photon absorption of 900 nm and detected by a 535/60 bandpass filter. Likewise, mRFP fluorescence was excited by two-photon absorption of 1000 nm and detected by a 630/100 bandpass filter. HeLa cells were imaged by phase contrast microscopy and wide-field immunofluorescence (470/40 excitation filter and 525/50 emission filter), both using a 20x objective.

6.2.7. Quantification of fluorescence images

Fluorescence images were processed using MATLAB (MathWorks, Natick, MA) software (see Appendix E for the code). For HeLa cells, damaged nuclei were distinguished from the background by creating a mask from images that had been smoothed by a lowpass Gaussian filter. The unfiltered immunofluorescence intensity within each masked nucleus was averaged and the nonspecific background staining

subtracted to generate a data set. Error bars are the standard deviation between different data sets. At least three (n ≥ 3) different data sets are averaged for each power or wavelength.   Each data set contains between 20 and 40 nuclei. Immunofluorescence in polytene cells was quantified by averaging the pixels above the nonspecific background threshold inside a damaged region. The average value of the nonspecific background was then subtracted from the immunofluorescence intensity. TopI-GFP recruitment or bleaching in polytene cells were processed in a similar way, except that masks of the irradiated and unirradiated regions of each nucleus were generated from a projection of the maximum pixel intensity for all times. The same masks were then applied to each image to determine the fluorescence intensity at each time for a given nucleus. The plotted data are the average and standard deviation of intensities from three polytene nuclei, taken from different glands.

6.3. Results

6.3.1. Immunocyctochemistry selectively stains thymine-thymine CPDs

We determined the amount of DNA damage in cells using an immunofluorescence-based assay with a CPD-specific antibody.[25,26] To validate this method, HeLa cell monolayers were irradiated by UV light (Mercury vapor, 254 nm) at an approximate dosage of 1.6 kJ/m^2. *Drosophila* salivary glands dissected from a fly line that expresses mRFP tagged H2B histones[23] were irradiated at an approximate UV dosage of 6.6 kJ/m^2. The cells and glands were each fixed, incubated with the anti-CPD antibody and visualized after staining with an Alexa Fluor 488-labeled secondary antibody (Figure 6.1C).   In comparison with phase-contrast images, the immunofluorescence of the HeLa cells is uniformly distributed within cell nuclei. In the

140

salivary glands, the brightest regions of immunofluorescence colocalize with the mRFP fluorescent protein, which mark the polytene chromosomes in cell nuclei. In both organisms, immunofluorescence in the UV exposed samples was more than 10 times brighter than the control. The immunofluorescence intensity increases linearly with UV dosage (Figure D.1 in the Appendix).

6.3.2. Use of high intensity IR pulses results in physical damage

Previous reports demonstrate that UV-like lesions, including thymine CPDs, result from multiphoton absorption of near-IR femtosecond pulses.[12,17,18] However, we found that irradiation of unstained HeLa cells or polytene cells with near-IR pulses at intensities necessary to produce CPDs also disrupted their physical structure. Figure 6.2 presents HeLa cells and a salivary gland that had been irradiated with focused 750 nm femtosecond pulses at an average power of 80 mW, which is approximately the minimal power that allowed for the detectable creation of CPDs with near-IR pulses (Figure D.2 in the Appendix). Similar irradiation conditions were required to produce DNA damage in previous studies.[12] Unfortunately, irradiated HeLa cells are either destroyed or exhibit pronounced morphological changes in the phase contrast images. Likewise, irradiation of salivary glands results in the appearance of localized structures that may be due to the formation of cavitation bubbles. These results are not particularly surprising since several groups have performed laser-based cellular nanosurgery and ablation using nearly identical irradiation conditions.[19-22] Previous studies that generated DNA photolesions with near-IR pulses have limited irradiation to subnuclear regions in cultured cells, which either prevented or masked this type of unwanted cellular damage. However, it becomes difficult to avoid when studying
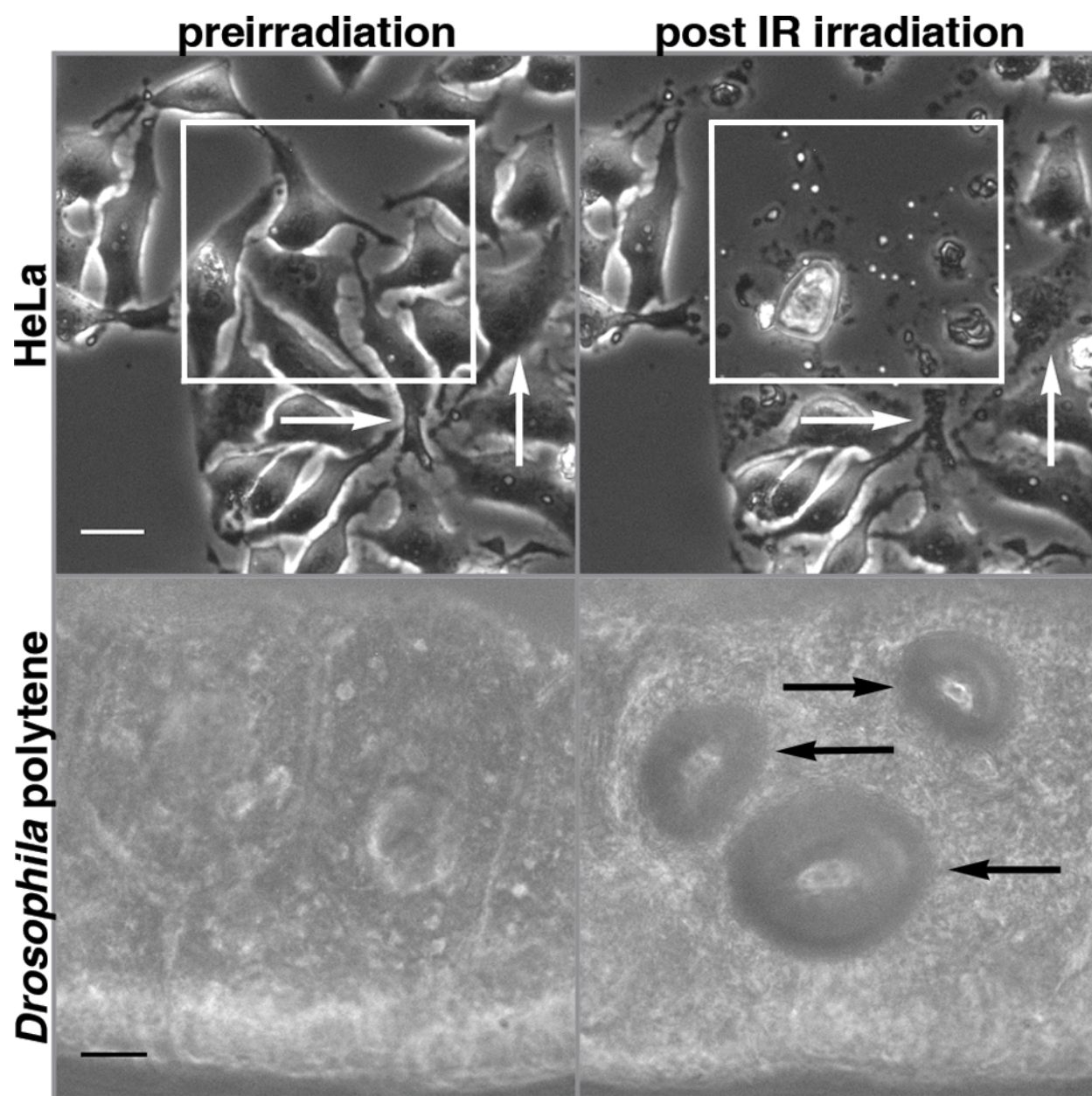
Figure 6.2: Irradiation with high intensity IR pulses at 750 nm and 80 mW, which is approximately the minimal power required to induce thymine CPDs with near-IR light, results in the unintended damage of cells. As shown by phase contrast microscopy, the HeLa cells in the area irradiated by the IR beam (indicated by a white box) are obliterated, leaving behind only portions of the cell that can be stained for CPDs. Portions of cells that had been partially irradiated (white arrows) survive but also show damage. Likewise, *Drosophila* salivary gland cells exhibit pronounced morphological changes (black arrows) as a result of irradiation with the IR pulses. Scale bars are 30 μm.

optically thick tissue samples, such as salivary glands containing polytene nuclei. The introduction of unwanted cellular damage is not desirable for imaging DNA repair dynamics in live cells, so there is a clear need to develop an alternative method to create localized lesions that does not significantly disrupt other cellular processes.

6.3.3. Femtosecond visible pulses induce localized thymine CPD formation in HeLa cells

Our previous *in vitro* study[16] indicated that the two-photon absorption cross-section of DNA is largest at 425 nm, so we started at this wavelength to investigate DIMED-Vis *in vivo*. Visible femtosecond pulses generated by frequency-doubling the near-IR output of a Ti:sapphire oscillator were focused into a monolayer of unstained HeLa cells by a 60X, 1.2NA objective lens. The beam (80 MHz repetition rate, 14 mW average power after the objective) was raster scanned over a square region of cells, resulting in a total pixel (~0.1 μm^2) dwell time of 20 μs. Cells were then fixed, stained for CPD production and imaged using widefield fluorescence microscopy (Figure 6.3A). The immunofluorescence clearly demonstrates DNA damage in the nuclei of cells within the square region that had been irradiated by visible femtosecond pulses. Cells outside of the irradiated region exhibit only background fluorescence equivalent to the amount of nonspecific staining of unirradiated samples from the UV control. It is notable that cells at the boundary of the irradiated region show a sharp intranuclear boundary between the damaged and undamaged regions. Importantly, the phase contrast image shows no physical malformations of the irradiated HeLa cells, in contrast to irradiation with near IR pulses. To demonstrate that DNA damage is caused by multiphoton absorption and exclude the possible involvement of endogenous sensitizers, we compared irradiation of HeLa cells with a beam of ultrashort visible pulses to irradiation

143

with a continuous-wave (CW) beam at the same wavelength and power (Figure 6.3B). The thymine CPDs were only produced when using pulsed sources of light, demonstrating that the high peak intensities of femtosecond pulses are necessary to generate CPDs.

6.3.4. Thymine CPDs are axially localized

We also investigated the generation of CPDs via DIMED-Vis in polytene cells. To locate cell nuclei, salivary glands that express histone H2B-mRFP fusion proteins were imaged using confocal microscopy, excited by the 425 nm beam of femtoseond pulses at a reduced power (< 1 mW). Selected regions of cells were then irradiated by the same beam at a higher power to generate DNA damage (10 mW average power and a 10 µs total pixel dwell time). The glands were subsequently fixed and stained for CPD production. The immunofluorescence and mRFP were imaged using standard two-photon microscopy (Figure 6.3C). The applied laser light bleaches the mRFP, marking the location of high-power laser irradiation. The immunofluorescence colocalizes with the mRFP bleach, establishing that CPDs had been created in the region irradiated by the high-power beam of 425 nm femtosecond pulses. Only a thin axial region (2.5 µm FWHM) contained the CPDs (Figure 6.3D), implying that the damage was due to multiphoton absorption. The intensity used to ensure a strong staining probably saturated the multiphoton absorption, resulting in a thicker axial section than would be expected based on the theoretical diffraction-limited point spread function of the objective lens. Note that the orientation of the gland when the immunofluorescence was imaged differed slightly from its orientation when the damage
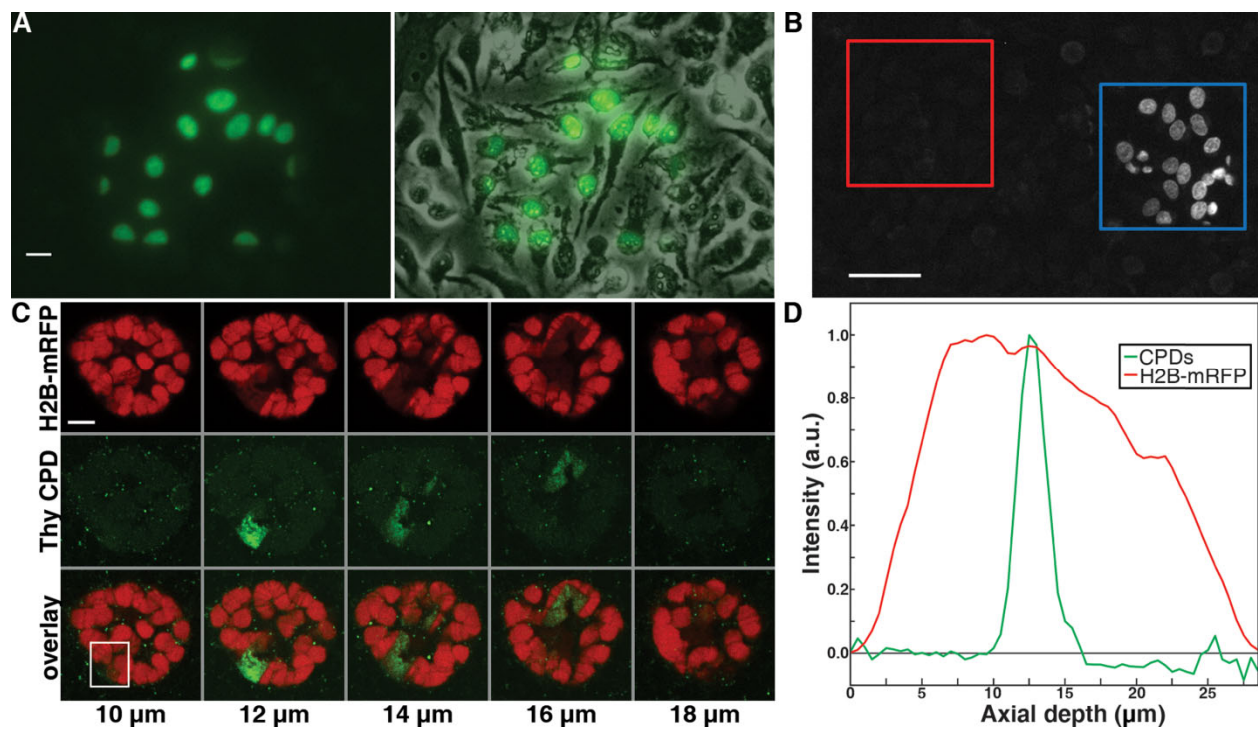
Figure 6.3: Production of CPDs using 425 nm femtosecond pulses. (A) HeLa cells were irradiated by femtosecond pulses in a square region that included intra-and extra-nuclear regions, then stained for CPDs and imaged with wide field epifluorescence (top). Only cells inside the irradiation region show immunofluorescence, even though there are cells outside of this region. Furthermore, the immunofluorescence is confined to nuclear regions only although the entire cell was irradiated. The overlay on the phase contrast image (bottom) demonstrates that CPDs are laterally confined, even in nuclei of cells that were only partially irradiated. Scale bar is 20 μm. (B) The generation of thymine CPDs due to visible laser light is due to a nonlinear process; therefore, the required photon flux (GW/cm^2) can only be achieved with a pulsed laser. HeLa cells were irradiated with light at 488 nm and 13 mW average intensity from a 150 fs pulsed (blue box) and continuous wave (red box) laser source, each focused by the same 60X 1.2NA objective lens. Only the pulsed laser source created thymine CPDs further indicating that the production of thymine CPDs with visible light is a nonlinear process. The bounding boxes are slightly larger than the irradiated region to prevent obscuring of the epifluorescence. Scale bar is 16 μm. (C) Selected slices from a z-series of a *Drosophila* polytene nucleus that had been irradiated by femtosecond pulses in a rectangular region before staining. The CPDs are axially confined to a much smaller region than the depth of the nucleus. The orientation of the gland when it was imaged after the CPD staining procedure is different from when it was damaged; therefore, the damage and bleach shifts across the gland through the z-series. For panel (D), the CPD immunofluorescence is quantified in the white box, and the mRFP fluorescence is quantified for the entire cell. Scale bar is 5 μm. The contrast of images was uniformly enhanced to assist in viewing. (*d*) Plot of the intensity of the mRFP labeled H2B histone (red line) and immunofluorescence labeling of CPDs (green line) as a function of the axial depth of the sample. The nucleus is approximately spherical 20 μm (FWHM) in diameter. The region of the production of photolesions is confined to an approximately 2.5 μm (FWHM) thick region of the chromosome.

was generated, resulting in CPDs that are localized on opposite sides of the nucleus in subsequent optical sections. Chromosomes outside of the region irradiated with the high power beam exhibit the same amount of immunofluorescence and mRFP fluorescence as those in unirradiated glands. This observation confirms that the lower power used for confocal imaging does not generate damage, as would be expected for a nonlinear intensity dependence. Finally, since it is possible that the presence of a fluorescent histone protein fusion could sensitize DNA to photodamage, we confirmed that the same amount of CPDs are created in the nuclei of salivary glands that do not express a fluorescent marker (Figure D.3 in the Appendix).

6.3.5. Thymine CPDs are produced with 400-525 nm femtosecond pulses

To determine the ideal wavelength for CPD production, HeLa cells were irradiated with various wavelengths of visible pulses, ranging from 400-525 nm at 25 nm intervals, and subsequently assayed for the amount of CPDs produced. The same power and pixel dwell time were used at each wavelength within a particular data set. CPDs were created at each wavelength tested, though there is a clear maximum at 400 nm and a general trend of decreasing efficiency with wavelength (Figure 6.4A). The large multiphoton absorption cross section difference between 400 and 425 nm is somewhat surprising since the UV absorption spectrum is quite broad, but the similar cross sections from 425-475 nm agree with our previous *in vitro* findings.[16] It should be noted that the lower efficiency at longer wavelengths can easily be overcome by using higher powers. The ability to create CPDs over a broad range of wavelengths allows for the tailoring of a damage method according to the fluorophore being used in a given
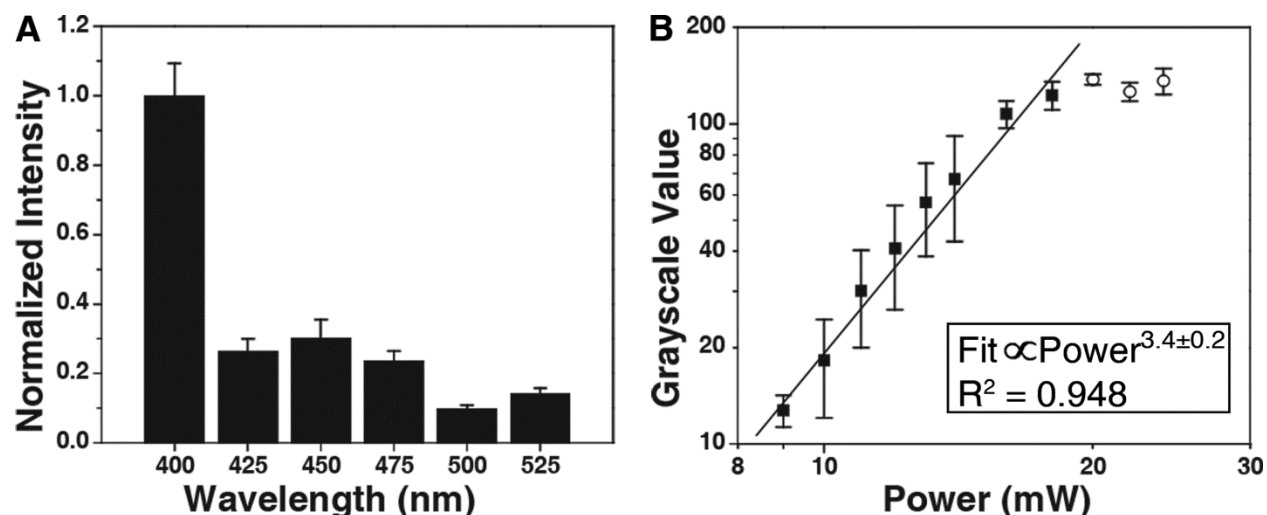
Figure 6.4: Characterization of the photophysical parameters that lead to the production of CPDs. (A) The production of CPDs were quantified in HeLa cells using various irradiation wavelengths from 400-525 nm in 25 nm intervals. Error bars are standard deviation between the average intensity of cells in three different irradiation regions. (B) HeLa cells were irradiated at 425 nm from 6-24 mW and data are plotted on a log scale. Data points at 6, 7, and 8 mW were below threshold of detection and are not plotted. Filled square points are included in the regression. Unfilled circle points are excluded due to saturation. The fit scales with the irradiation power raised to the 3.4±0.2 power with a coefficient of determination of 0.948. Error bars are standard deviations between the average intensity of cells in three different irradiation regions (n=3).

study: the damaging wavelength can be chosen to minimize or maximize fluorophore bleaching depending on the experiment.

6.3.6. Power dependence of thymine CPD production

We examined the intensity dependence of CPD production by irradiating HeLa cells with 425 nm femtosecond pulses at various powers, ranging from 6 to 24 mW (Figure 6.4B). Based on the strong 200-300 nm UV absorption of DNA that leads to CPD production and our previous *in vitro* results, we expected that the amount of damage would scale with the square of the applied laser power, indicating a photochemical mechanism involving two-photon absorption. Somewhat surprisingly, we found that the data is fit best by a super-cubic (3.4 ± 0.2) function of incident power, implicating higher order nonlinearities. The 425 nm light was tested because it allowed for a relatively large range of powers to be tested, but similar results were obtained at 400 nm (3.0 ± 0.5) and 500 nm (3.5 ± 0.2).

6.3.7. Recruitment of topoisomerase I to DNA photolesions in polytene cells

To assess the utility of DIMED-Vis for investigating the dynamics of protein recruitment to spatially localized CPDs, we studied the localization of TopI in polytene cells following irradiation with visible femtosecond pulses. TopI is an enzyme that changes the topology of DNA by introducing a transient break in one strand of its backbone, through which the other strand can pass. TopI activity has previously been implicated in transcription, replication and repair;[27] it is essential for the viability of multicellular organisms, including Drosophila.[28] Using multiphoton microscopy, we imaged the localization of TopI-GFP fusion proteins in polytene cells from a GFP protein trap fly line.[24] Prior to DNA damage induction, TopI-GFP is localized within the nucleus

and exhibits well-defined banding along polytene chromosomes, as well as diffuse localization between bands and within the nucleoplasm.[23] Irradiation of approximately one quarter of the nucleus in a single axial plane with intense 425 nm femtosecond pulses (10 mW, 10 µs total pixel dwell time) completely bleaches the GFP fluorescence within the selected region. Fluorescent TopI-GFP subsequently diffuses into the selected region, starting from its intranuclear boundaries and reaching an equilibrium fluorescence distribution within 3-4 min (Figure 6.5A). Fluorescence of TopI-GFP outside the selected region decreases on the same timescale to a final intensity that is significantly less than the final intensity within the selected region (Figure 6.5B). This intensity difference likely arises from the preferential accumulation of TopI-GFP at DNA damaged by multiphoton absorption of visible pulses, in agreement with previous studies that observed TopI recruitment to the site of DNA photolesions.[29,30] This interpretation is also supported by a post-damage z-series that shows the TopI-GFP is axially localized to the irradiated region, similar to the axial profile of CPDs (Figure D.4 in the Appendix). To test our interpretation that TopI-GFP preferentially localizes to damaged DNA, we irradiated nuclei with a 488 nm CW laser, which bleaches GFP but does not damage DNA. As expected, the bleached and unbleached regions recover to the same final intensity (Figure 6.5B). Interestingly, the TopI-GFP banding pattern after DNA damage with visible femtosecond pulses largely antilocalizes with the banding pattern prior to damage. In contrast, cells irradiated by the continuous wave laser exhibit the same banding pattern before and after bleaching (Figure 6.5C). These observations are consistent with a model in which TopI associates with DNA transiently
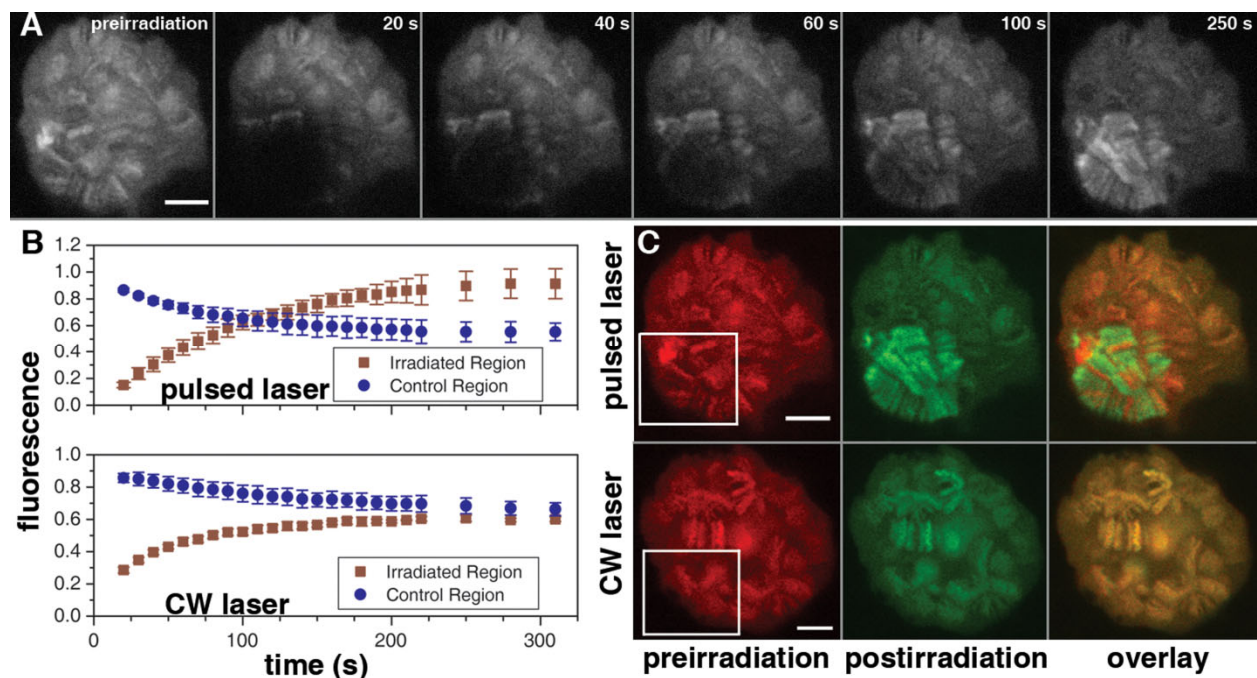
Figure 6.5: Localization of TopI to DNA photolesions. (A) DNA in a *Drosophila* polytene cell that expresses a TopI–GFP fusion protein was damaged using DIMED-Vis by irradiating the lower left quadrant of a single nuclear plane with 425 nm femtosecond pulses. The irradiation also bleaches the GFP fluorescence in the damaged region. Multiphoton microscopy images recorded as a function of time after irradiation reveal that fluorescent TopI-GFP preferentially accumulates in the damaged region, beginning with the intranuclear edges and subsequently populating the entire region. (B) The integrated fluorescence intensity in the damaged region (top, maroon squares) recovers to a value close to its initial intensity, while the integrated fluorescence in the unirradiated region decreases below this value (top, blue circles). By contrast, the fluorescence in nuclei irradiated by a 488 nm CW laser under similar conditions, which bleaches GFP but does not generate DNA damage, recovers to the same value in the irradiated and unirradiated regions (bottom plot). Plots are normalized to the preirradiation intensity. Error bars are the standard deviation between three different cell nuclei (n=3). (C) For the cell damaged in panel a, the preirradiation TopI-GFP fluorescence distribution (top, red) within the irradiated region (white box) antilocalizes with the TopI-GFP fluorescence distribution in the postirradiation (after 250 s) fluorescence (top, green) image. In contrast, a cell irradiated by the CW laser exhibits the same TopI-GFP fluorescence distribution in the pre- and post-irradiated images (bottom panels). All scale bars are 5 μm. The contrast of images was uniformly enhanced to assist in viewing.

151

in the absence of damage, but localizes to damaged sites more stably, as discussed below.

6.4. Discussion

For the study of DNA repair protein dynamics, it is desirable to produce spatially localized damage sites to observe the mechanism by which repair proteins locate damage sites. The direct multiphoton absorption of DNA creates spatially confined photolesions ideal for the observation of the recruitment of repair proteins to the damage site. In this report, we have damaged large regions of the chromosome for the purpose of quantifying and observing immunofluorescence, but it would be straightforward to create damage only in a diffraction limited spot, approximately 200 x 200 x 500 nm.

Previous attempts on producing DNA damage via multiphoton absorption have focused on near-IR pulses, which require millisecond pixel dwell times,[18] very intense pulses, or chemical sensitizers.[12] Our current setup configuration was optimized for microsecond (rather than millisecond) dwell times, which is typical for multiphoton and confocal microscopes. However, we did determine that the conditions required to create DNA damage using high intensity IR pulses also resulted in other unwanted damage to the cells when large scan regions were used (Figure 6.2). We note that the large regions irradiated in this study created more severe damage than if a smaller region were chosen, but even localized, intranuclear near-IR irradiation that preserves the cell's macrostructure likely causes unwanted disturbances. Our results are consistent with earlier reports that similar irradiation conditions can dissect chromosomes[22], induce strand breaks[12,18] and invoke cell death[21]. Thus, DIMED with

near-IR pulses is undesirable for the study of protein dynamics in thick tissues where multiple cells are damaged. Furthermore, the chemical sensitization of DNA, while allowing for the usage of nonlethal irradiation intensities, can adversely affect the DNA repair pathway under study and preferentially results in non-UV type lesions. By using 25-44 ms pixel dwell times, as presented in the reports by Meldrum et al.[17] and Trautlein et al.[18], the powers needed to generate DNA photolesions may be below the threshold for unintended cellular damage. However, even scanning a small area (~10x10 pixels) requires several seconds, thus reducing the time resolution to measure the protein response, and such long pixel dwell times can be difficult to implement on some laser-scanning microscopes.

The method characterized in this chapter, DIMED-Vis, allows for the production of axially localized CPD type photolesions in thick tissues without physical damage to the cell, providing a useful alternative to previously reported methods of creating damage. Additionally, it is relatively easy to implement, by modifying an existing two-photon microscopy setup with the addition of a frequency doubling β-barium borate (BBO) crystal. We have shown that DIMED-Vis works on two very different cell types. It is especially powerful when paired with the polytene nucleus of *Drosophila* larva salivary gland, since the large chromosomes of the polytene nucleus allow regions of DNA to be distinguished from nucleoplasm. However, the large nuclei present the need for axial confinement, which our method addresses. The successful use of DIMED on cells containing polytene chromosomes and diffuse chromatin and with or without transgenic fluorescent markers indicates its flexibility. The observed wavelength dependence was somewhat unexpected; in particular, it is unclear why CPDs are

produced more efficiently with 400 nm pulses than with the other observed wavelengths since such sharp transitions are not observed in the UV absorption spectrum of DNA. At the measured wavelengths of 400, 425 and 500 nm, the production of CPDs all scaled with an approximate cubic power dependence. Therefore, it can be reasonably concluded that the same transition is being excited at each wavelength. However, it is important to note that CPDs can be efficiently produced at all wavelengths tested, thereby granting the flexibility to choose a damaging wavelength that is most appropriate considering other parts of the experiment, such as minimizing fluorophore photobleaching.

We expect DIMED to produce UV-type lesions which is why we tested for thymine-thymine CPDs, the primary UV photoproduct. Several observations point toward the direct multiphoton absorbance of DNA as the source of photolesion formation, indicating that the photoreactions should be UV-like. The applied visible pulses are off-resonant for DNA linear absorption; the linear absorption of the nitrogen bases is strongest between 200-300 nm and is completely transparent in the range from 400-525 nm. Therefore, the damage is due either to the multiphoton absorption of DNA or through the sensitization of damage by other fluorophores (e.g. mRFP). However, as shown in HeLa cells and polytene cells devoid of fluorophores, we can induce CPDs in cells without fluorescent proteins. This evidence excludes mRFP as a possible sensitizing agent. Furthermore, when using a continuous wave laser at the same wavelength and time averaged power as a pulsed laser, the thymine CPDs are not produced. The production of the photolesions using blue light, therefore, requires the high peak intensities provided by an ultrashort pulsed laser, indicative of nonlinear

154

excitation of DNA and excluding linearly absorbing sensitizing agents (Figure 6.3B). Finally, the power series is nonlinear, indicating a multiphoton process (Figure 6.4B). Although the cubic power dependence was unexpected, others[18] have shown higher order nonlinearities in the formation of thymine CPD using IR pulses. Therefore, the observed DNA damage is likely due to multiphoton excitation of DNA. We cannot be certain the damage is not mediated by multiphoton absorption of a secondary species, such as histones, but we believe this interaction is unlikely because such a mechanism would preferentially create strand breaks with few, if any, CPD photoproducts. Other types of UV photolesions are also likely produced by DIMED-Vis, such as 6-4 photoproducts. We do not expect to form a large quantity of double strand breaks, as these are not typically produced by UV exposure; however, near-IR ultrafast irradiation has resulted in the production of double strand breaks. In the future, we plan to measure the distribution of lesions to determine how DIMED-Vis compares to other published methods of DNA damage induction.

We have demonstrated one application of DIMED-Vis by measuring the time-resolved localization of TopI-GFP to a region of damaged DNA in polytene cells. After inducing DNA photodamage, TopI-GFP accumulates within the irradiated region of the nucleus and is depleted in the unirradiated region (Figure 6.5), indicating TopI is recruited to damaged DNA (CPDs and other potential types of damage). This observation strengthens earlier suggestions[27] that TopI is involved in DNA damage repair. However, the application of DIMED-Vis in polytene cells offers much more information about the spatiotemporal dynamics of TopI than is available using other methods. After localized damage, the fluorescent protein is confined within a 2 μm axial

155

plane (Figure D.4 in the Appendix) and exhibits antilocalized banding compared to the preirradiated image. Presumably, the TopI-GFP that had been in the irradiated region prior to damage associates stably with the newly damaged DNA, but is no longer visible since the GFP is bleached. The TopI-GFP that had been in the unirradiated region thus fills in chromosomal regions that contained a lower density of TopI-GFP prior to damage, resulting in the observed antilocalization. In contrast when TopI-GFP is only bleached without creating photolesions by using a 488 nm CW laser, antilocalization is not observed since the equilibrium distribution of DNA-associated TopI-GFP is constantly exchanging. We also observe that the TopI-GFP initially exhibits a preferential localization to chromosomes near the boundary between the damaged and undamaged regions following damage, leaving region farther from this boundary that remains depleted for more than a minute. This behavior is not observed in nuclei bleached by a CW laser, which recover fluorescence more uniformly (Figure D.5 in the Appendix), and is another consequence of the accumulation of TopI-GFP at damaged DNA. Finally, we note that optical resolution limits prevent us from unambiguously proving that TopI is recruited to damaged DNA on a molecular length scale. For example, it is also possible that DIMED-Vis changes the nuclear matrix in a way that causes TopI to be immobilized on chromosomes; however, we consider this unlikely since the morphology of H2B-mRFP is unchanged by irradiation. We are continuing to investigate the spatiotemporal localization of TopI-GFP and will present a more detailed analysis in a future publication.

6.5. Conclusion

We have developed a method, DIMED-Vis, for creating localized DNA photolesions ideal for the study of DNA repair. We showed that photolesions could be created by laser irradiation between 400-525 nm in both HeLa cells and the polytene chromosomes of the *Drosophila*. The creation of thymine CPDs was confirmed through the use of an immunocytochemistry assay. As an example of the application of DIMED-Vis, we showed the recruitment of TopI to DNA photolesions demonstrating the utility for this technique to resolve spatiotemporal dynamics of DNA repair.

REFERENCES

1. Gorner, H. Photochemistry of DNA and related biomolecules: quantum yields and consequences of photoionization. *J. Photochem. Photobiol. B, Biol.* **1994**, *26*, 117-139.

2. Wang, S. Y., Ed.; In *Photochemistry and Photobiology of Nucleic Acids;* Academic Press: New York, 1976; .

3. Essers, J.; Vermeulen, W.; Houtsmuller, A. B. DNA damage repair: anytime, anywhere? *Curr. Opin. Cell Biol.* **2006**, *18*, 240-246.

4. Cremer, C.; Cremer, T.; Fukuda, M.; Nakanishi, K. Detection of laser-UV microirradiation-induced DNA photolesions by immunofluorescent staining. *Hum. Genet.* **1980**, *54*, 107-110.

5. Mone, M. J.; Volker, M.; Nikaido, O.; Mullenders, L. H. F.; Zeeland, A. A. v.; Verschure, P. J.; Manders, E. M. M.; Driel, R. v. Local UV-induced DNA damage in cell nuclei results in local transcription inhibition. *EMBO Rep.* **2001**, *2*, 1013-1017.

6. Mone, M. J.; Bernas, T.; Dinant, C.; Goedvree, F. A.; Manders, E. M. M.; Volker, M.; Houtsmuller, A. B.; Hoeijmakers, J. H. J.; Vermeulen, W.; Driel, R. v. *In vivo*dynamics of chromatin-associated complex formation in mammalian nucleotide excision repair. *P. Natl. Acad. Sci. USA* **2004**, *101*, 15933-15937.

7. Katsumi, S.; Kobayashi, N.; Imoto, K.; Nakagawa, A.; Yamashina, Y.; Muramatsu, T.; Shirai, T.; Miyagawa, S.; Sugiura, S.; Hanaoka, F.; Matsunaga, T.; Nikaido, O.; Mori, T. *In situ*visualization of ultraviolet-light-induced DNA damage repair in locally irradiated human fibroblasts. *J. Invest. Dermatol.* **2001**, *117*, 1156-1161.

8. Imoto, K.; Kobayashi, N.; Katsumi, S.; Nishiwaki, Y.; Iwamoto, T.; Yamamoto, A.; Yamashina, Y.; Shirai, T.; Miyagawa, S.; Dohi, Y.; Sugiura, S.; Mori, T. The total amount of DNA damage determines ultraviolet-radiation-induced cytotoxicity after uniform or localized irradiation of human cells. *J. Invest. Dermatol.* **2002**, *119*, 1177-1182.

9. Limoli, C. L.; Ward, J. F. A new method for introducing double-strand breaks into cellular DNA. *Radiat. Res* **1993**, *134*, 160-169.

10. Lukas, C.; Falck, J.; Bartkova, J.; Bartek, J.; Lukas, J. Distinct spatiotemporal dynamics of mammalian checkpoint regulators induced by DNA damage. *Nat. Cell Biol.* **2003**, *5*, 255-260.

11. Kruhlak, M. J.; Celeste, A.; Dellaire, G.; Fernandez-Capetillo, O.; Muller, W. G.; McNally, J. G.; Bazett-Jones, D. P.; Nussenzweig, A. Changes in chromatin

structure and mobility in living cells at sites of DNA double-strand breaks. *J. Cell Biol.* **2006***, 172*, 823-834.

12. Dinant, C.; Jager, M. d.; Essers, J.; Cappellen, W. A. v.; Kanaar, R.; Houtsmuller, A. B.; Vermeulen, W. Activation of multiple DNA repair pathways by sub-nuclear damage induction methods. *J. Cell Sci.* **2007***, 120*, 2731-2740.

13. Lakowicz, J. R., Ed.; In *Nonlinear and two-photon-induced fluorescence;* Topics in Fluorescence Spectroscopy; Kluwer Academic Publishers: New York, 1997; Vol. 5.

14. Denk, W.; Strickler, J. H.; Webb, W. W. Two-photon laser scanning fluorescence microscopy. *Science* **1990***, 248*, 73-76.

15. Zipfel, W. R.; Williams, R. M.; Webb, W. W. Nonlinear magic: Multiphoton microscopy in the biosciences. *Nat. Biotechnol.* **2003***, 21*, 1369-1377.

16. Tycon, M. A.; Chakraborty, A.; Fecko, C. J. Generation of DNA photolesions by two-photon absorption of a frequency-doubled Ti:sapphire laser. *J. Photochem. Photobiol. B, Biol.* **2011***, 102*, 161-168.

17. Meldrum, R. A.; Botchway, S. W.; Wharton, C. W.; Hirst, G. J. Nanoscale spatial induction of ultraviolet photoproducts in cellular DNA by three-photon near-infrared absorption. *EMBO Rep.* **2003***, 4*, 1144-1149.

18. Trautlein, D.; Deibler, M.; Leitenstorfer, A.; Ferrando-May, E. Specific local induction of DNA strand breaks by infrared multi-photon absorption. *Nucleic Acids Res.* **2010***, 38*, e14.

19. Kuetemeyer, K.; Rezgui, R.; Lubatschowski, H.; Heisterkamp, A. Influence of laser parameters and staining on femtosecond laser-based intracellular nanosurgery. *Biomed. Opt. Express* **2010***, 1*, 587-597.

20. Supatto, W.; Debarre, D.; Moulia, B.; Brouzes, E.; Martin, J.; Farge, E.; Beaurepaire, E. *In vivo* modulation of morphogenetic movements in *Drosophila* embryos with femtosecond laser pulses. *P. Natl. Acad. Sci. USA* **2005***, 102*, 1047-1052.

21. Tirlapur, U. K.; Konig, K.; Peuckert, C.; Krieg, R.; Halbhuber, K. Femtosecond near-infrared laser pulses elicit generation of reactive oxygen species in mammalian cells leading to apoptosis-like death. *Exp. Cell Res.* **2001***, 263*, 88-97.

22. Konig, K.; Riemann, I.; Fritzsche, W. Nanodissection of human chromosomes with near-infrared femtosecond laser pulses. *Opt. Lett.* **2001***, 26*, 819-821.

23. Zobeck, K. L.; Buckley, M. S.; Zipfel, W. R.; Lis, J. T. Recruitment Timing and Dynamics of Transcription Factors at the Hsp70 Loci in Living Cells. *Mol. Cell* **2010***, 40*, 965-975.

24. Buszczak, M.; Paterno, S.; Lighthouse, D.; Bachman, J.; Planck, J.; Owen, S.; Skora, A. D.; Nystul, T. G.; Ohlstein, B.; Allen, A.; Wilhelm, J. E.; Murphy, T. D.; Levis, R. W.; Matunis, E.; Srivali, N.; Hoskins, R. A.; Spradling, A. C. The Carnegie Protein Trap Library: A Versatile Tool for Drosophila Developmental Studies. *Genetics* **2007**, *175*, 1505-1531.

25. Rubbi, C. P.; Milner, J. p53 is a chromatin accessibility factor for nucleotide excision repair of DNA damage. *EMBO J.* **2003**, *22*, 975-986.

26. Katiyar, S. K.; Matsui, M. S.; Mukhtar, H. Kinetics of UV Light–induced Cyclobutane Pyrimidine Dimers in Human Skin In Vivo: An Immunohistochemical Analysis of both Epidermis and Dermis. *Photochem. Photobiol.* **2000**, *72*, 788-793.

27. Leppard, J. B.; Champoux, J. J. Human DNA topoisomerase I: relaxation, roles, and damage control. *Chromosoma* **2005**, *114*, 75-85.

28. Lee, M. P.; Brown, S. D.; Chen, A.; Hsieh, T. S. DNA topoisomerase I is essential in *Drosophila melanogaster*. *P. Natl. Acad. Sci. USA* **1993**, *90*, 6656-6660.

29. Mao, Y.; Muller, M. T. Down modulation of topoisomerase I affects DNA repair efficiency. *DNA Repair* **2003**, *2*, 1115-1126.

30. Mielke, C.; Kalfalah, F. M.; Christensen, M. O.; Boege, F. Rapid and prolonged stalling of human DNA topoisomerase I in UVA-irradiated genomic areas. *DNA Repair* **2007**, *6*, 1757-1763.

APPENDICES

APPENDIX A: SUPPORTING INFORMATION FOR CHAPTER 2

A.1. FRAP procedure details: Intermittent data collection scheme

When moved over long distances, the galvanometer positions ring for as long as 300 μs. Therefore, the laser power was turned off after image collection and the galvanometers were moved to focus on a point 1.0 μm away from the region of interest for 700 μs. The galvanometers were then moved the short distance to the region of interest, the laser was adjusted to the observation power, and pre-bleach data points were recorded for 200 μs, beginning cycle I in Figure 2.1. The laser power was increased to the bleach power for 20 μs and returned to the observation power. The next 400 μs were recorded at the observation power and then the laser was switched off for 600 μs concluding cycle I. From 1 - 10 ms at 1 ms intervals, the laser was turned on for 200 μs periods of data collectection (cycles II and III). From 20 - 50 ms at 10 ms intervals, the laser was turned on for 100 μs periods of data collectection (cycle IV). This long time data collection was primarily to distinguish anomalous diffusion and check for an immobile fraction. Observation powers were selected to achieve a signal of between 0.1 to 0.3 volts and ranged between 10 to 14 mW at the sample. Bleach powers were selected to achieve post-bleach fluorescence signals between 50-70% of the pre-bleach signal; bleach powers ranged from 35 to 60 mW at the sample.

A.2. Effect of reversible photobleaching on point FRAP measurements

Two unexpected experimental observations using previous point FRAP methods led us to consider the impact of reversible photobleaching on point FRAP measurements: (1) the time-dependent fluorescence recovery after photobleaching

dilute solutions of free GFP was best fit by an anomalous diffusion model, and (2) immobilized GFP samples exhibited a apparent FRAP recovery. Careful examination of the bleach and control data for immobilized samples led us to hypothesize that the apparent recovery can be attributed to differences in the photobleaching kinetics between these two experiments. Motivated by single-molecule experiments that have observed nearly all fluorophores exhibit emission intermittency (i.e. "blinking"),[1] we decided to consider the impact of reversible photobleaching on point FRAP signals.

A.2.1. Reversible photobleaching kinetics

Reversible bleaching can be incorporated by considering a photophysical model in which fluorophores (*Fl*) can be converted to either a reversibly bleached (RB) or an irreversibly bleached (*IB*) state:

$$RB \underset{k_{-1}}{\overset{k_1}{\rightleftharpoons}} Fl \overset{k_2}{\rightarrow} IB$$

(A.1)

Rate constants for processes driven by photon absorption (k_1 and k_2, and likely k_{-1}) depend on the intensity of incident light. To influence experimental results, the reversible bleaching kinetics must be more rapid or occur on a timescale similar to irreversible bleaching; numerous single-molecule studies indicate that the reversible kinetics typically occur faster than irreversible bleaching. We assume that division of the signal from the bleached sample by the signal from the unbleached control sample properly accounts for irreversible observational photobleaching, so this kinetic process can be neglected. We are thus concerned only with the impact of the reversible photobleaching kinetics:

$$RB \underset{k_{-1}}{\overset{k_1}{\rightleftharpoons}} Fl$$

(A.2)

The influence of interconversion on the FRAP signal is determined by two coupled reaction-diffusion equations:[2, 3]

$$\frac{\partial c_{Fl}(\vec{r},t)}{\partial t} = D\nabla^2 c_{Fl}(\vec{r},t) - k_1 c_{Fl}(\vec{r},t) + k_{-1} c_{RB}(\vec{r},t) \tag{A.3a}$$

$$\frac{\partial c_{RB}(\vec{r},t)}{\partial t} = D\nabla^2 c_{RB}(\vec{r},t) - k_{-1} c_{RB}(\vec{r},t) + k_1 c_{Fl}(\vec{r},t) \tag{A.3b}$$

where $c_{Fl}(\vec{r},t)$ and $c_{RB}(\vec{r},t)$ are the concentrations of Fl and RB at the point $\vec{r}$ in space and t in time, and the diffusion coefficient D of both species is the same. Solutions to these equations can be determined most easily in the Fourier domain:

$$\frac{\partial c_{Fl}(\vec{q},t)}{\partial t} = -q^2 D c_{Fl}(\vec{q},t) - k_1 c_{Fl}(\vec{q},t) + k_{-1} c_{RB}(\vec{q},t) \tag{A.4a}$$

$$\frac{\partial c_{RB}(\vec{q},t)}{\partial t} = -q^2 D c_{RB}(\vec{q},t) - k_{-1} c_{RB}(\vec{q},t) + k_1 c_{Fl}(\vec{q},t) \tag{A.4b}$$

where $c_{Fl}(\vec{q},t) = (2\pi)^{-3/2} \int c_{Fl}(\vec{r},t) exp(i\vec{q}\cdot\vec{r}) d^3\vec{r}$. Recast in matrix notation, Eq. A.4 becomes:

$$\frac{\partial c_j(\vec{q},t)}{\partial t} = \sum_{l=1}^{2} M_{jl} c_l(\vec{q},t) \tag{A.5}$$

where:

$$M_{jl} = \begin{pmatrix} -q^2 D - k_1 & k_{-1} \\ k_1 & -q^2 D - k_{-1} \end{pmatrix} \tag{A.6}$$

Thus, the time-dependent concentrations in the Fourier domain can be determined from the initial concentrations using the eigenvalues, $\lambda^{(s)}$, and eivenvectors, $X^{(s)}$, of the matrix M:

$$c_j(\vec{q},t) = \sum_{s=1}^{2} X_j^{(s)} exp(\lambda^{(s)}t) \sum_{l=1}^{2} (X^{-1})_l^{(s)} c_l(\vec{q},0) \tag{A.7}$$

where X^{-1} is the inverse of the eigenvector matrix. The eigenvalues and eigenvectors for the matrix M in Eq. 2.6 are:

$$\lambda = \begin{pmatrix} -q^2 D & \\ -q^2 D - k_1 - k_{-1} & \end{pmatrix} \tag{A.8}$$

$$X = \begin{pmatrix} k_{-1}/k_1 & -1 \\ 1 & 1 \end{pmatrix} \tag{A.9}$$

Since only the fluorescent species is detected in a FRAP experiment, we are primarily concerned with the quantity $c_{Fl}(\vec{q}, t)$. We first consider the time-dependence of this quantity for a system that is initially at equilibrium by defining the equilibrium concentration of species Fl as $c_{Fl}(\vec{q}, 0) \equiv c_{Fl,eq}$ and of species RB by $c_{RB}(\vec{q}, 0) \equiv c_{RB,eq}$ and noting that $k_1 c_{Fl,eq} = k_{-1} c_{RB,eq}$. These initial conditions applied to Eqs. A.7, A.8 and A.9 yields $c_{Fl}(\vec{q}, t) = c_{Fl,eq} exp(-q^2 Dt)$. Substitution of this solution into the Fourier expression for a point FRAP experiment (*vide infra*) yields the standard expression for a point FRAP signal derived by Brown *et. al.* (Eq. 2.4 in Chapter 2). Therefore, the presence of a reversibly bleached fluorophore state that constantly maintains equilibrium with its unbleached state has no impact on a FRAP experiment.

We now consider a system in which the initial concentrations differ from their equilibrium values by a small amount: $c_{Fl}(\vec{q}, 0) \equiv c_{Fl,eq} + \delta$ and $c_{RB}(\vec{q}, 0) \equiv c_{RB,eq} - \delta$. These initial conditions applied to Eqs. A.7, A.8 and A.9 yields

$$c_{Fl}(\vec{q}, t) = c_{Fl,eq} exp(-q^2 Dt) + \delta exp(-q^2 Dt - (k_1 + k_{-1})t) \tag{A.10}$$

$$= c_{Fl,eq} exp(-q^2 Dt)[1 + \delta exp(-t/\tau_{PP})]$$

where $\tau_{PP} = (k_1 + k_{-1})^{-1}$ is the characteristic equilibrium relaxation time.

A.2.2. Point FRAP signal

The fluorescence signal detected from a sample of fluorescent species Fl that is excited by two-photon absorption of a pulsed laser, but measured using detectors whose response time is much longer than the pulse repetition time is given by the convolution:

$$f(t) = Q_{Fl} \int \langle I(x,y,z) \rangle^2 c_{Fl}(x,y,z,t) dx\,dy\,dz \tag{A.11}$$

where $\langle I(x,y,z) \rangle$ is the spatially-varying excitation beam intensity averaged over many pulse cycles and Q_F accounts for various constants (temporal coherence factor of the excitation source, fluorescence quantum yield, photon collection efficiency, etc.) In a FRAP experiment, the concentration of fluorescent species is altered at t=0 by the bleaching pulse, denoted by $\Delta c_{Fl}(x,y,z,t=0)$ and the recovery is:

$$\Delta f(t) = Q_{Fl} \int \langle I(x,y,z) \rangle^2 \Delta c_{Fl}(x,y,z,t) dx\,dy\,dz \tag{A.12}$$

In a standard FRAP model, $\Delta c_{Fl}(x,y,z,t=0)$ is entirely due to irreversible bleaching that results from photon absorption, but our model also allows for absorption-induced changes in the concentration of Fl and RB from their equilibrium values. In both cases, the change in the concentration of Fl and RB depends on the amount of light absorbed via two-photon excitation using the bleaching beam:

$$\Delta c_{Fl}(x,y,z,t=0) = c_{Fl,eq}(1+\delta) exp[-\beta \langle I(x,y,z) \rangle^2] \tag{A.13}$$

where β is the bleaching depth parameter that depends on the absorption cross section, the time-average excitation intensity at the center of the focal spot and bleach pulse duration. We assume that the spatial beam profile has a Gaussian form and expand this function in a Taylor series for further calculations:

$$\Delta c_{Fl}(x,y,z,t=0) = c_{Fl,eq}(1+\delta) exp\left[-\beta exp\left[-\frac{4(x^2+y^2)}{w_{xy}^2} - \frac{4z^2}{w_z^2}\right]\right] \tag{A.14a}$$

$$= c_{Fl,eq}(1+\delta) \sum_{n=0}^{\infty} \frac{(-\beta)^n}{n!} exp\left[-\frac{4n(x^2+y^2)}{w_{xy}^2} - \frac{4nz^2}{w_z^2}\right] \tag{A.14b}$$

The time-dependent concentration of fluorophore *Fl* is given by the solution of the coupled reaction diffusion equations (Eq. 2.3). To apply the solution derived in the Fourier domain, we must also express the initial conditions by transforming Eq. A.14b:

$$\Delta c_{Fl}(q_x, q_y, q_z, t = 0)$$

$$= c_{Fl,eq}(1 + \delta) \sum_{n=0}^{\infty} \frac{(-\beta)^n}{n!} (2\pi)^{-\frac{3}{2}}$$

$$\times \int \int \int exp\left[-\frac{4n(x^2+y^2)}{w_{xy}^2} - \frac{4nz^2}{w_z^2}\right] e^{-iq_x x - iq_y y - iq_z z} dx\,dy\,dz \qquad (A.15a)$$

$$= c_{Fl,eq}(1 + \delta) \sum_{n=0}^{\infty} \frac{(-\beta)^n}{n!} \left[\frac{w_{xy}^2 w_z}{8(2n)^{3/2}}\right] exp\left[-\frac{w_{xy}^2(q_x^2+q_y^2)}{16n} - \frac{w_z^2 q_z^2}{16n}\right] \qquad (A.15b)$$

This initial condition may be propagated in time according to Eq. A.7, which is equivalent to Eq. A.10 in the reversible bleaching model:

$$\Delta c_{Fl}(q_x, q_y, q_z, t) = c_{Fl,eq} exp\left(-(q_x^2 + q_y^2 + q_z^2)Dt\right)\left[1 + \delta exp\left(-\frac{t}{\tau_{PP}}\right)\right]$$

$$\times \sum_{n=0}^{\infty} \frac{(-\beta)^n}{n!} \left[\frac{w_{xy}^2 w_z}{8(2n)^{3/2}}\right] exp\left[-\frac{w_{xy}^2(q_x^2+q_y^2)}{16n} - \frac{w_z^2 q_z^2}{16n}\right] (A.16)$$

To derive the final expression for the point FRAP signal, Eq. A.16 is convolved with the point spread function of the detection beam (expressed the Fourier domain) according to Eq. A.12, yielding:

$$F(t) = F_0[1 + \delta exp(-t/\tau_{PP})] \sum_{n=0}^{\infty} \frac{(-\beta)^n}{n!} \left[1 + n\left(1 + \frac{16Dt}{w_{xy}^2}\right)\right]^{-1} \left[1 + n\left(1 + \frac{16Dt}{w_z^2}\right)\right]^{-1/2} \quad (A.17)$$

Thus, the result of this lengthy calculation is an expression for the point FRAP signal including reversible bleaching differs from that of the standard expression (without considering reversible bleaching) only by the multiplicative factor $[1 + \delta exp(-t/\tau_{PP})]$. This factor accounts for the relaxation of the initial concentrations of *Fl* and *RB* to equilibrium. If these species remain at equilibrium throughout the experiment, $\delta = 0$

and the FRAP signal is unaffected by the presence of the reversible bleached form, in agreement with the discussion following Eq. A.9.

One subtle point regarding the equilibrium of FI and RB is that the amounts of these species present in solution may depend on the intensity of incident light, since their interconversion is driven by photon absorption. Thus, the equilibrium constant in the absence of an excitation light source may differ from its value when irradiated by the observation or bleaching intensity. In this case, the relative amounts of FI and RB at the outset of the FRAP experiment would not be at the irradiated equilibrium value, leading to a nonzero value of δ. Alternatively, it is possible that k_1 and k_{-1} share the same excitation intensity dependence, leading to an intensity-independent equilibrium constant, but that the initial FRAP condition is still not at equilibrium because the absence of a sufficient excitation source prior to the experiment has not yet allowed the system to reach equilibrium. In either case, the FRAP signal would contain contributions from reversible bleaching. Importantly, the time dependence of these contributions would differ in the bleaching signal and control signal, since the relaxation rate depends on the inverse sum of the intensity-dependent rate constants. As described in the text, we believe this relaxation is the source of the unexpected observations that motivated this section (the apparent anomalous diffusion of free GFP and apparent FRAP recovery of immobilized samples). Since k_1 and k_{-1} have a vanishingly small value without laser illumination (compare Figure 2.3 panels D & G and E & H), the τ_{PP} time constant in the photophysics correction term only depends on the amount of time that the sample has been illuminated by the laser for our experiments. Therefore, we modified eq. A.17 to reflect this dependence as:

$$F(t) = F_0[1 + \delta exp(-t_{laser}/\tau_{PP})] \sum_{n=0}^{\infty} \frac{(-\beta)^n}{n!} \left[1 + n\left(1 + \frac{16Dt}{w_{xy}^2}\right)\right]^{-1} \left[1 + n\left(1 + \frac{16Dt}{w_z^2}\right)\right]^{-1/2} \quad (A.18)$$

This is Eq. 2.6 in Chapter 2.

A.3. Explanation of weighting for fitting

Since our point FRAP method collects data at equally spaced time intervals during intermittent time blocks, rather than using logarithmically spaced time bins, we fit data using weighting factors that are equivalent to fitting logarithmically spaced time bins. This requires two weighting factors: one to account for gaps in the data collection, and a second to account for data points spaced linearly rather than logarithmically in time.

To account for gaps in the data the residuals from each cycle were multiplied by a value, or weight, to account for the number of data points that should have been measured over that range. The weight values are summarized in table S1 below. The weight values were determined by assigning each data collection cycle to a range of times. The weight is equal to the number of points collected in a cycle divided by the time of the cycle. The weight then acts as if the data were taken equally spaced in that time interval.

Table A.1: Weighting values to account for intermittent data collection blocks

Cycle (Figure 2.1)	Time range after bleach (µs)	Time per cycle (µs)	Number of data points collected	Weight applied to residuals
I	1 – 400	400	400	1
II	501 – 1500, …, 8501 – 9500	1000	200	5
III	9501 – 15000	5500	100	55
IV	15001 – 25000, …, 45001 – 55000	10000	100	100

We now determine the multiplicative weighting factor needed to convert data collected at points equally spaced in time to points spaced logarithmically in time. Consider an expression for j data bins spaced logarithmically in time using scaling constants of *c* and *c0*:

$$t_j = 10^{c \cdot j + c_0} \qquad (A.19)$$

As the value of *j* increases, the bins become more widely spaced in time. Thus, if data is collected at equally spaced intervals in time and then placed into logarithmically spaced bins, the number of data points per bin becomes larger with time. Instead of binning the data, we weight each point by the fraction of a bin it would occupy by calculating the number of bins per unit time:

$$\frac{dj}{dt} = \frac{d}{dt}\left(\frac{\log_{10}(t) - c_0}{c}\right) = \frac{1}{t \cdot c \ln(10)} \qquad (A.20)$$

Thus, weighting the residuals of data points that are equally spaced in time by 1/time is equivalent to placing them into bins spaced logarithmically in time. (The constants are unimportant since only relatively weighting matters.) This 1/time weighting factor was multiplied by the weights listed in Table A.1 to apply logarithmical time binning to point FRAP data collected at equally spaced time intervals during intermittent time blocks.

A.4. Accounting for the ringing of the preamplifier

During the bleach pulse we drove our preamplifier into saturation. The readings of the preamplifier were restored to an acceptable value ~10 μs after the bleach pulse was finished. However, the signal still displayed an anomaly that we referred to as ringing due to its cyclic wave appearance. This ringing "dampened out" usually between 50 – 70 μs after the bleach pulse. Therefore, we begin fitting after the ringing stops to prevent the fit from being influenced by the ringing structure. Each plot was

examined for ringing by hand to determine the starting point for fitting. Figure A.2 shows the first 400 μs after the bleach pulse for a sample of GFP in PBS. The fit for this sample was started at 50 μs (dashed line) after the ringing was dampened.

However, by removing the first several points after the bleach we lost information on the bleach depth. The bleach depth was important for distinguishing between the anomalous and Brownian diffusion models. In Figure A.3, a Brownian FRAP curve was simulated for a diffusion coefficient of 25 $\mu m^2 s^{-1}$ and fitted with an anomalous model with different values of alpha starting the fit 50 μs after the bleach (dashed line). As shown in the Figure A.3 insert, it was difficult to distinguish between Brownian and anomalous diffusion from 50 μs onward. However, one key feature that did distinguish the curves was the bleach depth. If we included the earliest time points, the bleach depth would be restricted by the data; however, the structure of this data was influenced by the preamplifier ringing. Although the structure of the data was incorrect, the magnitude of the data was correct. Therefore, by averaging to remove the ringing we gained an approximation of the bleach depth. In the fits, we restricted the bleach depth to be ± 10% of the average of the points from 15 – 25 μs. The solid line box in Figure A.2 contained the points that were averaged for this data set. The height of the box showed the ± 10% window that was used to constrain the bleach depth. As observed on Figure A.3 the fit tended to be level for physically relevant values of alpha. Therefore, by estimating the bleach depth in this way we did not introduce bias into our fits and furthermore we recovered some of the information lost by removing the earlier time points due to ringing.

A.5. Confidence intervals on the fits of alpha

Table A.2: 95% Confidence Intervals for alpha values

| Sample | Average Alpha Value | 95% Confidence Interval | | Propagation of Uncertainty |
		Minimum Value	Maximum Value	
GFP in PBS*	0.95	0.033	0.105	0.040
GFP in 60% Glycerol	0.95	0.028	0.041	0.020
Alexa Fluor 488 in PBS*	0.96	0.024	0.113	0.043
GFP in HeLa – Nucleus	0.84	0.016	0.034	0.016
GFP in HeLa – Cytoplasm	0.76	0.016	0.030	0.014
GFP in Polytene – Chromosome	0.79	0.042	0.055	0.034
GFP in Polytene – Interchromatin space*	1.00	0.061	0.116	0.050
GFP in Polytene – Cytoplasm	0.56	0.061	0.072	0.047

Confidence intervals were calculated for each parameter in each fit at the 95% level using the *nlparci* routine in MatLab. The 95% confidence intervals for the values of alpha are listed in Table A.2 above. These values were calculated with alpha being allowed to float. For the three models noted with an asterisk (*), the BIC test indicated that the anomalous parameter did not produce a statistically better fit; however, the anomalous parameter did not necessarily converge to 1.0. The alpha values listed here are the ones given by the anomalous model regardless if the BIC indicated that it was the best fit. Three separate data sets were fit for each sample and listed in the table are the minimum and maximum confidence interval given on a particular replicate for a sample. The propagation of uncertainty gives the 95% confidence interval for the average alpha value between the replicates. It was calculated by

171

$$\Delta\bar{x} = \frac{\sqrt{\Delta x_1^2 + \Delta x_2^2 + \Delta x_3^2}}{3} \qquad (A.21)$$

where $\Delta\bar{x}$ and Δx_n is the uncertainty of the mean and the nth replicate respectively.
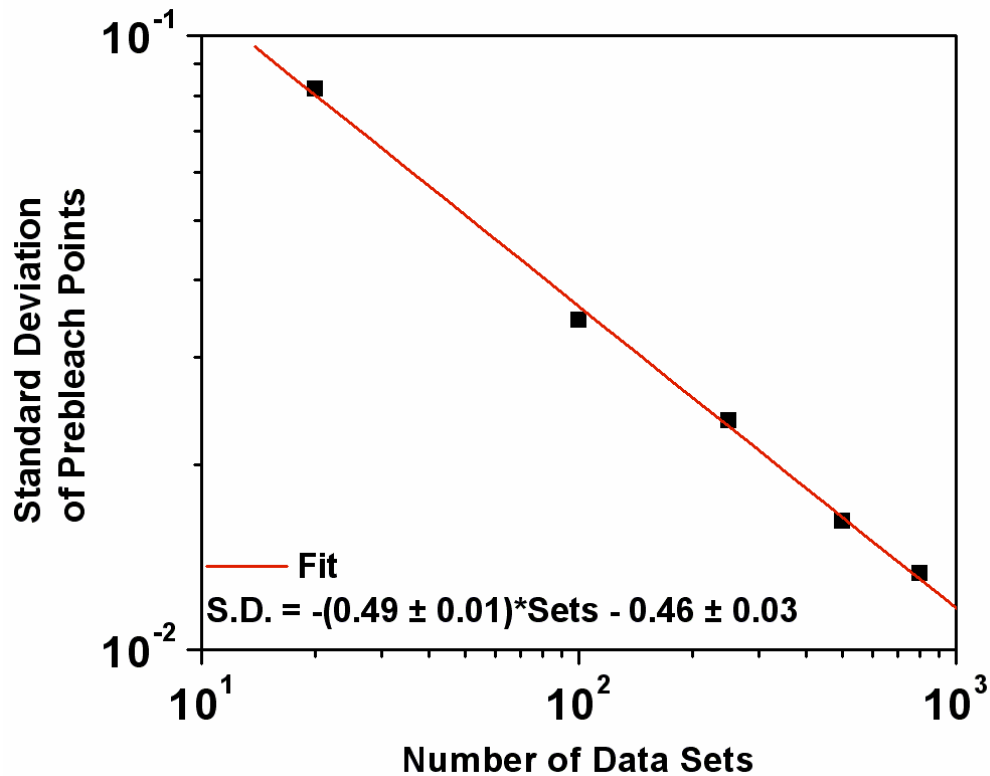
Figure A.1: Quantifying decrease in noise vs. number of data sets. In order to determine a reasonable number of point FRAP data sets to average to create a replicate for fitting; we measured the decrease in noise as the number of data sets increased. We quantified the noise as the standard deviation of the pre-bleach data points. Since the noise present should obey Poisson statistics, the noise should decrease as a square root of the number of data sets. Plotting the noise verse the number of data sets on a log-log plot resulted in a slope of -0.49 indicating that the noise does in fact decrease by the square root of the number of data sets. We decided on the number of data sets to average per replicate to be 500. Five hundred data sets offered a low level of noise while still being reasonable for data collection and processing. The correlation coefficient of the fit was -0.99892.
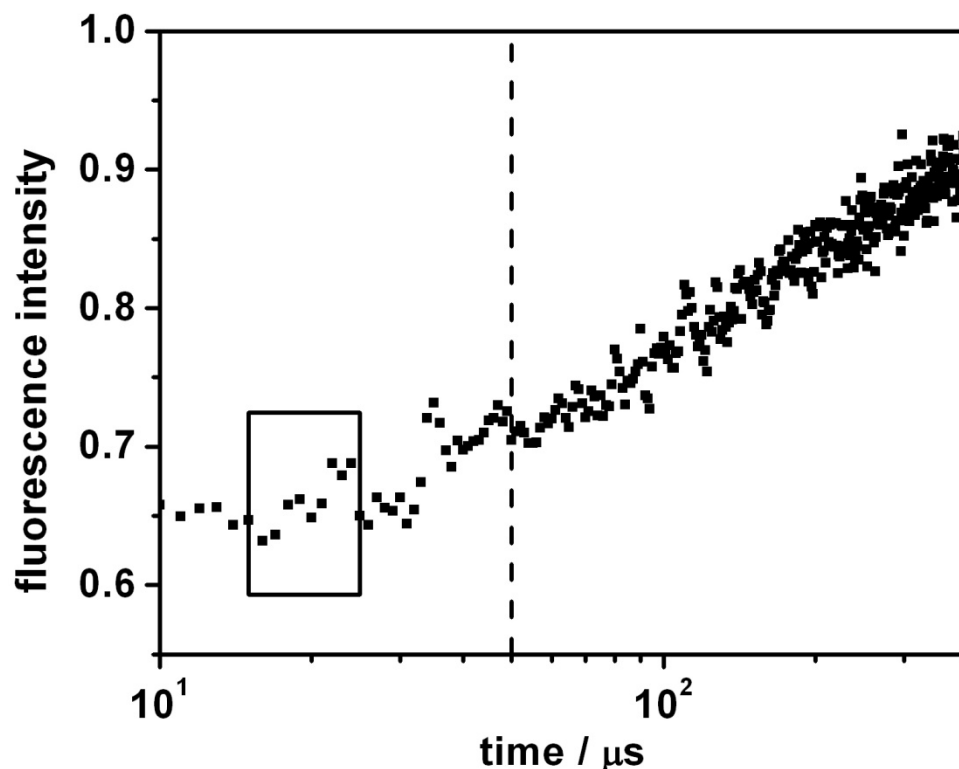
Figure A.2: Ringing in the preamplifier. Due to driving the preamplifier into saturation during bleaching, a brief phenomenon that we referred to as "ringing" occurred for ~50 µs after bleach until it "dampened out." In the sample above of GFP in PBS, the ringing stopped at 50 µs after the bleach (dotted line). The solid line box contains the points (15 – 25 µs) that were averaged to approximate the bleach depth. The height of the box indicates ± 10% of average of these points which was the range used to restrict the bleach depth for GFP samples. Although the structure of the data was incorrect over the ringing range, we justified the use of the magnitude to predict the bleach depth by examining fixed samples. In fixed samples the ringing occurred, but the average intensity during the ringing and after the ringing was dampened out was the same.
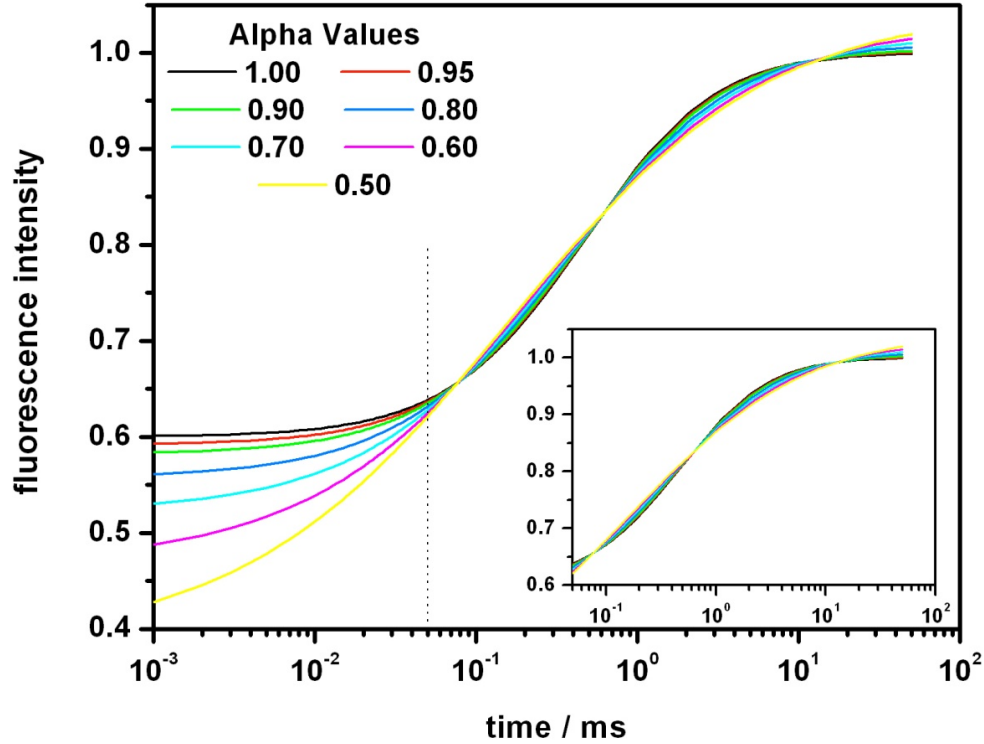
Figure A.3: Simulations of the importance of bleach depth to distinguishing between anomalous and normal diffusion. A normal diffusion curve (D = 25 $\mu m^2 s^{-1}$; α = 1) was simulated using Eq. 2.4 from chapter 2 (black line). This curve was fit with an anomalous model with different values of alpha using Eq. 2.4 starting the fit 50 μs after the bleach (dashed line). Insert is the same data plotted after 50 μs demonstrating that it is difficult to distinguish between normal and anomalous diffusion based on the fitted data alone. One feature that did distinguish the curves was the bleach depth; therefore, by restricting the bleach depth to physically relevant values, we could help ensure that the fits were physically realistic.
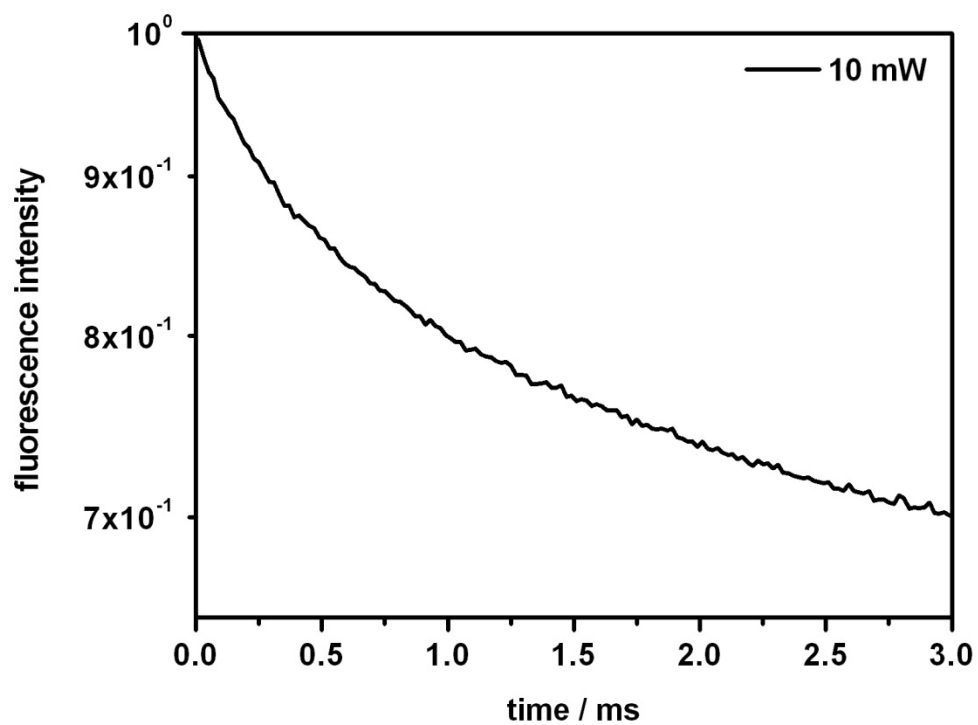
Figure A.4: Non-exponential nature of GFP photophysics. GFP immobilized in polyacrylamide gel was continuously irradiated with 10 mW of power. The fluorescence intensity is plotted on a semi-log scale revealing the non-exponential nature of the bleaching kinetics.
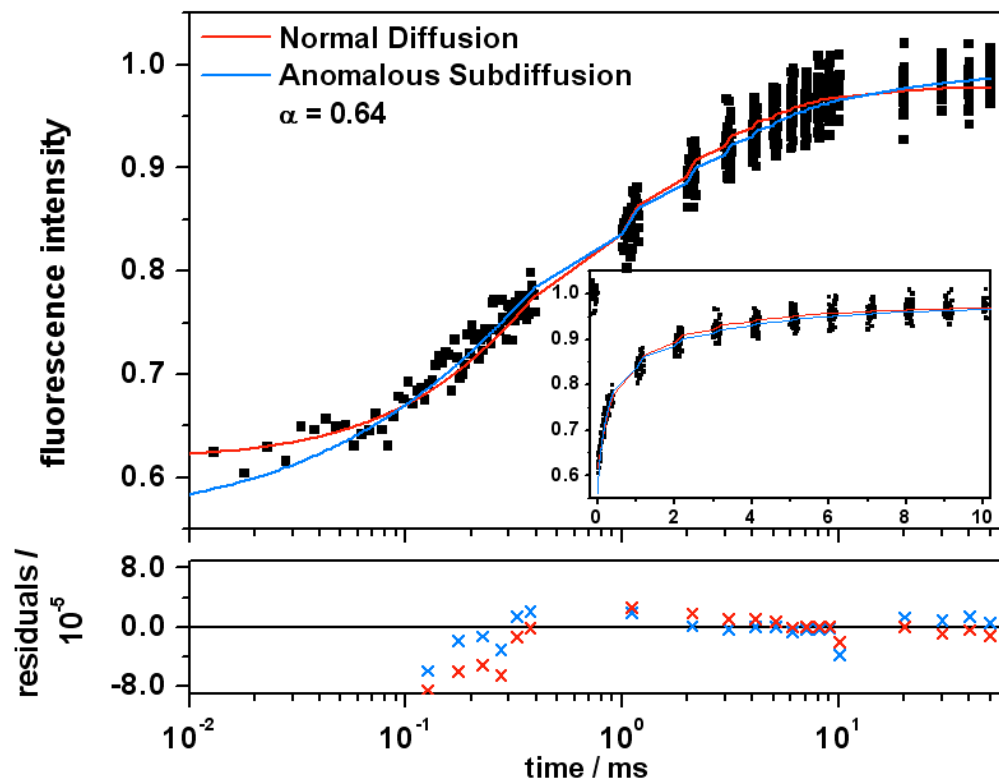
Figure A.5: FRAP curve of GFP in polytene cytoplasm. The GFP in the cytoplasm was isolated due to exclusion from the vacuoles. These isolated pockets of GFP (Figure 2.6 B in chapter 2) may have been the source of the large average anomalous factor of 0.54 ± 0.11 observed in this sample (see Table 2.2). Additionally, the anomalous factor varied more from replicate to replicate than the other GFP samples.
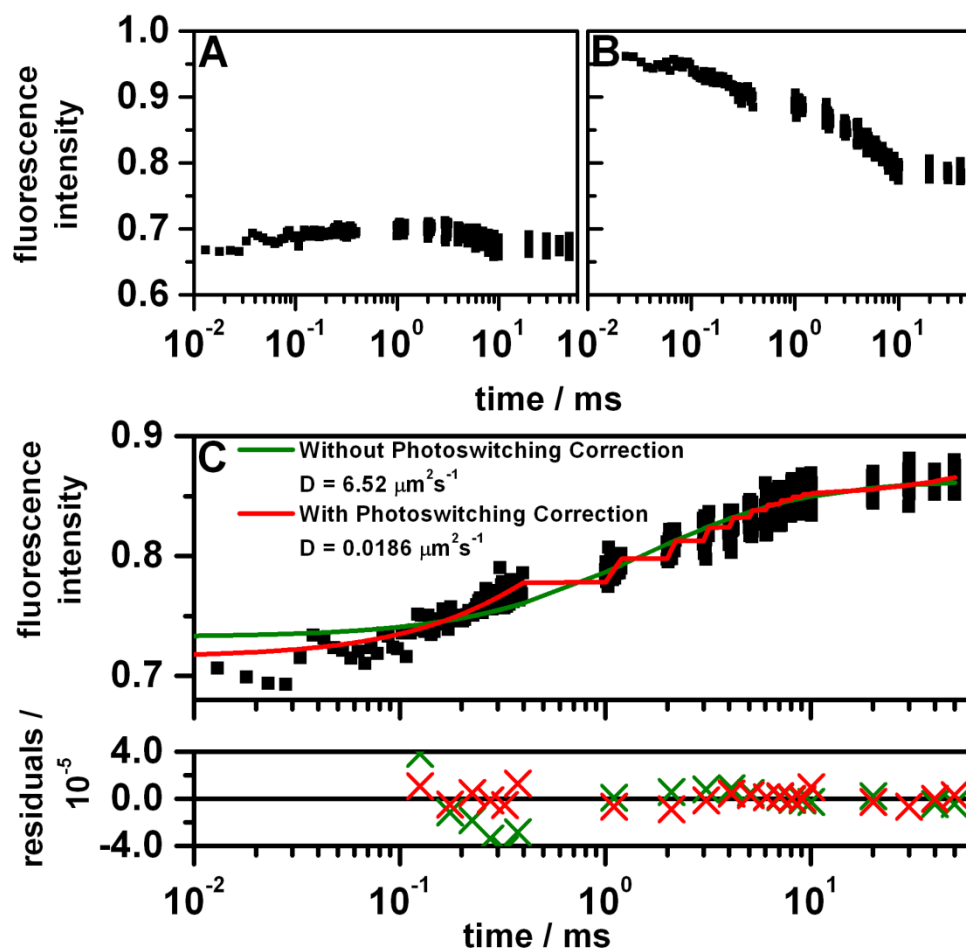
Figure A.6: Fitting GFP immobilized in a gel to a FRAP recovery curve. Point FRAPs of GFP immobilized in a gel were collected as described in chapter 2. (A) The raw bleach curve perhaps showing a small rapid recovery and then slow irreversible photobleaching. (B) The raw control curve showing a rapid and steep reversible photobleach that eventually slows at long times. (C) The resulting data (bleach divided by control) were fit with a model assuming Brownian diffusion ($\alpha = 1$) that did not include a correction for photophysics (green line, Eq. 2.4 in chapter 2) or included a correction for photophysics (red line, Eq. 2.6). The model that includes a correction for photophysics yields a diffusion coefficient that is ~4500 fold less than GFP in aqueous solution, or ~200 fold less than GFP in glycerol. The glycerol sample took ~30 ms to reach full recovery; therefore, this diffusion coefficient shows a full recovery that would take ~6s for our region of interest size (radius is ~250 nm). Such a slow recovery cannot be accurately detected by the 50 ms data collection time of the experiment and is best interpreted as an immobile fraction.
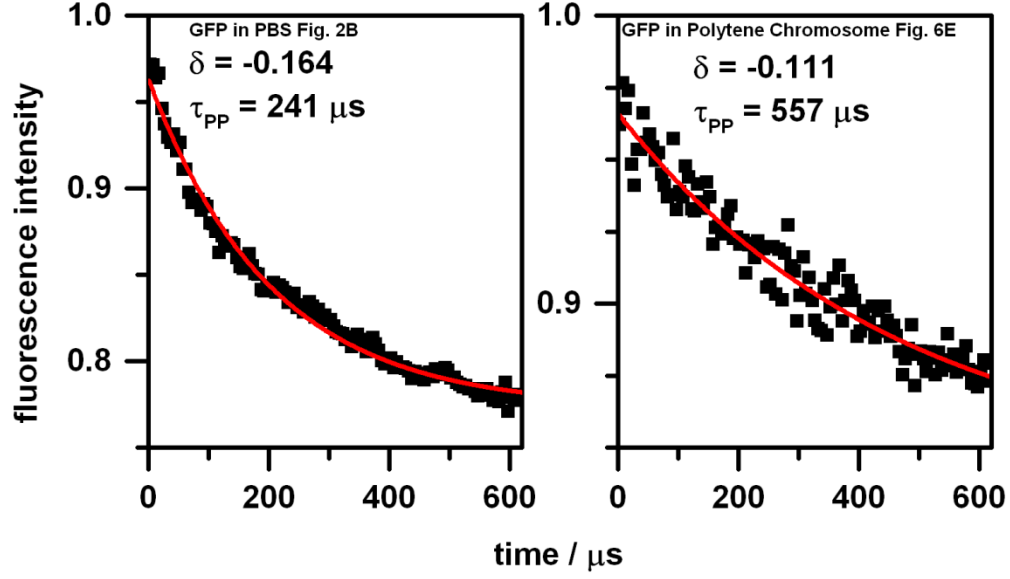
Figure A.7: Determination of δ and τ$_{PP}$ for the application of the photoswitching correction. To determine the values of δ and τ$_{PP}$ to be used in Eq. 2.6 in chapter 2, we fit the control curves from each sample for the first 600 µs to the equation $\delta e^{t/\tau_{PP}} + C$ where *C* is an offset used to account for the long-time non-exponential photophysics. Note that δ was converted to a fraction of the bleach depth before being used in Eq. 2.6. The parameters were dependent on the sample and the imaging parameters. Example fits and data are shown for GFP in PBS (left; data from Figure 2.2B) and GFP in polytene chromosome (right; data from Figure 2.6E).
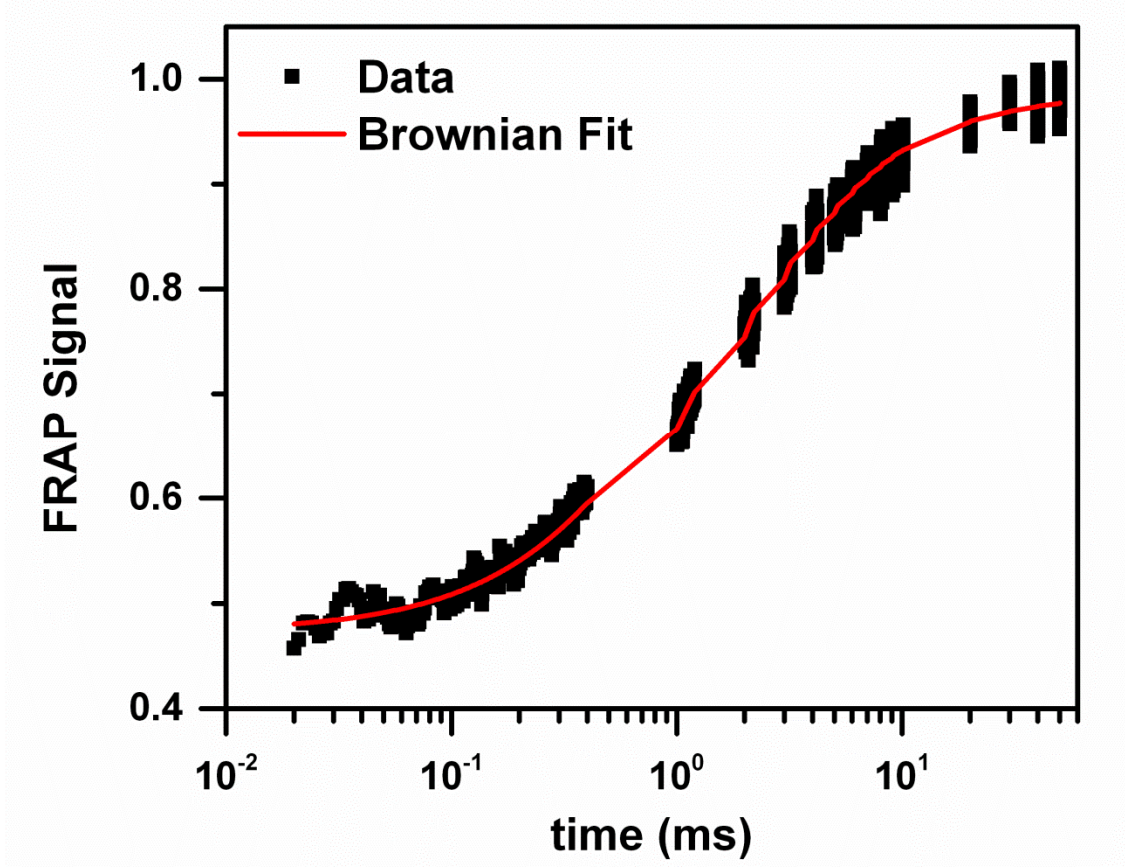
Figure B.1: Dextran FRAP data from the 38 kDa dextran crowder at a concentration of 303 mg/mL fit to a FRAP model that only accounts for Brownian diffusion.

The data were fit according to the following point FRAP model:

$$F(t) = F_0 [1 + \delta \exp(\frac{-t_{laser}}{\tau_{PP}})] \sum_{n=0}^{\infty} \frac{(-\beta)^n}{n!} \left[1 + n\left(1 + \frac{16Dt}{\omega_r^2}\right)\right]^{-1} \left[1 + n\left(1 + \frac{16Dt}{\omega_z^2}\right)\right]^{-\frac{1}{2}} \quad \text{(B.1)}$$
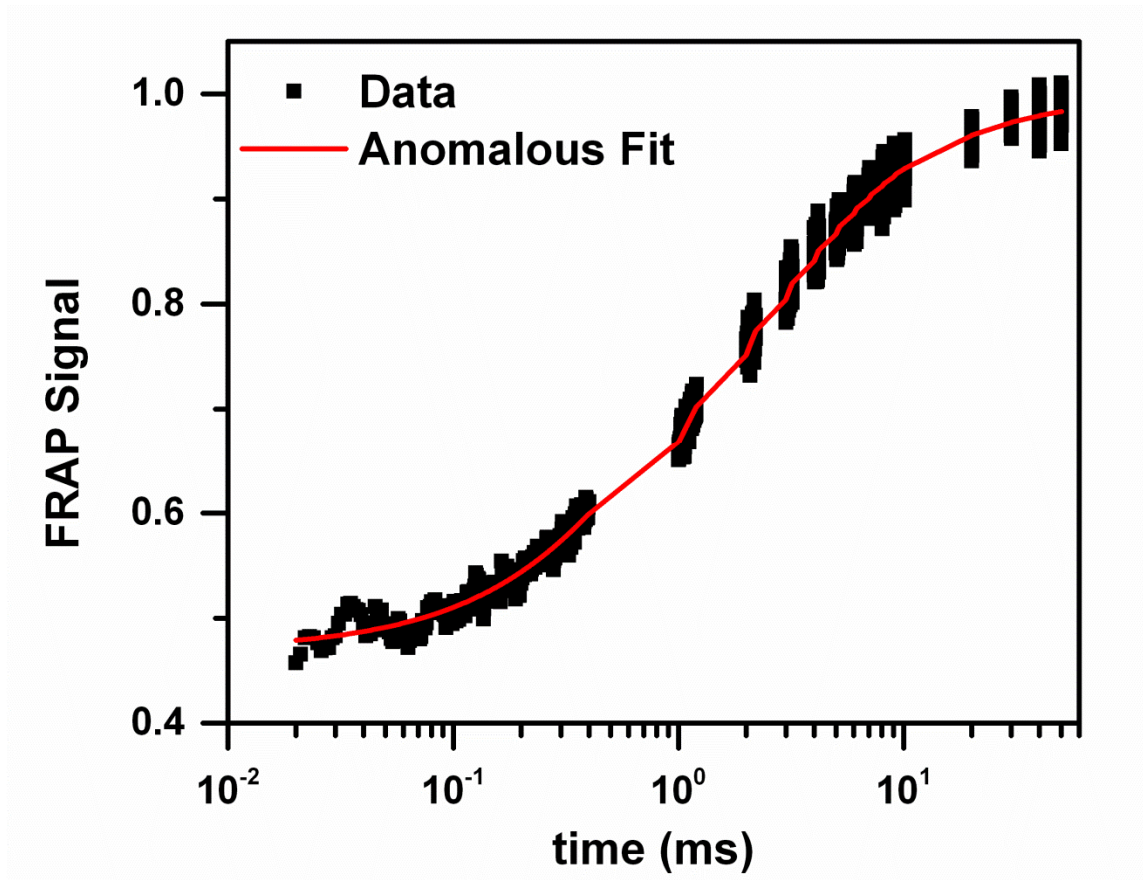
Figure B.2: Dextran FRAP data from the 38 kDa dextran crowder at a concentration of 303 mg/mL (same data as Figure B.1) fit to a FRAP model that allows for the possibility of anomalous diffusion.

The data were fit according to the following point FRAP model which allowed for anomalous diffusion:

$$F(t) = F_0 [1 + \delta \exp(\frac{-t_{laser}}{\tau_{PP}})] \sum_{n=0}^{\infty} \frac{(-\beta)^n}{n!} \left[1 + n\left(1 + \frac{16\Gamma t^{\alpha}}{\alpha \omega_r^2}\right) \right]^{-1} \left[1 + n\left(1 + \frac{16\Gamma t^{\alpha}}{\alpha \omega_z^2}\right) \right]^{-1/2} \quad \text{(B.2)}$$
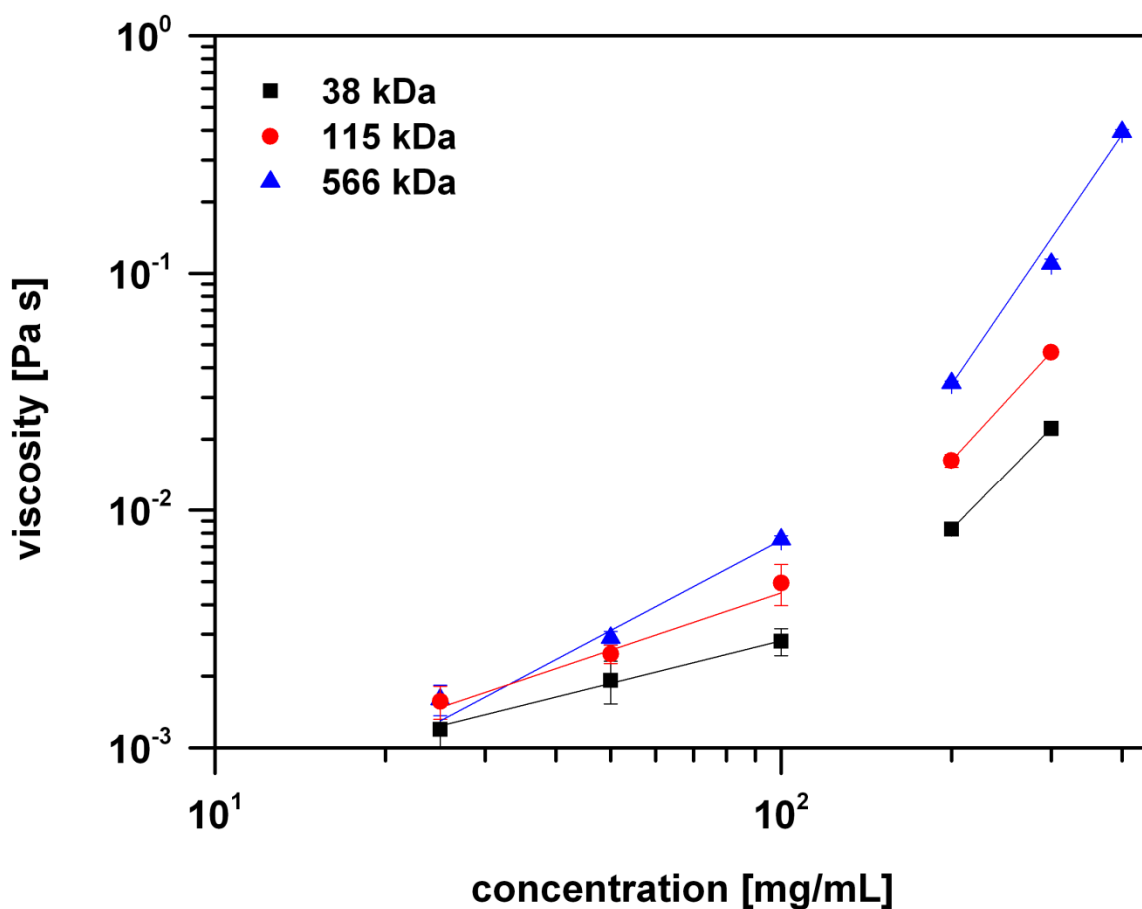
Figure B.3: The macroviscosity of the dextran solutions as measured by a rheometer is plotted against concentration on a log-log axis. This plot is used to determine the overlap concentration. The lines of best fit intersect at the overlap concentration which is define as the point at which the scaling power changes on the viscosity vs. concentration power law. The best fit slopes (powers) are listed in Table B.1 along with the resulting overlap concentrations.

Table B.1: Fitting parameters from Figure B.3 used to determine the overlap concentrations of dextran solutions.

Dextran	Slope 1	Slope 2	Overlap Concentration
38 kDa	0.594 ± 0.038	2.43	139 mg/mL
115 kDa	0.800 ± 0.132	2.60	133 mg/mL
566 kDa	1.26 ± 0.14	3.49 ± 0.21	150 mg/mL

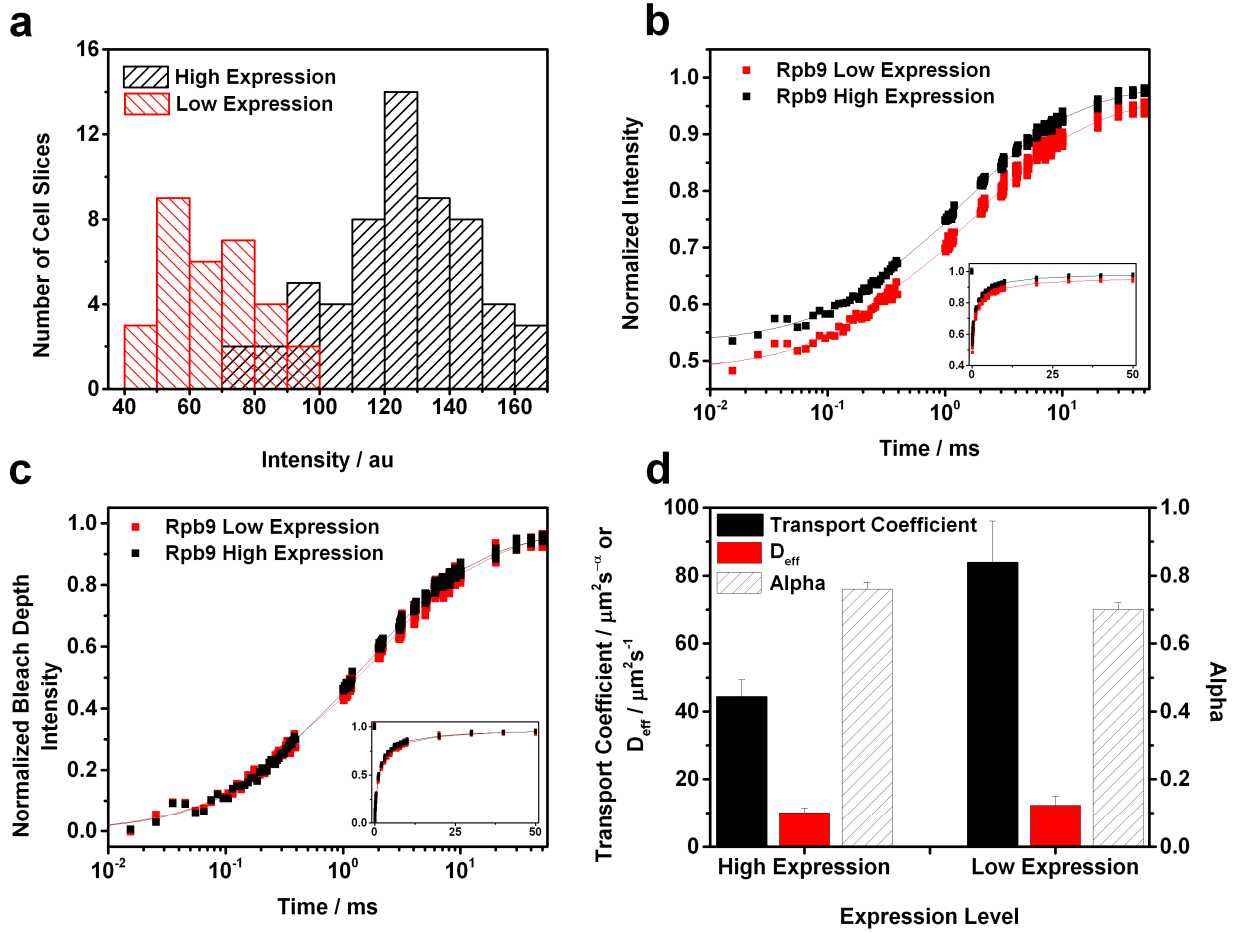**Figure C.1:** High expression levels of fusion proteins are not responsible for the observed anomalous diffusion. The Rpb3-GFP and Rpb9-GFP fusion proteins are exogenous insertions expressed under the control of the GAL4 driver system and believed to be functional due to recruitment to HSP promoter sites.[4] As a result they are highly over-expressed compared to the native, untagged RNAPII subunits. To test if the over-expression was creating a population of unincorporated subunit that was being manifest as apparent anomalous diffusion, we crossed our Rpb9-GFP with a GAL4 driver under the control of a heat shock induced promoter (Bloomington Stock Center #1799).(d) The expression level of this cross, Rpb9-GFPx1799, can be lowered by raising the fly larvae at 18°C (red bars) and was determined to reduce expression levels by up to 50% compared to the Rpb9-GFPxH2B-mRFP line raised at 22°C (black bars). The mean expression levels of these two populations were found to be statistically different (p<0.001). While this construct did not have the chromatin labeled by the H2B-mRFP histone protein, the Rpb9-GFP showed strong exclusion from chromatin regions (determined previously) still enabling us to restrict the FRAP analysis to the interchromatin space. (a) The FRAP recoveries and (b) normalized recoveries for the

high (black) and low (red) Rpb9-GFP expression levels flies are shown. (c) Within experimental error, the effective diffusion coefficient and anomlity value of the reduced expression line matched the results found using the Rpb9-GFPxH2B-mRFP line. Thus we are confident that the over expression is not responsible for the anomalous diffusion. This could not be repeated for the Rpb3-GFP construct since it is expressed by a GAL4 driver sequence previously bred into the fly line.
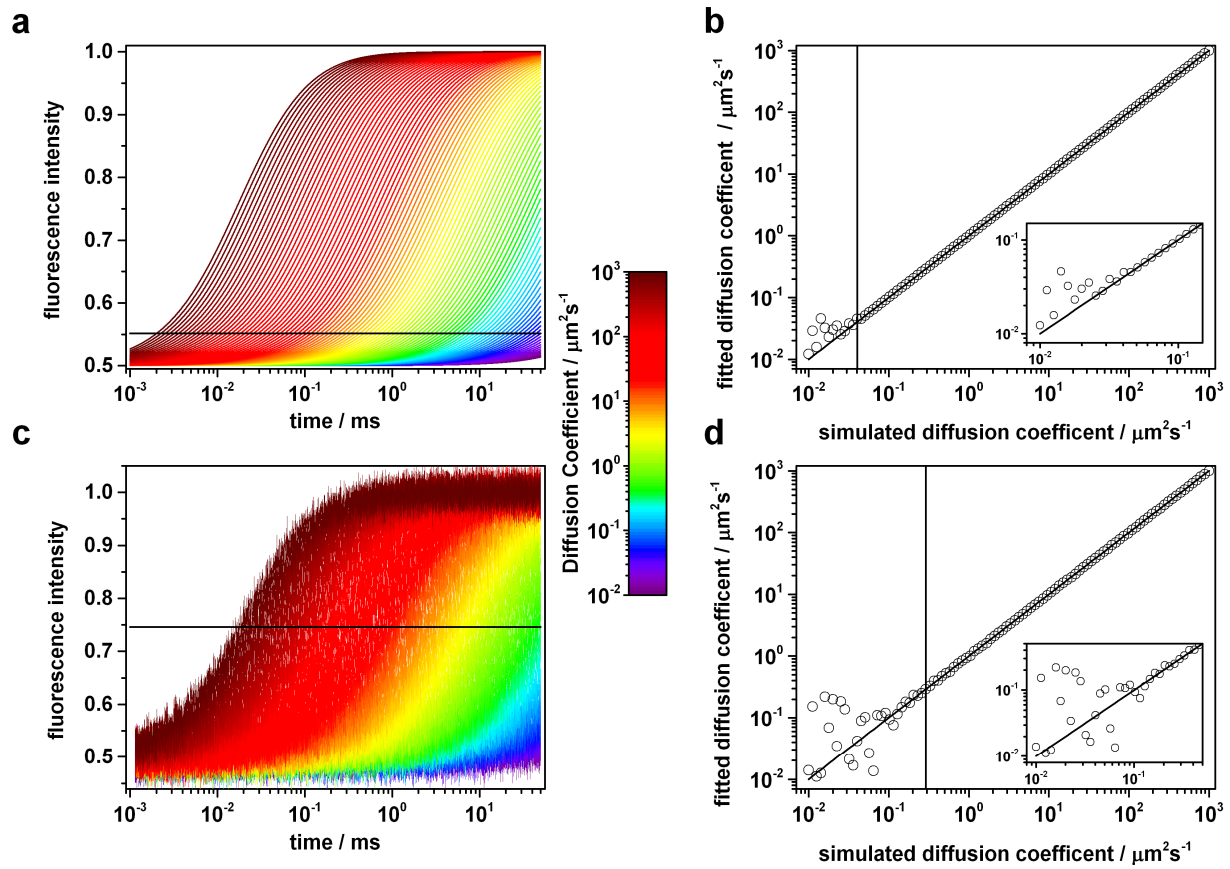
Figure C.2: Determining the resolution of the point FRAP method. For slow moving species, determining the diffusion coefficient is difficult if the FRAP curve does not fully recovery to the pre-bleach level on the time course of the measurement. Despite the rapid time resolution of our data collection method, we are limited in how slow a diffusion component we can accurately measure by the 50 ms time duration of our recovery collection. If Brownian diffusion is assumed, our fitting algorithm estimates the final recovery extent based on the slope of the FRAP curve once it begins to level off. Further, the estimation of the recovery extent will strongly affect the estimated diffusion coefficient. For very slow moving species, the recovery will be very shallow and the algorithm is unable to accurately estimate the diffusion coefficient. This became a significant concern when applying the distribution model[5] as a threshold for reliable determination of diffusion coefficients needed to be established. We chose to empirically evaluate which diffusion coefficients were reliable by applying our fitting algorithm to simulated data and determining where the estimated diffusion coefficients began to deviate from the input value. (a) FRAP recovery curves were simulated that correspond to diffusion coefficients from 0.01 to 1000 μm^2/s. As can be seen, the majority of the curves exhibit a significant recovery, but the slow moving components are nearly flat on the 50 ms timescale of the simulation. (b) The fitting algorithm was applied to each curve and the estimated diffusion coefficient was plotted against the initial input value. We determined the diffusion coefficient estimation was accurate with

as little as 10.3% recovery (a-horizontal black line), corresponding to a diffusion coefficient of 0.04 um^2/s (b-vertical black line). (c) Next, white noise was added to the FRAP curves resulting in simulated data with a signal to noise ratio (SNR) of 35 dB. This SNR corresponds well our experimental FRAP data. Again, we applied the fitting algorithm to the noisy data and compared the estimated diffusion coefficients to the input values. At this SNR, the estimations begin to deviate once the recovery is less than 47.6% complete (c-horizontal black line), corresponding to a diffusion coefficient of 0.29 um^2/s (d-vertical black line). Thus we can see the accuracy of the fitting depends on the SNR of the data. Erring on the side of caution, we rejected any diffusion components that showed less than a 50% recovery. This method outlines a framework for evaluating the robustness of a FRAP fitting method as long as the SNR of the data can accurately be estimated.
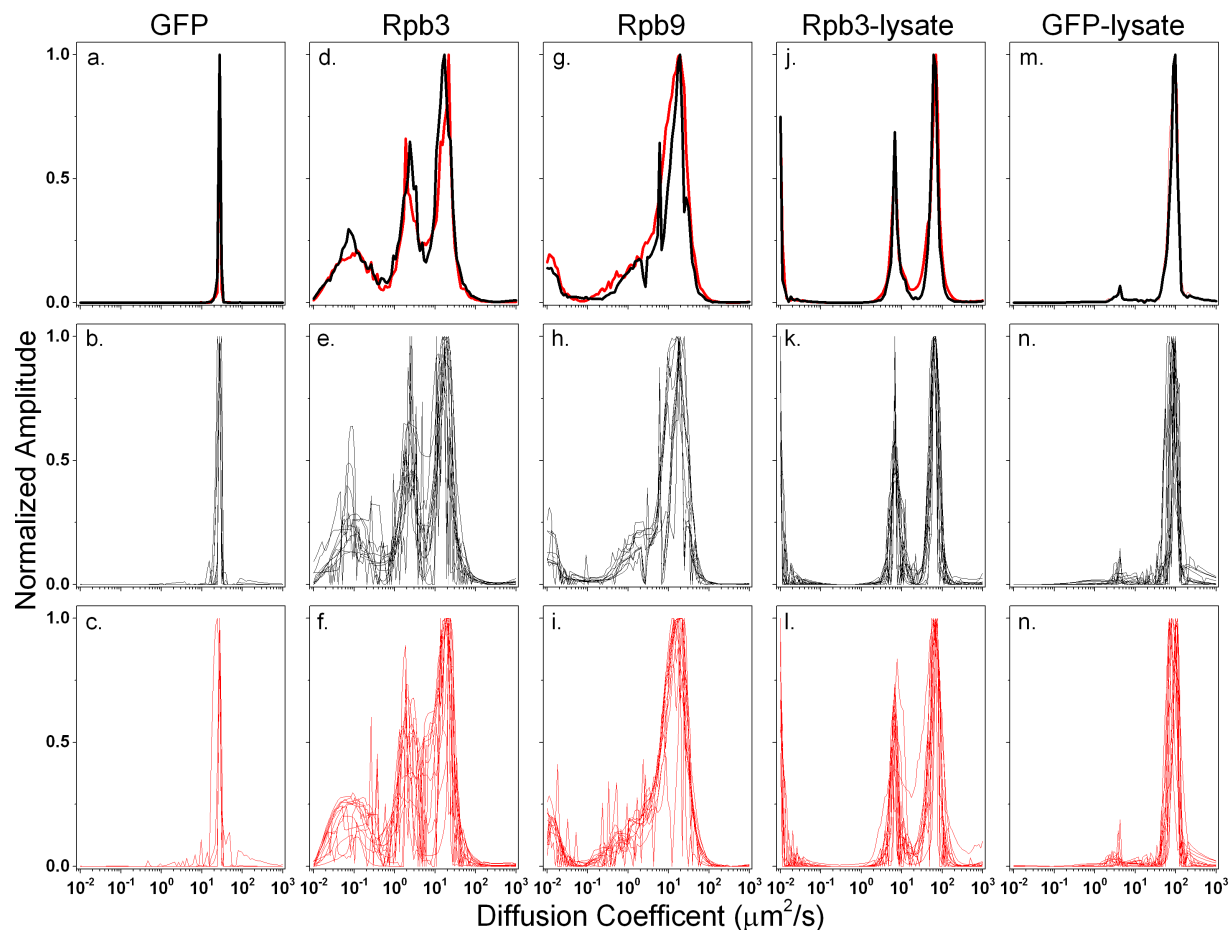
Figure C.3: Establishing the robustness of the distribution model on experimental data. As presented in the Results and Discussion in Chapter 4, the Rpb3 datasets indicate a bimodal distribution. We wanted to ensure the robustness of the Distribution model to predict bimodal distributions without a bias predicated on the initial component amplitudes. To achieve this, we tested the output of the Distribution model in response to different initial amplitude profiles, as well as different fitting protocols. Four sets of initial conditions were tested: (1,2-Gaussian) shaped the initial amplitudes in a Gaussian envelope with 35 or 15 dB noise added, (3,4-Flat) provided 35 or 15 dB Gaussian white noise as the input. To test for reproducibility, each input condition was tested three times. In the first, unbiased implementation (panels b,e,h,k,n), the input profile amplitudes were floated to achieve a best-fit to the FRAP data. The output distribution was then smoothed with a median filter. This process was repeated five times until the fit residuals no longer improved. The last step omitted smoothing to prevent distorting the output. All the outputs are overlaid indicating the similarity regardless of input profile. Next, the effect of biasing the distribution to a single component by implementing a Gaussian smoothing step was tested. A five-step procedure was used, but in contrast to the previous method, between the third and fourth smoothing steps the output was fit to a Gaussian envelope. The final fit output was not forced to a Gaussian to reveal the most stable output. The fitting outputs from all twelve input distributions

are shown (panels c,f,l,n); again the outputs are (1) very similar and (2) show the same structure as the un-biased fitting method. The results of the twelve outputs for both fitting methods were averaged and compared (panels a,d,g,j,m), indicating nearly identical distributions. This indicates that random noise on the input does not affect the output and the distribution fit find the most stable output. This test was significant for the Rpb3 distribution results. If biasing the output to one component altered the final output away from a bimodal fit, then the distribution model algorithm could not be considered robust. However, since even when the fit was forced to conform to a single peak it still "stepped away" to a bimodal fit on the next iteration, the fitting method was considered stable.
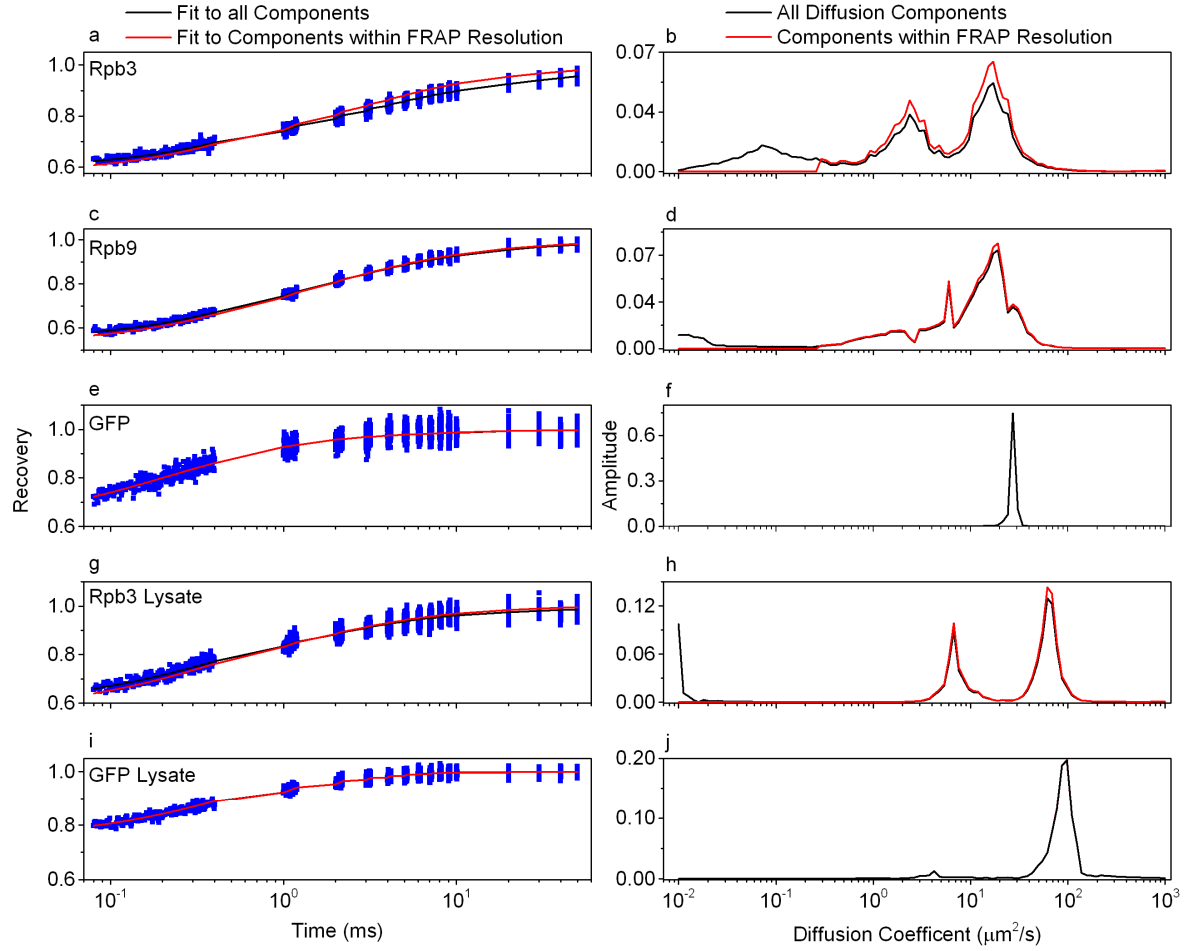
Figure C.4: Fit quality excluding diffusion components under FRAP resolution. After confirming that the Distribution modeling can robustly determine the number of components that comprise a FRAP curve and having established the FRAP resolution limit, we chose to investigate how accurately the retained components recapitulated the original data. The output distributions (panels b,d,f,h,j, black lines) were truncated at 0.30 μm²/s (red lines), and renormalized so the total distribution summed to unity. This slightly increased the amplitudes of the retained components. These truncated distributions were used to establish a fit to the data (panels a,c,e,g,I, fit to all components black line, fit to truncated distribution red line). For the Rpb3 *in vivo* data, the retained components do alter the recovery dynamics, shifting the curve to a faster recovery. For all other samples, the fits are unchanged.

Table C.1: FRAP fitting results for each dataset

Conditions	Sample	Set	Gamma (um^2/s^α)	D (um^2/s)	Alpha
		I	-	32.7±16.1	0.99±0.08
	GFP	II	-	36.2±20.1	1.00±0.09
		III	-	27.5±20.1	1.00±0.12
		Ensemble*	-	32.0±6.0	1.00
		I	70.8±11.7	21.0±4.5	0.78±0.06
		II	37.3±15.9	6.2±3.9	0.73±0.07
In vivo		III	54.1±33.3	4.4±5.0	0.64±0.10
(live polytenes)	Rpb3	IV	105.6±37.3	7.4±5.1	0.58±0.06
		V	271.9±130.0	9.2±13.6	0.43±0.08
		VI	90.3±23.5	5.0±2.5	0.57±0.05
		Ensemble*	69.1±10.5	5.5±1.4	0.62±0.03
		I	45.7±7.2	7.9±1.7	0.73±0.03
		II	38.9±14.3	9.70±4.8	0.78±0.06
	Rpb9	III	30.7±8.9	7.6±2.9	0.78±0.05
		IV	46.8±7.3	12.8±2.6	0.78±0.02
		Ensemble*	44.4±5.0	10.0±1.5	0.76±0.02
		I	98.0±50.0	79.8±43.0	0.96±0.07
	GFP	II	75.1±33.8	71.1±32.5	0.99±0.07
		Ensemble*	112.2±37.5	79.1±29.0	0.92±0.05
In vitro		I	69.4±11.3	43.8±7.85	0.91±0.05
(cell lysate)		II	246±136.7	41.2±40.1	0.65±0.08
	Rpb3	III	85.4±37.4	30.6±17.2	0.81±0.07
		IV	115.4±45.9	23.2±13.7	0.72±0.06
		Ensemble*	150±36.4	33.0±11.7	0.72±0.04
In vivo		I	83.9±12.2	12.3±2.65	0.70±0.02
Low Expression	Rpb9	II	118.3±21.9	10.7±3.3	0.65±0.03
Level		Ensemble*	97.3±12.1	11.7±2.2	0.67±0.02

*Parameters resulting from fitting the average of all the listed datasets. This procedure improves the fitting results by increasing the SNR of the data.

For each experiment, several datasets were collected and the resulting raw data averaged together to yield finalized data with a high SNR. The finalized data was fit with the apparent anomalous diffusion and distribution models. To ensure that the averaging of several datasets did not distort the final results, each individual dataset was fit with the apparent anomalous diffusion model. Typically, the subset of the finalized data shows nearly the same anomlity and effective diffusion coefficient, but the 95% confidence error intervals are larger than if the datasets are compiled.

APPENDIX D: SUPPORTING INFORMATION FOR CHAPTER 6

D.1. Estimation of pulse duration at the sample

As described in section 6.2, the durations of the near-IR and visible pulses were measured just before the laser-scanner using background-free autocorrelation and cross-correlation. The relay lenses in the laser-scanner and objective lens introduce substantial dispersion, further broadening the duration of the ultrashort pulses. In this section, we outline calculations to estimate the duration of these pulses at the sample. Because the near-IR pulses have a transform-limited duration of ~150 fs, we consider only the group-delay dispersion (GDD) of the optical elements. In this regime, the effect of third- and higher-order dispersion is small compared with the GDD[6].

We used Sellmeier equations to calculate the GDD introduced by the two achromatic relay lenses, based on their materials and on-axis thicknesses; the total GDD of these elements is 3200 fs^2 for 750 nm pulses and 9180 fs^2 for 425 nm pulses. We estimated the GDD of the Olympus 60X/1.2NA plan apochromatic objective lens at 750 nm to be 2000 fs^2, which was based on values reported for a similar objective (Zeiss 40X/1.2NA plan apochromatic objective lens)[6]. The objective lens GDD in the visible region was not available, but since the GDD of many glasses commonly used for objective lenses is approximately three times larger at 425 nm than at 750 nm, we estimated that the GDD of the objective lens at 425 nm is 6000 fs^2.

The duration of Gaussian pulses broadened only by second-order dispersion is[6]:

$$T_f = T_i \sqrt{1 + \left[\frac{(4ln2)\varphi''}{(T_i)^2} \right]^2} \qquad (D.1)$$

where T_f and T_i are the final and initial pulse durations respectively, and φ'' is the GDD. Since the 750 nm pulses had a transform-limited duration of 150 fs and a duration of 200 fs after traversing the Pockels cell, polarizer and a beam-expanding telescope, we conclude that these elements introduce a GDD of 7200 fs^2. Therefore, the total GDD accumulated by 750 nm pulses at the sample is 7200 + 5200 = 12,400 fs^2, resulting in a 275 fs pulse duration. The duration of the 425 nm pulses before entering the laser-scanner was 210 fs, indicating the GDD to this point was 8000 fs^2. The additional 15,180 fs^2 introduced by the relay lenses and objective would broaden the 425 nm pulse duration to approximately 450 fs at the sample.
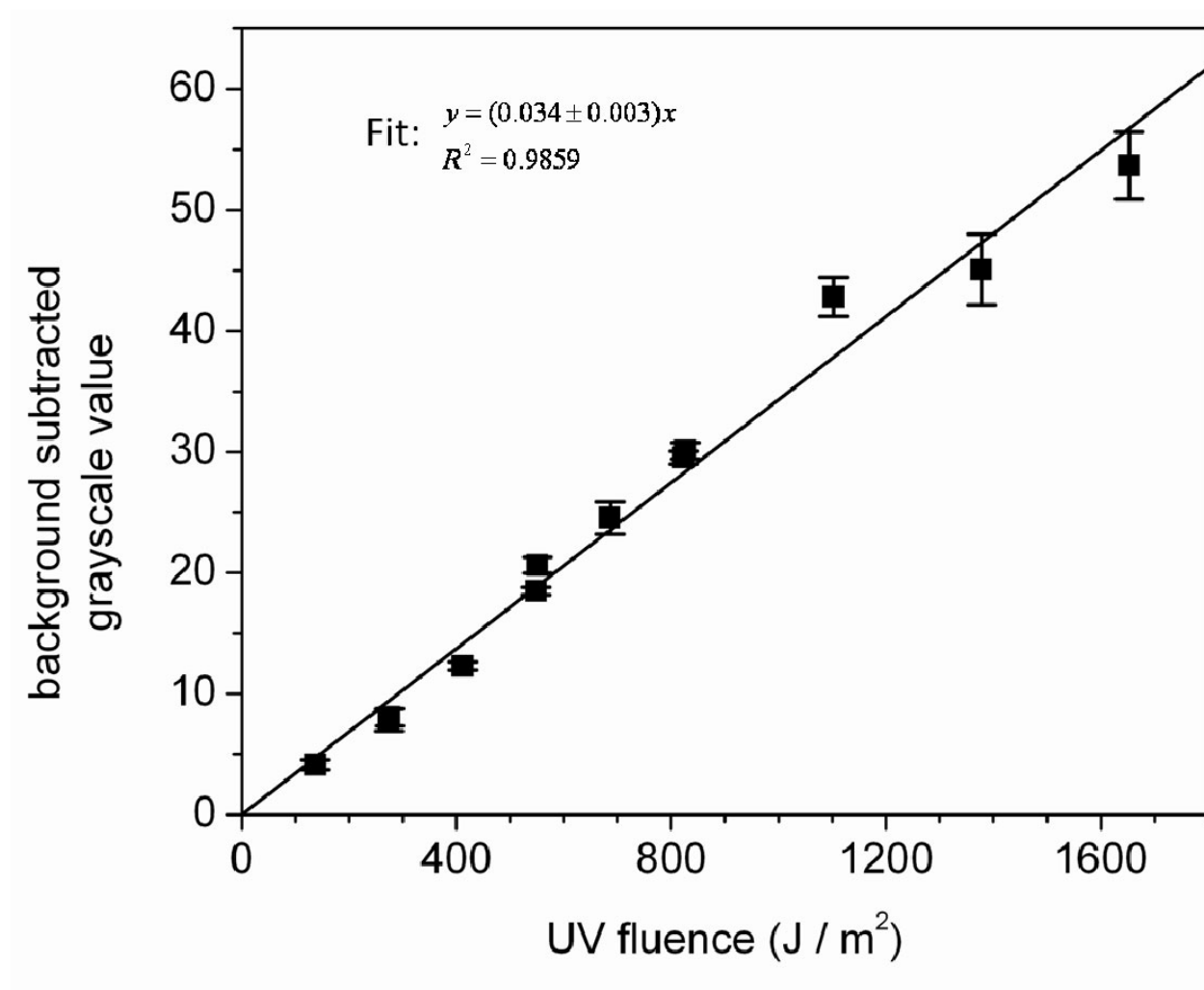
Figure D.1: A calibration curve for the immunofluorescence assay for the detection of thymine-thymine CPDs. HeLa cell monolayers were exposed to a range of UV fluences from mercury vapor lamps at 254 nm. The assay was linear over the range of values tested with a slope of 0.034±0.003 and a coefficient of determination of 0.986.
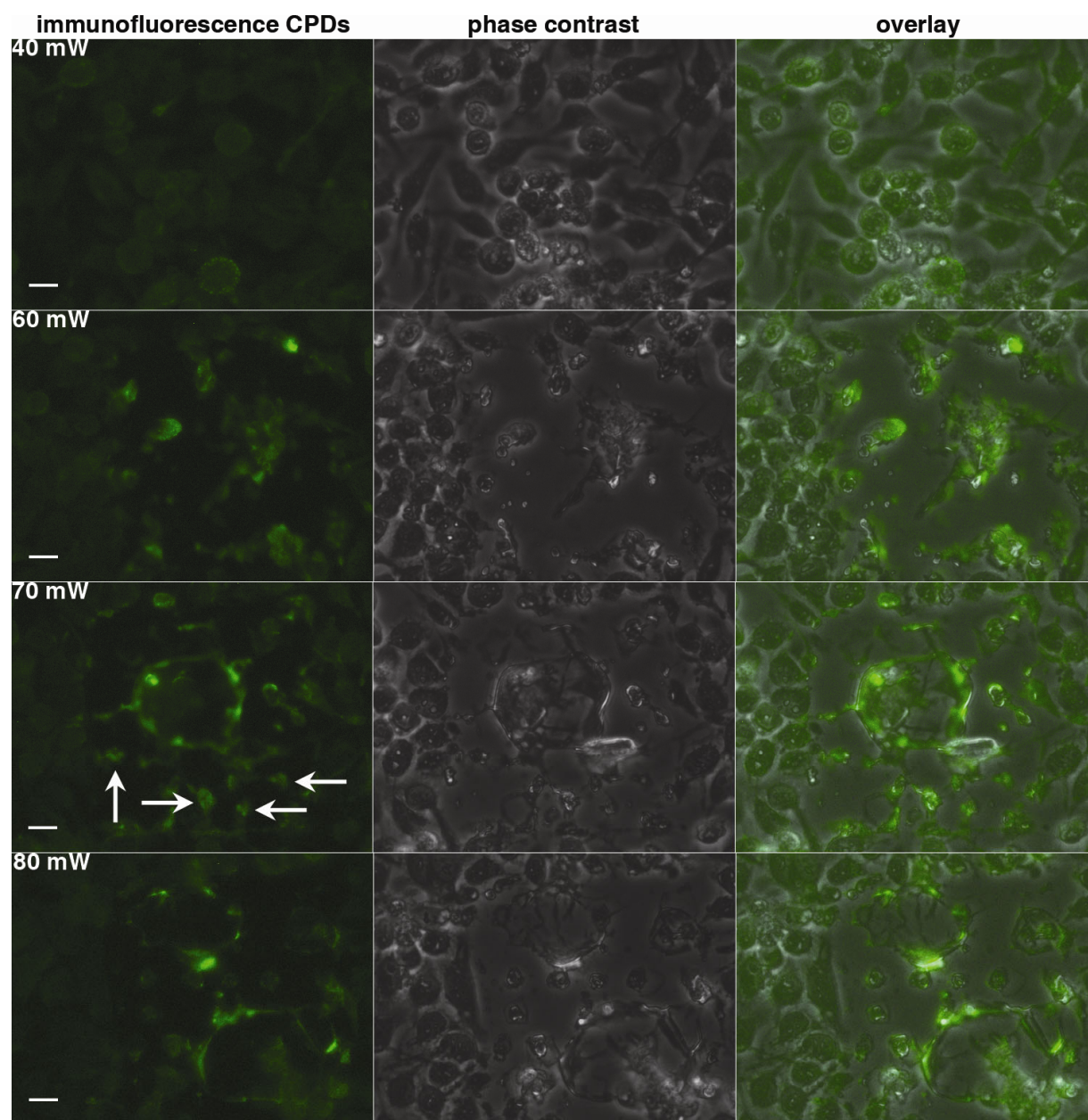
Figure D.2: Thymine CPD staining of HeLa cells irradiated with IR pulses. A square region of HeLa cells were irradiated with IR pulses at 750 nm and 40, 60, 70, and 80 mW. The staining confirms the production of CPDs at 70 (white arrows) and possibly 80 mW; however, it also reveals severe malformations of the cells as a result of the irradiation (Fig. 2). The destruction of cells is especially relevant at 80 mW where the damage makes the stain hard to observe due to lack of cells. Damage (CPD and physical) was not detected after irradiation with IR pulses at 750 nm at 40 mW. Physical malformations resulting in staining but without nuclear localization occur at 60 mW. Scale bar is 20 μm. Cells were seeded at a density of 6.0 x 10^5 cells/mL. The typical seeding concentration of 2.5 x 10^5 cells/mL resulting in no staining as all the cells were burned away at the lower density (data not shown).
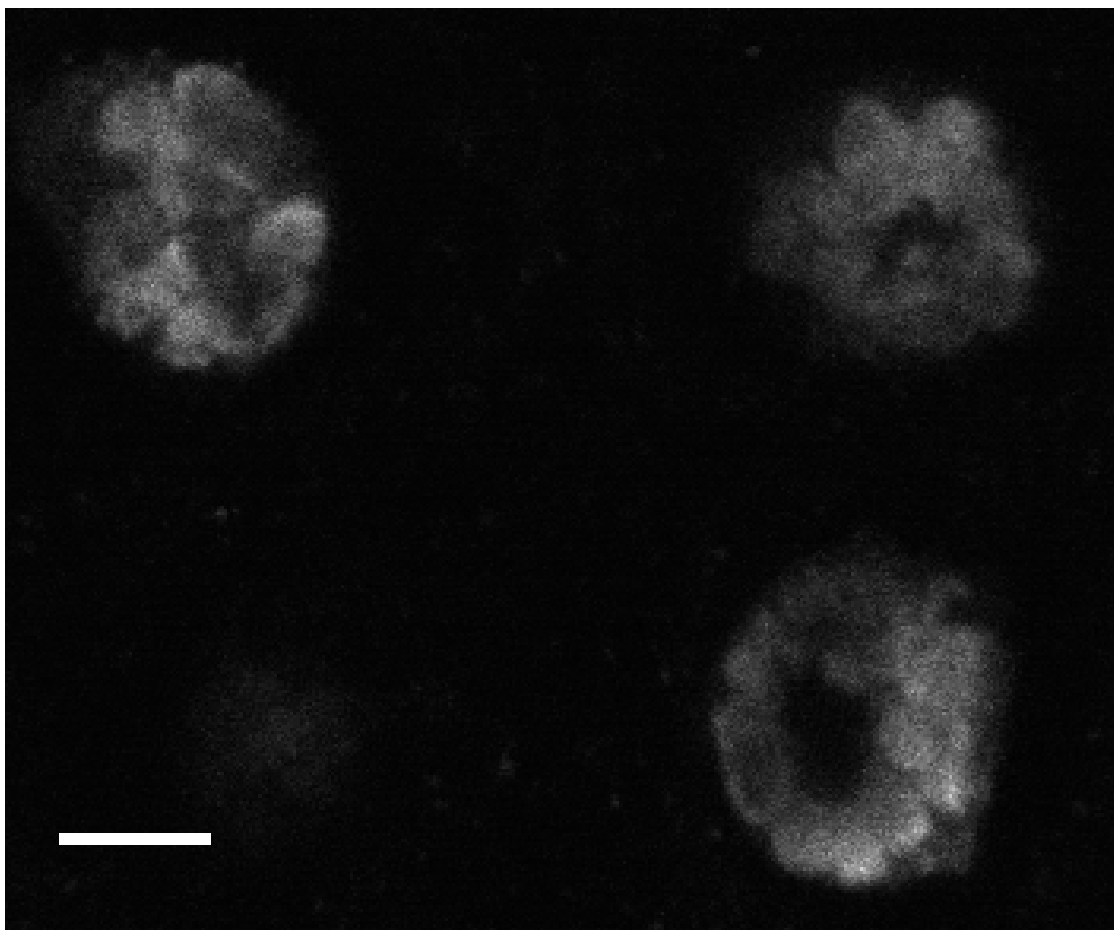
Figure D.3: Glands without florescence markers from the w[1118] fly line were damaged using light at 425 nm. The immunofluorescence indicates the production of CPDs demonstrating that thymine CPDs are produced as a result of direct thymine photon absorption and not as a result of dye mediated photochemistry in the *Drosophila* salivary glands. Since there are not fluorescence markers on the chromosomes, wide laser scans were used to ensure that the DNA was damaged. Accordingly, the entire chromosomes of four closely packed cells are damaged due to the challenge of the experiment. The level of immunofluorescence was the same as glands with fluorescent proteins under the same experimental conditions. Scale bar is 10 μm.
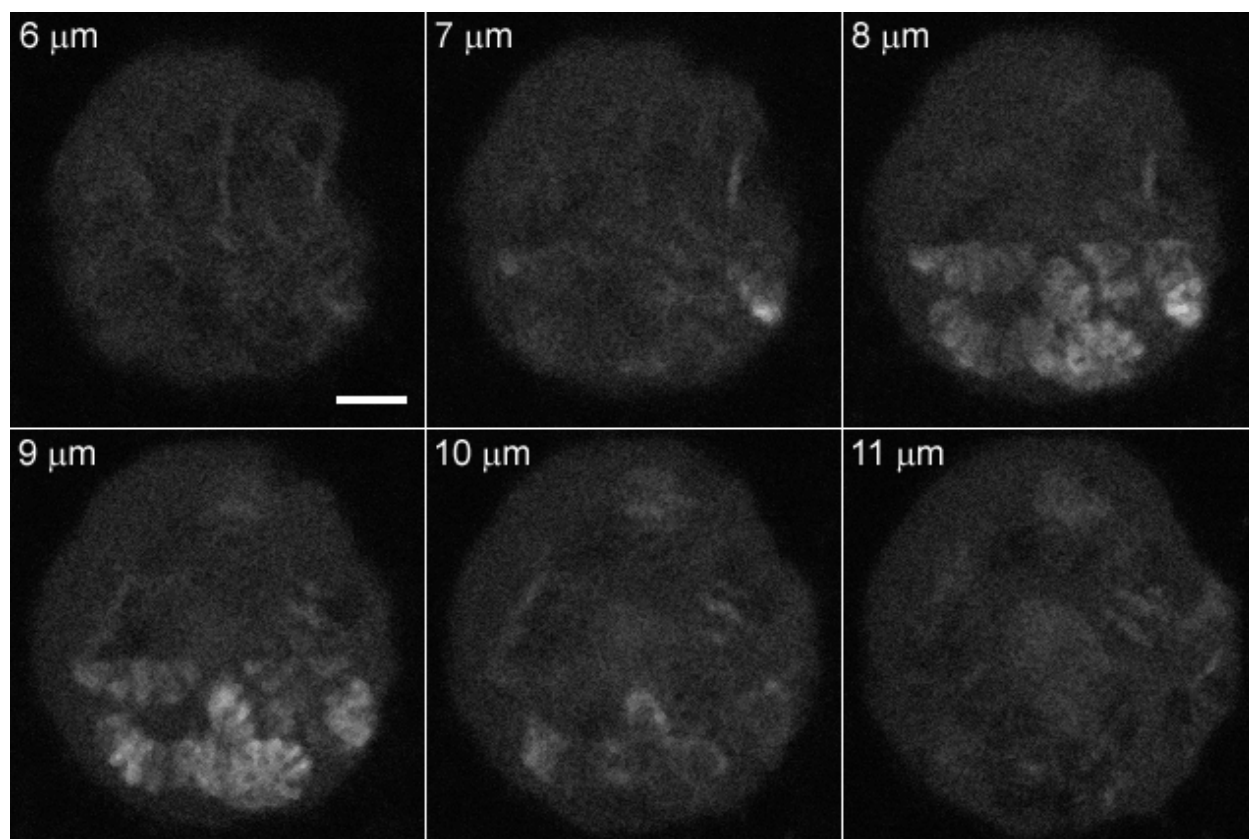
Figure D.4: Postirradiation z-series of a *Drosophila* polytene nucleus expressing TopI-GFP. The z-series was taken after 4 minutes of recovery. The TopI is localized to a ~2 µm thick region noting the axially localized nature of the region. The cell was irradiated with 425 nm, 10 mW. Scale bar is 5 µm.
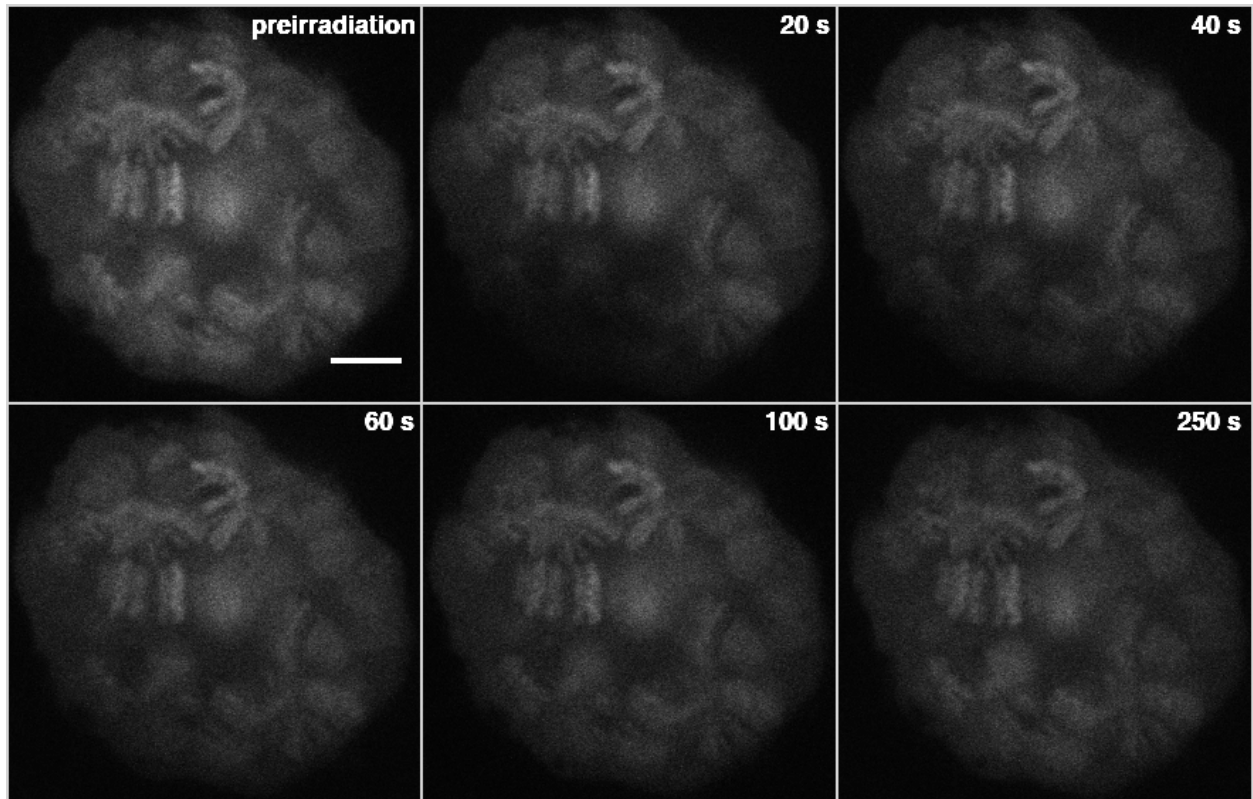
Figure D.5: Postirradiation time lapse series of a *Drosophila* polytene nucleus expressing TopI-GFP with a CW laser. The lower left quarter of the cell was irradiated with 488 CW laser at 13 mW bleaching the GFP in the region. The fluorescence in the irradiated region recovers uniformly. This is in contrast with cells that contain DNA damage in which the recovery proceeds stepwise from the edges of the irradiated region towards the center (Figure 6.5). Scale bar is 5 µm. The image contrast was uniformly enhanced to aid viewing.

"Part of the inhumanity of the computer is that, once it is completely programmed and working smoothly, it is completely honest." – Isaac Asimov

E.1. FRAP Fitting Program

The following programs were custom written in MatLab to process FRAP data in Chapters 2 and 3. Raw FRAP outputs in the form of voltages are collected over several different points. These output files are normalized and averaged using the *load_multipt_autoselect.m* routine. This routine takes a number of different zones (z-slices) and averages the points in each z-slice into one data set that it saves as filename.mat. The data are normalized to the prebleach data as part of the processing.

```matlab
%load_multipt_autoselect.m
%loads and saves data for different zones;

filename = 'data';
zones =1;
iterationsperpt = 1;
%to make matrix with the number of points per zone:

for k=1:zones;
    ptsperzone(k)=load([filename num2str(k) 'numbp.dat']);
end
%define datasets=total # of points bleached
datasets=iterationsperpt*sum(ptsperzone);

%Process Bleach datapoints:
c = 1;
%form of name = chromosome_dim_zone2_ptbl_pt15_r0.dat
for j =1:length(zones)
    k = ptsperzone(zones(j))-1;
    for i=1:k
        for l = 1:iterationsperpt
            %file = fopen(zone2_ptbl_pt0_r0);
            file = fopen([filename num2str(zones(j)) '_ptbl_pt' num2str(i)
                '_r' num2str(l-1) '.dat'],'r');
            data1 = fscanf(file,'%f');
            max1 = mean(data1(801:1000));
            normavg1(:,c) = data1 ./ max1;
            fclose(file);
            c = c+1;
        end
    end
end
```

```
end
avg1 = sum(normavg1,2) ./ datasets;


clear data1 max1 normavg1
%Process Control Datapoints
c = 1;
for j = 1:length(zones)
    k = ptsperzone(zones(j))-1;
    for i=1:k
        for l = 1:iterationsperpt
            file = fopen([filename num2str(zones(j)) '_ptcon_pt' num2str(i)
                '_r' num2str(l-1) '.dat'],'r');
            data2 = fscanf(file,'%f');
            max2 = mean(data2(801:1000));
            normavg2(:,c) = data2 ./ max2;
            fclose(file);
            c = c+1;
        end
    end
end

avg2 = sum(normavg2,2) ./ datasets;

clear data2 max2 normavg2 c

save([filename '.mat'],'avg1','avg2');
```

The averaged data file is then processed by the *loadandfit_2model.m* routine. The data_filename parameter is set to the .mat file created using the previous script. The start variable specifics the time (in microseconds) after the conclusion of the bleach at which fitting is to begin. The beam radius and initial guess for the fitting algorithm are also specified.

```
%loadandfit_2model.m
tic
clear all
close all
global wr wz
data_filename = 'Data_File_Name';
start=20; %time after bleach to begin the fit
wr=0.305; %1/e^2 radius in um
wz=1.092; %1/e^2 radius in um
x0=[80 1 1];  %initial guess [D (or G) alpha F t=inf]
          %the initial guess for F t=0 is supplied by the script
calci = 0;  % Is the 95% confidence interval calculated? (1 = Yes; 0 = No)
```

```
            % Not calculating the 95% CI speeds up the fitting
pointb_smallfile %or pointb
FRAPfitweightedpsc_2model
savetable_2model
toc
```

The above program contains three subroutines that process the FRAP data and place

the voltages on the proper time axis (*pointb_smallfile.m* or *pointb.m*), fit the FRAP data

to a FRAP model (*FRAPfitweightedpsc_2model.m*), and save the best fit parameters to

a text file for importing into Excel for further analysis (*savetable_2model.m*).   Each of

these subroutines will be discussed in further detail below. However, after running the

above script eight figures and one output table are produced. There are four pre-fit

figures which are output as MatLab Figures 1-4 (shown in Figure E.1). The four post-fit

figures are output as MatLab Figures 10,12-14 (shown in Figure E.2). The output table

is saved as the *data_filename*_table.dat. An example is shown in Table E.1. Table E.1

shows four results. The first two models account for photophysics using Eq. 2.6 and list

the values of *δ* and τ_{PP} used in the fit (corresponding to the fits shown in Figure E.2B).

The third and fourth model are fit using Eq. 2.4 and do not take into account

photophysics (corresponding to the fits shown in Figure E.2C).

Figure E.1: Pre-fitting figures generated by the FRAP fitting MatLab script. (A) MatLab output Figure 1. This figure plots the raw data of the bleach and control curves. Careful examination of these curves is necessary to ensure that the FRAP recovery is a real event and not an artifact of the observational photobleaching correction as explained in **Chapter 2** (see Figure 2.3). (B) Figure 2 output from MatLab. Same data as shown in panel A except the time axis is changed to include the long time points. (C) MatLab output Figure 3. This is the entire FRAP curve plotted on logarithmic time axis (in μs). The plot is used to check before fitting if the curve looks qualitatively acceptable. (D) MatLab output Figure 4. This figure plots the first 300 μs after bleach on a linear time axis. This plot is used to check of ringing of the preamplifier as explained in Figure A.2.
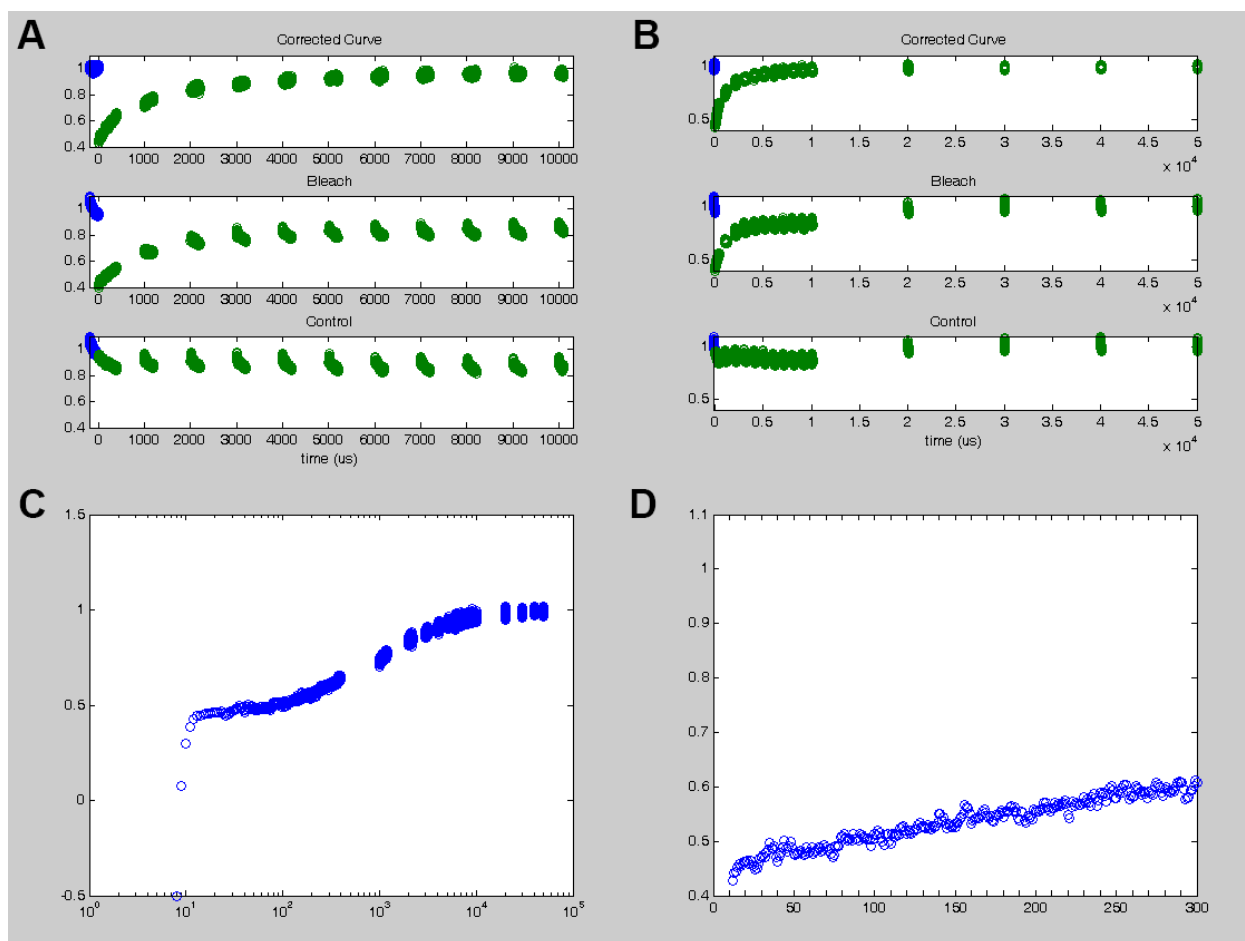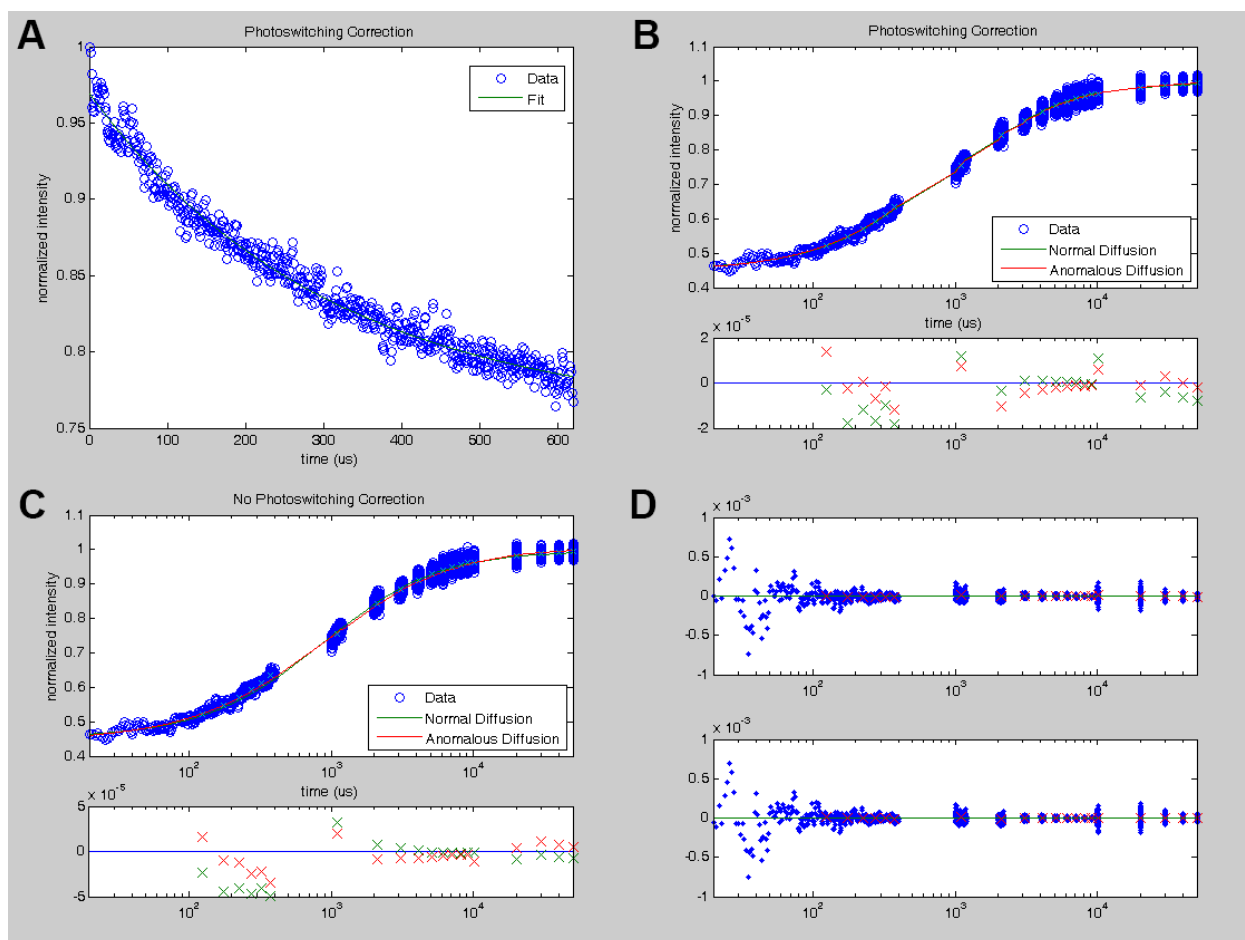
Figure E.2: Post-fitting figures generated by the FRAP fitting MatLab script. (A) MatLab output Figure 10. This figure shows the first 620 µs of the control curve and is fit to an exponential decay to determine τ_{PP} and δ used in Eq. 2.6 for fitting. (B) MatLab output Figure 12. The FRAP data are fit using Eq. 2.6 (correction for photoswitching is included in the model) with the anomalous parameter fixed to 1 (Normal Diffusion, green line) or allowed to float (Anomalous Diffusion, red line). The bottom plot shows the averaged residuals of each of the fits. (C) MatLab output Figure 13. Same data and color scheme as in B except data are fit using Eq. 2.4 (correction for photoswitching is *not* used). (D) MatLab output Figure 14. This figure plots the raw, un-averaged residuals from the fits in panel B. The top plot shows the residuals from the Normal Diffusion fit and the bottom shows the residuals from the Anomalous Diffusion fit.

Table E.1: Example output table from running the FRAP fitting MatLab script.

Data : Dextran2_tube5_run1			Data Pts:	624	Control Pts:	624	
Normal	**D**	**Alpha**	**F t=0**	**F t=inf**	**Delta**	**Tau**	
Values	14.52	0.9999	0.4512	0.9942	-0.1402	390.0	
95% CI	1.297981	0.015329	0.001151	0.00174	0	0	
RN	0.696442	BIC	36.94	BIC%	0.0000		
Anomalous	**Gamma**	**Alpha**	**Deff**	**F t=0**	**F t=inf**	**Delta**	**Tau**
Values	19.51	0.9484	14.35	0.4475	0.9985	-0.1390	390.0
95% CI	1.640613	0.014568	1.274654	0.001268	0.001862	0	0
RN	0.684892	BIC	0.00	BIC%	1.0000		
Normal	**D**	**Alpha**	**F t=0**	**F t=inf**			
Values	15.64	0.9999	0.4522	0.9945			
95% CI	1.158771	0.01285	0.001142	0.001762			
RN	0.783515						
Anomalous	**Gamma**	**Alpha**	**Deff**	**F t=0**	**F t=inf**		
Values	26.57	0.9060	15.31	0.4441	1.0041		
95% CI	1.730819	0.01154	1.104069	0.001301	0.001947		
RN	0.718548						
Start:	20	Low F0:	0.412995	High F0:	0.458883	Tau:	304.3286

Since the output is plain text the name of Greek variables are used in place of their symbols (i.e. Tau instead of τ_{PP}, the photophysics decay constant). Additionally, *F t=0* refers to the bleach depth (the fluorescence at time 0), and *F t=inf* refers to the final fluorescence intensity (the fluorescence at time infinity). A value of *F t=inf* that is less than ~1 indicates the presence of an immobile fraction. *RN* is the squared 2 norm of the residual. *BIC* and *BIC%* are the BIC score and percentage of model likelihood respectively (see section 2.2.4). *Low* and *High F0* refer to the lower and upper bounds placed on the bleach depth as a replacement for early time points as described in Appendix A.

The choice of the subroutine *pointb.m* or *pointb_smallfile.m* depends on how the raw FRAP data is stored. The initial method stored all of florescence data even when the laser was off during the intermittent data collection (as explained in Figure 2.1). Data stored in this manner is processed using the *pointb.m* script. A latter revision of the point FRAP LabView program only stored the florescence data when the laser is turned on. Process these data using the *pointb_smallfile.m* script. Each of these scripts use the *expfit.m* subroutine listed after them.

```
%pointb.m
global pstime psdata pstau psdelta xpsc

data = open([data_filename '.mat']);
avg1 = data.avg1;
avg2 = data.avg2;

xbound1 = [-200 10300];
xbound2 = [-200 50000];
ybound = [0.4 1.1];

plot1i = avg1(801:1000);
plot1renorm = avg2(801:1000);

plot1 = plot1i ./ plot1renorm;
plot1ble = plot1i;
plot1con = plot1renorm;

%Now process the postbleach data

avgpost(1:400)    = avg1(1021:1420);
avgpost(401:600)  = avg1(2021:2220);
avgpost(601:800)  = avg1(3021:3220);
avgpost(801:1000) = avg1(4021:4220);
avgpost(1001:1200) = avg1(5021:5220);
avgpost(1201:1400) = avg1(6021:6220);
avgpost(1401:1600) = avg1(7021:7220);
avgpost(1601:1800) = avg1(8021:8220);
avgpost(1801:2000) = avg1(9021:9220);
avgpost(2001:2200) = avg1(10021:10220);
avgpost(2201:2300) = avg1(11021:11120);
avgpost(2301:2400) = avg1(21021:21120);
avgpost(2401:2500) = avg1(31021:31120);
avgpost(2501:2600) = avg1(41021:41120);
avgpost(2601:2700) = avg1(51021:51120);


avgpost2(1:400)   = avg2(1021:1420);
```

```
avgpost2(401:600) = avg2(2021:2220);
avgpost2(601:800) = avg2(3021:3220);
avgpost2(801:1000) = avg2(4021:4220);
avgpost2(1001:1200) = avg2(5021:5220);
avgpost2(1201:1400) = avg2(6021:6220);
avgpost2(1401:1600) = avg2(7021:7220);
avgpost2(1601:1800) = avg2(8021:8220);
avgpost2(1801:2000) = avg2(9021:9220);
avgpost2(2001:2200) = avg2(10021:10220);
avgpost2(2201:2300) = avg2(11021:11120);
avgpost2(2301:2400) = avg2(21021:21120);
avgpost2(2401:2500) = avg2(31021:31120);
avgpost2(2501:2600) = avg2(41021:41120);
avgpost2(2601:2700) = avg2(51021:51120);

plot2 = avgpost ./ avgpost2;
plot2ble = avgpost;
plot2con = avgpost2;


%t1 is just 200 microseconds before the bleach
t1=-200:-1;


t2(1:400) = 1:400;
t2(401:600) = 1001:1200;
t2(601:800) = 2001:2200;
t2(801:1000) = 3001:3200;
t2(1001:1200) = 4001:4200;
t2(1201:1400) = 5001:5200;
t2(1401:1600) = 6001:6200;
t2(1601:1800) = 7001:7200;
t2(1801:2000) = 8001:8200;
t2(2001:2200) = 9001:9200;
t2(2201:2300) = 10001:10100;
t2(2301:2400) = 20001:20100;
t2(2401:2500) = 30001:30100;
t2(2501:2600) = 40001:40100;
t2(2601:2700) = 50001:50100;


%now make the photoswitching plot
pstime = 1:620; %620 us of photoswitching data (200 "prebleach" 20 "bleach"
400 "postbleach")
%take the control data
pscon = avg2(801:1420) ./ max(avg2(801:1420));
%create the flat bleach plot
psble = mean(plot2(25:35))*ones(1,620);
%now make the photoswitching plot
psplot = psble ./ pscon';
psdata = psplot;
pscon2 = pscon';


x0psc = [0.1 400 0.8];
xpsc = lsqcurvefit('expfit',x0psc,pstime,pscon2);
fitps = expfit(xpsc,pstime);
pstau = xpsc(2);
psdelta = -xpsc(1);
```

```matlab
figure(1)
subplot(3,1,1);
plot(t1',plot1,'o',t2',plot2,'o')
xlim(xbound1)
ylim(ybound)
title('Corrected Curve')
subplot(3,1,2);
plot(t1',plot1ble,'o',t2', plot2ble,'o')
xlim(xbound1)
ylim(ybound)
title('Bleach')
subplot(3,1,3);
plot(t1',plot1con,'o',t2', plot2con,'o')
xlim(xbound1)
ylim(ybound)
title('Control')
xlabel('time (us)')

figure(2)
subplot(3,1,1);
plot(t1',plot1,'o',t2',plot2,'o')
xlim(xbound2)
ylim(ybound)
title('Corrected Curve')
subplot(3,1,2);
plot(t1',plot1ble,'o',t2', plot2ble,'o')
xlim(xbound2)
ylim(ybound)
title('Bleach')
subplot(3,1,3);
plot(t1',plot1con,'o',t2', plot2con,'o')
xlim(xbound2)
ylim(ybound)
title('Control')
xlabel('time (us)')


figure(3)
semilogx(t2',plot2,'o')
ylim(ybound)

figure(4)
plot(t2',plot2,'o')
ylim(ybound)
xlim([0 300])
set(gca,'XTick',0:10:300);
labels =
{'0','','','','','50','','','','','100','','','','','150','','','','','200','
','','','','250','','','','','300'};
set(gca,'XTickLabels',labels);
```

```matlab
%pointb_smallfile.m
global pstime psdata pstau psdelta xpsc
```

206

```
data = open([data_filename '.mat']);
avg1 = data.avg1;
avg2 = data.avg2;
totalblepts = data.avg1sets;
totalconpts = data.avg2sets;


xbound1 = [-200 10300];
xbound2 = [-200 50000];
ybound = [0.4 1.1];


plot1i = avg1(801:1000);
plot1renorm = avg2(801:1000);


plot1 = plot1i ./ plot1renorm;
plot1ble = plot1i;
plot1con = plot1renorm;


%Now process the postbleach data


avgpost(1:2700) = avg1(1021:3720);


avgpost2(1:2700) = avg2(1021:3720);


plot2 = avgpost ./ avgpost2;
plot2ble = avgpost;
plot2con = avgpost2;


%t1 is just 200 microseconds before the bleach
t1=-200:-1;


t2(1:400) = 1:400;
t2(401:600) = 1001:1200;
t2(601:800) = 2001:2200;
t2(801:1000) = 3001:3200;
t2(1001:1200) = 4001:4200;
t2(1201:1400) = 5001:5200;
t2(1401:1600) = 6001:6200;
t2(1601:1800) = 7001:7200;
t2(1801:2000) = 8001:8200;
t2(2001:2200) = 9001:9200;
t2(2201:2300) = 10001:10100;
t2(2301:2400) = 20001:20100;
t2(2401:2500) = 30001:30100;
t2(2501:2600) = 40001:40100;
t2(2601:2700) = 50001:50100;


%now make the photoswitching plot
pstime = 1:620; %620 us of photoswitching data (200 "prebleach" 20 "bleach"
400 "postbleach")
%take the control data
pscon = avg2(801:1420) ./ max(avg2(801:1420));
%create the flat bleach plot
psble = mean(plot2(25:35))*ones(1,620);
%now make the photoswitching plot
psplot = psble ./ pscon';
```

```matlab
psdata = psplot;
pscon2 = pscon';


x0psc = [0.1 400 0.8];
xpsc = lsqcurvefit('expfit',x0psc,pstime,pscon2);
fitps = expfit(xpsc,pstime);
pstau = xpsc(2);
psdelta = -xpsc(1);



figure(1)
subplot(3,1,1);
plot(t1',plot1,'o',t2',plot2,'o')
xlim(xbound1)
ylim(ybound)
title('Corrected Curve')
subplot(3,1,2);
plot(t1',plot1ble,'o',t2', plot2ble,'o')
xlim(xbound1)
ylim(ybound)
title('Bleach')
subplot(3,1,3);
plot(t1',plot1con,'o',t2', plot2con,'o')
xlim(xbound1)
ylim(ybound)
title('Control')
xlabel('time (us)')


figure(2)
subplot(3,1,1);
plot(t1',plot1,'o',t2',plot2,'o')
xlim(xbound2)
ylim(ybound)
title('Corrected Curve')
subplot(3,1,2);
plot(t1',plot1ble,'o',t2', plot2ble,'o')
xlim(xbound2)
ylim(ybound)
title('Bleach')
subplot(3,1,3);
plot(t1',plot1con,'o',t2', plot2con,'o')
xlim(xbound2)
ylim(ybound)
title('Control')
xlabel('time (us)')



figure(3)
semilogx(t2',plot2,'o')
ylim([-0.5 1.5])

figure(4)
plot(t2',plot2,'o')
ylim(ybound)
xlim([0 300])
```

```
set(gca,'XTick',0:10:300);
labels =
{'0','','','','','50','','','','','100','','','','','150','','','','','200','
','','','','250','','','','','300'};
set(gca,'XTickLabels',labels);
```

```
%expfit.m
function y=expfit(x,t)

y = x(1).*exp(-t./x(2)) + x(3);
```

The next subroutine *FRAPfitweightedpsc_2model.m* is listed below. It is dependent on

the following subroutines listed in alphabetical order: *meanvals2.m*, *ptFRAP.m*,

ptFRAPpsc.m, *ptFRAPpscweighted.m*, and *ptFRAPweighted.m*.

```
%FRAPfitweightedpsc_2model.m
global time data weightvect lowpt pstime z

time=t2;
data=plot2;


Fnotavg = mean(data(15:25));
Fnotmax = 1.1*Fnotavg;
Fnotmin = 0.90*Fnotavg;
Fnot = Fnotavg;

delmin = -1; %delmin = 1.2*del;
delmax = 0; %delmax = 0.8*del;

av=1;
timemat=reshape(t2(start:end),av,((length(time)-start+1)/av));
time=mean(timemat,1);
datamat=reshape(plot2(start:end),av,((length(data)-start+1)/av));
data=mean(datamat,1);
meant = meanvals2(t2);
meand = meanvals2(plot2);
n = size(timemat,2);
n1 = 20;
lowpt = 0; %0.9*mean(data(20:60));

%del = 0.09; %0.0525
fulltime = time; %start:10:50200;

weightvector(1:400) = ones(1,400);%400 points in 400 us
weightvector(401:2200) = 5*ones(1,1800);%200 points per 1000 us (500-
        1500,...,8500-9500)
weightvector(2201:2300) = 55*ones(1,100);%100 points per 5500 us (9500-15000)
```

```matlab
weightvector(2301:2700) = 100*ones(1,400);%100 points per 10000 us (15000-
      25000,...,45000-55000)

weightvect = reshape(weightvector(start:end),av,((length(weightvector)-
      start+1)/av));

lb = [];
ub = [];
options = optimset('Display','iter','Algorithm','levenberg-marquardt',
      'TolFun',10^-11,'TolX',10^-8,'FinDiffType','central');
ci = zeros(4,2);
xnot(1:2) = x0(1:2); xnot(3) = Fnot; xnot(4) = x0(3);
%model 1 diffusion and immoble frac
lb = [0 0.9999 Fnotmin 0];
ub = [10000 1 Fnotmax 2];

[x,resnorm,residual,exitflag,output,lambda,jacobian]=
      lsqnonlin('ptFRAPpscweighted',xnot,lb,ub,options);
if(calci == 1)
    ci = nlparci(x,residual,jacobian);
end
plusminus=((ci(:,2)-ci(:,1))/2)'; %calculates +/- value from confidence
      intervals
fit=ptFRAPpsc(x,fulltime);
x1b=x; resnorm1b=resnorm; plusminus1b=plusminus; fit1b=fit;
residual1b=residual; z1b = z;

%model 2 - full anomalous diff and immobile frac
lb = [0 0 Fnotmin 0];
ub = [10000 1 Fnotmax 2];

[x,resnorm,residual,exitflag,output,lambda,jacobian]=
      lsqnonlin('ptFRAPpscweighted',xnot,lb,ub,options);
if(calci == 1)
    ci = nlparci(x,residual,jacobian);
end
plusminus=((ci(:,2)-ci(:,1))/2)'; %calculates +/- value from confidence
      intervals
fit=ptFRAPpsc(x,fulltime);
x2b=x; resnorm2b=resnorm; plusminus2b=plusminus; fit2b=fit;
residual2b=residual; z2b = z;

%model 3 diffusion and immoble frac w/o PSC
lb = [0 0.9999 Fnotmin 0];
ub = [10000 1 Fnotmax 2];

[x,resnorm,residual,exitflag,output,lambda,jacobian]=
      lsqnonlin('ptFRAPweighted',xnot,lb,ub,options);
if(calci == 1)
    ci = nlparci(x,residual,jacobian);
end
plusminus=((ci(:,2)-ci(:,1))/2)'; %calculates +/- value from confidence
      intervals
fit=ptFRAP(x,fulltime);
x3=x; resnorm3=resnorm; plusminus3=plusminus; fit3=fit; residual3=residual;
```

```matlab
%model 4 - full anomalous diff and immobile frac w/o PSC
lb = [0 0 Fnotmin 0];
ub = [10000 1 Fnotmax 2];

[x,resnorm,residual,exitflag,output,lambda,jacobian]=
      lsqnonlin('ptFRAPweighted',xnot,lb,ub,options);
if(calci == 1)
    ci = nlparci(x,residual,jacobian);
end
plusminus=((ci(:,2)-ci(:,1))/2)'; %calculates +/- value from confidence
      intervals
fit=ptFRAP(x,fulltime);
x4=x; resnorm4=resnorm; plusminus4=plusminus; fit4=fit; residual4=residual;

%find BIC
rn = [resnorm1b resnorm2b];
K = [4 5];
BIC = (n*log(rn/n)) + log(n).*K;
BICF = BIC - min(BIC);
BICPercent = exp(-0.5*BICF) / sum(exp(-0.5*BICF));

%Find center resnorm

mresnorm1b = 0;

mresnorm2b = 0;
wv(1:6) = 1;
wv(7:15) = 5;
wv(16) = 55;
wv(17:20) = 100;
for i=1:20
    index = find(time > meant(i));

    mresnorm1b = mresnorm1b + (fit1b(index(1)) - meand(i))^2*wv(i)/meant(i);

    mresnorm2b = mresnorm2b + (fit2b(index(1)) - meand(i))^2*wv(i)/meant(i);
end
mrn = [mresnorm1b mresnorm2b];

mBIC = (n1*log(mrn/n1)) + log(n1).*K;
mBICF = mBIC - min(mBIC);
mBICPercent = exp(-0.5*mBICF) / sum(exp(-0.5*mBICF));


res1b = meanvals2([zeros(1,start-1) residual1b]);
res2b = meanvals2([zeros(1,start-1) residual2b]);
res3 = meanvals2([zeros(1,start-1) residual3]);
res4 = meanvals2([zeros(1,start-1) residual4]);

figure(10)
plot(pstime,pscon,'o',pstime,fitps)
xlim([0 620])
legend('Data','Fit','Location','SouthEast')
```

```matlab
title('Photoswitching Correction')
ylabel('normalized intensity')
xlabel('time (us)')

figure(12)
subplot(3,1,[1 2])
semilogx(time,data,'o',fulltime,fit1b,fulltime,fit2b,meant,meand,'x')
xlim([start 50000])
legend('Data','Normal Diffusion','Anomalous
Diffusion','Location','SouthEast')
title('Photoswitching Correction')
ylabel('normalized intensity')
xlabel('time (us)')
subplot(3,1,3)
semilogx(time,zeros(1,length(time)),meant,res1b,'x',meant,res2b,'x','MarkerSi
ze',10)
xlim([start 50000])

figure(13)
subplot(3,1,[1 2])
semilogx(time,data,'o',fulltime,fit3,fulltime,fit4,meant,meand,'x')
xlim([start 50000])
legend('Data','Normal Diffusion','Anomalous
Diffusion','Location','SouthEast')
title('No Photoswitching Correction')
ylabel('normalized intensity')
xlabel('time (us)')
subplot(3,1,3)
semilogx(time,zeros(1,length(time)),meant,res3,'x',meant,res4,'x','MarkerSize
',10)
xlim([start 50000])


figure(14)
subplot(2,1,1)
semilogx(time,residual1b,'.',time,zeros(1,length(time)),meant,res1b,'x','Mark
erSize',10)
xlim([start 50000])
subplot(2,1,2)
semilogx(time,residual2b,'.',time,zeros(1,length(time)),meant,res2b,'x','Mark
erSize',10)
xlim([start 50000])

x1bmat=[x1b;plusminus1b;100000*resnorm1b*ones(1,4)]
x2bmat=[x2b;plusminus2b;100000*resnorm2b*ones(1,4)]
x3mat=[x3;plusminus3;100000*resnorm3*ones(1,4)]
x4mat=[x4;plusminus4;100000*resnorm4*ones(1,4)]

Bounds = [Fnotmin Fnot delmin delmax]

saveas(12,[data_filename '_combo_psc.fig']);
saveas(13,[data_filename '_combo_nopsc.fig']);
saveas(14,[data_filename '_resdual.fig']);
```

```matlab
%meanvals2.m
function y = meanvals2(x)

y(1) = mean(x(101:150));
y(2) = mean(x(151:200));
y(3) = mean(x(201:250));
y(4) = mean(x(251:300));
y(5) = mean(x(301:350));
y(6) = mean(x(351:400));
y(7) = mean(x(401:600));
y(8) = mean(x(601:800));
y(9) = mean(x(801:1000));
y(10) = mean(x(1001:1200));
y(11) = mean(x(1201:1400));
y(12) = mean(x(1401:1600));
y(13) = mean(x(1601:1800));
y(14) = mean(x(1801:2000));
y(15) = mean(x(2001:2200));
y(16) = mean(x(2201:2300));
y(17) = mean(x(2301:2400));
y(18) = mean(x(2401:2500));
y(19) = mean(x(2501:2600));
y(20) = mean(x(2601:2700));
```

```matlab
%ptFRAP.m
function y=ptFRAP(x,t)

global wr wz

%functional form from corrected Feder, et al, article BiophysJ 100, 791;
%modified for 3D diffusion with additional denominator factor

G=x(1)*10^-6;
alpha=x(2);
Fpre=1;
F0=x(3);
Finf=x(4);

n=0:20; %seems to converge by 10 terms, so 20 should be plenty
[nmat,tmat]=meshgrid(n,t);

opt = optimset('Display','off');

R=(Finf-F0)/(Fpre-F0);
beta=lsqnonlin(@(x)sum(((-x).^n)./factorial(n)./(1+n).^(3/2))-
F0/Fpre,[1],[],[],opt);

%See Feder et al Biophys J 1996 70 2767
%Brown et al Biophys J 1998 77 2837
%Schnell et al J. Biomed Optics 2008 13(6) 064037
Fmat=((-beta).^nmat)./factorial(nmat)./(1+nmat.*(1+16*G.*(tmat.^alpha)./
      (alpha*wr^2)))./sqrt(1+nmat.*(1+16*G.*(tmat.^alpha)./(alpha*wz^2)));
F=Fpre*sum(Fmat,2)*R+(1-R)*F0;
```

213

```matlab
y=F';
```

```matlab
%ptFRAPpsc.m
function y=ptFRAPpsc(x,t)

global wr wz pstau psdelta xpsc z

%functional form from corrected Feder, et al, article BiophysJ 100, 791;

G=x(1)*10^-6;
alpha=x(2);
Fpre=1;
F0=x(3);
Finf=x(4);

n=0:20; %seems to converge by 10 terms, so 20 should be plenty
[nmat,tmat]=meshgrid(n,t);
l = length(t);
s = t(1);
tpsc = s:(l+s-1);
[nmat2,tpscmat] = meshgrid(n,tpsc);

opt = optimset('Display','off');
cont = 1:620;
curve = expfit(xpsc,cont);
fitcurve = F0 ./ curve;
z = lsqcurvefit('expfit',[psdelta pstau 0.8],cont,fitcurve,[],[],opt);

delta = z(1);
tau = z(2);
if(tau > 2000)
    delta = 0;
end

R=(Finf-F0)/(Fpre-F0);
beta=lsqnonlin(@(x)sum(((-x).^n)./factorial(n)./(1+n).^(3/2).*(1+delta))-
F0/Fpre,[1],[],[],opt);
%assume two-photon excitation and bleaching, m=2; b=2;
%See Feder et al Biophys J 1996 70 2767
%Brown et al Biophys J 1998 77 2837
%Schnell et al J. Biomed Optics 2008 13(6) 064037
l = length(t);
tpsc = 1:l;
Fmat=(R+delta.*exp(-tpscmat./tau)).*((-beta).^nmat)./factorial(nmat)./
      (1+nmat.*(1+16*G.*(tmat.^alpha)./(alpha*wr^2)))./sqrt(1+nmat.*(1+16*G.*
      (tmat.^alpha)./(alpha*wz^2)));
F=Fpre*sum(Fmat,2)+(1-R)*F0;

y=F';
```

```matlab
%ptFRAPpscweighted.m
```

```
function y=ptFRAPpscweighted(x)

global wr wz time data weightvect pstau psdelta xpsc z
t = time;

%functional form from corrected Feder, et al, article BiophysJ 100, 791;

G=x(1)*10^-6;
alpha=x(2);
Fpre=1;
F0=x(3);
Finf=x(4);

n=0:20; %seems to converge by 10 terms, so 20 should be plenty
[nmat,tmat]=meshgrid(n,t);
l = length(t);
s = t(1);
tpsc = s:(l+s-1);
[nmat2,tpscmat] = meshgrid(n,tpsc);

opt = optimset('Display','off');
cont = 1:620;
curve = expfit(xpsc,cont);
fitcurve = F0 ./ curve;
z = lsqcurvefit('expfit',[psdelta pstau 0.8],cont,fitcurve,[],[],opt);

delta = z(1);
tau = z(2);
if(tau > 2000)
    delta = 0;
end
R=(Finf-F0)/(Fpre-F0);
beta=lsqnonlin(@(x)sum(((-x).^n)./factorial(n)./(1+n).^(3/2).*(1+delta))-
F0/Fpre,[1],[],[],opt);

%assume two-photon excitation and bleaching, m=2; b=2;
%See Feder et al Biophys J 1996 70 2767
%Brown et al Biophys J 1998 77 2837
%Schnell et al J. Biomed Optics 2008 13(6) 064037
l = length(t);
tpsc = 1:l;
Fmat=(R+delta.*exp(-tpscmat./tau)).*((-beta).^nmat)./factorial(nmat)./
     (1+nmat.*(1+16*G.*(tmat.^alpha)./(alpha*wr^2)))./sqrt(1+nmat.*(1+16*G.*
     (tmat.^alpha)./(alpha*wz^2)));
F=Fpre*sum(Fmat,2)+(1-R)*F0;

y=(F'-data)./time.*weightvect;
```

```
%ptFRAPweighted.m
function y=ptFRAPweighted(x)

global wr wz time data weightvect
t = time;
```

```
%functional form from corrected Feder, et al, article BiophysJ 100, 791;

G=x(1)*10^-6;

Fpre=1;
F0=x(3);
Finf=x(4);

n=0:20; %seems to converge by 10 terms, so 20 should be plenty
[nmat,tmat]=meshgrid(n,t);

opt = optimset('Display','off');

R=(Finf-F0)/(Fpre-F0);
beta=lsqnonlin(@(x)sum(((-x).^n)./factorial(n)./(1+n).^(3/2))-
F0/Fpre,[1],[],[],opt);

%assume two-photon excitation and bleaching, m=2; b=2;
%See Feder et al Biophys J 1996 70 2767
%Brown et al Biophys J 1998 77 2837
%Schnell et al J. Biomed Optics 2008 13(6) 064037
l = length(t);

Fmat=((-beta).^nmat)./factorial(nmat)./(1+nmat.*(1+16*G.*(tmat.^alpha)./
      (alpha*wr^2)))./sqrt(1+nmat.*(1+16*G.*(tmat.^alpha)./(alpha*wz^2)));
F=Fpre*sum(Fmat,2)*R+(1-R)*F0;

y=(F'-data)./time.*weightvect;
```

The final subroutine listed in *loadandfit_2model.m* is *savetable_2model.m*. This script

saves the output table of the fitting results (Table E.1) to the file with the name

*data_filename*_table.dat. The script also calculates the value of D_{eff} for the output table.

```
%savetable_2model.m
fid = fopen([data_filename '_table.dat'],'w');

tau2 = (x2bmat(1,2)*wr^2/(6*x2bmat(1,1)*10^-6))^(1/x2bmat(1,2));
deff2 = wr^2 / (6*tau2*10^-6);

tau2err = (x2bmat(1,2)*wr^2/((x2bmat(1,1)+x2bmat(2,1))*6*10^-
6))^(1/x2bmat(1,2));
deff2err = (wr^2 / (6*tau2err*10^-6)) - deff2 ;

tau4 = (x4mat(1,2)*wr^2/(6*x4mat(1,1)*10^-6))^(1/x4mat(1,2));
deff4 = wr^2 / (6*tau4*10^-6);

tau4err = (x4mat(1,2)*wr^2/((x4mat(1,1)+x4mat(2,1))*6*10^-6))^(1/x4mat(1,2));
```

```
deff4err = (wr^2 / (6*tau4err*10^-6)) - deff4 ;


fprintf(fid,'Data : %s\t\t\t Data Pts:\t %f\t Control Pts:\t
%f\n',data_filename,totalblepts,totalconpts);

fprintf(fid,'Normal\t D\t Alpha\t F t=0\t F t=inf\t Delta\t Tau\n');
fprintf(fid,'Values\t %f\t %f\t %f\t %f\t %f\t
%f\n',x1bmat(1,1),x1bmat(1,2),x1bmat(1,3),x1bmat(1,4),z1b(1),z1b(2));
fprintf(fid,'95%% CI\t %f\t %f\t %f\t %f\t %f\t
%f\n',x1bmat(2,1),x1bmat(2,2),x1bmat(2,3),x1bmat(2,4),0,0);
fprintf(fid,'RN\t %f\t BIC\t %f\t BIC%%\t
%f\n',x1bmat(3,1),BICF(1),BICPercent(1));

fprintf(fid,'Anomalous\t Gamma\t Alpha\t Deff\t F t=0\t F t=inf\t Delta\t
Tau\n');
fprintf(fid,'Values\t %f\t %f\t %f\t %f\t %f\t %f\t
%f\n',x2bmat(1,1),x2bmat(1,2),deff2,x2bmat(1,3),x2bmat(1,4),z2b(1),z2b(2));
fprintf(fid,'95%% CI\t %f\t %f\t %f\t %f\t %f\t %f\t
%f\n',x2bmat(2,1),x2bmat(2,2),deff2err,x2bmat(2,3),x2bmat(2,4),0,0);
fprintf(fid,'RN\t %f\t BIC\t %f\t BIC%%\t
%f\n',x2bmat(3,1),BICF(2),BICPercent(2));

fprintf(fid,'Normal\t D\t Alpha\t F t=0\t F t=inf\n');
fprintf(fid,'Values\t %f\t %f\t %f\t
%f\n',x3mat(1,1),x3mat(1,2),x3mat(1,3),x3mat(1,4));
fprintf(fid,'95%% CI\t %f\t %f\t %f\t
%f\n',x3mat(2,1),x3mat(2,2),x3mat(2,3),x3mat(2,4));
fprintf(fid,'RN\t %f\n',x3mat(3,1));

fprintf(fid,'Anomalous\t Gamma\t Alpha\t Deff\t F t=0\t F t=inf\n');
fprintf(fid,'Values\t %f\t %f\t %f\t %f\t
%f\n',x4mat(1,1),x4mat(1,2),deff4,x4mat(1,3),x4mat(1,4));
fprintf(fid,'95%% CI\t %f\t %f\t %f\t %f\t
%f\n',x4mat(2,1),x4mat(2,2),deff4err,x4mat(2,3),x4mat(2,4));
fprintf(fid,'RN\t %f\n',x4mat(3,1));

fprintf(fid,'Start:\t %f\t Low F0:\t %f\t High F0:\t %f\t Tau:\t
%f\n',start,Fnotmin,Fnot,pstau);
fclose(fid);
```

E.2. Distribution model fitting program.

The following program was written and used to determine the distributions

presented in Chapter 4. The main program *fit_to_distribution.m* that is configured like

the FRAP fitting program described in section E.1. The data filename, point spread

function, and fitting start point are entered at the beginning of the script. The distribution

217

model uses a hundred FRAP curves as a basis set; therefore, the FRAP curve is over fitted. To minimize the influence of the initial guess and to remove "spikes" in the curve several fitting iterations are performed in the script. The initial distribution guess is made either as a flat line input, random noise, or as a log-normal distribution. A total of six fits of FRAP curve to the distribution are made. After the first, third, and fifth iterations, a mediation filter is used to smooth the distribution and the smoothed iteration is used as the initial guess for the next fitting iteration. After the second and fourth iterations, the resulting distribution is not only smoothed but then fit to a Gaussian. The resulting Gaussian is then used as the initial guess for the next round of fitting.

The script produces nine figures as an output. Output Figures 1-3 are the same as described in section E.1 (Figure E.1A-C). The next two figures (MatLab output Figures 11 & 12) display an anomalous fit to the data and the basis set of FRAP equations that are used to produce the distribution (Figure E.3). The final four figures display the fitting results and initial guesses used (Figure E.4). The routine *fit_to_distribution.m* relies on six subroutines. The following four subroutines are the same as used in the FRAP fitting program described in section E.1: *pointb.m* (or *pointb_smallfile.m*), *ptFRAPpscweighted.m, expfit.m,* and *ptFRAPpsc.m*. Two new subroutines, *distfit_weighted.m* and *gauss.m*, are listed after the code for the main program.
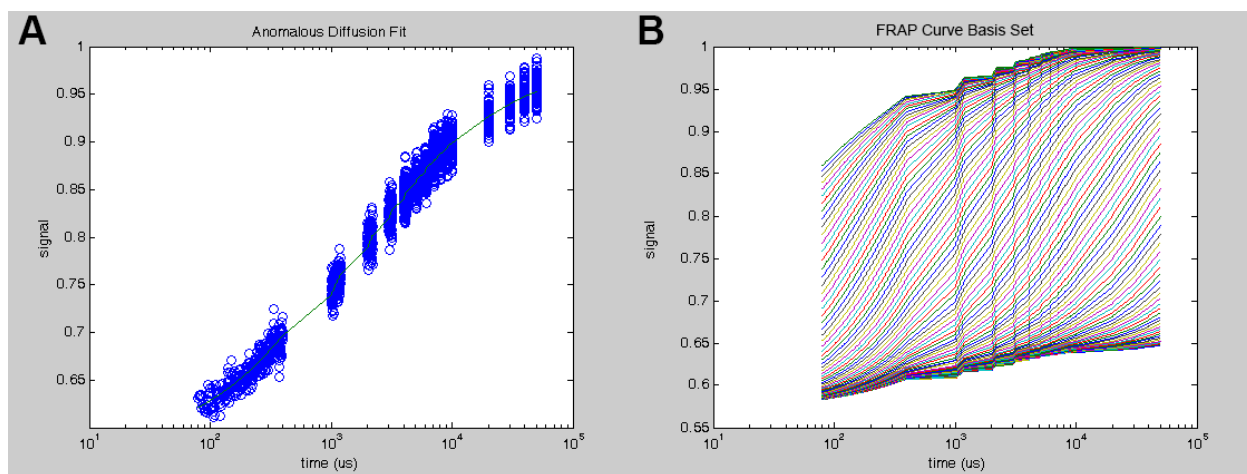
Figure E.3: Pre-fitting output figures of the distribution FRAP fitting script. (A) MatLab output Figure 11 shows the anomalous curve fit to the FRAP data. The anomalous fit is used to determine the photophysics parameters, the bleach depth, and the final recovery value that are implemented in the FRAP Curve basis set. (B) MatLab output Figure 12 shows the hundred curve basis set that will be used in the distribution modeling.
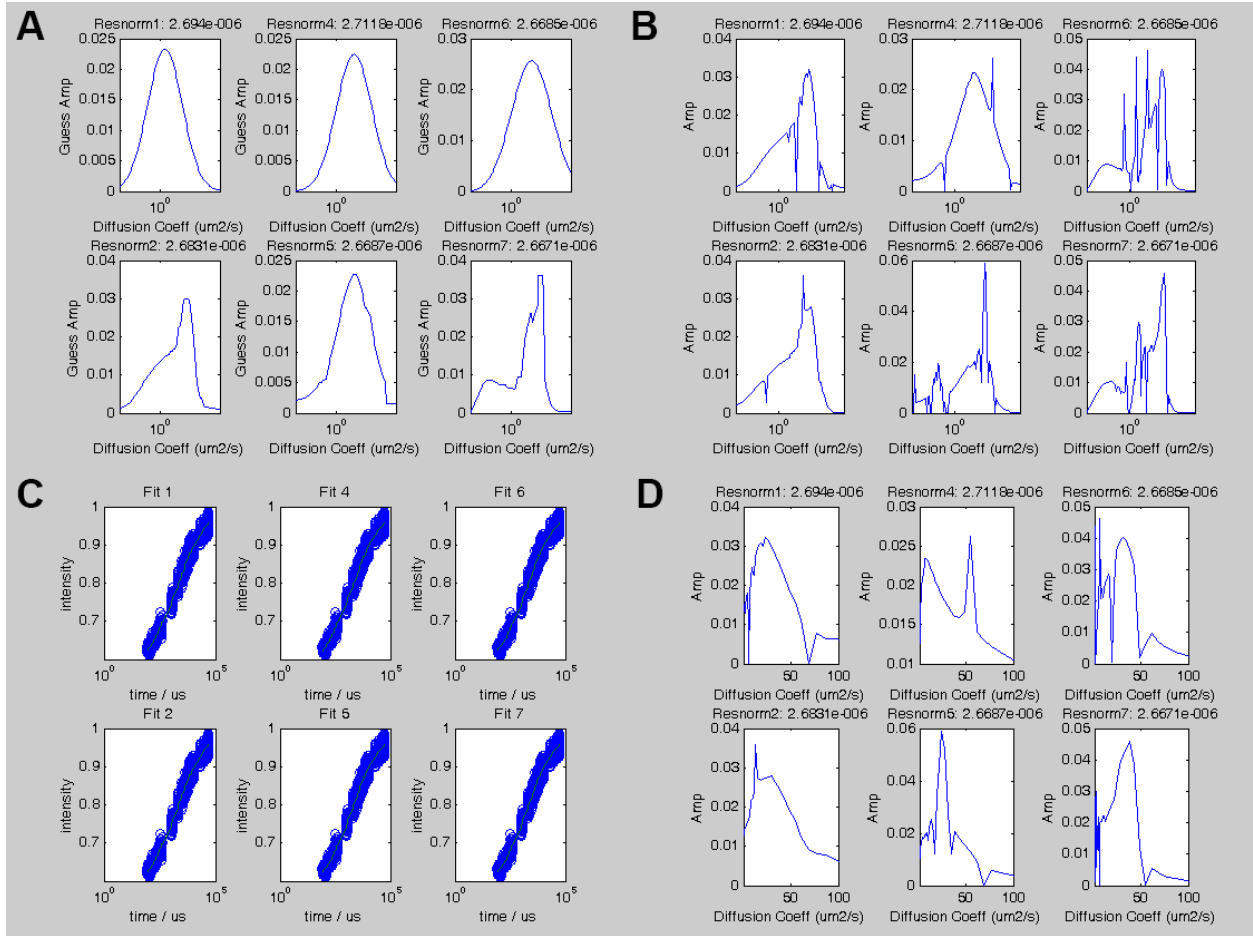
Figure E.4: Post-fitting output figures of the distribution FRAP fitting script. (A) MatLab output Figure 20 displays the initial guess used for each iteration of the fitting function. (B) MatLab output Figure 21 shows the resulting distribution on a logarithmic diffusion coefficient axes. The squared norm of the residuals are shown above each iteration. (C) MatLab output Figure 22 shows the FRAP data (blue circles) with the corresponding distribution fit line (green line). (D) MatLab output Figure 24 shows the same data as listed in panel B but now the data is shown zoomed in on a linear diffusion axis from 0 to 100 μm^2/s.

220

```matlab
%fit_to_distribution.m
clear all
close all
tic
global Dvect Fdist wr wz time data weightvect pstau psdelta xpsc z
wr = 0.305;
wz = 1.092;
data_filename = 'Rpb3_avg';
start = 80;

pointb %or pointb_smallfile

%Select data to be fitted and make weightvector
time = t2(start:end);
data = plot2(start:end);
weightvector(1:400) = ones(1,400);%400 points in 400 us
weightvector(401:2200) = 5*ones(1,1800);%200 points per 1000 us (500-
      1500,...,8500-9500)
weightvector(2201:2300) = 55*ones(1,100);%100 points per 5500 us (9500-15000)
weightvector(2301:2700) = 100*ones(1,400);%100 points per 10000 us (15000-
      25000,...,45000-55000)
weightvect = weightvector(start:end);

%First fit data to an anomalous subdiffusion model
Fnotavg = mean(plot2(15:25));
Fnotmax = 1.1*Fnotavg;
Fnotmin = 0.90*Fnotavg;

options = optimset('Display','iter','Algorithm','levenberg-marquardt',
      'TolFun',10^-11,'TolX',10^-8,'FinDiffType','central');
xnot = [80 0.8 Fnotavg 1];
lb = [0 0 Fnotmin 0];
ub = [10000 1 Fnotmax 2];

[xAnom,resnormAnom,residualAnom]=lsqnonlin('ptFRAPpscweighted',xnot,lb,ub,opt
ions);
fitAnom=ptFRAPpsc(xAnom,time);
zAnom = z;

figure(11)
semilogx(time,data,'o',time,fitAnom)
title('Anomalous Diffusion Fit')
xlabel('time (us)')
ylabel('signal')

%Now take the anomalous data and plug it into the dist fit
F0 = xAnom(3);
Fpre = 1;
Finf = xAnom(4);
delta = zAnom(1);
tau = zAnom(2);

nmax=10;
n = 0:nmax;
opt = optimset('Display','none');
```

```matlab
B=lsqnonlin(@(x)sum(((-x).^n)./factorial(n)./(1+n).^(3/2).*
    (1+delta))-F0/Fpre,[1],[],[],opt);

Dvect = logspace(-8,-3,100);
l = length(time);
s = time(1);
tpsc = s:(l+s-1);
[Dmat,tmat] = meshgrid(Dvect,time);
[Dmat2,tpscmat] = meshgrid(Dvect,tpsc);
clear Dmat2
Fdist = zeros(size(Dmat,1),size(Dmat,2));
for m=0:nmax
    Fdist = Fdist+(1+delta.*exp(-tpscmat./tau)).*((-B).^m)./factorial(m)./
        (1+m.*(1+16*Dmat.*(tmat.^1)./(1*wr^2)))./
        sqrt(1+m.*(1+16*Dmat.*(tmat.^1)./(1*wz^2)));
end

figure(12)
semilogx(time,Fdist)

%Random number initial guess
%x0 = rand(1,100);
%Flat line initial guess
%x0 = 0.01*ones(1,100);
%log-normal initial guess
mu = log(10^-4); sig = 2;
x0 = 1./(Dvect.*sqrt(2*pi*sig^2)).*exp(-((log(Dvect)-mu).^2/2/sig^2));
%Normalize
xnotD1 = x0 ./ sum(x0);
lb = zeros(1,100);
ub = ones(1,100);

maxit=200;
options = optimset('Display','iter','MaxIter',maxit,'TolFun',10^-10,
    'TolX',10^-10,'FinDiffType','central');

%first fit
[x,resnorm,residual]=lsqnonlin('distfit_weighted',xnotD1,lb,ub,options);
[FdistFITmat,tmat] = meshgrid(x,time);
fit = sum(FdistFITmat.*Fdist,2);
xDist1=x;
resnormDist1=resnorm;
fitDist1=fit;
residualDist1=residual;

%subtract baseline, smooth and fit again
y=x(1:100);
y2=nlfilter(y,[1,9],'median');
xnotD2(1:100)=y2;
[x,resnorm,residual]=lsqnonlin('distfit_weighted',xnotD2,lb,ub,options);
[FdistFITmat,tmat] = meshgrid(x,time);
fit = sum(FdistFITmat.*Fdist,2);
xDist2=x;
resnormDist2=resnorm;
fitDist2=fit;
residualDist2=residual;
```

```matlab
%fit Gaussian to output and fit again
y=x(1:100);
y2=nlfilter(y,[1,9],'median');
y3=nlfilter(y,[1,5],'mean');
idx=1:length(y3);
over=find(y3>(max(y3)/2));
yy=lsqcurvefit('gauss',[max(y3) find(y3==max(y3)) over(end)-over(1)],idx,(y3-
min(y3)));
y4=gauss(yy,idx);
xnotD4(1:100)=y4;
[x,resnorm,residual]=lsqnonlin('distfit_weighted',xnotD4,lb,ub,options);
[FdistFITmat,tmat] = meshgrid(x,time);
fit = sum(FdistFITmat.*Fdist,2);
xDist4=x; resnormDist4=resnorm; fitDist4=fit; residualDist4=residual;


options = optimset('Display','iter','MaxIter',maxit,'TolFun',10^-15,
        'TolX',10^-15,'FinDiffType','central');


%smooth again and fit again
y=x(1:100);
y2=nlfilter(y,[1,9],'median');
xnotD5(1:100)=y2;
[x,resnorm,residual]=lsqnonlin('distfit_weighted',xnotD5,lb,ub,options);
[FdistFITmat,tmat] = meshgrid(x,time);
fit = sum(FdistFITmat.*Fdist,2);
xDist5=x; resnormDist5=resnorm; fitDist5=fit; residualDist5=residual;


%one more time - fit a broad Gaussian to output and fit again
y=x(1:100);
y2=nlfilter(y,[1,9],'median');
y3=nlfilter(y,[1,5],'mean');
idx=1:length(y3);
over=find(y3>(max(y3)/2));
yy=lsqcurvefit('gauss',[max(y3) find(y3==max(y3)) over(end)-over(1)],idx,(y3-
min(y3)));
yy2=yy;
yy2(3)=1.5*yy(3);
y4=gauss(yy2,idx);
y5=(y4-y4(1)).*((y4-y4(1))>0);
xnotD6(1:100)=y5;
[x,resnorm,residual]=lsqnonlin('distfit_weighted',xnotD6,lb,ub,options);
[FdistFITmat,tmat] = meshgrid(x,time);
fit = sum(FdistFITmat.*Fdist,2);
xDist6=x; resnormDist6=resnorm; fitDist6=fit; residualDist6=residual;


%smooth again and fit again
y=x(1:100);
y2=nlfilter(y,[1,9],'median');
xnotD7(1:100)=y2;
[x,resnorm,residual]=lsqnonlin('distfit_weighted',xnotD7,lb,ub,options);
[FdistFITmat,tmat] = meshgrid(x,time);
fit = sum(FdistFITmat.*Fdist,2);
xDist7=x; resnormDist7=resnorm; fitDist7=fit; residualDist7=residual;


figure(21)
```

```
subplot(2,3,1)
semilogx(Dvect.*10^6,xDist1(1:100))
xlabel('Diffusion Coeff (um2/s)')
ylabel('Amp')
title(['Resnorm1: ' num2str(resnormDist1)])
xlim([0.01 1000])
subplot(2,3,4)
semilogx(Dvect.*10^6,xDist2(1:100))
xlabel('Diffusion Coeff (um2/s)')
ylabel('Amp')
title(['Resnorm2: ' num2str(resnormDist2)])
xlim([0.01 1000])
subplot(2,3,2)
semilogx(Dvect.*10^6,xDist4(1:100))
xlabel('Diffusion Coeff (um2/s)')
ylabel('Amp')
title(['Resnorm4: ' num2str(resnormDist4)])
xlim([0.01 1000])
subplot(2,3,5)
semilogx(Dvect.*10^6,xDist5(1:100))
xlabel('Diffusion Coeff (um2/s)')
ylabel('Amp')
title(['Resnorm5: ' num2str(resnormDist5)])
xlim([0.01 1000])
subplot(2,3,3)
semilogx(Dvect.*10^6,xDist6(1:100))
xlabel('Diffusion Coeff (um2/s)')
ylabel('Amp')
title(['Resnorm6: ' num2str(resnormDist6)])
xlim([0.01 1000])
subplot(2,3,6)
semilogx(Dvect.*10^6,xDist7(1:100))
xlabel('Diffusion Coeff (um2/s)')
ylabel('Amp')
title(['Resnorm7: ' num2str(resnormDist7)])
xlim([0.01 1000])

figure(20)
subplot(2,3,1)
semilogx(Dvect.*10^6,xnotD1(1:100))
xlabel('Diffusion Coeff (um2/s)')
ylabel('Guess Amp')
title(['Resnorm1: ' num2str(resnormDist1)])
xlim([0.01 1000])
subplot(2,3,4)
semilogx(Dvect.*10^6,xnotD2(1:100))
xlabel('Diffusion Coeff (um2/s)')
ylabel('Guess Amp')
title(['Resnorm2: ' num2str(resnormDist2)])
xlim([0.01 1000])
subplot(2,3,2)
semilogx(Dvect.*10^6,xnotD4(1:100))
xlabel('Diffusion Coeff (um2/s)')
ylabel('Guess Amp')
title(['Resnorm4: ' num2str(resnormDist4)])
xlim([0.01 1000])
subplot(2,3,5)
```

```
semilogx(Dvect.*10^6,xnotD5(1:100))
xlabel('Diffusion Coeff (um2/s)')
ylabel('Guess Amp')
title(['Resnorm5: ' num2str(resnormDist5)])
xlim([0.01 1000])
subplot(2,3,3)
semilogx(Dvect.*10^6,xnotD6(1:100))
xlabel('Diffusion Coeff (um2/s)')
ylabel('Guess Amp')
title(['Resnorm6: ' num2str(resnormDist6)])
xlim([0.01 1000])
subplot(2,3,6)
semilogx(Dvect.*10^6,xnotD7(1:100))
xlabel('Diffusion Coeff (um2/s)')
ylabel('Guess Amp')
title(['Resnorm7: ' num2str(resnormDist7)])
xlim([0.01 1000])

figure(22)
subplot(2,3,1)
semilogx(time,data,'o',time,fitDist1)
xlabel('time / us')
ylabel('intensity')
title('Fit 1')
xlim([1 100000])
subplot(2,3,4)
semilogx(time,data,'o',time,fitDist2)
xlabel('time / us')
ylabel('intensity')
title('Fit 2')
xlim([1 100000])
subplot(2,3,2)
semilogx(time,data,'o',time,fitDist4)
xlabel('time / us')
ylabel('intensity')
title('Fit 4')
xlim([1 100000])
subplot(2,3,5)
semilogx(time,data,'o',time,fitDist5)
xlabel('time / us')
ylabel('intensity')
title('Fit 5')
xlim([1 100000])
subplot(2,3,3)
semilogx(time,data,'o',time,fitDist6)
xlabel('time / us')
ylabel('intensity')
title('Fit 6')
xlim([1 100000])
subplot(2,3,6)
semilogx(time,data,'o',time,fitDist7)
xlabel('time / us')
ylabel('intensity')
title('Fit 7')
xlim([1 100000])
```

```matlab
figure(24)
subplot(2,3,1)
plot(Dvect.*10^6,xDist1(1:100))
xlabel('Diffusion Coeff (um2/s)')
ylabel('Amp')
title(['Resnorm1: ' num2str(resnormDist1)])
xlim([1 100])
subplot(2,3,4)
plot(Dvect.*10^6,xDist2(1:100))
xlabel('Diffusion Coeff (um2/s)')
ylabel('Amp')
title(['Resnorm2: ' num2str(resnormDist2)])
xlim([1 100])
subplot(2,3,2)
plot(Dvect.*10^6,xDist4(1:100))
xlabel('Diffusion Coeff (um2/s)')
ylabel('Amp')
title(['Resnorm4: ' num2str(resnormDist4)])
xlim([1 100])
subplot(2,3,5)
plot(Dvect.*10^6,xDist5(1:100))
xlabel('Diffusion Coeff (um2/s)')
ylabel('Amp')
title(['Resnorm5: ' num2str(resnormDist5)])
xlim([1 100])
subplot(2,3,3)
plot(Dvect.*10^6,xDist6(1:100))
xlabel('Diffusion Coeff (um2/s)')
ylabel('Amp')
title(['Resnorm6: ' num2str(resnormDist6)])
xlim([1 100])
subplot(2,3,6)
plot(Dvect.*10^6,xDist7(1:100))
xlabel('Diffusion Coeff (um2/s)')
ylabel('Amp')
title(['Resnorm7: ' num2str(resnormDist7)])
xlim([1 100])

toc
```

```matlab
%distfit_weighted.m
function y=distfit_weighted(x)

global Dvect time data weightvect Fdist

amp = x;

[ampmat,dummy] = meshgrid(amp,time);
[Dmat,dummy] = meshgrid(Dvect,time);
Fresult = sum(ampmat.*Fdist,2);


y=(Fresult'-data)./time.*weightvect;
```

```matlab
%gauss.m
function y=gauss(x,t)
```

```
y=x(1)*exp(-(t-x(2)).^2/(x(3))^2);
```

E.3. Quantification of immunocytochemistry results in HeLa cells.

The following program was written to quantify the fluorescence intensity in HeLa cells after immunocytochemistry staining with Alexa 488 as described in Chapter 6. Images for analysis were collected by epifluorescence imaging with a CCD camera. The images stored in png format were then processed by the *HeLa_CellCount_Boxes.m* program. This program selects for bright regions above the background (damaged cell nuclei). The program then quantifies the fluorescence intensity in each cell, excludes any bright regions (due to non-specific fluorophore clumping), averages the total fluorescent intensity of all the cells, and counts the number of cells present.

The script contains several adjustable parameters. The name of the image is set by the *name* string. The images contain a region of damaged cells that are selected by adjusting the variables *x* and *y* which correspond to the coordinates of the upper left corner of the bounding box shown in MatLab output Figure 1 (Figure E.5A). The length of the bounding box is set by the *xsize* and *ysize* parameters. Also in Figure 1 is a small box that is used the set the background fluorescence. Adjusting the variables *av1, av2,* and *thresh* determine the thresholding requirements to determine damaged cell nuclei. The mask is shown in MatLab output Figure 2 (Figure E.5B). The output variable *meanpix1_bkgcorr* gives the average intensity of the cells in Figure 2 after subtracting the background intensity. Output Figure 4 (Figure E.5D) is the same mask as Figure 2 except any cell with an average intensity greater than *cutoff* has been excluded from the analysis. The output variable *meanpix2_bkgcorr* gives the average intensity of the cells

in Figure 4 after subtracting the background intensity. Finally, output Figure 5 (Figure E.6) counts the number of cells in the region of interest. The cell count is given by the output variable *cells*. The minimum area for a cell is set by *cellsize* and the number of cells meeting this criterion are output in *cells_threshold*.
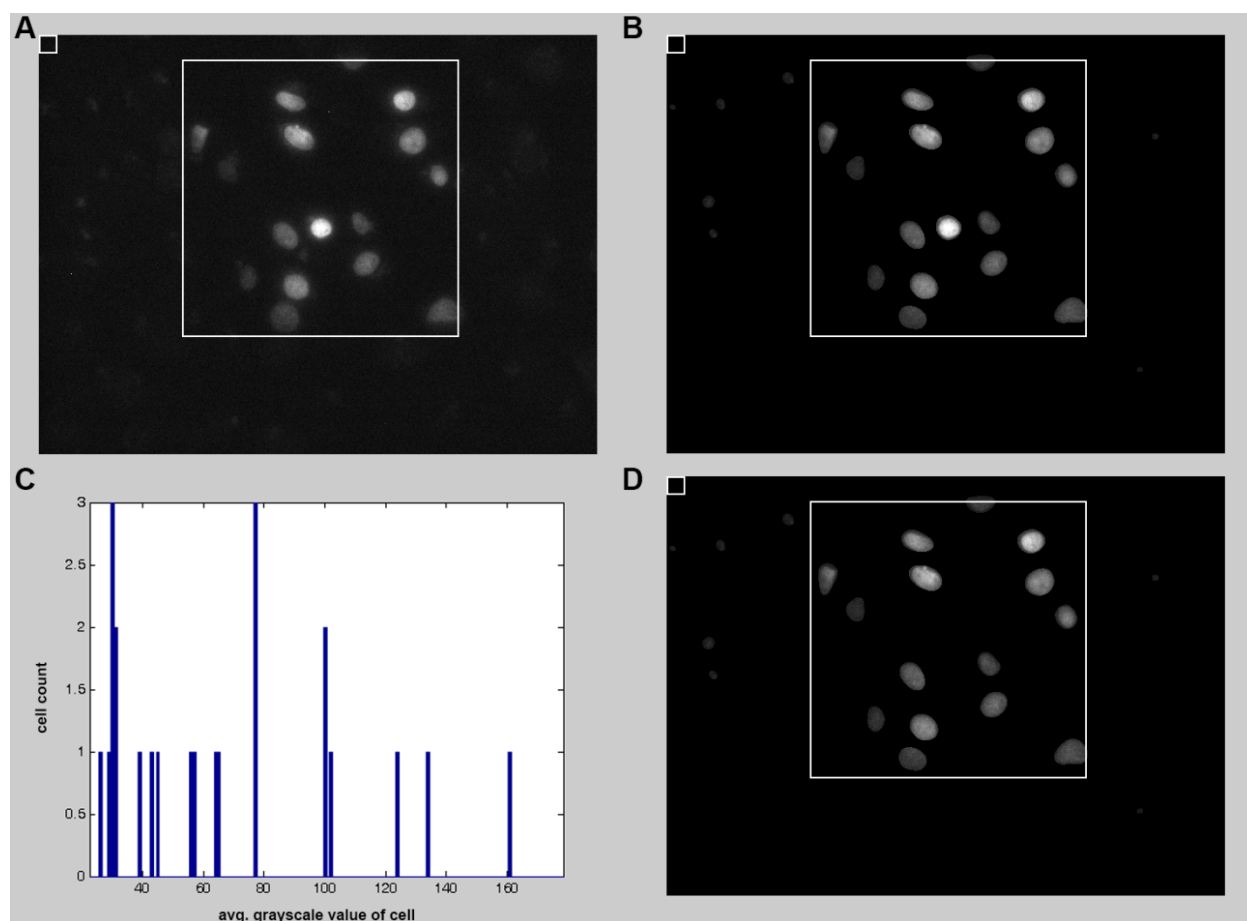
Figure E.5: MatLab figure output of the HeLa cell counting program. These figures are used to adjust parameters of the program to ensure that the cell region is properly bound and any non-specific, bright staining regions are excluded. (A) Figure 1 output from the MatLab program. This figure shows the original image with the bounding boxes for the cells that are to be quantified (large box) and the fluorescence background for background subtraction (small box in upper left hand corner). (B) Figure 2 output from the MatLab program. This figure shows the original image multiplied by a binary mask to only show the cell nuclei that meet the thresholding requirements. (C) Figure 3 output from the MatLab program. This figure is a histogram of the cellular intensities. Bright outliers are isolated using this histogram. For the purposes of this figure, the bright threshold is set to a grayscale value of 150. (D) Figure 4 output from the MatLab program. The same data as in panel B except the cells with an average intensity above 150 grayscale value have been excluded. Note that the bright cell near the middle of the box in panel B is gone in this panel.
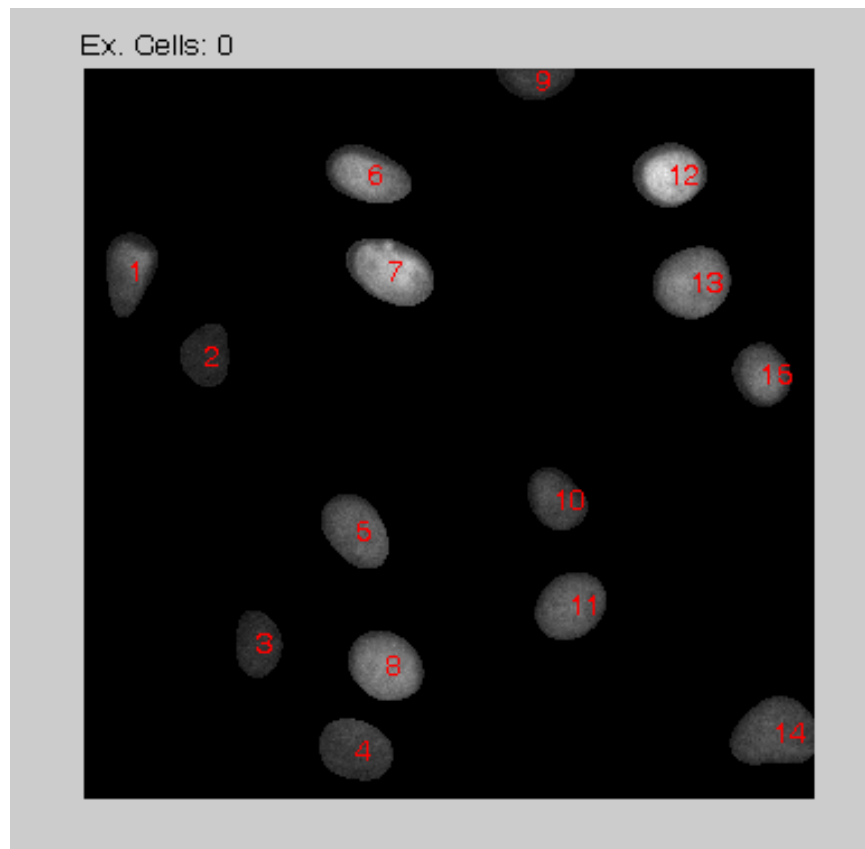
229

Figure E.6: MatLab figure output of the HeLa cell counting program identifying which cells were counted by the program. Any cells that were exclude due to having too small of an area are listed at the top by number to the right of "Ex. Cells:".

```
%HeLa_CellCount_Boxes.m
clear all

av1=7;
av2=12;
thresh=1.5;
cutoff=150;
name='point1.png';

%box
x = 170;
y = 30;
xsize = 325;
ysize = 325;

xbkg = 1;
ybkg = 1;
cellsize = 150;
textcolor = 'r';

A = 256*uint16(imread(name));
A_box = A;
A_box(y:y+ysize,x:x+1) = 65536;
A_box(y:y+1,x:x+xsize) = 65536;
A_box(y:y+ysize,x+xsize:x+xsize+1) = 65536;
A_box(y+ysize:y+ysize+1,x:x+xsize+1) = 65536;
A_box(ybkg:ybkg+20,xbkg:xbkg+1) = 65536;
A_box(ybkg:ybkg+1,xbkg:xbkg+20) = 65536;
A_box(ybkg:ybkg+20,xbkg+20:xbkg+21) = 65536;
A_box(ybkg+20:ybkg+21,xbkg:xbkg+21) = 65536;
figure(1); imshow(A_box)

H1=fspecial('gaussian',40,av1);
H2=fspecial('gaussian',40,av2);
a1=imfilter(A,H1,'replicate');
a2=imfilter(A,H2,'replicate');
a=a1-a2;

a_bw=medfilt2(a>(thresh*256));
a_bw2=bwmorph(a_bw,'open',inf);
a_bw3=imfill(a_bw2,'holes');

Amasked1=uint16(a_bw3).*A;
Am_box1 = Amasked1;
Am_box1(y:y+ysize,x:x+1) = 65536;
Am_box1(y:y+1,x:x+xsize) = 65536;
Am_box1(y:y+ysize,x+xsize:x+xsize+1) = 65536;
Am_box1(y+ysize:y+ysize+1,x:x+xsize+1) = 65536;
Am_box1(ybkg:ybkg+20,xbkg:xbkg+1) = 65536;
Am_box1(ybkg:ybkg+1,xbkg:xbkg+20) = 65536;
Am_box1(ybkg:ybkg+20,xbkg+20:xbkg+21) = 65536;
Am_box1(ybkg+20:ybkg+21,xbkg:xbkg+21) = 65536;

figure(2), imshow(Am_box1)
```

```
bkg=mean2(A(ybkg:20+ybkg,xbkg:20+xbkg))/256;
meanpix1=sum(sum(Amasked1(y:y+ysize,x:x+xsize)))/sum(sum(a_bw3(y:y+ysize,x:x+
xsize)))/256;
meanpix1_bkgcorr=meanpix1-bkg

number_bins=20;
L=bwlabel(a_bw3);
objects=max(max(L));
a_bw4=logical(zeros(size(a_bw3)));
for i=1:objects
    av(i)=sum(sum(uint16(L==i).*A))./sum(sum(uint16(L==i)))/256;
    if av(i)<cutoff
        a_bw4=a_bw4+(L==i);
    end
end

bins=(floor(0.9*min(av))):(ceil(1.1*max(av)));
figure(3)
hist(av,bins), axis tight
avg=mean(av);
stdev=std(av);
av_2stdev=avg+2*stdev;

Amasked2=uint16(a_bw4).*A;
Am_box2 = Amasked2;
Am_box2(y:y+ysize,x:x+1) = 65536;
Am_box2(y:y+1,x:x+xsize) = 65536;
Am_box2(y:y+ysize,x+xsize:x+xsize+1) = 65536;
Am_box2(y+ysize:y+ysize+1,x:x+xsize+1) = 65536;
Am_box2(ybkg:ybkg+20,xbkg:xbkg+1) = 65536;
Am_box2(ybkg:ybkg+1,xbkg:xbkg+20) = 65536;
Am_box2(ybkg:ybkg+20,xbkg+20:xbkg+21) = 65536;
Am_box2(ybkg+20:ybkg+21,xbkg:xbkg+21) = 65536;
figure(4), imshow(Am_box2)
meanpix2=sum(sum(Amasked2(y:y+ysize,x:x+xsize)))/sum(sum(a_bw4(y:y+ysize,x:x+
xsize)))/256;
meanpix2_bkgcorr=meanpix2-bkg

a_interest = a_bw4(y:y+ysize,x:x+xsize);

[L cells] = bwlabel(a_interest);
cells
STATS = regionprops(L,'basic');
smallcells = 0;
scidenity = 0;
for i=1:cells
    centroid(i,1) = STATS(i).Centroid(1,1);
    centroid(i,2) = STATS(i).Centroid(1,2);
    area(i) = STATS(i).Area;
    if(area(i) < cellsize)
        smallcells = smallcells + 1;
        scidenity(smallcells) = i;
    end
end
cells_threshold = cells - smallcells
figure(5)
```

```
imshow(uint16(a_interest).*A(y:y+ysize,x:x+xsize))
for i=1:cells
    text(centroid(i,1),centroid(i,2),num2str(i),'Color',textcolor)
end
text(0,-10,['Ex. Cells: ' num2str(scidenity)],'Color','k')
```

REFERENCES

1. Dickson, R. M.; Cubitt, A. B.; Tsien, R. Y.; Moerner, W. E. On/off blinking and switching behaviour of single molecules of green fluorescent protein. *Nature* **1997**, *388*, 355-358.

2. Krichevsky, O.; Bonnet, G. Fluorescence correlation spectroscopy: the technique and its applications. *Rep. Prog. Phys.* **2002**, *65*, 251-297.

3. Elson, E. L. Fluorescence Correlation Spectroscopy and Photobleaching Recovery. *Annu. Rev. Phys. Chem.* **1985**, *36*, 379-406.

4. Yao, J.; Ardehali, M. B.; Fecko, C. J.; Webb, W. W.; Lis, J. T. Intranuclear distribution and local dynamics of RNA polymerase II during transcription activation. *Mol. Cell* **2007**, *28*, 978-990.

5. Periasamy,N.; Verkman, A.S Analysis of Fluorphore Diffusion by Continuous Distributions of Diffusion Coefficients: Application to Photobleaching Measurements of Multicomponent and Anomalous Diffusion. *Biophys. J.* **1998**, *75*, 557.

6. Guild, J. B.; Xu, C.; Webb, W.W. Measurement of group delay dispersion of high numerical aperture objective lenses using two-photon excited fluorescence. *Appl. Opt.* **1997**, *36*, 397-401.